Sources of solutes, groundwater fluxes and weathering processes in an active mountain belt, Taiwan

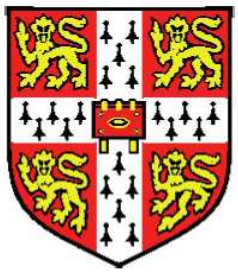

Caroline Elizabeth Anne Martin

St John's College and the Department of Earth Sciences

University of Cambridge

This thesis is submitted for the degree of

Doctor of Philosophy

September 2013

Declaration

This dissertation is the result of my own work and includes nothing which is the outcome of work done in collaboration, except as declared in the Acknowledgements and stated in the main body of the text. It is not substantially the same as any other work that has been or shall be submitted for any other qualification at the University of Cambridge or any other institution. This thesis does not exceed the total page limit of 275, or the limit of 225 pages of text, figures, bibliography and appendices (except data tables), as approved for the Department of Earth Sciences by the Degree Committee for the Faculty of Earth Sciences and Geography.

Caroline Elizabeth Anne Martin

20th of September 2013

Acknowledgements

Like a landscape, my course towards the PhD has been filled with ups and downs which, with the passing of time, have been worn gently smooth.

I wish to thank the people with whom I have shared my time with here for their many kindnesses and shows of friendship. The efforts of, in the order in which we met, Mike Bickle, Niels Hovius and Albert Galy, have left no possible area of supervision unfilled. They never wasted an opportunity to bestow on me a share of their wisdom and wisdom never came in such a diverse arrangement. It is as a result of their sound support and our insightful discussions that have enabled me to write this book. If I could take one thing from each of them with me on my way, from Mike it would be his openness that greeted me every time, without exception, when I popped my head through his door along with a query into my health and an invitation to sit down. Mike, it never mattered what it was you were doing that I was interrupting: thank you for always welcoming me and for being so consistently and thoroughly knowledgeable and helpful. It is a wonderful thing to be understood, and for this reason, from Niels, it is his eloquence that I would take. Niels, for demanding from me an effort towards the same in return, thank you, for you have taught me the value of communication. From Albert, I will keep a segment of his childlike wonder, out of which flashes of magic sometimes spark. Albert, thank you for inspiring me, and for never once suggesting that anything was merely good enough.

The master, fellows, scholars and staff of St. John's College provided a setting of domestic luxury and cultural opulence. Special thanks go to Nick McCave, whose scientific endeavour enticed me to come to Cambridge and whose reference made it financially possible. Also to Sue Colwell, whose tireless activity for the benefit of her graduate students ensured that I, and many others, enjoyed security and peace of mind throughout. To Pat Boyde for his charming role as our Borderer, who brought me on ancient thespian journeys and even put me on the stage. I will be forever grateful to Rita Barnes, our bedder at 12 Madingley Road, who humbled me daily with her motherly care and attention, bespeaking her selfless character and innate kindness.

The faculty, staff and fellow students of the Department of Earth Sciences comprised my home in Cambridge. In particular, thank you to Vicky Rennie, for our sisterly bond and to Yama Dixit for her friendliness, generosity, buoyancy and

humour. Also, thanks to Hazel Chapman and Sasha Turchyn for their kind support, Jo Smith for her staid and solid example and Rob Sparkes for his brotherly affection, and to Peter Friend, Alan Smith, Ken McNamara and the Friday Running Club and all who talked with me at morning coffee and shared other parts of their days.

Leanne Lacey has been the true sister I never had and I thank her for her unconditional love. I also thank many friends and colleagues for their great company and active support over many years, and in particular: Edmund O'Toole, Celine Maher, Katriona McNamara, Miriam O'Grady, Jack McCafferty, Tan Nguyen, João Abreu, David Conlon, Tom Nolan, Luke Butcher, Damien Calmels, Josh West, Jason Day, Martin Walker, Mervyn Greaves, James Rolfe, Sarah Humbert, Simon Crowhurst, Iris Buisman, Shunji Ouchi, Paul Wilson, Colin Brown, Paul Ryan, Mike Williams, John Murray, Eve Daly, Tiernan Henry, Kate Moore, Martin Feely, Ian Somerville, Jay Gregg, Liviu Giosan, Rob Evans, and Lloyd Keigwin.

The O'Reilly Foundation, the Irish Fulbright Association and St. John's College Benefactors' Fund supported my maintenance and university fees. The field work and geochemical analyses were funded by the UK Natural Environment Research Council grant NE/E003192/1 and a Royal Society International Joint Project. The Learning and Research Fund offered by St. John's College amply supported my attendance at several international conferences and other such research related trips and expenses. Many people gave their time freely in assisting with the field work in Taiwan, but in particular, I'd like to thank Hongey Chen, Ming-Jame Horng, Chung-Ho Wang, Chen-Feng You, Meng-Chiang Chen, Nien-Chiao Tsou, David Chang, brothers Sui-Hsien Chan and Sui-Ming Chan and In-Tian Lin.

I thank my Mam and Dad for everything. In particular, thank you Mam for your spontaneity, your wicked sense of humour and your terrific company, usually on the phone, but no matter. And thanks Da, whose gifts of moral guidance, intellectual insight, poetical wonderment, competitive fun and boundless adventure are mere appendages against his core of benevolence and humane example, for the Elephant Stone and the Black Hills and the Natural History Museum. I love you both.

My darling husband, Deep, whose love has infused every beautiful and happy thought and feeling that I've had during the past four years, showered me with utter devotion. He came with me to Taiwan to collect samples and to keep the hornets away and still honeymooned with me later on the Skye field trip. Without you, darling, there would have been little reason to endeavour to succeed.

Sources of solutes, groundwater fluxes and weathering processes in an active mountain belt, Taiwan

Caroline Elizabeth Anne Martin

Chemical weathering is the chemical dissolution of rocks at and near Earth's surface. Chemical weathering is important for climate stabilisation, regulating ocean chemistry, nutrient supply and landscape evolution. Chemical weathering most rapidly occurs where physical conditions are such that fresh mineral surfaces are readily replenished and where the rates of surface runoff are high. This thesis investigates the role of groundwater in transporting chemical weathering fluxes directly to the ocean, and develops an understanding of the link between physical erosion and chemical weathering.

The tectonically and climatically hyperactive island of Taiwan, with extreme rainfall and some of the highest physical erosion rates on record was chosen for this study because it offers an excellent combination of physical attributes and ease of access. In Taiwan, some of the processes pertinent to chemical weathering, such as coupled erosion and mineral dissolution, are observable on the timescale of months, which together with its accessibility makes it the ideal location in which to study chemical weathering. More than 150 groundwater samples and several surface water samples were collected from two distinct settings in Taiwan. The first was the deep coastal plain alluvial-fill aquifers that fringe the high mountain topography along the western margin of Taiwan. Several government-managed monitoring wells were granted access to for the purpose of groundwater collection from two of these coastal plains. The second was the bedrock-hosted aquifers in the elevated uplands of the island. For groundwater access in these steeply-elevated catchments, two distinct sets of disused transport tunnels, from inside of which percolating drip-waters were recovered, were exploited.

Three principal lines of inquiry were followed. First, the sources of dissolved mass integrated in coastal plain aquifer systems were delineated so as to distinguish solutes resulting from local and near-local rock-water interactions from those derived directly from the modern ocean and atmosphere. To do this, several distinct sources of solutes were considered, and the end-member chemistries were used to quantify and

trace their relative variability throughout the drilled depths of the sampled basins. Second, the amount of this weathered mass that is potentially available for discharge to the ocean was quantified with a view to assessing the importance of groundwater chemical fluxes relative to solute delivery to the ocean by rivers. For this, the physical parameters governing groundwater flow in the coastal aquifers were assessed and combined with the results of major chemical analyses of groundwater to compute subsurface chemical fluxes. In addition, discharge data and the analyses of water chemistry from two major rivers were used to compute surface chemical fluxes with which to compare to the subsurface counterparts. Third, the interplay between rapidly eroding hillslopes and chemical weathering was investigated towards understanding the link between physical erosion and chemical weathering. The principal data-set for this consisted of a groundwater time series that was collected from drip sites inside a bedrock tunnel that cut through an actively eroding mountain ridge. The spatial and temporal chemical variability of this groundwater was related to the effects of a major landslide that disrupted the overlying hillslope during the sampling campaign.

Results show that chemical weathering is a function of lithology and groundwater residence times in alluvial-fill coastal plains. The groundwater chemistry in both plains is derived from four distinct sources; rainwater, hydrothermally sourced water, seawater (ancient and modern) and from the dissolution of minerals within the sediments of the plains and from the surrounding hillslopes. Mineral formation involving Na^+, K^+ and SO_4^{2-} is observed in localised regions of the aquifers, but most samples record increases in silicate-derived components (Na^+ and SiO_2) and a decrease in Ca^{2+}, reflecting positive chemical weathering of silicates and precipitation of secondary calcite along the groundwater flow paths. The groundwater weathering fluxes from both plains range between 1.4 % and 4.6 % for Ca^{2+}, Mg^{2+}, K^+, $SO_4^{2-,}$ Sr^{2+} and Li^+, between 5.0 % and 6.1 % for Na^+ and SiO_2, and are 11.8 % for Ba^{2+} of total runoff, (combined surface and subsurface chemical fluxes), demonstrating that subsurface weathering fluxes in the drilled depth of the plains (~300 m) are modest. An assessment of tunnel drip-waters collected before and after a major landslide that had occurred above the tunnel in question shows that in rapidly-eroding regions like Taiwan, chemical fluxes are tightly controlled by geomorphic processes. It is shown that landslides drive weathering reactions in the deep biosphere, highlighting the coupled behaviour between the carbon, sulphur and oxygen cycles and the importance of the climate-erosion feedback in active mountain belts.

Contents

List of figures and plates

List of tables

"How, as the wind sweeps on, upon these breezy downs, it tracks its flight in darkening ripples on the grass, and smoothest shadows on the hills! Look round and round upon this bare bleak plain, and see even here, upon a winter's day, how beautiful the shadows are! Alas! it is the nature of their kind to be so. The loveliest things in life… are but shadows; and they come and go, and change and fade away, as rapidly as these!"—Charles Dickens

This book is dedicated to my parents and to my and Deep's first little one who has been keeping me most intimate company during the write up.

Chapter 1

Introduction

1.1 Summary

In this thesis I endeavour to assess the activities of groundwater circulation and subsurface biogeochemical processes in the active mountain belt system that is the island of Taiwan within the context of some of the outstanding questions related to the chemical weathering of Earth's continents. Herein the first principles of hydrogeology are coupled with concepts of aqueous chemistry and rock-water interactions (low-temperature geochemistry) in a venture to define some aspects of the participation of groundwater in the transfer of dissolved mass from the continents to the ocean.

1.2 Primary aims, major questions and thesis structure

The aim of this thesis is to understand the activity of groundwater in the chemical weathering factory of an active mountain belt system. Fundamental concerns are constraining the geochemical sources of solutes in aquifers and quantifying the rates of dissolved mass flow through the subsurface to track the weathering history of groundwaters and to resolve some of the controls on chemical weathering in fractured bedrock host media. The surface processes that initiate chemical weathering reactions in the subsurface and the role of different weathering agents are of particular interest. Through investigating the mechanisms that govern groundwater chemistry an effort has been made to understand how the chemical weathering of active mountain belts could potentially impact on global climate and ocean geochemical budgets. The specific questions towards addressing these goals that this thesis endeavours to answer are:

1. What is the chemical variability of groundwater with depth and along subsurface flow paths within major aquifers of an active mountain belt system?
2. What are the sources of dissolved mass available for discharge to the ocean through an active mountain belt system?

3. How does the magnitude of geochemical fluxes derived from chemical weathering processes in the subsurface and discharged to the ocean through outflow points along the continental shelf compare to those delivered to the coastal ocean by surface runoff?
4. Where in the subsurface of an active mountain belt is chemical weathering happening?
5. How do surface processes affect chemical weathering responses in the deeper subsurface?
6. What are the respective roles of carbonic and sulphuric acids in the weathering of fractured-bedrock host media and how do their particular contributions to weathering processes in an active mountain belt bear on the carbon, sulphur and oxygen cycles?

Following this chapter, in Chapter 2, the case study locations selected on the island of Taiwan for addressing the research aims of this thesis are described and illustrated in detail. The geographic, tectonic, geologic and climatic characteristics of Taiwan as a whole are outlined together with detailed descriptions of the hydrogeology and the general groundwater chemical characteristics of the specific locations studied.

In Chapter 3 the sampling strategies and collection procedures are outlined together with details of the sample preparation techniques, geochemical methods and analytical techniques used to ascertain the compositions of the collected materials.

Chapter 4 presents results of the chemical analysis of groundwaters and river waters from two of the island's main aquifers, which are in the alluvial-fill coastal plains of west and southwest Taiwan, respectively. The compositionally different sources giving rise to the dissolved mass in these aquifers are constrained using end-member chemical mixing relationships and the relative magnitudes of dissolved-mass contributions from each source are calculated.

In Chapter 5 an assessment of the two aquifers' physical properties is combined with the source-water characterisation developed in Chapter 4 to compute the subsurface chemical fluxes resulting from rock-water interactions that are potentially available for discharge to the ocean in that region. The subsurface chemical fluxes are compared to the transfer of dissolved mass to the ocean via the major sources of surface runoff along Taiwan's western and southwestern margins. In addition, an evaluation of the geochemical

fluxes is presented in the context of other estimates of groundwater flow in the studied regions, and the subsurface chemical fluxes are compared to analogous global estimates.

Chapter 6 explores the chemical variability and mixing relationships of groundwaters collected from two fractured-bedrock aquifers in central and northeast Taiwan, respectively, and of how such might be related to the thickness of the rock masses and geological structure above the groundwater discharge points. The fundamental impact of a major geomorphological perturbation on primary and secondary chemical and biogeochemical weathering processes in the subsurface of the bedrock aquifer in the northeast is addressed. In particular, a time series of groundwater chemistry collected along an array inside a 520 m-tunnel overlain by up to 200 m of rock-mass is assessed, where special focus is placed on the change in chemistry and on the ensuing geochemical reactions observed after a major landslide had occurred in the middle of the sampling campaign. The relative roles of carbonic and sulphuric acids at depth in responding to a large-scale surface disruption are observed and the importance of their respective processes within the carbon, sulphur and oxygen cycles is proposed.

Where appropriate, there are sections at the ends of Chapters 4, 5 and 6 addressing the respective results within the wider contexts of global weathering cycles and ocean geochemical budgets, and in which potential related research avenues for the future are suggested. Selected parts of Chapters 4 and 5 have been combined and published by Martin et al. (2013).

Chapter 7 presents a summary of the central findings that are presented and discussed in the main body of the thesis.

The remaining sections of this chapter outline the motivation behind studying chemical weathering and present the wider context within which the main findings of this thesis offer further understanding. The reasons for addressing the role of groundwater in relation to chemical weathering are suggested and a summary of the chemical characteristics of groundwater that need to be considered before interpreting chemical weathering processes in the subsurface is presented. In addition, the all important question of why Taiwan was chosen as a case study is addressed.

1.3 Motivation

Chemical weathering of Earth's crust exerts a primary control on ocean geochemical budgets. The weathering of silicate minerals in particular, through consumption of atmospheric CO_2, is thought to regulate the global carbon cycle and thus mediate climate over geological timescales (Aumont et al. 2001; Berner et al. 1983; Gislason et al. 2009; Walker et al. 1981). It is continental chemical weathering and the subsequent delivery of dissolved mass to the ocean, which in conjunction with the counterpart processes of carbonate precipitation, ocean-plate subduction with related volcanism and metamorphic de-gassing that is thought to maintain long-term equable conditions for life on Earth (e.g. Kasting 1987). Furthermore, biogeochemical cycles are maintained and balanced by the delivery of fluids to the terrestrial and marine sectors of the biosphere that are laden with nutrients resulting from chemical weathering. Further still, the disaggregated products of rock weathering serve as support for root anchorage along valleys and hillslopes, and thus the effect of water flowing through the subsurface is to control aspects of landscape evolution (Sharp 1982; Anderson 2012). In turn, during landscape evolution, weathering converts solid rock mass into erodible material.

One major objective in the field of geochemistry has been to quantify the dissolved mass in the world's major rivers that is discharged to the oceans (e.g. Garrels and Mackenzie 1971; Gaillardet et al. 1999) and to constrain the chemical pathways that give rise to these geochemical fluxes. This is necessary to understand past and present ocean chemistry and how global climate is regulated over geological timescales (Berner et al. 1983). Dissolved elements delivered to the oceans are returned to the solid Earth by the biogenic and the abiotic trapping of materials that accumulate as sediments on the ocean-floor, and through interaction with the oceanic crust at hydrothermal vent settings and mid-ocean ridges. It is the degassing of sediments and oceanic crust in subduction zones and other orogenic environments that allows CO_2 and other gases to return to the atmosphere.

The uptake of elements during hydrothermal and sedimentary exchanges with the oceanic crust is out of balance with estimates of global fluvial fluxes to the ocean making it difficult to quantify ocean geochemical cycles. During glaciations, increased physical erosion on the continents enhances the amount of mineral surface area available for weathering and it has been argued that a pulse of weathering related to the last glaciation, having yet to fully decay, could be responsible for observed imbalances in marine geochemical budgets (Vance et al. 2009). Likewise, shifts in tectonic forces, (such as the extent of mountain uplift), which affect the silicate weathering regime on the continents

have been purported to explain secular variations in ocean geochemical budgets (Misra et al. 2012). By focusing solely on fluvial chemical fluxes, however, and not considering groundwater discharge to the ocean that can bypass the surface drainage network, these and similar studies could potentially be misrepresenting the roles of glaciations and tectonic uplift in explaining significant discrepancies in ocean geochemical budgets.

Although elemental enrichment in subsurface fluids relative to that in surface waters has been being documented for over a century (e.g Miller 1865), it is only relatively recently that robust estimates of direct groundwater fluxes to the ocean have been highlighted as being potentially significant in quantifying global geochemical fluxes and understanding biogeochemical cycles (Moore 2010 and references therein). It is therefore important to have good estimates of chemical weathering fluxes from varied surface and subsurface environments across different climatic zones and spatial scales.

1.3.1 Rock weathering, riverine fluxes and the carbon-cycle

A key greenhouse gas is CO_2, which is continually replenished by active volcanism and metamorphic degassing. The carbon reservoirs on Earth differ greatly in size and their carbon stores exhibit a variety of residence times. The transfer of carbon between the atmosphere and the biosphere, which occurs over relatively short timescales, results in seasonal fluctuations of measured CO_2 concentrations in the atmosphere (Keeling et al. 2001). Over longer timescales, CO_2 that has been converted to vegetation can become sequestered as particulate organic carbon that gets stored on land and transported from continental regions (especially those with particularly short routing systems) during storms and buried in ocean canyons as turbidite deposits (Hovius et al. 2011a). However, it is the exchange of CO_2 between the atmosphere and the continental lithosphere that facilitates large-scale carbon sequestration over millions of years, ensuring a long-term balance between CO_2 out-gassing and drawdown, and stable climatic conditions on Earth over geological timescales (Figure 1.1).

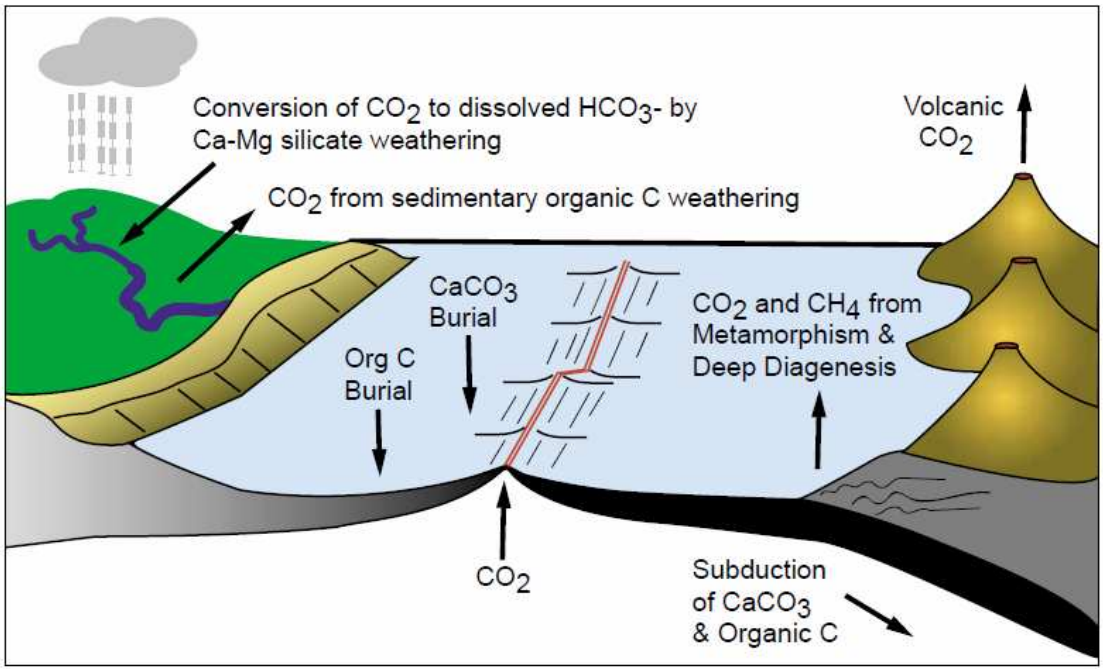

Figure 1.1. The Earth's long-term carbon cycle (after Berner (1999)). Schematic representation of the biogeochemical cycling of carbon between the crust, the atmosphere, the ocean and the biosphere. The transfer of carbon is facilitated by the weathering of silicate minerals on the continents, drawing down atmospheric CO_2, coupled with carbonate precipitation and burial in the ocean, before the return of CO_2 to the atmosphere via volcanism and metamorphic degassing.

The fundamental principles of chemical weathering have long since been described and understood (Ebelmen 1845). The primary continental weathering agent is carbonic acid (H_2CO_3), formed in the subsurface when CO_2 from the atmosphere, often concentrated during soil respiration, speciates with H_2O. During mineral dissolution CO_2 is converted to bicarbonate (HCO_3^-). The generalised reaction below for the chemical dissolution of a calcium silicate mineral (in this case wollastonite ($CaSiO_3$)), shows how:

$$CaSiO_3 + 2H_2CO_3 \rightarrow Ca^{2+} + 2HCO_3^- + SiO_2 + H_2O \quad (1)$$

The dissolved products of silicate weathering reprecipitate forming carbonate, in this example calcium carbonate ($CaCO_3$) by the inverse reaction:

$$Ca^{2+} + 2HCO_3^- \rightarrow CaCO_3 + H_2O + CO_2 \quad (2)$$

The precipitation of carbonate is most readily facilitated in the oceans primarily during the skeletal growth of marine organisms. If substituted for calcium into the above equations, magnesium will get reincorporated into solid Earth also by calcite growth and via processes such as clay formation and dolomitisation (e.g. Hart 1970; Vasconcelos and McKenzie 1997). Therefore, the weathering of the silicate-bound alkali earth elements directly contributes to the long-term carbon sink (France-Lanord and Derry 1997). However, the alkali elements, sodium and potassium, whilst not incorporated into the skeletons of marine organisms to any significant degree, readily exchange for any calcium and magnesium bound to detrital clays and with calcium at mid ocean ridges and therefore also contribute to the long-term carbon sink (Sayles and Mangelsdorf 1977; Von Damm et al. 1985).

The above reactions detailing the exchange of CO_2 between the atmosphere and the lithosphere via silicate weathering and carbonate precipitation can be summarised as follows:

$$CO_2 + CaSiO_3 \rightarrow CaCO_3 + SiO_2 \quad (3)$$

It is shown in the above equations that for every mole of Ca^{2+} released during silicate weathering, one mole of CO_2 becomes sequestered into the framework of a carbonate mineral. Conversely, the weathering of carbonates results in no net drawdown of CO_2, but the reservoir of inorganic carbon in the form of sediments on the ocean floor is currently thought to represent 48×10^6 Gt (4.00×10^{15} mol) relative to an atmospheric reservoir of carbon estimated at 760 Gt (6.33×10^{10} mol). If the weathering of silicates and the precipitation of carbonates is in balance, then carbon fluxes to the atmosphere must be coupled to the carbon sinks by a negative feedback mechanism in order to avoid drastic excursions in the much smaller atmospheric reservoir maintaining stability of Earth's long-term climate (Berner and Caldeira 1997; Bickle 1998; Caldeira and Berner 1998; Berner 1999).

The degree of silicate weathering can be seen in the compilation after Gaillardet et al. (1999) illustrating that despite the relatively low solubility of silicate minerals their contributions exceed those from carbonates in many of Earth's major rivers (Figure 1.2).

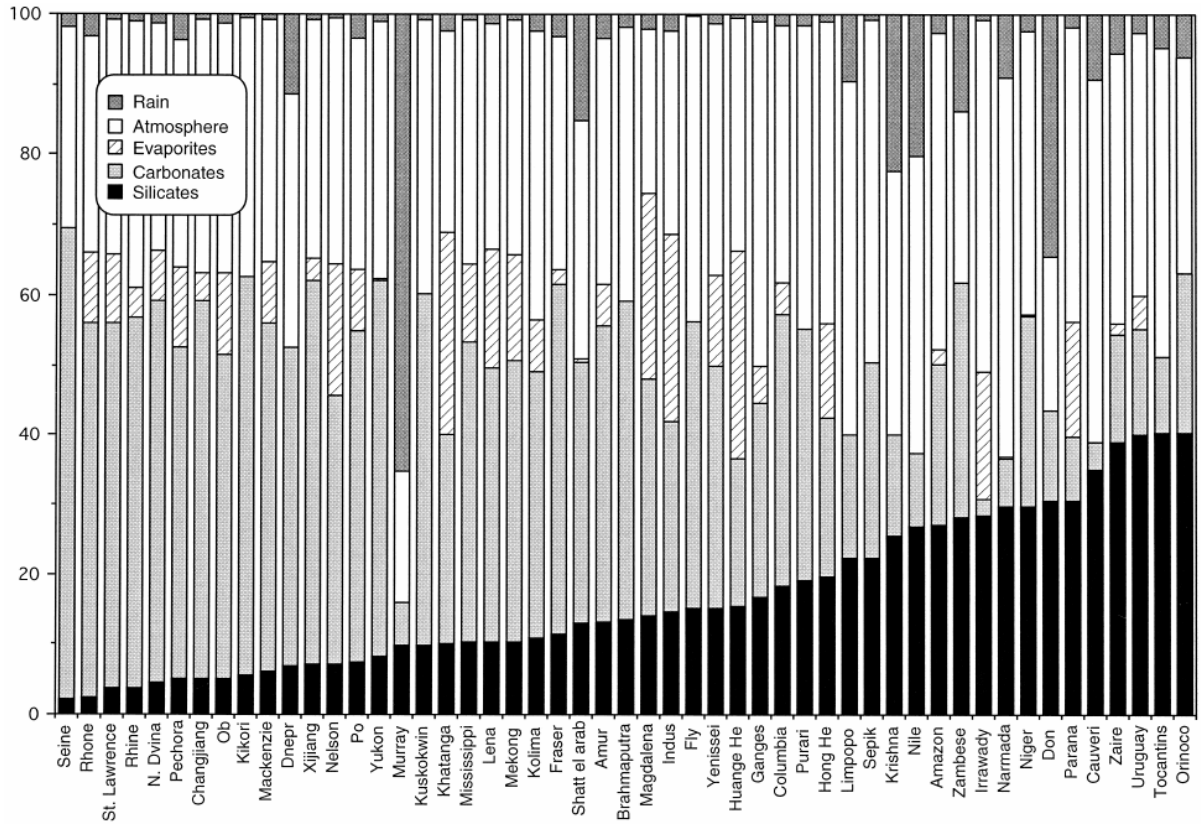

Figure 1.2. The proportional contribution (%) of solutes to a selection of the world's major rivers from the different atmospheric and lithologic sources (after Gaillardet et al. 1999), with increasing contributions of dissolved mass from silicates arranged from left to right. The atmospheric contributions are bicarbonate ions from the dry deposition of cyclic salts that resulted from silicate and carbonate weathering, and the rain contributions are derived from the measurement of Na-Cl ions that resulted from sea-salt dissolution.

The first-order factors controlling the rates of the carbonic-acid dissolution of silicates outlined in the Equations 1-3 might include the supply of water and acid and the supply of silicate minerals by physical erosion with reaction rates controlled by temperature-dependence in an Arrhenius rate law (Bluth and Kump 1994; Lasaga et al. 1994). Raymo and Ruddiman (1992) and Raymo et al. (1988) have argued that erosion rates are the dominant control although most authors have argued that climate (rainfall and temperature) is the prime control (Walker et al. 1981; Berner 1983). West et al. (2005) compiled riverine silicate-derived chemical flux data from catchments that varied in climate, lithology and runoff and erosion rate and demonstrated that it is possible to distinguish and quantify the sensitivity of silicate weathering rates to rainfall, temperature and physical erosion rates. This study reemphasised the important distinction between transport-limited (weathering rates exceeding mass transport ability) and kinetically-

limited (where mass transport is more rapid than weathering) weathering regimes (Carson and Kirkby 1972; Stallard and Edmond 1983). But the question as to whether the transport-limited or the kinetically-limited regime is the more important in determining Earth system's response to climate-weathering feedbacks through time remains debated (von Blanckenburg and Dixon 2012).

The database of global riverine silicate chemical fluxes, temperature, rainfalls and physical erosion rates has been integrated into the debate on climate-weathering-erosion feedbacks, but the addition of subsurface chemical fluxes that bypass the river drainage network has yet to be fully incorporated (Moore 2010). First, robust quantitative estimates of groundwater fluxes from a variety of spatial scales and physical settings are needed to evaluate the significance of groundwater fluxes to the total global silicate chemical weathering flux.

1.3.2 An alternative weathering agent: sulphuric acid

The importance of plate tectonics (particularly seafloor spreading and total continental surface area) in modulating global climate was suggested by the BLAG climate model (Berner et al. 1983), which constrained a set of initial boundary conditions at time −100 Ma selected as those that could simulate present-day atmospheric CO_2 concentrations and other present-day major molecular abundances such as marine bicarbonate. Contradictions between the ratios of calcium to bicarbonate predicted by the BLAG model and the evaporite record have been attributed to assumptions in the model concerning the sulphur (and organic carbon) cycle(s) (Kasting 1984). Of critical importance is that the original assumption that most riverine sulphate is derived from evaporites has since given way to the generally accepted principle that sulphide oxidation is potentially an important source of dissolved sulphate to rivers and the ocean. As will be shown below, sulphuric acid generated by the oxidative weathering of pyrite, whilst not as volumetrically significant as carbonic acid (at least in the shallow subsurface) is an important weathering agent on the continents (Figure 1.3).

Due to rapid kinetics (Williamson and Rimstidt 1994), the sustained oxidative weathering of pyrite (FeS_2), outlined in the following equation, produces significant quantities of sulphuric acid (H_2SO_4):

$$FeS_2 + 15/4O_2 + 7/2H_2O \rightarrow Fe(OH)_3 + 2H_2SO_4 \quad (4)$$

As shown in the next equation, the production of dissolved inorganic carbon by the sulphuric-acid-driven weathering of carbonates, in contrast to the weathering of silicates by carbonic acid, can return ancient sedimentary CO_2 directly to the atmosphere and ocean sinks (Figure 1.3) (Lerman and Wu 2006; Lerman et al. 2007):

$$2CaCO_3 + H_2SO_4 \leftrightarrow 2Ca^{2+} + 2HCO_3^- + SO_4^{2-}$$
$$\leftrightarrow CaCO_3 + CO_2 + SO_4^{2-} + Ca^{2+} + H_2O \quad (5)$$

In contrast to the net production of CO_2 derived from sedimentary carbon shown in Equation 5, the following carbonate weathering reaction details the production of dissolved inorganic carbon using one mole of atmospheric CO_2 and one mole of water:

$$CaCO_3 + CO_2 + H_2O \leftrightarrow Ca^{2+} + 2HCO_3^- \quad (6)$$

Subsequent precipitation of carbonate in the depositional environment (going from right to left in Equation 6) releases the mole of atmospheric CO_2 that was initially used, thus showing that carbonate weathering by carbonic acid (unlike carbonate weathering by sulphuric acid) has no effect on climate.

Isotopes of sulphur and oxygen in aqueous sulphate and carbon isotopes of dissolved inorganic carbon have been used to distinguish between the ancient sedimentary source of dissolved inorganic carbon to rivers in Equation 5, the generation of which produces atmospheric CO_2, and that from an atmospheric source as shown in Equation 6, which over appreciable timescales has no impact on climate (Galy and France-Lanord 1999; Karim and Veizer 2000; Pawellek et al. 2002; Calmels et al. 2007).

Reduction of the sulphate produced by the oxidative weathering of pyrite, involving the oxidation of organic matter and methane in ocean pore waters (Niewöhner et al. 1998), can counter the net release of CO_2 outlined in Equation 5 because the alkalinity produced during sulphate reduction reacts with oceanic calcium. However, the antithesis between the sulphur and carbon cycles observed through time is imperfect (Holser et al. 1989). One of the reasons for this is that the typical residence time of sulphate in the ocean is greater than 10^7 years (Holser et al. 1979; Claypool et al. 1980) allowing for intermittent decoupling of sulphide oxidation on the continents and sulphate reduction in the oceans (Li et al. 2008), with 10 Ma required for the sulphur cycle to respond to changes in continental

sulphate fluxes. Contrastingly, dissolved inorganic carbon has a residence time in the ocean of approximately 10^5 years (Walker 1986; Berner and Berner 1996), which indicates that changes in riverine and subsurface carbon fluxes will have no impact on the sulphate reduction rate in the ocean, but will alter carbonate deposition and the related net production of atmospheric CO_2 on 100 ka timescales.

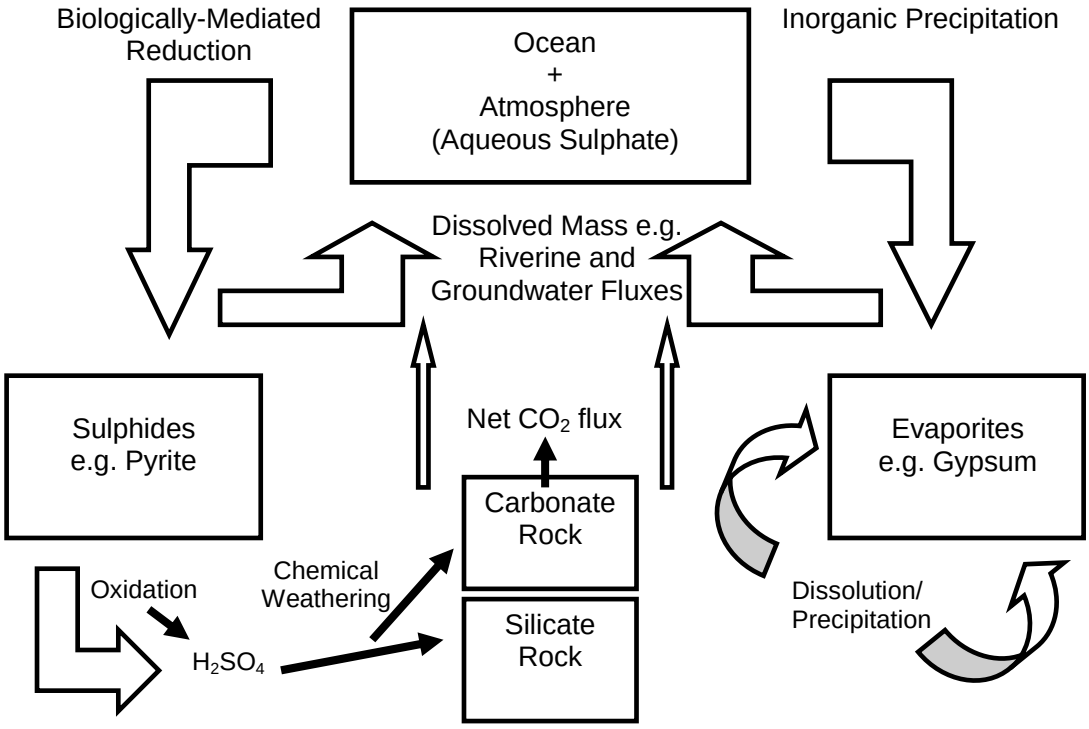

Figure 1.3. The Earth's long-term sulphur cycle. A simple box model illustrating the transfer of sulphur between the reservoir of aqueous sulphate in the Ocean+Atmosphere system and the primary solid sinks, sulphides and evaporates. The oxidation of sulphides generates sulphuric acid (H_2SO_4) that in dissolving carbonate rock can lead to net atmospheric CO_2 production.

One of the key drivers in the production of sulphuric acid by the oxidative weathering of pyrite on the continents is held to be physical erosion. Pointing towards a direct link between the production of sulphuric acid and physical erosion are, for example, the observation that the oxidative weathering of sulphides positively correlates with multi-annual riverine sediment yields (Environment Canada 1998; Calmels et al. 2007) and that sulphide oxidation rates are related to the weathering of recently exposed sediments due to glacial mechanics (Anderson et al. 2000). However, because sulphide oxidation rates can be rapid, evaluation of sulphate fluxes from present-day eroding landscapes is needed.

Knowledge of where the production of sulphuric acid in rapidly eroding landscapes takes place is lacking. As such, analysis of groundwater in aquifers containing sulphide-bearing rocks in landscapes that are eroding rapidly by landsliding is needed to provide insight into the mechanisms of sulphuric acid-driven weathering and related net atmospheric CO_2 production.

1.4 The role of groundwater: a subsurface route

Catchments have input primarily in the form of rainwater, and outputs (runoff and groundwater discharge) with dissolved chemistries reflecting internal processes that cause *denudation*, i.e., net loss of mass from the landscape (Figure 1.4). Much of the effective chemical interchange (i.e. production of dissolved mass subsequently available for delivery to the ocean) is classically thought to occur in the soil zone (Birkeland 1999) and most delivery of dissolved chemistry to the oceans is attributed to rivers, which are easily sampled (Garrels and MacKenzie 1971; Meybeck 1987). Catchments, however, are hydrologically complex, with groundwater flow paths penetrating below the well-studied soil and saprolitic zones (Figure 1.4).

Groundwater has residence/response times in the subsurface that vary between days to thousands of years depending on the physical properties of aquifers, namely hydraulic head (liquid surface elevation) and hydraulic conductivity (the ease with which a fluid moves through porous media and typically denoted as k) that govern groundwater flow. The chemistry of groundwater becomes enriched relative to surface waters as the residence time of an aquifer increases, which typically occurs with distance and depth along groundwater flow paths. Thus, assuming that hydraulic conductivity decreases with increasing depth, there is potential for an inverse correlation existing between residence times and fluxes. However, another means of groundwater chemical enrichment occurs when subsurface flow paths intercept deep sources of highly-concentrated brines, such a hydrothermal fluids (Figure 1.4). Irrespective of the duration of rock-water interactions and the sources of solutes to the subsurface, dissolved chemical compositions in groundwaters of any age are typically enriched relative to surface waters (Zektzer et al. 1973), but due to the expectation that volumetric fluxes of water from the subsurface should be tiny in comparison to surface runoff, groundwater flow has not until fairly recently been considered as a potentially important mode of transferring dissolved mass from the continents to the oceans. Due to this paucity of investigations quantifying

subsurface chemical fluxes, compared to estimations of riverine fluxes to the ocean, the chemical flux of groundwater discharge that bypasses the river drainage network poses as a largely unknown contribution to global ocean chemistry.

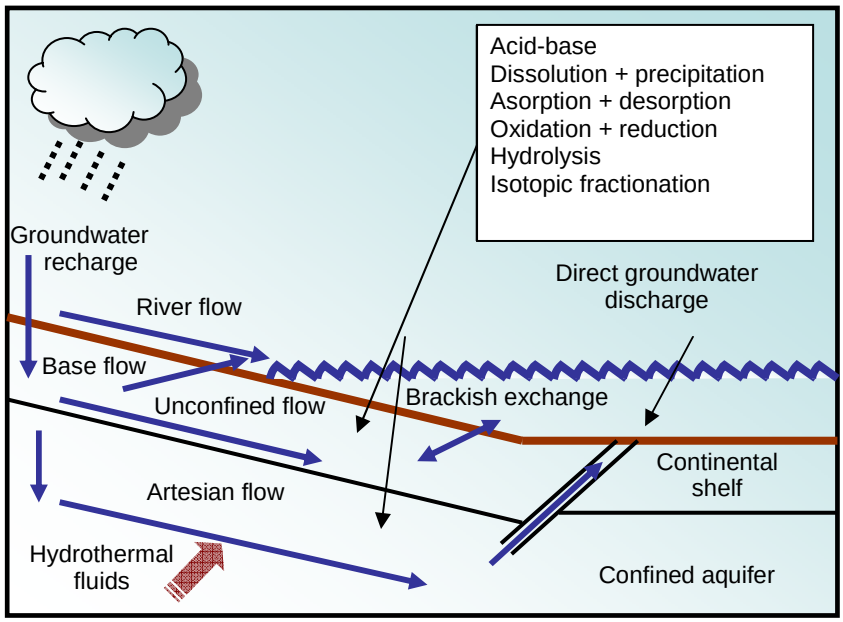

Figure 1.4. Water flow to the ocean. Groundwater provides the baseflow of rivers and mixes with seawater via diffusion and advection along the continental shelf. The flow of deep groundwater through confined horizons can bypass the surface drainage network entirely and via breaches in confining units can discharge directly to the ocean.

1.4.1 General characteristics of groundwater flow and chemistry

The primary modes of dissolved-mass transportation are advection, whereby the controls on groundwater flow are the same as those that determine the flow of mass, and dispersion, during which concentration gradients force the mixing and chemical interchange of two or more fluid types. Dissolved mass in groundwater, in the form of ions and molecules undergoes several types of chemical weathering reactions during transportation leading to the redistribution of mass between solid, liquid and gaseous phases (Figure 1.4). This thesis is mainly concerned with the redistribution of charged inorganic substances, major and trace cations; Ca^{2+}, Mg^{2+}, Na^{+}, K^{+}, Sr^{2+} and Ba^{2+} and anions; Cl^{-}, SO_4^{2-} and HCO_3^{-} constrained by organically-mediated isotopic fractionation processes involving the oxygen, hydrogen, carbon, sulphur and strontium cycles.

The concentration of dissolved mass in groundwaters varies widely and depends on a host of factors related to geology, climate and the physical and chemical (mineralogical) properties of the aquifer. The rates at which primary chemical weathering reactions occur vary from as little as seconds in the case of some dissolution and adsorption/desorption reactions to up to greater than 10^6 years for certain forms of mineral crystallization (Langmuir and Mahoney 1984). In general, the most important weathering reactions in the subsurface are faster than the flow of groundwater and therefore at a stipulated temperature can often be modelled at equilibrium (Nordstrum and Munoz 1986). Groundwaters close to the surface tend to be relatively enriched in Ca^{2+} and HCO_3^- representing the dissolution of calcite, which is highly soluble under typical recharge conditions, with monotonic increases in all other major ions usually observed with increasing depth due to extended residence times allowing for further rock-water interactions.

Formation brines, typically found at depths greater than 1 km and which can have dissolved concentrations in excess of seawater, owe their chemical evolution to that of the rock mass, and can exist as fluid inclusions of trapped ancient seawater (connate water) (Meinzer 1923), aqueous fluids held in deep fractures (Holland et al. 2013), or can be metamorphic waters derived from the dehydration of clay minerals during pressure and temperature changes in the host lithologies. This chemically enriched dissolved mass can find its way to the surface via hot spring activity related to uplift, meteoric-water mixing and decompressional loading in sedimentary basins. The use of radioactive bomb-produced tritium (^3H, half-life of 12.43 years) as a tracer for water derived from the atmosphere since 1952 (IAEA 1983a,b) has demonstrated that modern recharge waters interact with highly enriched formation brines at depth and that a coupling of hydrogeochemical and thermomechanical stresses can explain the increase in dissolved Cl^-, Br^- and other ions observed with depth (Nordstrom et al. 1989).

Less well known is the occurrence and contribution to groundwaters of dissolved constituents from hydrothermal activity (e.g. hot-springs), which can be especially prevalent in tectonically active regions (Becker et al., 2008; Evans et al., 2004; Kopf et al., 2001; Kopf et al., 2003; Milkov, 2000; Yassir, 1987). The chemical concentrations of hot springs are typically enriched relative to surface waters and groundwaters. For example, the lithium concentration in hot springs is typically 1000× more concentrated over likely local weathering inputs and rain (Kısakűrek et al. 2005).

1.4.2 Subsurface geochemical fluxes

A comprehensive discussion of subsurface geochemical fluxes is presented in Section 2.3, Chapter 2. The key points are outlined here.

Ocean islands, particularly of volcanic origin and with short routing systems between topographic highs and the coastline characterised by steep hydraulic gradients through permeable volcanic or karstic rocks, have been shown to exhibit significant chemical fluxes to the ocean through subsurface paths (Rad et al. 2007; Schopka and Derry 2012). In some locations, such as parts of Hawaii (Kay et al. 1977) and the Yucatan Peninsula (Hanshaw and Back 1980), almost all of the fresh water entering the ocean, despite annual rainfall amounts in excess of 1000 mm, occurs via subsurface drainage. Such observations have added to the importance of assessing subsurface discharge to the ocean within the contexts of nutrient delivery to coastal waters (Slomp and Cappellen 2004), ocean geochemical budgets (Moore 1996) and chemical weathering. Less well characterised is the contribution of dissolved mass to the oceans from small islands centred at compressive plate margins such as Taiwan. These regions have high elevations and short length-scales between the hinterland and the coast and due to active tectonics can be highly fractured, but unlike the much-studied volcanic islands, they exhibit typical clastic continental margins with well developed alluvial-fill basins that exhibit high permeabilities and established surface drainage networks. It is important to constrain the subsurface chemical fluxes through these alluvial-fill deposits because they dominate many of the major continental coastlines around the globe.

1.5 Importance of source water characterisation

As well as knowledge of the weathering agents involved and the volumetric significance of dissolved mass to the ocean, a robust characterisation of the sources of dissolved chemistry in groundwater has important bearings on the wider set of implications related to chemical weathering.

Terrestrial waters are supplied primarily during the precipitation of evaporated seawater from the atmosphere. At some stages during periods of intense runoff water may flow directly off the surface of a landscape returning unimpeded to the ocean. During normal atmospheric conditions, rainfall ordinarily resides temporarily on the surfaces of vegetation or soil in the form of droplets and infiltrates the subsurface to some degree. Depending mainly on the measure of humidity and the dew point, a proportion of this rested and infiltrated water will return to the atmosphere through varying degrees of

evaporation and evapotranspiration, leaving behind a concentrated residue of either dissolved or solid ionic mass. The remaining water, groundwater, is available for recharging aquifers and, via lateral migration, for contributing to stream baseflow.

Once rainfall enters the subsurface and becomes groundwater its chemistry undergoes significant changes due to its interaction with sediments and rock. It is from this point forward in the hydrological cycle that the weathering history of the continents is recorded and therefore an effort must be made to account for and remove from calculations traces of atmospheric salts and chemical enrichment due to evapotranspiration.

Once atmospheric salts and chemical enrichment due to evapotranspiration have been accounted for, the residual chemical composition of groundwaters sampled near Earth's surface is derived either from relatively recent rock weathering processes or from ancient rock or water sources. Knowledge of the bulk chemical and/or the isotopic end-member compositions of the different fluid sources can help to constrain the different hydrological contributions that together give rise to the integrated chemical signals in groundwater. The weathering products of the terrestrial component of this circulation system comprise the chemical fluxes that reflect denudation of the landscape and which set ocean geochemical budgets. It is therefore important to understand the trace element and isotopic chemistry of the sources of solutes in groundwaters and, where possible, to consider the end-member chemical characterisations of the aquifer host rocks.

1.6 Active mountain belts: Taiwan

The loss of mass from a landscape (denudation) has long been observed to involve coupled physical erosion and chemical weathering (e.g. Gilbert 1877). Indeed, the silicate chemical weathering fluxes of many of the world's major rivers in transport-limited regimes show a tight positive correlation with total denudation rates calculated for their catchments (West et al. 2005). Chemical weathering rates being significantly determined by the production and replenishment of fresh mineral surfaces suggests that areas of high physical erosion and denudation are important to global yields of dissolved mass. This link between physical erosion and chemical weathering indicates that tectonically active regions of the continental crust, which have been shown to be a major source of sediment to rivers (Milliman and Syvitski 1992), should be significant in the production and transfer of chemical weathering products to the ocean. This has been demonstrated to be the case through combined measurements of chemical and sediment yields for several small rivers draining active mountain belts in the Western Pacific (Jacobson and Blum 2003; Carey et

al. 2005; Lyons et al. 2005). However, Dixon et al. (2012), reiterate the point that rapid uplift and extremely high physical erosion rates may limit chemical weathering rates as weathering minerals do not have sufficient time under such conditions to dissolve completely.

The analysis of groundwater and rock chemistry in settings that undergo frequent physical disruption, such as landsliding, may answer questions such as where exactly in the subsurface is the relationship between physical erosion and chemical weathering most active? And what are the processes that give rise to chemical fluxes in such dynamic settings?

The mountainous island of Taiwan, situated in the western Pacific Ocean, exhibits extreme rainfall, high uplift rates and some of the highest physical erosion rates on record. It was chosen as a case study because some of the processes pertinent to chemical weathering, such as the nature of the link between physical erosion and chemical weathering at high erosion rates, are observable on the timescale of months, which coupled with its excellent infrastructure and accessibility, makes it an ideal location in which to study chemical weathering. As will be discussed in detail in Chapter 2, Taiwan also offers a variety of settings that differ physically and lithologically, allowing for the range of questions outlined in Section 1.2 to be addressed.

Chapter 2

Case study sites

2.1 Introduction

This chapter illustrates the geographical locations, and describes the geology, climate, tectonics, surface processes, hydrology and hydrogeology of the field study sites representing the samples that are presented in this thesis. All the samples collected for this study were recovered from the island of Taiwan, situated approximately 180 km off the southeastern coast of mainland China (Figure 2.1). The majority of the ~200 samples that were recovered and analysed are groundwaters, with a smaller number of surface-water samples and rock samples also collected.

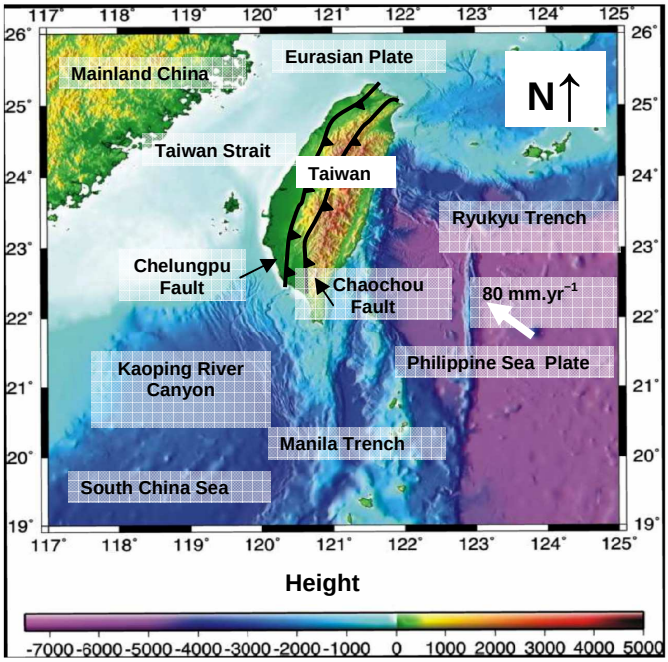

Figure 2.1. Topographic map of Taiwan showing its geographical location off the eastern margin of mainland China and bathymetric detail (Liu et al. 1998) of the surrounding ocean. The island is characterised by the elongate Central Mountain Range and alluvial-fill coastal plains along the western margin. To the northeast of Taiwan, the Philippine Sea Plate is subducting beneath the Eurasian plate in the north-east dipping Ryuku trench-arc system. South of Taiwan the Philippine Sea plate is overriding the east-dipping Luzon-arc Manila trench system. Taiwan is separated from the Eurasian continent by the narrow Taiwan Strait where the average water depth is 100 m. Also shown schematically are the Chelungpu and Chaochou thrust faults which bound the Western Foothills, the Central Range and coastal plains along Taiwan's western margin.

The primary purposes in gathering this collection of samples and in assimilating the results of their geochemical analysis were A) to track the weathering histories of the groundwaters by investigating the variability of dissolved chemistry in endeavouring to

understand where in the subsurface of active mountain belts chemical weathering occurs, B) to characterise the sources of solutes found in groundwaters and calculate the subsurface chemical fluxes resulting from weathering that are available for discharge to the ocean through an active mountain belt system, and C) to then endeavour to understand the mechanistic controls on when and how and why chemical weathering happens where it does, with a particular focus on the interception of surface processes with the subsurface.

In order to address these aims, two seemingly distinct aquifers in Taiwan were identified for sample recovery. Firstly, an evaluation of the physical and chemical characteristics of groundwater in two alluvial-fill coastal-plain settings provides insight into how dissolved solutes evolve through sediment wedges that vary regionally in their length scales and which have the potential to buffer direct hydrological routing through active mountain belts to the ocean. The physical parameters that control groundwater flow through these permeable media are generally well understood, making it possible to relatively easily calculate linked dissolved subsurface fluxes to the ocean. Secondly, assessments of the groundwater chemistry and the physical nature of aquifers in two steeply-elevated fractured bedrock settings have been undertaken. Despite the physical properties of these bedrock aquifers being less well understood than are the features that govern groundwater flow in sediment wedges, time-series groundwater chemistry from one of these locations offers insight into how the subsurface responds to active surface processes, which has implications for understanding the erosion-climate feedback.

2.2 The island of Taiwan

2.2.1 Geographic characteristics

Taiwan is situated at subtropical latitudes of 22-25 °N in the western margin of the Pacific Ocean, separated from the Eurasian continent via the narrow Taiwan Strait, which has an average water depth of 100 m (Figure 2.1). It has a surface area of 35,873 km^2 with the main topographic feature being the north-south trending 300 km-long Central Range, which has greater than 200 peaks over 3000 m in elevation. Also topographically significant is the 120 km-long Coastal Range along the eastern coast, which has peaks up to 1500 m in elevation, and is separated from the Central Range by the Longitudinal Valley. The west flank of the orogen is comprised of the Western Foothills thrust belt. The total area of mountain terrain above 1000 m, together with foothills and terraces between 100 and 1000 m comprise 63 % of the surface area, with coastal plains occupying the

remaining 37 %. Despite its low-lying latitude, Taiwan has experienced substantial glaciation as recently as 8.9±0.5 ka (Hebenstreit et al. 2006).

There are numerous major transverse rivers crosscutting the main structural grain of the Taiwan orogen, the catchments of fourteen of which are monitored for discharge and sediment transport properties by the Water Resources Agency (WRA), Ministry of

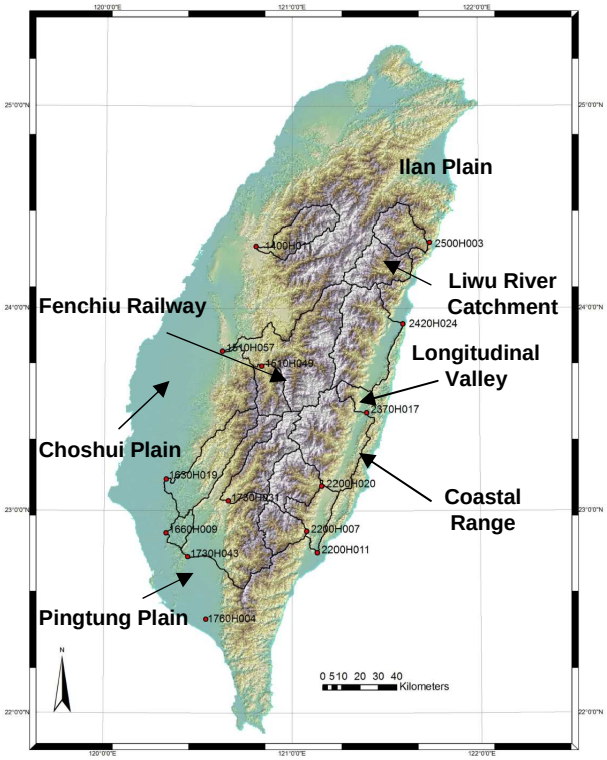

Figure 2.2. River gauging stations monitored by the WRA. A total of 14 of Taiwan's major rivers are routinely sampled for dissolved chemistry and measured for discharge. Gauging stations 1510H057 and 1730H043 are located on the Choshui and Kaoping Rivers, respectively, where the average annual discharge for the period 2005-2006 was 1.06 × 10^{13} L.yr^{-1} (Choshui) and for the period 1981-1990 was 7.40 × 10^{12} L.yr^{-1} (Kaoping). Indicated are the main study sites for this thesis; the Choshui and Pingtung coastal plains along Taiwan's western margin, the region of the Fenchui Railway network in the central uplands and the Liwu River Catchment containing the Bayyang Tunnel Trail situated along the northeastern flank of the Central Range to the north of the Coastal Range and the Longitudinal Valley.

Economic Affairs, Taiwan (Figure 2.2).

Due to their short length and steep gradients, the rivers are fast-flowing, with limited water flow when dry, but flows of up to 10,000 $m^3.s^{-1}$ during typhoons have been recorded (Lee et al. 2006). In terms of specific discharge ($m.s^{-1}$), this peak flow (~3 $m.s^{-1}$) is ~100 times that of the average discharge of the Amazon River (~0.03 $m.s^{-1}$). Two of the largest watercourses in terms of catchment drainage area are the Kaoping and Choshui Rivers, which flow into the Taiwan Strait via the west flank of the orogen. The Western Foothills thrust belt is less steep than the east flank and is characterised by the presence of two large alluvial-fill accretionary wedges associated with the Kaoping and Choshui catchments, the Pingtung and Choshui Plains, respectively (Figure 2.2). With the exception

of river-flow into the narrow Longitudinal Valley, drainage off the steeper east flank of the Central Range is direct to the Pacific Ocean. This is the case for the Liwu River, draining one of the major catchments in east Taiwan, situated approximately 20 km to the north of the Coastal range (Figure 2.2). Offshore to the east of Taiwan, the ocean floor extends to depths of greater than 4000 m, making the total orographic relief up to 9000 m.

2.2.2 Tectonics and geology

Taiwan is a foreshortened and compressed passive continental margin sequence consisting of various grades of metasediments. It resulted from the Late Cenozoic collision of the Luzon Arc, on the Philippine Sea Plate, with the Eurasian continental margin (Figure 2.1) (Chai 1972; Bowin et al. 1978; Seno et al. 1987; Ho 1988; Teng 1990; Seno 1993). The island is located between two opposite-dipping subduction zones. To the northeast of Taiwan, the Philippine Sea plate is subducting beneath the Eurasian plate in the north-east dipping Ryuku trench-arc system and to the south of the island, the Philippine Sea plate is overriding the east-dipping Luzon-arc Manila trench system (Figure 2.1). The Luzon Arc has been in oblique collision with the continental margin of China since the mid-Miocene (Sibuet 2002). Increased obliquity of the plate boundary from northwest to west-northwest since around 5 Ma has led to the collision propagating southwards, which in turn has led to increased deformation and exhumation and the emergence of the Taiwan orogen above sea-level. Marine terrace uplift and rock exhumation rates over the past 5 Ma span 5-7 $mm.yr^{-1}$, with the highest rates observed in the east Central Range (Liu 1982; Liew et al. 1993; Dadson et al. 2003; Willett et al. 2003).

Across central Taiwan, the metamorphic grade increases from poorly consolidated Neogene sediments in the Western Foothills fold-and-thrust belt through to greenschist grade Late Palaeozoic-Mesozoic meta-sediments in the east Central Range and the Coastal Range (Figure 2.3). The oldest rocks in Taiwan are exposed in the east Central Range and were deposited in the Late Palaeozoic to Mesozoic on the continental margin of Eurasia. These clastic and limestone sequences have been subjected to two phases of metamorphism, an amphibolite-grade event in the Miocene, which was overprinted by a greenschist-grade episode more recently during the Plio-Pleistocene Penglay Orogeny (Lo and Onstott 1995). These rocks that outcrop along the east flank of the mountain belt are known as the Tananao Schists, and comprise graphitic ‘black schist’ units (PM4), siliceous

and micaceous schists (PM3) with associated interbedded marbles (PM2) and lesser abundances of gneisses and migmatites (PM1) (Figure 2.3).

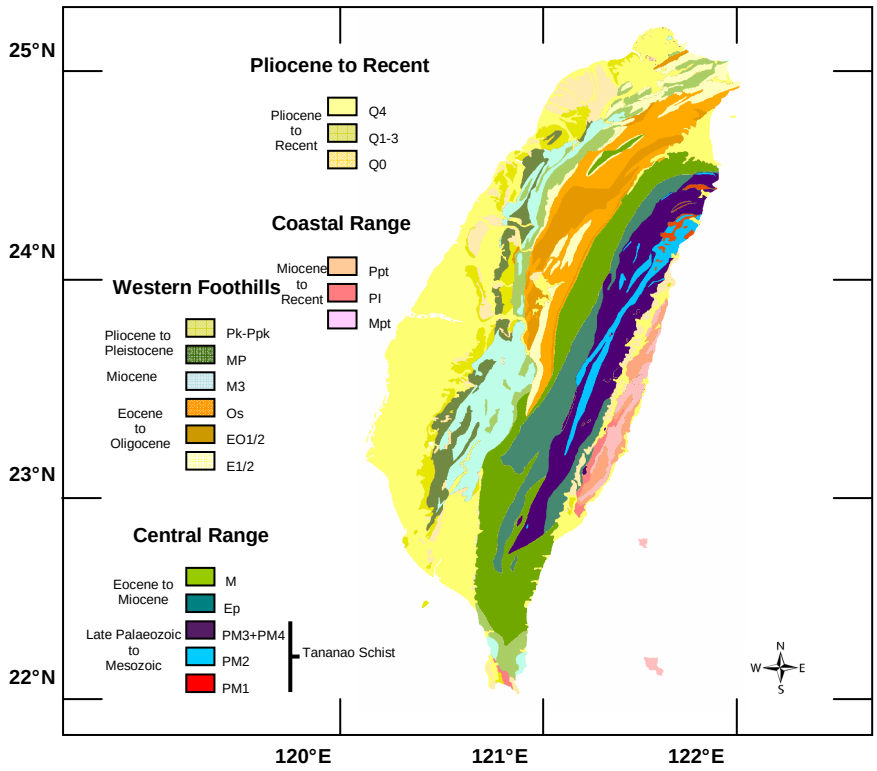

Figure 2.3. Geological Map of Taiwan, adapted from Chen et al. (2000), showing the main lithological formations comprising the island.

Subsequent deposition along the Eurasian continental margin in the Eocene and Miocene resulted in the accumulation of approximately 10 km of sandy and argillaceous sequences. These units outcrop along the main divide of the Central Range having since been deformed to give rise to slates and phyllites, which form the Pilushan (Ep) and the Lushan (MI) formations (Ho 1988) (Figure 2.3).

The Western Foothills geologic province is an active fold-and-thrust belt sequence composed of approximately 8 km of clastic sediments that have not undergone any substantial metamorphism during orogeny and are less indurated than the rocks in the east (Chen et al. 2001). The formations comprise turbidite sequences of mudstones, sandstones and shales that record deposition in a flexural foreland basin during the Oligocene to the Early Pliocene (Ho 1988, Lin and Watts 2002).

The Longitudinal Valley is generally thought to mark the present-day suturing of the Eurasian plate to the west and the Philippine Sea plate to the east (Figures 2.1 and 2.2).

The lithologically distinct Coastal Range, lying to the east of the suture on the Philippine Sea plate, is composed of Neogene volcano-clastic sediments related to the Luzon Arc (Teng 1987) (Figure 2.3). Estimates of uplift rates for the Coastal Range of 5 $mm.yr^{-1}$, determined by ^{14}C and $^{234}U/^{230}Th$ dating of exposed marine terraces (Liew et al. 1990), are similar to the long-term rates of 5-7 $mm.yr^{-1}$ estimated by Dadson et al. (2003) and others.

There are approximately 40 observed and inferred active major faults on the island of Taiwan and also several large faults associated with the submerged east flank and the nearby subduction zones operating offshore. Seismic rupturing along these faults has resulted in 15 earthquakes with a moment magnitude greater than 6.0 through the period 1990 to 2002. The Chi-Chi earthquake in September 1999, with a focal depth of 8 km, ruptured along 100 km of the north-south trending, east-dipping (~30°) reverse Chelungpu Fault in the Western Foothills (Heermance et al. 2006), causing up to 3 m of vertical displacement (Yu et al. 2001). With a moment magnitude of 7.6, it was the largest earthquake in Taiwan in the past 50 years (Shin and Teng 2001). The landscape was greatly perturbed and the rock significantly weakened as a result of the Chi-Chi earthquake. In particular, and as will be explored in Chapters 4 and 5, the event was documented to have profoundly affected the hydrology of the alluvial-fill Choshui Plain in the central west region of the Island, which is bounded to the east by the Chelungpu Fault. Observed vertical mixing between deep confined aquifers after the earthquake indicated that permeability increases and the fracturing of aquitards in the Choshui Plain resulted from the rupture (Chia et al. 2001; Wang et al. 2004a; Wang et al. 2005). Wang et al. (2005) also reported increased recharge from the Choshui River into the shallow portions of the aquifer system after the earthquake. In addition to the hydrological disturbance seen at depth, approximately 20,000 landslides in the Western Foothills were triggered by the Chi-Chi earthquake, and an increase in the rate of landsliding was observed for more than six years following the event (Dadson et al. 2004; Hovius et al. 2011b).

2.2.3 Geomorphology and hydrology

Taiwan's shoreline is approximately 1140 km long and has been historically divided into four types (Lin 1957). In the north, a crenulated coastline of alternating capes, bays and sandy beaches reflect eustatic changes and differential weathering of the Miocene sandstones and shales. Along the east coast the shoreline morphology responds primarily to uplift tectonism, characterised by steep cliffs, elevated terraces and sparse gravel beaches, with the only substantial alluvial fill being the Longitudinal Valley, wedged

between the Central and Coastal ranges, and the Ilan Plain in the northeast (Figure 2.2). In the south, the shoreline exhibits tidal flats and sand bars with living coral reefs forming barrier islands giving rise to lagoonal systems. The coastline in the south also has raised ancient reef limestones terraces. The west is typified by large alluvial-fill coastal plains and gently sloping hinterland, moving into elevated terraces associated with the Western Foothills (Figure 2.2).

It is estimated that groundwater storage in the coastal alluvial-fill plains is 45-58 × 10^8 m^3, compared to 125-165 × 10^8 m^3 in fractured bedrock mountain aquifers (Lee et al. 2002; Wu 2003). The long-term mean annual groundwater recharge, estimated using a coupled water-balance and base-flow separation approach that integrates discharge, meteorological measurements and geographic information, is approximately 18 × 10^9 m^3 (~500 $mm.yr^{-1}$) in total, with the highest values averaged over the full range of elevations, >1000 $mm.yr^{-1}$, calculated in the northeast and east Central Range (Lee et al. 2006). Groundwater recharge rates that exceed 2000 $mm.yr^{-1}$ were estimated for high mountain areas (over 1000 m) (Lee et al. 2006).

Several studies indicate that sea level off the eastern margin of China was between −155 and −130 m during the last glacial maximum (Wang and Wang 1980). Such sea-level fluctuations would have led to profound increases in the surface areas of alluvial fan systems on the west coast of Taiwan, extending the length scales of the river drainage and deposition networks and expanding the available volume of matrix for groundwater infiltration and storage during glacial low-stands.

Two distinct, yet interconnected, aquifer types occur in Taiwan. The first type is the alluvial-fill sediment wedges that primarily exist along the west coast, in which hydraulic gradients in the upper unconfined portions typically contour the overlying topography, and which are primarily recharged by precipitation that falls directly onto the basin and that which runs off and through surrounding hill-slopes. Permeabilities are relatively high due to large abundances of gravels and sands that infill these wedges and their physical properties are well understood and described (WRA 2001). The second aquifer type in Taiwan occurs at high elevations in the fracture network of the mountain bedrock mass, the physical properties of which are less well known. Groundwater recharge by precipitation is typically rapid, and interconnectivity with the surface and with alluvial-fill aquifers occurs via spring activity along joint and fault planes and via interchange with the river drainage network (Yoshimura et al. 2001).

2.2.4 Climate and surface processes

Taiwan has a subtropical climate with an average annual precipitation of 2515 $mm.yr^{-1}$. The WRA have measured a large altitudinal gradient in precipitation rates since 1970, with 1500 $mm.yr^{-1}$ observed in the low-lying plains and up to 6000 $mm.yr^{-1}$ recorded in the high peaks of the Central Range. Taiwan is situated in the Western Pacific tropical cyclone belt and is typically impacted by three to four typhoons per year (Figure 2.4).

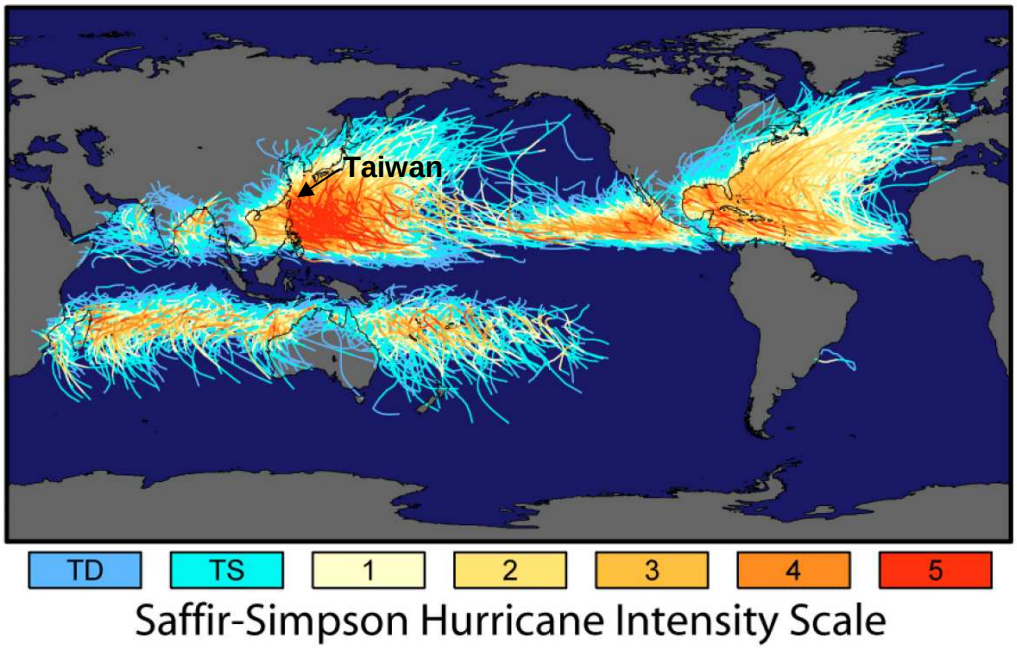

Figure 2.4. Tropical storm map. Taiwan is situated in the Western Pacific tropical cyclone belt and is impacted by 3-4 typhoons per year. Approximately 89 % of the average annual precipitation (2515 $mm.yr^{-1}$) falls during the typhoon season (June-October). Shown is 150 years worth of individual storm track data (National Hurricane Center and Joint Typhoon Warning Center) up to and including 2006 using the colour coded Saffir Simpson Intensity Scale (TD = tropical depression and TS = tropical storm). Image courtesy of Robert A. Rohde – http://earthobservatory.nasa.gov.

Most of the total precipitation (up to 89 %) falls during the typhoon season (June to October) (Wu and Kuo 1999), but the winter months are humid, too, with the number of wet days similar to or greater than in the summer months.

High rates of precipitation on the uplifting topography of the Central Range generate rapid fluvial incision and mass wasting. These processes have exhumed medium-grade metamorphic rocks to varying degrees across the strike of the lithologies exposing the metamorphic core of the Central Range (Willett et al. 2001). The pervasive fluvial

erosion of obdurate bedrock has resulted in the carving of steep mountain slopes (many greater than 45°) that fail by landsliding, which in Taiwan is the primary mechanism of clastic sediment export (Hovius et al. 2000). Importantly, and as will be demonstrated in detail in Chapter 6, landslides and related rock-mass shattering are effective mechanisms for replenishing mineral surface areas that are available for chemical weathering reactions.

2.2.5 Biosphere and land use

Taiwan supports the growth of over 4000 vascular plant species, approximately 25 % of which are endemic (Chou et al. 2011). The mountains of Taiwan are typical of subtropical slopes supporting thick vegetation and a dense canopy of mature trees. However, due to high rates of landsliding and debris flows, erosional loss of the biomass in Taiwan is comparatively greater than in other subtropical biomes (Lin et al. 1994; 2003; Hilton et al. 2012). Mainly natural forests prevail below the tree-line at approximately 2600 masl, which in some locations of the Central Range extends above 3000 m. The predominant vegetation there is subtropical evergreen broadleaved forest (Liew et al. 1998). Below 500 m elevation, ecosystems are dominated by *Ficus-Machilus* (Fig and Laurel), which above 500 m and up to 2500 m become replaced predominantly by *Castanopsis* (beech) and *Quercus* (white oak), which in turn are phased out to largely *Tsuga-Picea* (coniferous hemlock and spruce) up to 3100 m (Su 1984). Deciduous forests occur on relatively drier slopes, typified by *Alnus formosana* (alder) up to 2600 m, above which *Pinus* (pine) and meadows of sparse shrub grassland dominate. In the coastal plains, much of the land has been prepared for agriculture and undergoes extensive artificial flooding for aquiculture. Here, floodplain meadows of *Saccharum spontaneum* (perennial grass) grade into low to mid-altitude montane scree communities of Pouzolzia (flowering nettle) and Boehmeria (herbaceous shrubs) (Song and Xu 2003).

Taiwan has a history of logging for the lumber trade stretching back several centuries, but due to poor accessibility of the steeper slopes, this activity is limited to the lower-lying regions of the Central Range and the Western Foothills (Lu et al. 2001). There are three main roads that bisect the Central Range with several lesser roads and railways servicing small villages at mid to high elevations. Augmenting the transport network are several tunnelled portions of road - for example the Su-Hua Tunnel series that links the north and west coasts - bored through ridges where it is not feasible to build surface roads. Due to the difficulty in building on steep slopes and the relatively small surface area of transport networks, environmental impacts due to construction are minimal in the

mountains. With ~99 % of Taiwan's population of over 23 million residing below 500 m elevation (Ministry of the Interior, 2005 statistics: http://www.moi.gov.tw), the western low-lying plains in particular, where population densities are double Taiwan's average, support this majority. The land there is extensively urbanised, industrialised and exploited for agriculture and aquiculture, with there being significant strains on water resources as a consequence (Kao and Liu 1996; Liu et al. 2007).

2.3 Previous work on groundwater chemistry and fluxes

The Groundwater Monitoring Network Program in Taiwan was established in 1992 to enable better understanding and more effective development of groundwater resources and involved the construction and recovery of sediment cores from near to 1000 monitoring wells nationwide (Hsu 1998). Previous studies on groundwater chemistry in Taiwan have mainly focused on several of the environmental concerns regarding the quality of groundwater used for drinking and municipal purposes. Seawater intrusion into aquifers that supply potable water in the heavily populated Pingtung Plain has been attributed to the over-drawing of groundwater for agricultural uses from increasingly deeper aquifers in the coastal Pingtung region (Kuo et al. 2003; Wang et al. 2003).

Endemic black-foot disease, a chronic and sometimes life-threatening peripheral vascular disorder in humans, has been reported in the southwest coastal plains of Taiwan since 1910 (Kao and Kao 1954), and has been later linked to high arsenic concentrations in the groundwater there (Chen and Wu 1962). Studies of the Chianan Plain, located in the southern region of the Choshui alluvial fan, have showed that arsenic concentrations in several wells exceeded the World Health Organisation's recommended limit of 0.01 $mg.L^{-1}$, with the highest concentrations (0.10 to 1.2 $mg.L^{-1}$) in the aquifers deeper than 50 m below the surface, which were deposited before the Holocene marine transgression (Chen and Liu 2007). In comparison, Hsinchu City in the northwest region of Taiwan, with no reported cases of black-foot disease, has reported arsenic levels in the municipal groundwater supply of typically less than 0.0007 $mg.L^{-1}$ (Chen et al. 1994).

Linked to high arsenic and heavy-metal concentrations in the Chianan Plain are reducing conditions and high levels of methane gas, which are also characteristic of the groundwaters in the Ilan Plain in the northeast region of Taiwan (Liu et al. 2009). The Chianan Plain had previously been under investigation by the Chinese Petroleum

Corporation as a potential for profitable gas production (Hsu 1984), but since then concentrated hydrocarbon exploration efforts have moved offshore (Liu et al. 2006).

More than 120 hot springs have been described in Taiwan that typically outcrop along tectonic structures such as fault planes and anticline hinges (Song and Liu 2006) (see Figure 2.5). There are 21 of these hot springs that outcrop along tectonic structures in the Western Foothills zone draining mostly into the Pingtung Plain, for which water chemistry data has been made available for this study by personal communication (Professor Song, Sheng-Rong, National Taiwan University, P.O. Box 13-318, Taipei 106, Taiwan). Hot-spring chemistry is typically evolved relative to surface water compositions (Becker et al. 2008; Evans et al. 2004; Kopf et al. 2001) with geothermal rock-water interactions at depth resulting in lithium concentrations that are typically 1000× enriched over most low-temperature weathering inputs and rain (Kısakűrek et al. 2005). The chemistry of the hot-spring waters described in Taiwan display a range from Na^++K^++HCO_3^- to Ca^{2+}+Mg^{2+} to SO_4^{2-}+Cl^--dominated compositions (Song and Liu 2006), likely reflecting mineralogical assemblages of the rock surround at depth and geothermal heterogeneities (Millot et al. 2010). The average concentration of Cl^- from the 21 hot-springs draining into the Pingtung Plain was 3.49 $mmol.L^{-1}$ (Song and Liu 2006), comparable to a single spot measurement made on water from one of these hot-springs by Joshua West (Department of Earth Sciences, University of Southern California, 3651 Trousdale Pkwy, Los Angeles, CA 90089 USA (personal communication), which was 3.99 $mmol.L^{-1}$. The Li^+ concentration in this sample was 734 $\mu mol.L^{-1}$, approximately 28-times the value of average seawater.

Chemically enriched fluids are also associated with mud volcanoes, which result from tectonic compression and the related dewatering of clays in accretionary prisms (Kopf et al. 2003; Milkov 2000; Yassir 1987). At least 17 active mud volcanoes have been described in southwest Taiwan, which outcrop within the Western Foothills zone (Wang et al. 1988), from which CH_4 and CO_2 degas (Shih 1967). The fluids from these mud volcanoes are available for groundwater recharge to the Pingtung and Choshui Plains. At 200 $mmol.L^{-1}$, the average concentration of Cl^- in 12 of these mud volcanoes approaches half that of seawater. To a first order, the concentrations of Na^+, K^+ and Li^+ in these mud volcanoes appeared to be mixtures of connate seawater and hot-spring water, whereas Ca^{2+} and Mg^{2+} were, on average, relatively depleted with respect to seawater and hot spring water (You et al. 2004).

The chemical concentrations and fluxes of the Kaoping River (see Figure 2.5 and Section 2.4.1.1) will be used as a comparison for assessing groundwater chemistry and

subsurface fluxes in the Pingtung Coastal Plain (Chapters 4 and 5). One striking feature of the Kaoping River is that higher than global-average riverine sulphate concentrations have been reported there (Das et al. 2012). Here it has been speculated that the correlation between sulphide oxidation and erosion rates (Calmels et al. 2007) explains these highly-elevated concentrations in the high-landslide-rate environment of Taiwan (Das et al. 2012). The high modal abundances of pyrite, originally deposited in Palaeozoic marine sediments, which are now hosted in the greenschist units of the Central Range, generate significant volumes of sulphuric acid upon oxidative weathering (Yoshimura et al. 2001). During the chemical weathering of carbonates in the Liwu River catchment, this excess of sulphuric acid, in conjunction with soil-respired carbonic acid, plays an important role in the carbon cycle (Yoshimura et al. 2001). Highlighting the importance of subsurface chemical weathering in fractured crystalline aquifers, Calmels et al. (2011) estimated that 40 % of the silicate weathering flux carried by the Liwu River is derived from meteoric water that had circulated at depth within surrounding bedrock.

With the exception of the study by Calmels et al. (2011), previous studies on groundwater flux estimates to the ocean from Taiwan have mainly concentrated on models and observations of submarine groundwater discharge into the ocean, and hint at the potential importance of the chemical load of these fluxes in terms of ocean geochemical budgets and nutrient cycling, but pay little or no attention to the potential role of chemical weathering in governing these fluxes, or of how these fluxes might inform on the processes controlling chemical weathering. Notwithstanding, a summary of the current understanding of groundwater fluxes to the ocean around Taiwan is useful in providing context for the results that will be discussed as part of this study in subsequent chapters.

Submarine groundwater discharge, widely referred to in the literature as simply SGD, is defined as “any and all flow of combined fresh and saline water on continental margins from the seabed to the coastal ocean, regardless of fluid composition or driving force” (Burnett et al. 2003). Peng et al. (2008) conducted a field and model based assessment of SGD in coastal pore waters at 17 locations around Taiwan’s coastline (predominantly along the south, west and north coasts). They used salinity measurements of seawater and terrestrial waters (groundwater and river water) to partition the fractions of fresh and saline waters contributing to their sampled offshore pore water values, and found that in most locations, the fraction of fresh water was similar to that of the global range (0-35 %) (Hussain et al. 1999; Taniguchi and Iwakawa 2004; Taniguchi et al. 2005). They focused on a site in southwest Taiwan, near the southern region of the Pingtung Plain,

where up to 99 % of the pore waters sampled was shown to be derived from a meteoric source. Seepage metres positioned at approximately 8 m water depth along 300 m shore-normal and 150 m shore-parallel transects at this site off the Pingtung Plain shoreline, indicated that groundwater flow rates into the ocean there were 34-42 $m.yr^{-1}$, exceeding most worldwide reported values (Taniguchi et al. 2002). Furthermore, their modelled SGD values - based on hydraulic-head hydrograph separations, previous estimates of groundwater recharge and measurements of the specific storage of the aquifers – fell significantly short of suggesting such flow rates as those observed via the seepage meters along the Pingtung Plain coastline. They concluded that groundwater flow via submerged faults - in this case, the authors argue, most likely the high-angle oblique-slip Chaochou Fault (Yen and Tien 1986) that is a major mid-orogen thrust fault between the Central Mountain Range and Western Foothills bounding the southern margin of the Pingtung Plain - could be a significant source of solutes to the ocean in such tectonically deformed regions, and that combined terrestrial and coastal approaches are needed to fully categorise and understand ocean-bound groundwater fluxes.

Lin et al. (2010) used combined $\delta^{18}O$, $\Delta^{87}Sr$, Sr^{2+} and Ba^{2+} as tracers for fresh water off the coast of the Pingtung Plain to detect groundwater flow up to 25 km offshore, extending the depth range of known submarine groundwater discharge to ~1200 m. In addition, Lin et al. (2011) used combined $\delta^{18}O$, δD, $\delta^{13}C_{DIC}$, tritium and $\Delta^{14}C$ fresh-water tracers to calculate that the delivery of groundwater to the ocean off the southwest coast of Taiwan amounted to 4.5×10^9 $m^3.yr^{-1}$, a water flux which they postulated could represent a significant source of trace elements and other chemical constituents to coastal waters. When compared to the long-term estimate of mean annual groundwater recharge of Lee et al. (2006) (18×10^9 m^3) (Section 2.2.3), the 4.5×10^9 $m^3.yr^{-1}$ estimate of fresh groundwater discharge to the ocean of Lin et al. (2011) is remarkably high. A comparison between the groundwater fluxes calculated for this study and the estimate of Lin et al. (2011) is presented in Section 5.6.5 (Chapter 5).

2.4 Sample sites for this study

2.4.1 Alluvial-fill coastal plains

The plains along Taiwan's west coast are approximately 2 km thick and underlain by pre-Cenozoic block-faulted basement, which was subsequently in-filled by Palaeogene and Neogene sediments. They are bounded to the east by the Western Foothills fold-and-

thrust belt. There are more than 200 wells distributed evenly within the coastal plains that are managed by the WRA as part of the Groundwater Monitoring Network Program, all of which are constructed out of 6-inch diameter galvanised or stainless steel casing with well screens ranging from 6-36 m. The gravel pack around the well screens is overlain by 3-5 m thick bentonite cladding to prevent groundwater from flowing between aquifers of different depths, ensuring that aquifer depth corresponds to the screen depth being sampled. All of the wells are fitted with either a pressure transducer or a float-type piezometer for measuring hydraulic head. A digital, or a combined strip-chart analogue and analogue-to-digital device, is used to record hydraulic heads. Measurements have been recorded hourly since 1994 with a precision of approximately 1-5 mm. All of the wells sampled as part of this study are of this type. The following subsections illustrate and discuss the two coastal plains that were selected for this study.

2.4.1.1 General characteristics of the Pingtung Plain

The Pingtung Plain coastal aquifer system is located in southwest Taiwan (Figure 2.5). It is an elongate, 2 km-deep alluvial wedge bounded to the northwest and southeast by two active oblique-slip faults, the Chelungpu and Chaochou Faults, respectively. The plain has a surface area of approximately 1210 km^2, and its underlying fill consists of poorly consolidated gravels, sands and fines compiled in broad braided river fans of Late-Pleistocene to Holocene age, as determined by borehole record PTG-1 of the Chinese Petroleum Company (Chiang et al. 2004). The plain has been subdivided into a coarse-grade gravel-rich ‘proximal region’, a medium-grade sand-rich ‘middle section’ and a fine-grade ‘distal zone’ with sands, silts and intercalated clays (Ting et al. 1998a).

To the east of the plain the mountains of the Central Range are composed of Eocene-Oligocene black slates intercalated with carbonaceous sandstones and quartzites. To the north of the plain foothills comprise Miocene-Pliocene sandy shales, carbonaceous sandstones and conglomerates. To the southwest the plain is bounded by the Taiwan Strait (Hsu 1961) (Figure 2.5). Soils in the Pingtung Plain are weakly developed to underdeveloped, consisting of older non-calcareous and younger calcareous alluvium together with red soils, lateritic terraces and metamorphic and sandstone-shale yellow colluvial soils, which typically display moderate to high permeabilities (Jean 1992; Ting et al. 1998b). Texturally, the alluvium and colluvium of the plain has been subdivided into approximately 63 % loam, 21 % clay, 9 % gravel and 7 % sand (WRPC 1985). Agriculture

is widespread in the Pingtung Plain, with large plots of land devoted to rice paddies, sugarcane and terrestrial aquiculture.

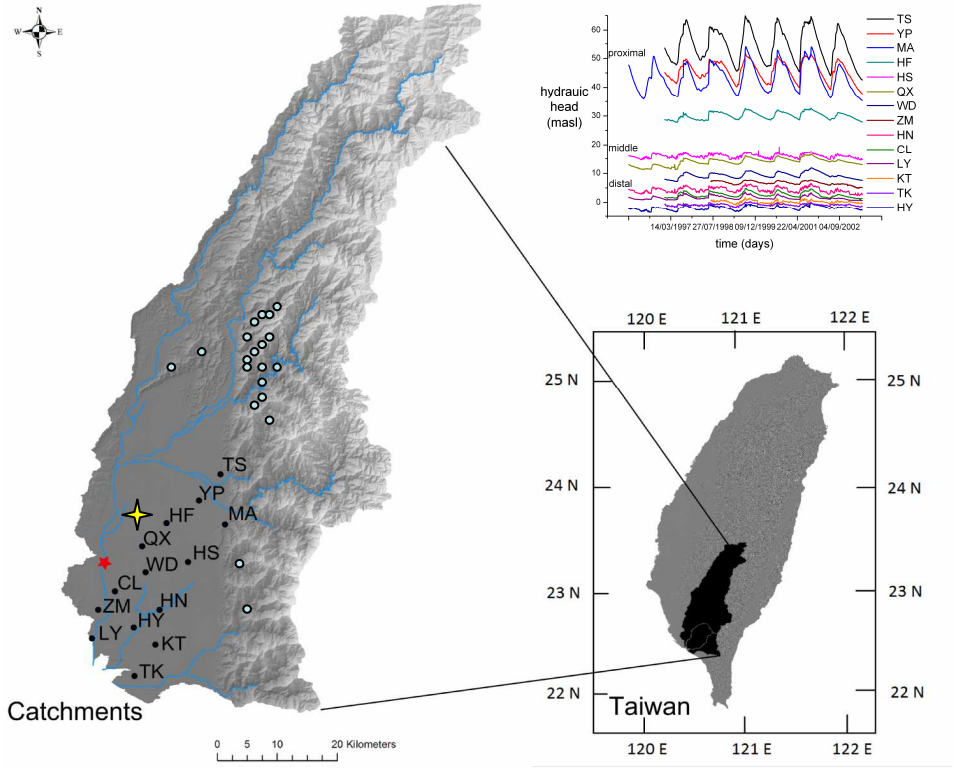

Figure 2.5. The Pingtung Plain and associated river catchments. Topographic map of the Kaoping, Tungkang and Linpien catchments showing the 14 well sites in the Pingtung Plain (circles), the Kaoping River gauging station 1730H043 (red star) and precipitation monitoring station Ping Dong-5 (yellow star). The blue circles are the locations of the hot springs sampled by Song and Liu (2006), the water chemistry of which is incorporated into this study. The graph shows the hydraulic head 5-year time series (averages of the 2−4 wells at each station) (WRA data) and the hydraulic gradient from the proximal region to the distal zone, indicating the south-westerly groundwater flow path.

The average air temperature of the Pingtung Plain is 24 °C and the average precipitation is 3130 mm.yr^{-1}, in excess of the island's average of 2515 mm.yr^{-1} (Ting et al. 1998b). The average annual potential evaporation, determined by the open-pan method is ~ 1200 mm.yr^{-1} (Ting 1993), giving an average effective precipitation estimate of ~1900 mm.yr^{-1}. The plain is a relatively flat area drained by three main rivers, the Kaoping, the Tungkang and the Linpien each with headwaters in the adjacent uplands (Figure 2.5). Of these three, the Kaoping is the most important, being the second largest river in Taiwan in terms of catchment size (3257 km^2) and with an average annual discharge rate during the period 1981-1990 of 7.40 × 10^{12} L.yr^{-1} (Ting et al. 1998a). Measured monthly discharges

ranged from 0.03 × 10^{12} L.month^{-1} in February 1984 to 3.30 × 10^{12} L.month^{-1} in September 1990 (Ting et al. 1998a).

Analysis of precipitation data collected from the Ping Dong-5 monitoring station (00Q070) located on Jianguo Road in Pingtung City (Figure 2.5) shows that one of the extreme rain events typifying Taiwan's summer months was captured during the Kaoping River sampling period for this study (March to August 2005) (WRA data); the first day of the flood caused by typhoon Haitang in late July 2005. However, due to a dilution effect - a first-order response of most dissolved constituents that are products of chemical weathering seen in river water chemistry at periods of high stage (e.g Salmon et al. 2001) - combined water flux and chemical concentrations likely give estimated integrated riverine chemical fluxes that are biased towards higher-than-average concentrations (Figure 2.6). Complementary discharge data was not available for the river water sampling dates for the Kaoping River. However, as will be shown below in Section 2.4.1.3 and discussed in Chapter 5, chemistry-flux relationships were investigated for the Choshui River.

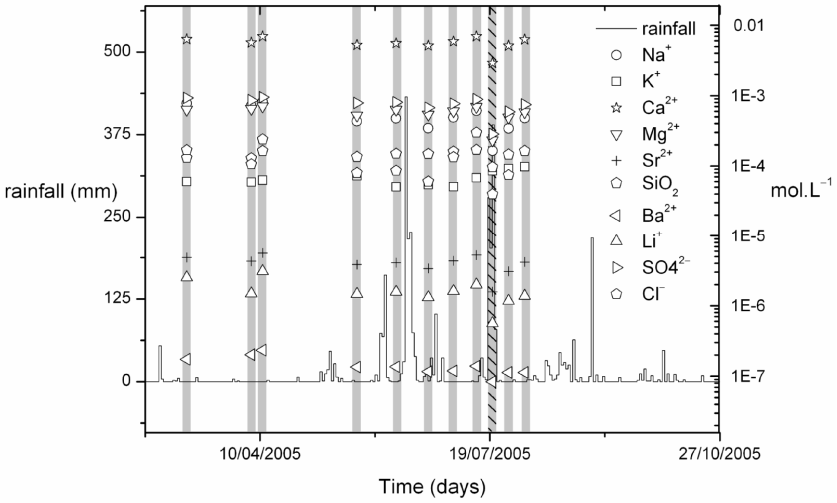

Figure 2.6.Precipitation during the Kaoping River sampling period (March to August 2005). Gray bars indicate the 11 river water sampling dates. The hatched bar shows the first day of the flooding event caused by typhoon Haitang in late July 2005. The chemical measurements of the sample taken on this day show that relative dilution had occurred in all elements excepting potassium. Similar dilution due to increased river discharges as a result of high rainfall would have likewise occurred during the other episodes of peak precipitation.

The groundwater chemical fluxes through the Pingtung Plain that are presented and discussed relative to the chemical fluxes of the Kaoping River in Chapter 5 are therefore likely to be lower-bound estimates of relative subsurface discharge to the ocean in the Pingtung region.

2.4.1.2 Hydrogeology of the Pingtung Plain

There are 36 monitoring-well stations in the Pingtung Plain managed by the WRA, 14 of which, comprising 43 individual wells, were selected for hydrological and chemical

evaluation for this study. The wells are located along a transect extending from the foothills to the coast (Figure 2.5). They range in depth from 6-237 m (see Figure 4.1A, Chapter 4; Data Table A) and have records of daily hydraulic head data measured by the WRA over a five-year time period (November 1998 - May 2003) (Figure 2.5; Data Table B). The hydraulic head data imply that groundwater generally flows parallel to the topographic slope with an average hydraulic gradient of 1.37×10^{-3} in a southwest direction tapering towards the coast, where it is generally thought to mix with intruding saline waters (Wang et al. 2003; Lin et al. 2011) before discharging into the Taiwan Strait.

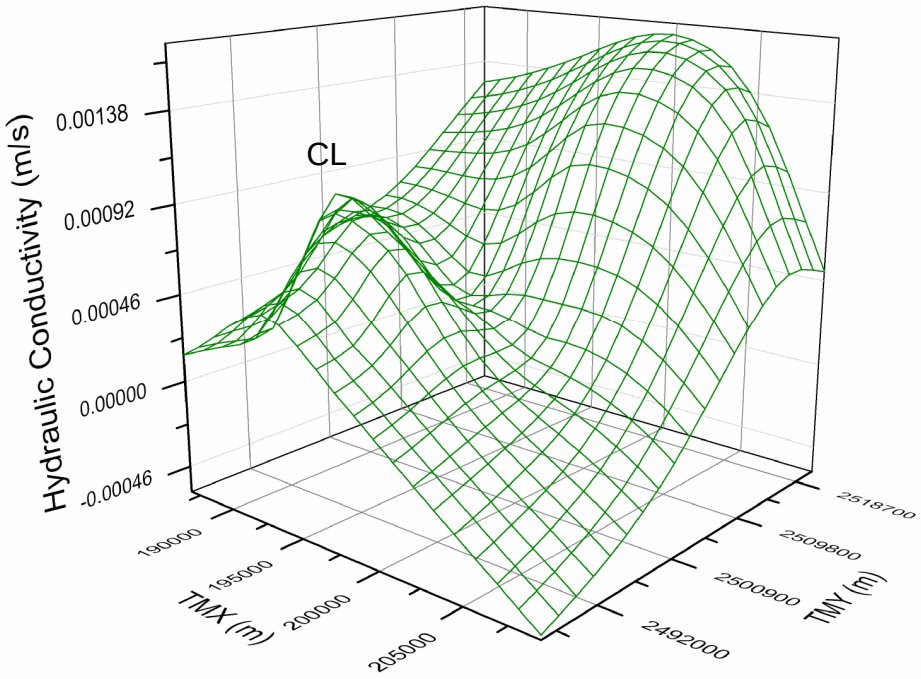

Figure 2.7. Hydraulic conductivity (k) in the Pingtung Plain (WRA data). The k−values used are averages of the 2−4 wells comprising each of the 14 stations and are smoothed using a random thin-plate spline function at a resolution of 0.05 to create a single representative surface of permeability. In general, k decreases towards the coast, but a localised high, illustrating the heterogeneous nature of the physical subsurface, is seen at well station CL.

The range in hydraulic conductivity (*k*) (WRA data) in the Pingtung Plain spans over four orders of magnitude with a mean value of 5.97×10^{-4} m.s^{-1} and exhibits a first-order decrease towards the coast where the average *k*-value is 5.06×10^{-4} m.s^{-1} (Figure 2.7; Data Table A). Superimposed on this decreasing gradient is a localised average high of 1.10×10^{-3} m.s^{-1} at distal station CL (Figure 2.7).

2.4.1.3 General characteristics of the Choshui Plain

The sampled region of the Choshui Plain coastal aquifer system comprises the middle portion of the Taichung Basin, which is the largest alluvial fan in Taiwan. Located in the central west (Figure 2.8), it has a surface area of approximately 1800 km^2. The plain is bounded to the east by two Pleistocene ridges, the Pakuashan and Touliu anticlines, to the north and south and by low foothills and to the west by the Taiwan Strait (Figure 2.8). The immediate portions of its underlying fill consist of poorly consolidated Holocene massive gravels in the proximal region near the foothills, which progressively grade into sands in the middle section and fines towards the distal zones in the west, northwest and southwest. Underlying this loose fill the subsurface geology consists of consolidated, folded and fractured Pleistocene sedimentary rocks (Suppe 1976).

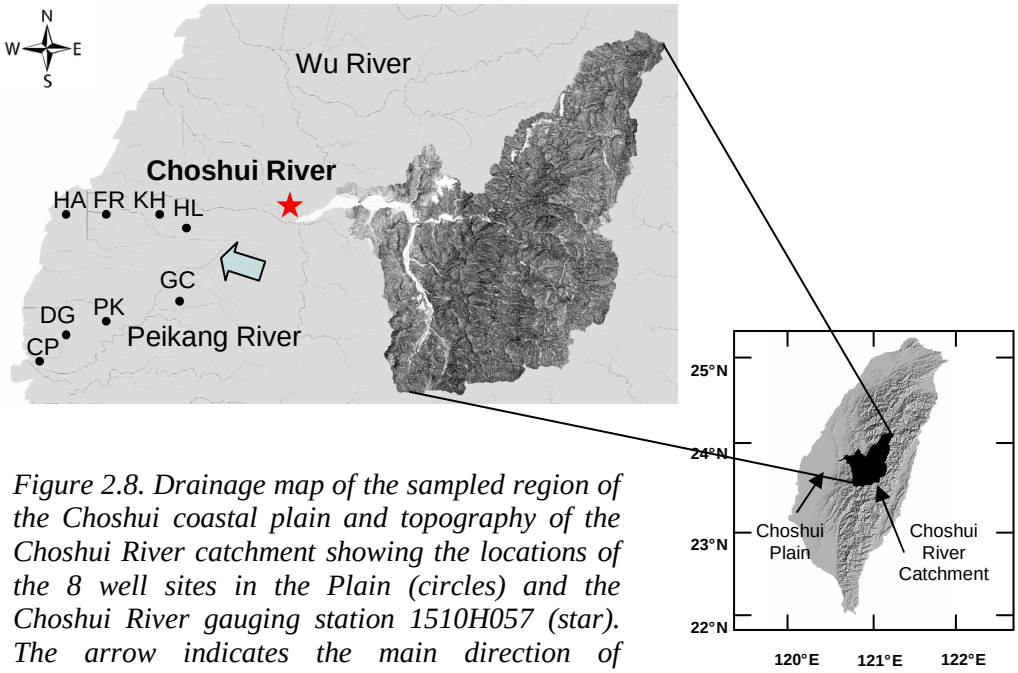

Figure 2.8. Drainage map of the sampled region of the Choshui coastal plain and topography of the Choshui River catchment showing the locations of the 8 well sites in the Plain (circles) and the Choshui River gauging station 1510H057 (star). The arrow indicates the main direction of groundwater flow in the region as described by Wang et al. (2005).

The main fluvial system in the plain is the Choshui River, which divides the basin into the Changhua region to the north and the Yunlin region to the south. Two other main streams are the Wu River in Changhua and the Peikang River in Yunlin (Figure 2.8). The Choshui River catchment drains an area of 3150 km^2 and had an annual discharge rate, calculated daily during the period March 2005-December 2006 of 9.18×10^{12} L.yr^{-1} (WRA data; Data Table C). Measured monthly discharges ranged from 1.23×10^{10} L.month^{-1} in Feb 2006 to 1.06×10^{13} L.month^{-1} in July 2005.

For each bi-weekly water sample collected by the WRA on behalf of this study (see Section 3.2.5.1, Chapter 3), complementary discharge measurements were made (Data Table C), allowing for precise calculations of riverine chemical flux estimates of some solutes based on rating curve relationships between chemical ions of interest and discharge (see Chapter 5 for discussion).

2.4.1.4 Hydrogeology of the Choshui Plain

There are 73 monitoring-well stations in the Choshui Plain managed by the WRA, 8 of which, comprising 22 individual wells that are located in the Yunlin region south of the Choshui River, were selected for hydrological and chemical evaluation for this study. The wells are located along two transects extending from near the foothills to the coast, chosen to bound the previously-described general west-northwest groundwater flow path in the region (Wang et al. 2005) (Figure 2.8). The wells range in depth from 24-294 m (see Figure 4.1A, Chapter 4; Data Table A).

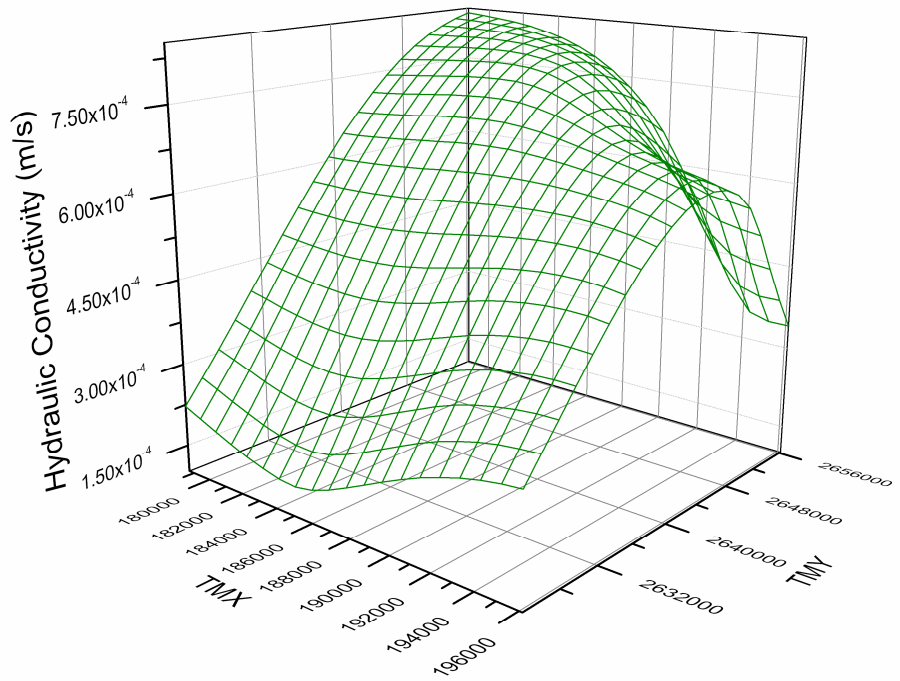

Figure 2.9. Hydraulic conductivity (k) in the Choshui Plain (WRA data after Lin et al. (2004)). The k−values are smoothed using a random thin-plate spline function at a resolution of 0.05 to create a single representative surface of permeability. In general, k decreases towards the coast.

The static water levels in the 22 sampled wells were measured at the time of sampling (Data Table A), which together with elevation and distance data for the well

stations provided an estimate of the hydraulic gradient. The water level data implied that across the 25,716 m of the flow path groundwater generally flows parallel to the topographic slope with an average hydraulic gradient of 1.58×10^{-3}.

The range in hydraulic conductivity in the Choshui Plain, taken from eight measurements ascertained by pump testing (WRA data after Lin et al. (2004)), spans from 1.34×10^{-4} m.s^{-1} to 7.77×10^{-4} m.s^{-1}, with an average of 4.16 m.s^{-1} (Figure 2.9; Table 2.1). The hydraulic conductivity measurements of Lin et al. (2004) were not from the wells sampled as part of this study, but provide likely values of the permeability range in the sampled portion of the Choshui Plain in general.

Table 2.1 Hydraulic conductivity properties of the Choshui Plain

TMX[a]	TMY[a]	Hydraulic Conductivity[b] (*k*) ($\times 10^{-4}$ m.s^{-1})
185350	2624184	1.43
178717[c]	2624989[c]	3.53
194052	2656100	3.11
190120	2656250	6.55
196133	2649778	6.07
187624	2648441	7.77
191168	2627781	3.46
178717[c]	2624989[c]	1.34

[a]Tranverse Mercator of 2°, central meridian = 121 °E
[b]Obtained by well pumping tests (WRA data after Lin et al. (2004))
[c]distal-most wells

2.4.2 Fractured-bedrock aquifers

For the sampling of groundwaters in fractured bedrock, drip sites in disused transport tunnels, which are effectively horizontal boreholes, were exploited. All tunnels were open at both ends. Only portions of tunnel networks that were uncased with concrete were selected for sampling, thus reducing the potential for collecting contaminated groundwaters. Although tunnels do disturb the natural groundwater flow patterns (typically by drawing groundwater flow lines toward them), it will be shown in Chapter 6 that significant groundwater chemical variability is related to active surface processes in the vicinity of tunnels. The tunnels sampled ranged in length from 80-534 m and were typically 3-5 m high with space enough for a standard small van to pass through. The

following subsections document the tunnels selected for this study, which are located in two distinct regions of the mountain ranges in Taiwan.

2.4.2.1 General characteristics of the Bayyang Tunnel Trail

The Bayyang Tunnel Trail, purpose built for road access, is a 2 km-long series of eight tunnels (three of which were sampled for this study) winding and cutting through bedrock along a mountain trail in the Liwu River catchment (400 km^2) in Taroko Gorge National Park (Figure 2.10). The tunnels are largely uncased and thus expose 'clean' ceilings under rock masses through which groundwater percolates down via fracture networks as drip-waters. The geologic setting consists of steep terrains in the east flank of the Central Range, with the steeply-dipping (~52° NW) lithologies in the region of the tunnels being relatively uniform consisting of chlorite siliceous schists containing plagioclase and K-feldspar and with high modal abundances of embedded pyrite. This lithology is known as the Tananao schists and includes relatively-abundant interspersed outcrops of marbles (see Figure 2.3).

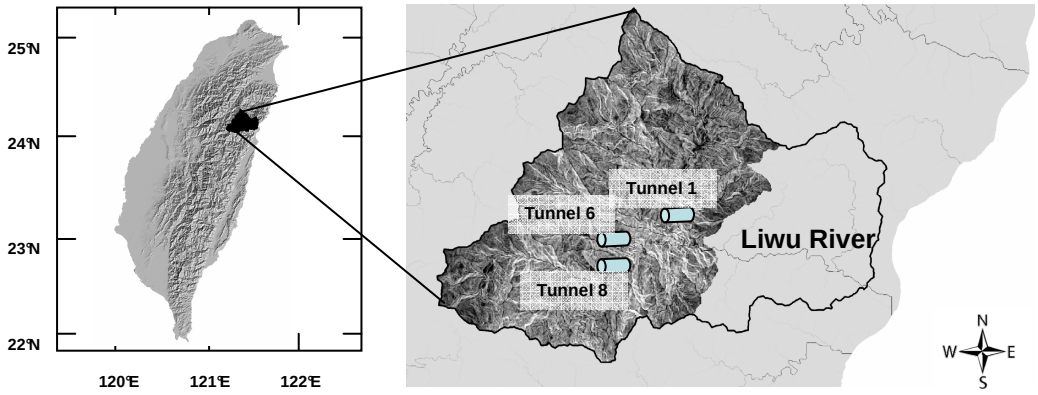

Figure 2.10. Drainage map and topography of the Liwu River catchment showing the sampling locations of the bedrock drip-waters at the three tunnels (cylinders) selected for this study. Also collected at these locations were rock and soil samples (see Sections 3.2.2 and 3.3.3, Chapter 3).

2.4.2.2 Tunnel 1

Tunnel 1 is a non-arcuate horizontal borehole approximately 520 m in length trending ~ E-W that cuts perpendicularly through the structural dip (52° N/NW) of the

overlying bedrock mass, which is an asymmetrical ridge with up to approximately 200 m of vertical relief (Figure 2.11). Given the abundant drip-sites along its entire length and the extent of overlying topographic relief, Tunnel 1 is the most important tunnel sampled as part of this study. The several discrete fracture zones that are dispersed along the entire length of Tunnel 1 make it the ideal location to observe any changes in groundwater chemistry that might relate to the overlying rock-mass thickness and to groundwater residence times.

Of significant note in Tunnel 1 were the dense fracture networks that were typically cemented with secondary calcite (Plate 1: DSCF4153). In addition, a small cave, approximately 1 m^3 in size, had naturally formed due to groundwater circulating through the fractured rock mass. Accumulated inside the cave were weathered rock fragments in a muddy and silty matrix and the surrounding walls were draped in secondary calcite curtain formations (Plate 1: DSCF3469). A particularly special feature of Tunnel 1 was the occurrence of a major landslide on the ridge over the tunnel entrance midway through the four-year sampling campaign pertaining to this study.

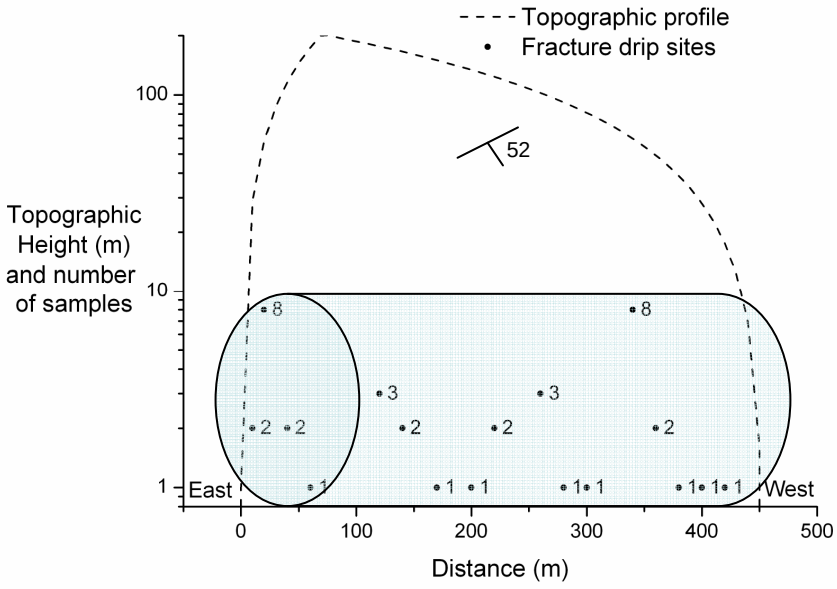

Figure 2.11. Tunnel 1 in Bayyang with overlying topographic profile and drip site locations. Shown is the number of groundwater samples recovered from each drip site over the course of the sampling campaign (see Section 3.2.2, Chapter 3). The height of the tunnel is exaggerated and the y-axis is also used to denote the number of samples collected from each drip site, i.e. all drip sites were actually located along the same horizontal plane. The symbol indicates the strike and structural dip of the bedrock.

2.4.2.3 Tunnel 6

Tunnel 6 is a 300 m-long arcuate tunnel cutting obliquely through the structural dip of the inherent lithology. Tunnel 6 is overlain by a maximum of approximately 40 m of bedrock. A striking feature of Tunnel 6 is the cave that has been naturally carved out due to groundwater circulation through the fractured rock mass between the surface and the tunnel interior. The cave is approximately 20 m long and 4-5 m deep and exhibited continuous fast-dripping to continual-flowing groundwater discharge along several fractures during the entire sampling campaign. The remaining portions of Tunnel 6 were largely dry throughout the sampling campaign. Significant in the cave was the abundance of secondary calcite in the form of curtains, which had draped the schist and marble surfaces and which had also precipitated within and along fractures and joints (Plate 1: DSCF4158). In addition, mud and silt had accumulated along fractures and joints (Plate 1: DSCF4158).

2.4.2.4 Tunnel 8

Tunnel 8 is an 80 m-long arcuate tunnel cutting obliquely through the structural dip of the bedrock. It is bored through approximately 50 m of overlying topography. It is known locally as the ‘Water Curtain’ because of the continual gushing of groundwater through into the tunnel interior from the encasing rock mass. The groundwater discharge rates are so high in Tunnel 8 that a continuous shallow stream runs through it (Plate 1: DSCF3477).

2.4.2.5 General characteristics of Tunnel 28 in Fenchihu

Tunnel 28 in Fenchihu is part of the Alishan Forest Railway system, an 86 km-long partly-disused rail network consisting of 77 tunnels in total, which was originally constructed for logging purposes. The rail network runs up to and throughout the Alishan Mountains in the Western Foothills where Tunnel 28 is located in the upper reaches of the Choshui and Tsengwen River catchments (Figure 2.12). To combat encroachment from tourism and intensive agriculture, the region was declared a National Scenic Area in 2001. Tunnel 28 is 534 m-long, arcuate, E-W trending and largely uncased, cutting perpendicularly through the structural dip of the overlying rock mass (48° N/W), which is a relatively uniformly east-sloping ridge of approximately 20-70 m of Late Miocene to Pliocene sandstones and shales at an elevation of 1339 masl (Figure 2.13). Weathering profiles associated with fracture zones were a feature of the interior of Tunnel 28 (Plate 1:

DSCF4179), which in discrete locations exhibited carbonate nodules with oxidised rims (Plate 1: DSCF4181).

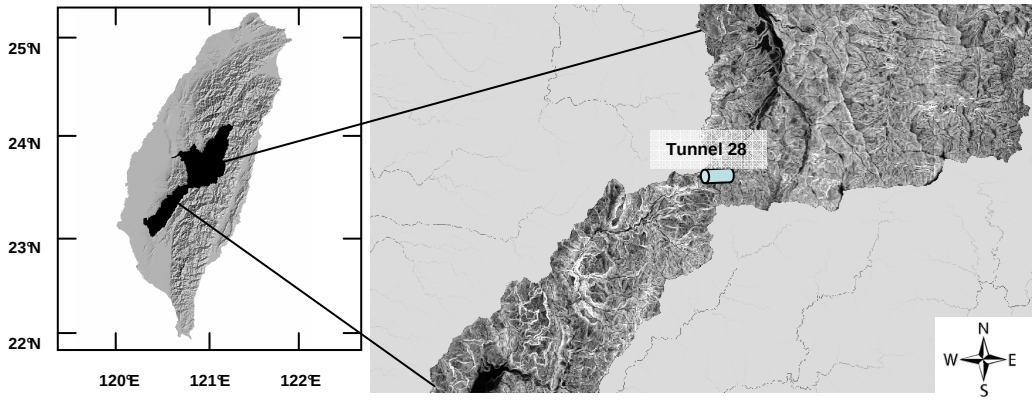

Figure 2.12. Drainage map and topography of the Choshui and Tsengwen River catchments showing the sampling location of the bedrock drip-waters at Tunnel 28 of the Fenchihu Railway network (cylinder) selected for this study (see Section 3.2.2, Chapter 3 for sample descriptions).

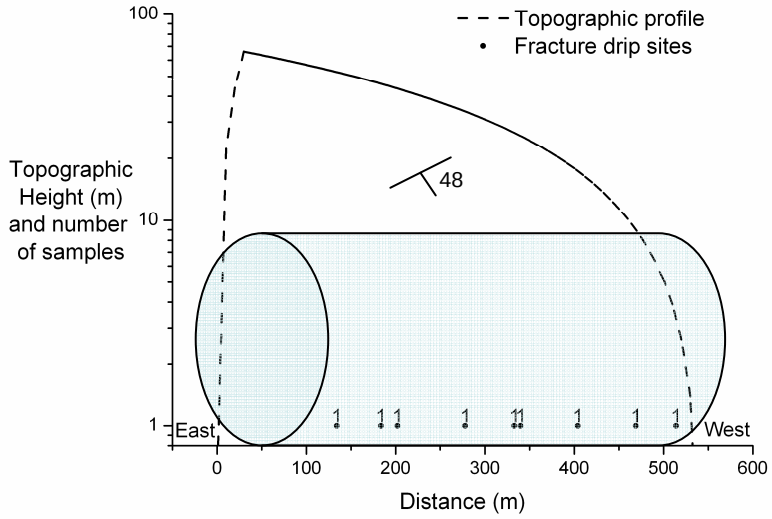

Figure 2.13. Tunnel 28 in Fenchihu with overlying topographic profile and drip site locations. Shown is the number of groundwater samples recovered from each drip site over the course of the sampling campaign (see Section 3.2.2, Chapter 3 for sample descriptions). The symbol indicates the strike and structural dip of the bedrock.

2.5 Summary

This chapter has presented and illustrated the geographical setting and the physical attributes of the island of Taiwan together with details of the specific study localities. In particular, the hydrogeology of these the sites has been discussed and a review of the previous work conducted on groundwater chemistry and/or fluxes from these areas has been outlined.

Plate 1. Photographic images of the lithological surrounds of the tunnels' interiors. DSCF4153, DSCF3469, DSCF4158 and DSCF3477 are from the Bayyang Tunnel Trail. DSCF4179 and DSCF4181 are from Tunnel 28 at Fenchihu. See text for descriptions.

In Chapters 4 and 5 the Pingtung and Choshui coastal plains are considered with respect to the variability of groundwater chemistry with depth and along subsurface flow paths, the sources of solutes to the aquifers and the chemical fluxes that are available for discharging into the Taiwan Strait. In Chapter 6, the results of the groundwater chemistry analyses conducted on drip waters in the Bayyang and Alishan tunnels is presented together and in particular, the results of the time series of groundwater chemistry from Tunnel 1 at Bayyang is investigated in relation to a major landslide that occurred during the sampling campaign.

Chapter 3

Materials and methods

3.1 Introduction

This chapter describes the collection strategies and procedures for aqueous and solid samples and outlines the laboratory preparation measures prior to geochemical analysis. A full description of sample and data acquisitions is presented and the analytical measurements of elemental and molecular concentrations and isotopic compositions of aqueous and solid samples are detailed. Due emphasis is placed on the estimation of uncertainties relating to these analyses, ensuring a robust framework is in place for discussing the observed geochemical variability that these samples display.

3.2 Collection of samples

3.2.1 Equipment preparation

High-density polyethylene (HDPE) water collection and sample storage bottles and 9″ collection funnels were cleaned in a stepwise procedure prior to going into the field. For collection bottles, cation and anion storage bottles and funnels, a three-stage rinse with Milli-Q water followed by room-temperature drying under controlled airflow conditions were performed. For cations, the storage bottles were additionally rinsed three times with 3 M quartz distilled HNO_3 before the water rinse and drying. Other clean equipment consisted of 1L of 3 M HNO_3 (distilled in quartz stills), with a separate acid dropper bottle, 0.2 µm nylon membrane Whatman filter packets with a combination of individual and reusable filter holders plus connector syringes for passing the sample through the filter membranes, plastic zip lock bags for holding the water sample bottles when recovered plus cloth bags for rock and soil samples and parafilm strips for sealing water storage bottles. All clean equipment was packaged in doubled zip-lock bags. Filter holders with filters in place were flushed prior to sampling with 60 mL of deionised water followed by 60 mL of

sample, which was then discarded, and pre-cleaned plastic tweezers were used to remove and replace the filter membranes prior to the collection of each sample.

The pH meter was calibrated against pH 4 and pH 7 buffer solutions once a day when in the field until a stable reading could be confirmed in both cases. No significant drift was observed between calibrations. For alkalinity determination in the field of a representative number of sample waters, calibration of the Lovibond Alka-M-Photometer measuring device was conducted with each sample providing its own reference. After calibration, a Lovibond Alka-M test tablet was added to the sample aliquot, whereupon an alkalinity concentration was determined based on the colour change in the sample brought about by the reaction with the tablet.

3.2.2 Groundwater and surface runoff recovery

3.2.2.1 The Pingtung and Choshui alluvial-fill coastal plains

The objectives for sampling groundwater from the Pingtung and Choshui alluvial-fill coastal plains were primarily to investigate the sources and evolution of solute chemistry along groundwater flow paths and with depth and to quantify the subsurface chemical fluxes available for discharge to the ocean. In assuming that shallow groundwater flow paths would broadly contour the topographic gradient, with the expectation that a first-order decrease in permeabilities along that gradient would be observed, the initial sampling strategy in the case of both regions was to collect water from wells defining trends perpendicular to the backdrop mountain topography. This sampling strategy was augmented using the five-year hydraulic head time series in the case of the Pingtung Plain and details of the main groundwater flow path from a description of the Choshui Plain hydrology (Wang et al. 2005) (see Chapters 2 and 5 for discussion).

One groundwater sample from each of 43 and 22 discrete monitoring wells in the Pingtung (see Figure 2.5, Chapter 2) and Choshui (see Figure 2.8, Chapter 2) coastal plains, respectively, was collected over a two week period in late November 2008 after the end of the typhoon season. A ‘Grundfos MP1 Groundwater Sampling Pump’ was used for sampling the wells. The MP 1 pump is made of inert materials, which do not affect the pumped liquid and thus the geochemical analysis results. The pump has a mechanism that ensures the steady flow of water. In this way, a steady air-free flow of water can be maintained. The maximum rate of flow is 2.40 $m^3.hour^{-1}$ to be used for liquid temperatures

between 0 and 35°C at a maximum hydraulic head of 95 m. Temperature and pH measurements were also made (Data Table A). The wells were flushed until temperature and pH values stabilised prior to sampling; stable values are assumed to represent the groundwater characteristics.

Volumes of 60 mL were collected for analysis of anions and 120 mL for cations and all samples were filtered on site through 0.2 µm nylon membranes and stored at 4°C in HDPE bottles. The 120 mL aliquot was acidified with purified 3 M HNO_3 for cation and strontium isotope analyses and the 60 mL aliquot was kept non-acidified for anion and light stable isotope analyses. Sample storage bottles were sealed tight with parafilm strips to keep the cap seals clean and to prevent air loss and leakage.

3.2.2.2 The Bayyang and Fenchiu tunnels

The objective for sampling in tunnels was to understand the chemical variability of groundwater within fractured bedrock aquifers. The Bayyang tunnels (Tunnels 1, 6 and 8) were purpose built for road access along a mountain trail in the Liwu River catchment. They are largely uncased and thus expose 'clean' ceilings under fractured bedrock ridges from where percolating groundwater samples were intercepted at drip points. At Fenchiu, an old disused railway tunnel series, again through fractured bedrock ridges, offered long sequences of uncased exposure to groundwater drip sites in Tunnel 28. Linear arrays of collection bottles were laid out along the length of the tunnels, with funnels used to gather multiple drips from discretely clustered fracture sites. Temperature and pH were ascertained in the field (Data Table D).

A combined total set of 40 tunnel groundwater samples from 17 discrete drip sites at different depths below the surface were collected from Tunnel 1 in 2007 (five samples), April 2009 (seven samples), September 2009 (six samples), May 2010 (six samples), June 2010 (five samples) and late July/early August 2010 (11 samples) (see Figure 2.11, Chapter 2). It was noted that during the interim between the September 2009 and May 2010 sampling campaigns, a landslide had occurred which had resulted in the removal of approximately ten metres' depth of material from the entire ridge face over Tunnel 1 of the Bayyang trail. With immediate effect, this prompted the collection of groundwater samples from Tunnel 1 during the period June to August 2010, which was undertaken on behalf of this study by Taroko Gorge National Park ranger, Meng-Chiang Cheng, who had prior training in all relevant sampling techniques as outlined here. The purpose of this sample

set was to establish a time series of drip waters from Tunnel 1 from June to September of 2010 so as to observe any changes in groundwater chemistry in response to the landslide.

In addition to the groundwater samples, four surface-runoff water samples were collected in Bayyang at discrete intervals: one in September 2009 and another in May 2010 from the same location 14 km from Tunnel 1 in the same lithological unit, and two in September 2010 from off the landslide scar face adjacent to the entrance to Tunnel 1.

Also collected on behalf of this study were the two groundwater sample sets from 2007 and 2009, respectively, at Tunnel 1, which were retrieved by Damien Calmels (now at Equipe de Geochimie des Isotopes Stables, Institut de Physique du Globe de Paris, Sorbonne Paris Cité, Univ Paris Diderot, UMR 7154 CNRS, F-75005 Paris, France, but who was based at Cambridge at the time of sampling) following similar sampling procedures as outlined here. The elemental chemistry of the 2007 dataset was published by Calmels et al. (2011) and the 2009 dataset was shared via personal communication. These additional sets added a further 12 samples to the pre-landslide dataset making a total of 18 pre-landslide samples and 22 post-landslide samples for Tunnel 1.

Augmenting the sample set from Tunnel 1 were three groundwater samples collected from drip-sites within the cave in Tunnel 6, one in September 2009 and two in May 2010, and a further five groundwater samples that were collected from Tunnel 8, three in September 2009 and an two in May 2010.

For groundwater characterisation in central west Taiwan, five groundwater samples were collected from midway through Tunnel 28 in Fenchihu in September 2008 and an additional four groundwater samples were recovered along the same transect in May 2010 (Figure 2.13, Chapter 2). Two surface runoff samples and one stream water sample were also recovered from nearby the tunnel in September 2009.

3.2.3 Rock and soil samples from the Bayyang Tunnel Trail

The objective for recovering rock and soil samples was to ascertain the end-member chemistry of the material being weathered. One soil sample and an underlying related bedrock sample from the outside vicinity of Tunnel 8 were collected. The bedrock sample was composed primarily of schist and calcite, representing the main lithological units of the region (Plate 2: 92A1 and 92A5). Of particular note in the rock sample, and which was also typical of the main lithological units hosting the tunnels, was the high abundance of large euhedral pyrite crystals, many of which exhibited oxidised surfaces,

and a much finer grained sulphide fraction embedded in the schist, juxtaposed alongside secondary calcite (Plate 2: 92A1 and 92A5). The uniform geology typifying the region of the tunnels justifies the collection of just two lithological samples.

Plate 2. Photographic images of rock samples from Bayyang. The images show the primary schist with secondary calcite and two populations of sulphides; large euhedral pyrite crystals with oxidised rims and a finer grained sulphide fraction.

3.2.4 Rain water collection and data acquisition by Josh West

The chlorine and lithium concentrations of rainwater were used for mass balance considerations in the geochemical budget of the Pingtung and Choshui coastal aquifers. The concentrations were adopted from the measurements of a spot sample taken by Josh West (Department of Earth Sciences, University of Southern California, 3651 Trousdale Pkwy, Los Angeles, CA 90089 USA) in 2009, which were shared by personal communication. The methods of collection and geochemical analysis were consistent with those presented here.

3.2.5 The Kaoping and Choshui Rivers

3.2.5.1 Water sample recovery by the WRA

The Water Resource Agency (WRA), Ministry of Economic Affairs, Taiwan, undertook, on behalf of this study, the collection of a time series of 11 water samples from the Kaoping River at the Li-Ling gauging station (1730H043) (see Figure 2.5, Chapter 2), and 41 samples from the Choshui River at the Chunyun gauging station (1510H057) (see Figure 2.8, Chapter 2), at roughly bi-weekly intervals during the periods March to August 2005 (Kaoping River) and March 2005 to December 2006 (Choshui River). Sample collection procedure followed the protocols outlined in Sections 3.2.1 and 3.2.2.1.

In the case of the Kaoping River, the sampling period covered the full range of contemporaneous precipitation that was measured by the WRA at Ping-Dong-5 monitoring station (00Q070). However, only one of the extreme rain events (the first day of the flood caused by typhoon Haitang in late July 2005) (WRA data) that typify Taiwan's summer months was captured by the time series sampling rendering the river chemistry composition potentially biased to higher concentrations at the lower flow rates (see Chapters 2 and 5 for discussion). In the case of the Choshui River, discharge measurements were made by the WRA during sampling (Data Table C), and so comparatively precise chemical fluxes in this instance were possible to compute for some solutes using rating curve relationships between dissolved ions and discharge (see Chapters 2 and 5 for discussion).

3.2.5.2 Discharge data

The 10-year average discharge for the Kaoping River during the period 1981-1990, (7.40×10^{12} $L.yr^{-1}$), used in estimating riverine chemical fluxes in the vicinity of the Pingtung coastal plain, was taken from Ting et al. (1998a). The average annual discharge for the Choshui River during the period March 2005-december 2006, (9.18×10^{12} $L.yr^{-1}$), used in calculating riverine chemical fluxes in the vicinity of the Choshui coastal plain, was calculated from the WRA database (Data Table C).

3.2.6 Other hydrometric data collected by the WRA

3.2.6.1 Pingtung Plain hydraulic head and conductivity

The WRA provided, by personal communication, records of hydraulic head data measured daily over a five-year time period from November 1998 to May 2003 (Data Table B). The measurements were made at each of the fourteen well sites comprising the 43 wells used for the Pingtung Plain study. In addition, the WRA also provided hydraulic conductivity data for each of the 43 wells in the Pingtung Plain (Data Table A). The hydraulic conductivity measurements were made once at each well by pump-testing.

3.3 Analytical techniques

3.3.1 Geochemical tools

An essential constituent of this thesis is the use of methods already established for the analysis of natural waters and rock. In addition to the routine chemical analyses performed to ascertain major elemental and molecular compositions (see Section 3.3.2) (Davis and DeWiest 1966), analytical measurements were made to determine the stable isotopic abundances of the aqueous and solid samples presented in subsequent chapters (see Sections 3.3.3-3.3.9).

Stable isotopes of water and of some dissolved constituents in water behave in predictable and understandable ways during the hydrological and geochemical pathways operating at or near Earth's surface. Due to their predictable behaviour and to low analytical uncertainties, stable isotopes of oxygen (^{16}O, ^{18}O), hydrogen (^{1}H, ^{2}H (deuterium (D)), carbon (^{12}C, ^{13}C) and sulphur (^{34}S, ^{32}S) are routinely used as geochemical indicators in a variety of contexts (Kendall and McDonnell 1998) serving as useful tools for tracing hydrological mixing and understanding and quantifying the transfer of mass through bio-geochemical pathways.

The terrestrial abundance ratios of the relatively heavy to light isotopes of oxygen, hydrogen, carbon and sulphur are 1:500 (oxygen), 1:6410 (hydrogen), 1: 90 (carbon) and 1:22 (sulphur). Variations of these ratios occur in response to fractionation processes, but the magnitude of change to the ratio is extremely subtle. It is therefore useful to use per mille (‰) notation where measurements are typically expressed relative to standards Vienna Standard Mean Ocean Water, VSMOW (oxygen and hydrogen, Vienna Pee Dee Belemnite, VPDB (carbon) and Vienna Canyon Diablo Troilite, VCDT (sulphur) (Craig 1961; Gonfiantini 1978; IAEA 1983a):

$$(R_{sample}/R_{standard} - 1) \times 1000 \text{ (‰)} \quad (1)$$

where 'R' is the ratio of the heavy to light isotope. The isotopic compositions of oxygen, hydrogen, carbon and sulphur are shifted by a fractionation factor, epsilon, or ε, from the isotopic ratios in the source fluid or rock (δ_{source}) in response to environmental processes:

$$\varepsilon = \delta_{source} - R \quad (2)$$

Examples of processes resulting in the fractionation of these stable isotopes, which render their use integral to this thesis, include evaporation/evapotranspiration (e.g. Gat 2000), source water identification (e.g. Warner et al. 2013), groundwater mixing (e.g. Laaksoharju et al. 2008), soil respiration (e.g. Cerling et al. 1991), silicate and carbonate weathering (e.g. Galy and France-Lanord 1999) and bacterially-mediated sulphate reduction (Turchyn et al. 2010).

Also used in this thesis for tracing weathering processes is the ratio in aqueous and solid samples of stable isotopes of strontium ($^{87}Sr/^{86}Sr$). Stable strontium isotopes are useful as geochemical tools because their ratios can trace the relative fractions of silicate and carbonate alteration, which has implications for understanding how weathering mediates global climate and how ocean geochemical budgets are set (e.g. Hodell et al. 1990, 1991). The strontium isotopic composition of the ocean and of marine carbonates is balanced between inputs from high $^{87}Sr/^{86}Sr$ ratios derived from the weathering of continental silicate rock and low $^{87}Sr/^{86}Sr$ ratios that exchange with seawater at hydrothermal vent settings (Palmer and Edmond 1989). Also of importance is change in the relative fluxes of strontium from these main sources. The $^{87}Sr/^{86}Sr$ ratios in continental water fluxes, by reflecting the relative fraction of altered silicates and carbonates, therefore offer powerful insights into the transfer of mass during rock-water interactions.

3.3.2 Major and trace dissolved cation and anion analysis

The measurement of dissolved ions in sample waters was conducted using a Varian 'Vista' Axial ICP-AES (Inductively Coupled Plasma-Atomic Emission Spectrometry) for cation (Na^+, K^+, Ca^{2+}, Mg^{2+}, Sr^{2+}, Li^+, Ba^{2+}), sulphur and silica, and a 'Dionex' ICS-3000 ion chromatograph for anions (Cl^-, SO_4^{2-}). Standard reference material included USGS (United States Geological Survey) natural river-water standards T-143 and P-35, and synthetic solutions made up in the Department of Earth Sciences, University of Cambridge, with materials procured from CPI International. The synthetic solutions were prepared with purified dilute nitric acid with separate standards for dissolved silica and sulphate made up using Milli-Q water to prevent speciation of these solutes, which is likely to occur at low pH values. The range in standard solution concentrations was 1-120 ppm for anions and 1-80 ppm for cations. The Dionex is especially sensitive to concentrations that exceed the standard reference material. To ensure that the concentration of dissolved ions in the ground and surface waters would be bounded by the standard ranges during analysis on the Dionex, each sample was initially diluted by a

factor of ten with Milli-Q water and analysed first on the Vista. For this, typically 500 µL of sample was weighed and added, using a pre-cleaned pipette tip, to 4500 µL of water, whereupon the solution was mixed and weighed again, giving a dilution factor with which to correct the measured quantities. The sulphate and sodium concentrations were directly measured on the Vista and could be used to adjust the dilution factor for sulphate and chlorine prior to analysis on the Dionex. For an estimate of the chlorine concentration of the samples using the sodium concentration measurement from the Vista analysis, it was assumed that the Na/Cl ratio would not be significantly grater than one.

Repeat measurements of USGS natural river-water standard, T-143, gave reproducibility (2σ, n = 20) of 4.34 % (Na^+), 4.01 % (K^+), 2.08 % (Ca^{2+}), 2.02 % (Mg^{2+}), 2.10 % (Sr^{2+}), 9.10 % (Li^+), 5.54 % (Ba^{2+}), 2.33 % (S), 1.64 % (Si) over a two-month period of analysis of the Taiwan ground and surface waters (Table 3.1). Repeat measurements of P-35 gave reproducibility (2σ, n = 40) of 2.88 % (Cl^-) and 5.71 % (SO_4^{2-}) (Table 3.1). Estimation of the bicarbonate concentration [HCO_3^-] in the samples was by equivalent charge balance. One sample (CP1) had a higher Eq% anion than cation content likely due to the precipitation of solids after collection. Whilst anion measurements are robust, cation concentrations in CP1 are therefore considered to be underestimates. Molar S analysed by ICP-AES and molar S from the SO_4^{2-} determinations by ion chromatography define a line with a gradient of 1.02 ($R^2 = 0.99$).

Table 3.1 USGS natural river-water standard T-143 and P-35 analysed by ICP-AES and Ion Chromatography against synthetic standards at the Department of Earth Sciences, University of Cambridge

standard	**T-143**	**T-143**	**T-143**	**T-143**	**T-143**	**T-143**	**T-143**	**T-143**	**T-143**	**P-35**	**P-35**
solute	Ba^{2+}	Ca^{2+}	K^+	Mg^{2+}	Na^+	S	SiO_2	Sr^{2+}	Li^+	Cl	SO_4^{2-}
unit	$\mu g.L^{-1}$	$mg.L^{-1}$	$mg.L^{-1}$	$mg.L^{-1}$	$mg.L^{-1}$	$mg.L^{-1}$	$mg.L^{-1}$	$mg.L^{-1}$	$mg.L^{-1}$	$mg.L^{-1}$	$mg.L^{-1}$
mean	74.9	53.0	2.7	10.22	30.04	21.42	20.82	0.28	0.02	5.33	0.48
1σ	2.1	0.6	0.1	0.10	0.65	0.25	0.08	0.00	0.00	0.08	0.01
RSD (%)	2.8	1.0	2.0	1.01	2.17	1.17	0.82	1.05	4.55	1.44	2.86
accepted value	81.9	53.7	2.5	10.40	34.00	22.00	23.40	0.31	0.02	5.31	0.67
n	20	20	20	20	20	20	20	20	20	40	40

3.3.3 Stable isotopes of dissolved inorganic carbon

The measurement of the carbon isotopic composition of dissolved inorganic carbon (DIC) ($\delta^{13}C_{DIC}$) was performed at the Godwin Laboratory for Palaeoclimate Research, Department of Earth Sciences, University of Cambridge using a Thermo Scientific Gas Bench attached via continuous flow to a Delta V Advantage Mass Spectrometer. For this, 3-4 drops of orthophosphoric acid (100 %) were preloaded into a glass reaction vial, sealed with silicone rubber septa using a dual-head screw cap and with the headspace flushed with helium gas. Approximately 1.5 mL of sample was injected using a sterile syringe and left to react for one hour, after which the vials were ready to be loaded into the mass spectrometer where the resulting CO_2 in the headspace was analysed. The dual cap system ensured that the septa used for injection of the sample into the reaction vial would not be penetrated again during analysis, thus minimising the potential for measurement interference due to the failure of a cap.

A series of internal standards and reference samples ('BOTTY' ($\delta^{13}C_{DIC}$: −4.22 ‰) and 'FLORIDA' ($\delta^{13}C_{DIC}$: −23.88 ‰)) prepared for distribution throughout the analysis run were used to calibrate to the international standard VPDB (Vienna Pee Dee Belemnite). Results had a reproducibility of better than 0.1 ‰. Typically, a run sequence consisted of two each of BOTTY and FLORIDA standard analyses bracketing 10 samples. To account for changes in peak amplitude diminishment due to monotonic decreases in sample concentration during repeat measurements, a correction method established at the Godwin Laboratory for Palaeoclimate Research, Department of Earth Sciences, University of Cambridge, was used:

$$\delta^{13}C_{observed} - \delta^{13}C_{expected} = 153.98 \times 1/A \quad (3)$$

where the 153.98 was the slope of multiple measurements made before and during the sampling period of several months and A is the peak amplitude (CO_2 = 44) of each injection, and whereby each set of observed ($1/A_{botty\text{-}observed}$) and observed average ($1/A_{botty\text{-}average}$) BOTTY amplitude measurements ($1/A_{average}$) on aliquots with varying volumes was used to correct the bracketed samples for external offsets and internal drift:

$$\delta^{13}C_{corrected} = 153.98 \times (1/A_{botty\text{-}observed} - 1/A_{botty\text{-}average}) \quad (4)$$

3.3.4 Stable isotopes of water

Stable isotopes of water (O^{16}, O^{18}, H^1 and H^2) were analysed using a 'Picarro' Wavelength-Scanned Cavity Ring-Down Spectroscope. For the measurement of stable isotopes of water, 0.5 mL each of sample and standard material were dispensed using a pre-cleaned pipette tip into individual analysis vials which were then ready to be loaded onto the Picarro. A series of internal standards and reference samples were prepared for distribution throughout the analysis run, which were calibrated against the isotopic ratios of international reference standard 'VSMOW'.

For each sample and standard reference material, nine independent 2 µl injections were sent into the vaporising chamber for isotope determination. Typically, results from the measurements made of the first three injections were discarded to eliminate any memory effect, with the average measurement of the last six injections taken to represent the precision of the analysis. The analytical precisions expressed as 1σ for the laboratory standards and for the samples were on average ± 1.0 ‰ for δD, and ± 0.08 ‰ for δ^{18}O. Differences of duplicate analyses were within this analytical uncertainty.

Water standards VSMOW (δ^{18}O and δD: 0 ‰), 'GISP' (Greenland Ice Sheet Precipitation) (δ^{18}O: −24.8 ‰; δD −189.5 ‰) and 'SLAP' (Standard Light Antarctic Precipitation) (δ^{18}O: −55.5 ‰; δD −428.0 ‰), were used to measure the accuracy of the analysis. Blocks of eight samples were typically bracketed by SMOW and GISP and then the next eight samples in the sequence by GISP and SLAP. A linear regression through each set of measured versus expected δ^{18}O and δD of SMOW, GISP and SLAP values was used to correct the bracketed samples for external offsets and internal drift (Figure 3.1).

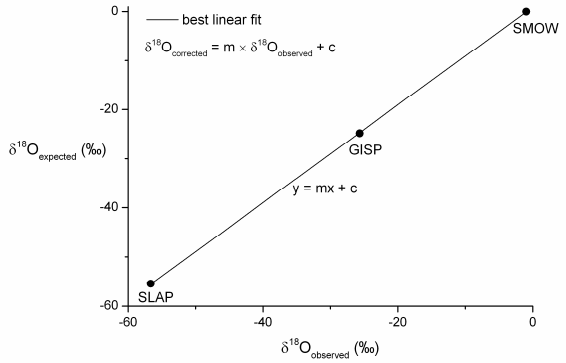

Figure 3.1. Schematic showing observed versus expected measurements of, in this example, δ^{18}O. Sample values are corrected using the relationship of the offset between accepted values for SMOW, GISP and SLAP. The same procedure is used for determining the offset of δD values.

The 2σ errors on the $\delta^{18}O$ and δD values presented in subsequent chapters are the combined analytical uncertainties ($SE\delta_{H2O}$) of the standard error of the internal precision (SE_i) and the standard error on the slope of the linear regressions through the set of measured versus expected SMOW, GISP and SLAP standard reference materials (E_s) for n number of bracketed samples, propagated as follows:

$$SE\delta_{H2O} = (\sqrt{\sum}(SE_i)^2 + (E_s)^2)/\sqrt{n} \quad (5)$$

3.3.5 Stable isotopes of aqueous sulphate

3.3.5.1 Sample preparation

To determine the sulphur and oxygen isotopic composition of aqueous sulphate ($\delta^{34}S_{SO4}$, $\delta^{18}O_{SO4}$), concentrated barium chloride (50g.L^{-1}) was added to approximately 30 mL of sample to precipitate barium sulphate out of solution. The resulting mixtures were left overnight to allow the settling of $BaSO_4$ precipitate particles. The samples were then centrifuged for 20 minutes at 3000 rpm. The excess liquid was decanted off using pre-cleaned pipette tips and discarded. A few drops of deionised water were added to mobilise the residues. The resulting solutions were transferred to 5 mL vials using pre-cleaned pipette tips. The vials were left in an air-flow controlled oven overnight at 50 °C.

To drive off any $BaCaCO_3$ that might have precipitated alongside $BaSO_4$, 6 M HCl was added to the vials which were then left for two hours to degas resultant CO_2. The vials were centrifuged for 5 minutes at 3000 rpm. The acid was decanted off using pre-cleaned pipette tips and discarded. Deionised water was added to the residues and the vials were centrifuged for 5 minutes at 3000 rpm, following which the water was decanted off using pre-cleaned pipette tips; this rinsing step was repeated three times. The vials were left again overnight to dry in an airflow-controlled oven at 50 °C.

For the measurement of the sulphur isotopic composition of sulphate using a Thermo Delta V Plus Flash Elemental Analyzer, approximately 60 µg of sulphur was required. The atomic weight of $BaSO_4$ being 233.400, approximately 60/0.137, or 440 µg of $BaSO_4$ was weighed out. To prepare the samples for combustion in the presence of an excess of oxygen, they were mixed with approximately five times their weight of V_2O_5 powder. The powdered mixtures were then crushed in tin capsules to facilitate combustion during analysis.

For the measurement of the oxygen isotopic composition of sulphate using a Thermo Delta V Advantage mass spectrometer, approximately 30 µg of oxygen was required or approximately 120 µg of $BaSO_4$. The sample weights were added to silver capsules to enable pyrolysis, and were then baked at 50 °C in an airflow-controlled oven for 12 hours to drive off any traces of water. Care was taken to ensure that none of capsules had tarnished, which would have indicated oxidation to have occurred during the drying process. The silver sample-containing capsules were then crushed and ready to be analysed.

3.3.5.2 Analysis of the sulphur isotopic composition of sulphate

The analysis of the sulphur isotopic composition of aqueous sulphate ($\delta^{34}S_{SO4}$) was conducted using a Thermo Delta V Plus Flash Elemental Analyzer at the Godwin Laboratory for Palaeoclimate Research, Department of Earth Sciences, University of Cambridge. The sulphur isotope measurements were calibrated to international standard Vienna Canyon Diablo Troilite (VCDT) by analysing inter-laboratory standards NBS-127 ($\delta^{34}S_S$: 20.3 ‰) and IAEA-SO6 ($\delta^{34}S_S$: −34.10 ‰) distributed by the International Atomic Energy Agency. Typically, 8-9 samples were bracketed by 3-6 of each standard. Reproducibility of NBS-127 gave an average $\delta^{34}S_{SO4}$ value of 20.51 ‰ and a precision of 0.42 ‰ (1σ, n = 13). Reproducibility of IAEA-SO6 gave an average $\delta^{34}S_{SO4}$ value of −30.59±0.39 ‰ (1σ, n = 13). Differences of duplicate analyses were within this analytical uncertainty.

The bracketed samples were corrected for external offsets and internal drift by fitting their values to a linear regression of the average observed versus the expected values for the reference standards analysed, in the same manner as previously described and illustrated for stable isotopes of water (Section 3.3.3).

3.3.5.3 Analysis of the oxygen isotopic composition of sulphate

The analysis of the oxygen isotopic composition of aqueous sulphate ($\delta^{18}O_{SO4}$) was conducted using a Thermo Finnigan High-Temperature Converter attached to a Thermo Delta V Advantage mass spectrometer via continuous carrier-gas flow at the Godwin Laboratory for Palaeoclimate Research, Department of Earth Sciences, University of Cambridge. The prepared silver capsules were loaded into an auto-sampler for analysis. The samples were continuously purged with helium to ensure no contamination with

oxygen or water. The samples were introduced to a high-temperature conversion reactor, consisting of an outer ceramic mantle tube of aluminium oxide and an inner glassy carbon reactor containing a glassy crucible, glassy carbon granules and silver wool. The vaporising reaction temperature is approximately 1450 °C with H_2, N_2 and CO gaseous products resulting during conversion. These products are separated by a packed gas chromatographic molecular sieve column at a temperature of 90 °C and then passed into the mass spectrometer by continuous helium gas flow for analysis.

The oxygen isotope measurements were calibrated to V-SMOW by analysing inter-laboratory standard NBS-127 distributed by the International Atomic Energy Agency. Typically, 6-8 samples were bracketed by 4-6 standards. Reproducibility of NBS-127 gave an average $\delta^{18}O_{SO4}$ value of 4.94 ‰ and a precision of 0.27 ‰ (1σ, n = 14). Differences of duplicate analyses were within this analytical uncertainty.

The accepted $\delta^{18}O_{SO4}$ value for NBS-127 is 8.60 ‰. The measurements of NBS-127 plotted against sequence time define a line with slope of −0.03 (R^2 = 0.17) indicating that no significant drift occurred during the analysis. Therefore, the samples were corrected by adjusting their values by the offset observed between the measured and expected values of NBS-127. The 2σ error bars on the $\delta^{18}O_{SO4}$ values presented in subsequent chapters are the combined analytical uncertainties ($SE\delta_{\delta OSO4}$) of the standard error of the internal precision of NBS-127 (SE_i) (0.14 ‰) and the standard error on the slope of the linear regression through the set of measured NBS-127 versus time (E_s) (0.02 ‰) for n number of measurements (14), propagated using Equation 5 by substituting $\delta^{18}O_{SO4}$ for δ_{H2O}.

The offset between the observed and expected $\delta^{18}O_{SO4}$ values of NBS-127 using the Thermo Delta V Advantage mass spectrometer at the Godwin Laboratory occurs systematically for a given cylinder of reference gas. The offset is owing to disparity between the absolute isotope composition of the standard and that of the reference gas.

3.3.6 Isotopic composition of dissolved strontium

The $^{87}Sr/^{86}Sr$ isotopic ratios of dissolved strontium were determined by multicollector thermal ionisation mass spectrometry on the VG Sector 54 TIMS at the Department of Earth Sciences, University of Cambridge using a triple collector dynamic algorithm and normalised to the $^{86}Sr/^{88}Sr$ isotopic ratio of 0.1194 with an exponential fractionation correction after Bickle et al. (2003). Strontium was separated by standard

cation exchange methods using a 5 cm bed of Dowex 50W x8 200-400 cation ion exchange mesh resin in a 1 cm diameter quartz column. The resin was pre-cleaned with 50 mL of 6N HCl and conditioned with 8 mL of 1N HCl. The samples were loaded onto the columns in 2 mL 1 M HCl with 5 mL 3N HCl added twice to ensure all sample had entered the top of resin bed. The Sr fractions were collected into cleaned Savillex vials with the next 5 mL of 3N HCl added to the column. The samples were eluted with 12 mL of 3N HCl and the Sr fractions were collected into Savillex vials in which 5 mL of 3N HCl had been pre-added. The samples were evaporated under controlled airflow conditions using infrared lamps.

For mass spectrometric analysis, the samples were re-dissolved in 2 µL of 1N HCl and loaded onto out-gassed tantalum filaments with 1.0 µL of 1N H_3PO_4 under an applied current of 0.8 A. The samples were dried as the current was increased to 2.0 A. Reproducibility of the internal standard NBS 987 gave 0.7102628 ± 0.0000090 (1σ, n = 242) for the duration of these analyses over the last seven years. Analytical blanks were less than 250 pg and negligible for the Sr concentration of these samples.

3.3.7 Separating the carbonate and silicate fractions of rock samples

3.3.7.1 Sample preparation

The elemental ratios of strontium to calcium in carbonate and in the carbonate-hosted waters were used to calculate the partition coefficient (K_d) describing the uptake of Sr^{2+} into secondary carbonate as follows:

$$K_d = (Sr/Ca)_{carbonate}/(Sr/Ca)_{water} \quad (5)$$

In order to measure the Sr/Ca ratio of the carbonate fraction in bulk rock, whole rock leaching was performed to isolate first the carbonate from the silicate fraction. The rock samples were shattered in a jaw crusher then pulverised to a fine powder using motorised agate-ball grinders.

A volume of 5 mL of distilled water was added to the recorded weight of approximately 200 mg of whole rock powder per sample (Data Table E) in a pre-cleaned centrifuge tube and shaken vigorously. Each tube was then placed in an ultrasonic bath for 10 minutes, shaken again and then left to sit for two hours. After this the tubes were shaken again and centrifuged for 20 minutes at 3000 rpm. The water was decanted off by pipette with clean, water-rinsed tips and discarded.

A volume of 5 mL of 10 % distilled acetic acid was added to the tubes to dissolve the carbonate minerals. The tubes were shaken and tube caps were unscrewed for 10 minutes to allow the CO_2 produced to degas; this degassing step was repeated three times before leaving the tubes to sit for eight hours. After eight hours, the CO_2 produced was allowed to degas and the tubes were shaken and the CO_2 produced was allowed again to degas. The tube caps were rinsed into the tubes using a minimum volume of deionised water. The tubes were centrifuged for 20 minutes at 3000 rpm.

At this stage, the carbonate fraction was ready to separate off: the acetic acid leachate solution was pipetted into one pre-weighed (Data Table E) and pre-cleaned 5 mL Savillex vial per sample, taking care not to disturb the residue of rock powder. The weights of the Savillex vials plus the acetic acid leachates were recorded (Data Table E). An additional volume of 0.5 mL of leachate was pipetted into a second set of pre-weighed Savillex vials and their combined weights were recorded (Data Table E). The weights of the initial set of Savillex vials minus the 0.5 mL of leachate that were removed were recorded (Data Table E).

To prepare the remaining silicate fraction for future geochemical analysis, a volume of 5 mL of 6M HCl was added to the rock powder residues to remove any remaining carbonate. The tubes were shaken and the tube caps were unscrewed for 10 minutes. The tubes were shaken again and centrifuged for 20 minutes at 3000 rpm. The acid was decanted off by pipette and discarded, taking care not to disturb the residue of rock powder; this rinsing step was repeated three times. A volume of 5 mL of deionised water was added to the tubes. The resulting solution was mixed and transferred by pipette into one, pre-weighed Savillex vial per sample (Data Table E). The weights of the Savillex vials plus the solutions were recorded (Data Table E).

The 0.5 mL acetic acid leachate fractions for cation concentrations were dried using infrared lamps under controlled airflow conditions. When completely dry, a few drops of 6 M HNO_3 were added to the vials to convert the acetates to nitrates. The resulting nitrate solution was dried down again. The resulting residue of nitrates was dissolved in 1 M HNO_3. A volume of 1.0 mL of nitrate solution was added to one pre-weighed beaker per sample (Data Table E) and the combined weight was recorded (Data Table E). The nitrate solution was then made up to 0.1 M, in accordance with the required molarity for ICP-AES analysis, by adding 1.0 mL of solution to 9.0 mL of Milli-Q water in a pre-weighed beaker (Data Table E). The combined weight of the beaker and the now 0.1 M HNO_3 solution was recorded (Data Table E). The 0.1 M solution was diluted by 10

and 100 by taking 1.0 and 0.1 mL of the 0.1 M HNO_3 solution, respectively and adding to those amounts 9 mL of 0.1 M HNO_3 (Data Table E). The diluted solutions were ready for Sr/Ca ratio determination of carbonate using ICP-AES.

3.3.7.2 Analysis of the Sr/Ca ratio in carbonate

The Sr/Ca ratio of secondary carbonate, $(Sr/Ca)_{carb}$, was measured using ICP-AES. Repeat ICP-AES analyses at the Department of Earth Sciences, University of Cambridge indicate reproducibility to within 5 % (2 standard deviations). Repeat analysis of an internal standard over the analysis run was within this analytical uncertainty.

3.3.7.3 Strontium isotopes of the carbonate end-member

The strontium isotopic composition of the carbonate end-member was performed on the carbonate leachates described in the above section, which were subsequently prepared for analysis by converting the acetate to chloride form with ~2 mL 6M HCl before evaporating to dryness for Sr separation on the cation exchange columns and then analysed according to the method outline in Section 3.3.6.

3.3.8 Carbon isotope abundances in carbonate

3.3.8.1 Determination of percent calcium carbonate

Weight percent $CaCO_3$ measurements were performed at the Godwin Laboratory for Palaeoclimate Research, Department of Earth Sciences, Cambridge by acidification of bulk sediment samples using an AutoMateFX carbonate preparation system. Evolved CO_2 was measured using a UIC (Coulometrics) 5011 CO_2 coulometer. Analytical precision is estimated to be ±1% by measurement of a carbonate standard.

3.3.8.2 Extraction of CO_2 and analysis of carbon isotopes

The measurement of the carbon isotopic composition of carbonate ($\delta^{13}C_{carb}$) was performed at the Godwin Laboratory for Palaeoclimate Research, Department of Earth Sciences, Cambridge, using a Thermo Scientific Gas Bench attached via continuous flow to a Delta V Advantage Mass Spectrometer. For analysis, approximately 2 mg of dried homogenised sample were transferred into glass reaction vials sealed with silicone rubber

septa using a screw cap. The samples were flushed with helium then acidified with orthophosphoric acid (100 %) and left to react for one hour at 70 °C. This releases CO_2 from the $CaCO_3$ in the sample, which is then carried by a helium carrier gas via continuous flow through a water trap and into the mass spectrometer via an open slit. Each run of samples was accompanied by 10 reference carbonates (Carrara Z) and two control samples (Fletton Clay). Carrara Z has been calibrated to VPDB using the international standard NBS-19. The results are reported relative to VPDB and the $\delta^{13}C_{carb}$ precision is better than ± 0.08 ‰.

3.3.9 Sulphur isotopes in bulk-rock and whole-pyrite crystals

3.3.9.1 Sample preparation

The bedrock samples from the Bayyang tunnel trail contained a high abundance of euhedral pyrite crystals observable to the naked eye (Plate 2: 92A1 and 92A5). It was also possible to discern with the naked eye a much finer grained pyrite fraction which was disseminated throughout the rock. The objective for analysing the sulphur isotopic composition of these two pools of sulphide was to understand the potential role of bacterial sulphate reduction in controlling weathering processes.

To extract the sulphide fraction from bulk rock, a variation of the method described by Thode et al. (1961) was used. The rock samples were first shattered using a jaw crusher and pulverised using motorised agate-ball grinders. The next step involved preparing a reducing reagent to facilitate the extraction of sulphide, in the form of Ag_2S, from the powders. To prepare the necessary reducing agent, a 1N solution of $CrCl_3$ was made by first mixing approximately 266 g of $CrCl_3*6H_2O$ with approximately 866 mL of 1N HCl. The $CrCl_3$ solution was reduced by adding it to a reaction vessel containing zinc grains (~15 g) on a hotplate. The zinc grains were pre-cleaned with 2N HCl to remove any oxide. The solution was boiled in an O_2-free environment in the presence of N_2 gas until it turned ‘sky-blue’ in colour.

Approximately 6 g of powdered rock sample were added to a reaction vessel containing scientific-grade glass beads to prevent the caking of clay-rich sediments. The sample was boiled in the presence of N_2 gas and the reduced $CrCl_3$ reagent. When sulphur was present, a digestion resulted in the production of H_2S gas. A purified gas stream was bubbled into a pre-cleaned centrifuge tube, which contained approximately 34 mL of a 0.2 M $AgNO_3$ in 10 % NH_4OH solution via a Teflon tube inserted through its cap. In the

presence of this solution, any sulphur present as H_2S gas was precipitated as Ag_2S while preventing the precipitation of any Cl^- to AgCl by complexation of ammonia with Ag^+.

To extract pyrite crystals from bulk rock the samples were lightly tapped with a hammer and tweezers were used to 'hand-pick' individual euhedral crystals that were approximately 1-3 mm in diameter. A dentist's dissecting kit and a soft toothbrush were used to clean the crystal surfaces. The crystals were gently washed in a deionised water bath and placed in an ultrasound bath for 10 minutes. Each crystal was individually crushed and weighed in preparation for analysis.

For the measurement of the sulphur isotopic compositions of Ag_2S from whole-rock extraction and FeS_2 from the crystals, using a Thermo Delta V Plus Flash Elemental Analyzer, approximately 60 µg of sulphur was required or approximately 464 µg of Ag_2S and 112 µg of FeS_2. The weighed samples of Ag_2S and FeS_2 were crushed in tin capsules to facilitate combustion during analysis.

3.3.9.2 Analysis of the sulphur isotopic composition of sulphide

The analysis of the sulphur isotopic composition of sulphide ($\delta^{34}S_S$) was conducted using a Thermo Delta V Plus Flash Elemental Analyzer. The sulphur isotope measurements were calibrated to international standard VCDT by analysing inter-laboratory standards NBS-127 ($\delta^{34}S_S$: 21.10 ‰) and IAEA-S3 ($\delta^{34}S_S$: −32.30 ‰) distributed by the International Atomic Energy Agency. Also used for reference was internal standard SI-1 ($\delta^{34}S_S$: 6.10 ‰). Typically, 10 samples were bracketed by 3-4 of each standard. Reproducibility of NBS-127 gave an average $\delta^{34}S_S$ value of 21.51 ‰ and a precision of 0.33 ‰ (1σ, n = 8). For IAEA-S3 the average $\delta^{34}S_S$ value was −29.19 ± 0.63 ‰ (1σ, n = 7). The average measured $\delta^{34}S_S$ value of internal standard SI-1 was 8.46 ± 0.41 ‰ (1σ, n = 7). Differences of duplicate analyses were within these analytical uncertainties.

The bracketed samples were corrected for external offsets and internal drift by fitting their values to a linear regression of the average observed versus the expected values for the three reference standards analysed, in the same manner as previously described and illustrated for stable isotopes of water (Section 3.3.3).

Chapter 4

Chemical variability, mixing and weathering in two semi-confined aquifers: the Pingtung and Choshui coastal plains

4.1 Summary

This chapter presents major and trace chemistry and isotopic compositions of groundwaters sampled from two semi-confined sandy aquifers, the Pingtung and Choshui coastal plains in southwest and west Taiwan, respectively, and details the chemical variability with depth and along groundwater flow paths and the methodology used to identify the sources of solutes in the groundwater. Solutes derived from rock-water interactions have been distinguished using end-member mixing relationships from dissolved mass contributed to the groundwaters from other sources. The main observations are summarised in the following section.

4.2 Aims, summary of main findings and outline of methodology

The primary aim of this chapter is two-fold. Firstly, to understand the type and relative magnitudes of those chemical weathering reactions that are predominantly occurring in the subsurface of alluvial-fill aquifers in Taiwan. To do this an investigation of the chemical variability of groundwaters with increasing depth and along the groundwater flow paths in these settings is presented and compared to the main characteristics of local surface-water chemistry. Secondly, to isolate the relative fractions comprising the total subsurface dissolved mass that are attributable to chemical weathering processes, both allochthonous and autochthonous with respect to the aquifer domains. To achieve this, four distinct sources of solutes were considered, and the end-member chemistries were used to quantify and trace their relative variability throughout the drilled depths of the sampled basins.

In particular, chemical changes with increasing depths and along groundwater flow paths provide insight into the respective importance of hydrological connectivity and

lithology in controlling dissolved chemistry. In addition, understanding the sources of dissolved mass has implications for the weathering and, potentially, the uplift histories of the basins. In the context of Taiwan, this chapter therefore demonstrates:

1. That combined major chemistry and temperature data show that the evolution of major groundwater chemistry in alluvial-fill sediments is broadly controlled by water residence times along flow paths, which are influenced by the parameters governing hydraulic head, such as proximity to the mountain topography, and hydraulic conductivity, such as grain size distribution and compaction/cementation within the basin.
2. How variations in the abundances of dissolved chlorine and lithium can be used to constrain the mixing relationships of all potential sources of fluids to the aquifers.
3. How the distribution of chlorine in groundwater shown to be derived from seawater provides insight into the weathering and uplift histories of the basin.
4. That combined isotopic and major chemistry data can show how localised chemical anomalies deviating from the main chemical trends implicate the roles of lithology, acid type and physical heterogeneities in controlling weathering processes.
5. How changes in major chemistry at depth across the transition between the fractured mountain backdrop and the alluvial-fill deposits can be used to understand hydrological connectivity and the transfer of solutes between the two domains.
6. That chemical enrichment of some solutes occurs along the groundwater flow paths, which highlights the potential importance of length scales across sedimentary basins in determining the concentration and type of dissolved subsurface mass available for discharge to the ocean.

For the purpose of the aforementioned aims a five-year daily hydraulic head time series (November 1998 - May 2003) together with hydraulic conductivity data taken from the WRA database were used to constrain the southwest groundwater flow path through the Pingtung Plain. Published details of the groundwater flow regime (Wang et al. 2005) were used to constrain the west-northwest direction of the primary groundwater flow path through the sampled portion of the Choshui Plain. To isolate the proportion of the groundwater solutes derived from rock-water interactions, source-chemistry evaluation

was conducted using the proportions of chloride and lithium in three end-member, two-tracer mixing space of rainwater, hot-spring water and seawater.

The chemical compositions of the samples considered in this chapter have been integrated with related groundwater and riverine water flux estimates in an assessment of the subsurface chemical fluxes potentially available for discharge to the ocean, presented and discussed in Chapter 5.

4.3 Background and motivation

At present, most of the work conducted on groundwater chemistry in Taiwan's coastal aquifers has been towards evaluating the infiltration of seawater (Wang et al. 2003) and groundwater-seawater interactions in the case of the Pingtung Plain (Lin et al. 2011), and in assessing the impact of arsenic poisoning through groundwater consumption (Chen and Wu 1962) and the effects that seismicity has on hydrological permeabilities in the case of the Choshui Plain (Wang et al. 2005).

It has been claimed that subsurface dissolved chemical fluxes can rival those of surface runoff in coastal regions prompting a spate of recent studies concerned with quantifying bulk groundwater chemical fluxes (e.g. Li et al. 1999; Moore et al. 2010 and references therein). However, lack of good constraints on groundwater fluxes, and lack of a mechanistic knowledge of how and where in the deeper subsurface weathering occurs and uncertainties as to the sources of solutes to groundwater make it difficult to measure the importance of groundwater processes within the global carbon cycle. To assess the significance of groundwater as a chemical weathering agent, and to quantify the volumetric importance of subsurface chemical fluxes resulting directly from rock-water interactions, the sources of dissolved solutes need to be constrained, and those resulting from weathering should be differentiated from the whole.

In addition to the atmospheric influx of cyclic salts via rain, subsequent surface runoff and sea spray, and solute enrichment due to evapotranspiration at and near the surface, another contribution to salinity in many coastal aquifers comes from natural or anthropogenically-induced seawater intrusion (both ancient and modern) (Faye et al. 2005). The presence of connate seawater, which would have been initially trapped in pore spaces during primary marine sediment deposition, and enriched fluids related to clay dehydration during previous metamorphic episodes, in relatively shallow aquifers has implications for understanding the uplift and tectonic histories of the aquifer host rock (e.g.

Nordstrom et al. 1989). It is also important to consider the occurrence and contribution of dissolved constituents from hydrothermal activity (e.g. hot-springs), which can be especially prevalent in tectonically active regions (Becker et al. 2008; Evans et al. 2004; Kopf et al. 2001; Kopf et al. 2003; Milkov 2000; Yassir 1987). As will be shown in the following sections, these sources, together with solutes resulting from local and relatively recent rock-water interactions comprise the dissolved chemical budget of the coastal aquifers in Taiwan.

4.4 General characteristics of groundwater and riverine chemistry

In order to assess sub-horizontal and down-well chemical gradients and hydrogeochemical mixing in the basins, the wells in the Pingtung and Choshui Plains were arbitrarily subdivided into three depth horizons, respectively: ‘shallow’ (6-60 m for the Pingtung Plain and 10-74 m for the Choshui Plain), ‘intermediate’ (61-140 m for the Pingtung Plain and 75-140 m for the Choshui Plain) and ‘deep’ (141-237 m for the Pingtung Plain and 141-294 m for the Choshui Plain) and into three sections, respectively, along the groundwater flow paths: the ‘proximal region’, ‘middle section’ and ‘distal zone’ (Figure 4.1A,B).

4.4.1 General characteristics of natural waters in the Pingtung Plain

The results of chemical analyses of the 43 groundwater and 11 Kaoping River samples, together with their physical and chemical parameters are presented in Data Table F. The temperature of the groundwaters ranged from 25.1 °C to 29.3 °C and systematically increased along the groundwater flow path (Figure 4.2A). The pH values ranged from slightly acidic to alkaline (5.5 to 7.7) and were relatively homogenous according to the spatial distribution of samples and the hydrological regime (Figure 4.2B). Total dissolved solids (TDS) ranged from 164 ppm to 30647 ppm. As will be discussed in Section 4.4.2, eight of the groundwater samples were found to have concentrations approaching bulk seawater values and were removed from source-water and chemical-flux calculations and major chemical trend interpretations bringing the upper bound of the range in TDS to 1626 ppm.

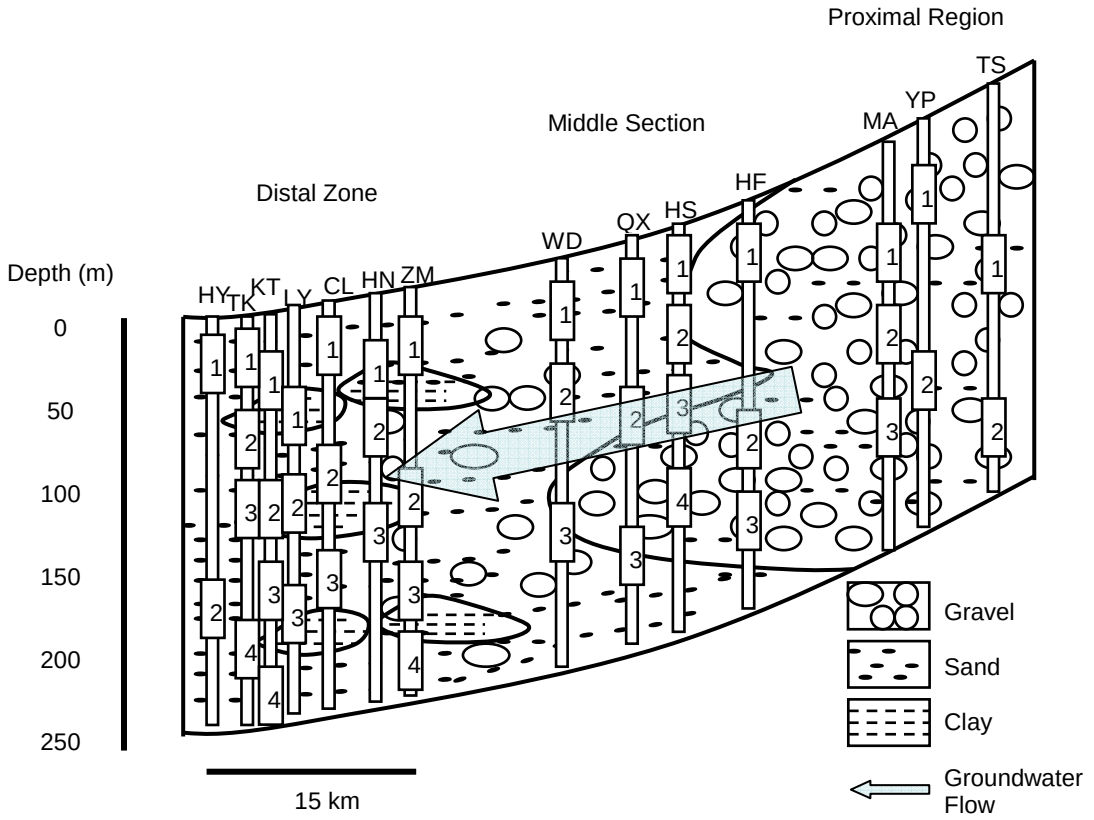

Figure 4.1A. Schematic cross section through the Pingtung Plain sediments. The Proximal Region, comprising seven discrete wells at various depths is predominantly composed of gravel that grades into the sand-rich Middle Section where there are 13 discrete wells at a range of depths. The Distal Zone, comprising 23 individual wells is sand rich with intercalated clay beds. The general direction of groundwater flow is S/W (arrow).

The relative proportions of major cations and anions in the groundwater and river water samples are shown in Figure 4.3. All major ions except SO_4^{2-} were, on average, enriched to varying degrees in the groundwaters relative to the river samples. With respect to average Ca^{2+} concentrations, the proximal region was comparable to the river (1.37 versus 1.41 mmol.L^{-1}) whereas the middle section and distal zone were relatively enriched (2.40 and 2.42 mmol.L^{-1}, respectively). This was also the case for dissolved Mg^{2+} with average concentrations in the proximal region comparable to the river (0.56 versus 0.57 mmol.L^{-1}) and with relative average increases observed in the middle section and distal zone (0.64 and 1.02 mmol.L^{-1}, respectively).

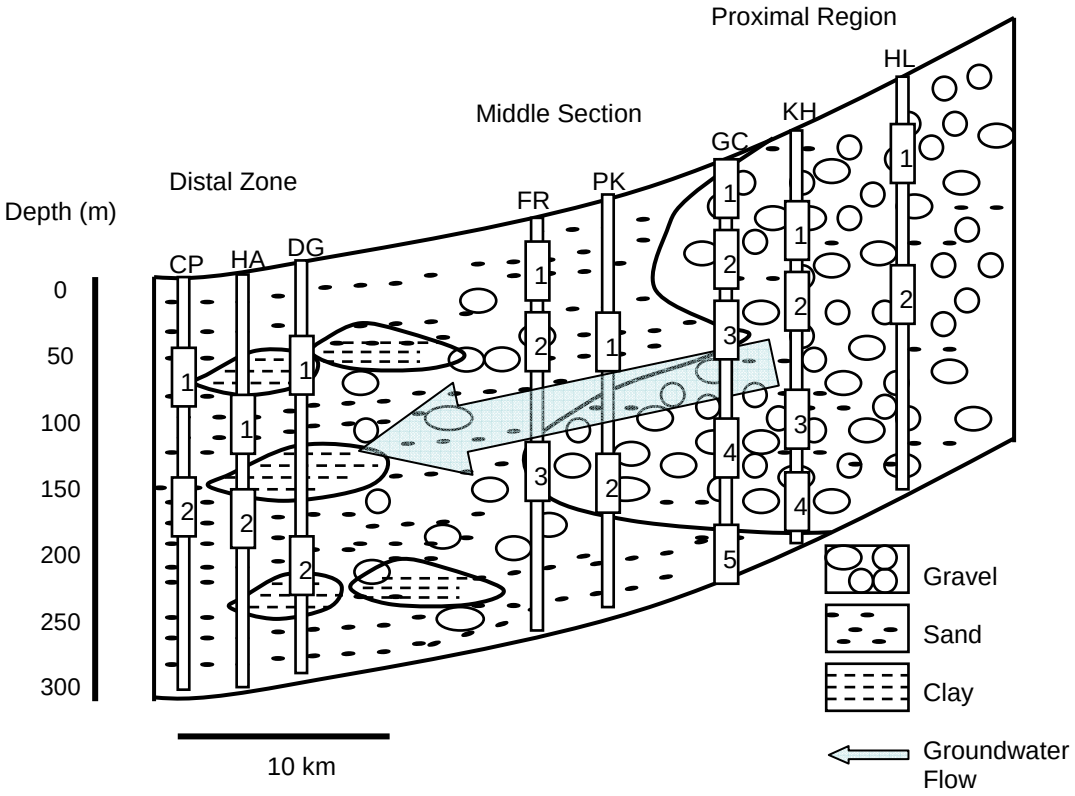

Figure 4.1B. Schematic cross section through the Choshui Plain sediments. The Proximal Region, comprising 11 discrete wells at various depths is predominantly composed of gravel that grades into the sand-rich Middle Section where there are an additional five discrete wells at a range of depths. The Distal Zone, comprising six individual wells is sand rich with intercalated clay beds. The general direction of groundwater flow is W-N/W (arrow).

For Na^+, the average concentration in the proximal region was depleted relative to the river by a factor of 1.4 (0.37 versus 0.51 mmol.L^{-1}) with increases of 1.5 and 6.2 relative to the river observed in the middle section (0.78 mmol.L^{-1}) and distal zone (3.17 mmol.L^{-1}), respectively. The relative enrichment of Na^+ in the distal zone is partly due to a minor degree of seawater mixing (see Section 4.6.4). Average K^+ concentrations in the proximal region and middle section (22.71 and 58.48 µmol.L^{-1}, respectively) were depleted relative to the river (68.39 µmol.L^{-1}), whereas the distal zone (145.36 µmol.L^{-1}) displayed relative enrichment (see Section 4.9.1 for discussion).

Unlike in the proximal region and the distal zone, where average sulphate concentrations (0.66 and 0.67 mmol.L^{-1}, respectively) were depleted relative to the river (0.75 mmol.L^{-1}), the middle section (0.85 mmol.L^{-1}) exhibited relative enrichment, possibly indicating the dissolution of sulphur-bearing bearing minerals in this location. As

will be investigated in Section 4.9.1, the extremely low sulphate values in several distal wells possibly indicate sulphide formation in this location.

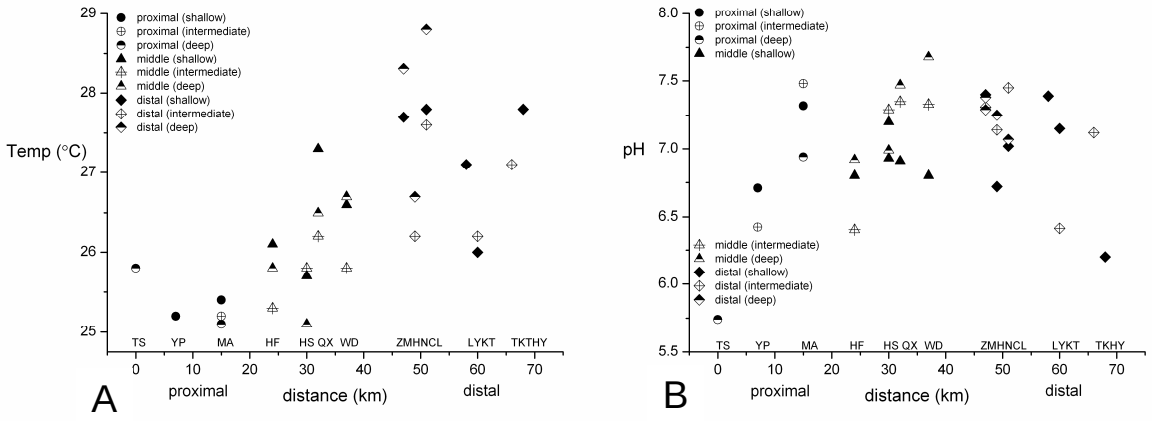

Figure 4.2. Temperature (A) and pH (B) according to distance along the groundwater flow path in the Pingtung Plain. A systematic increase in temperature according to the spatial distribution of samples along the main direction of groundwater flow was observed, whereas pH was relatively homogenous.

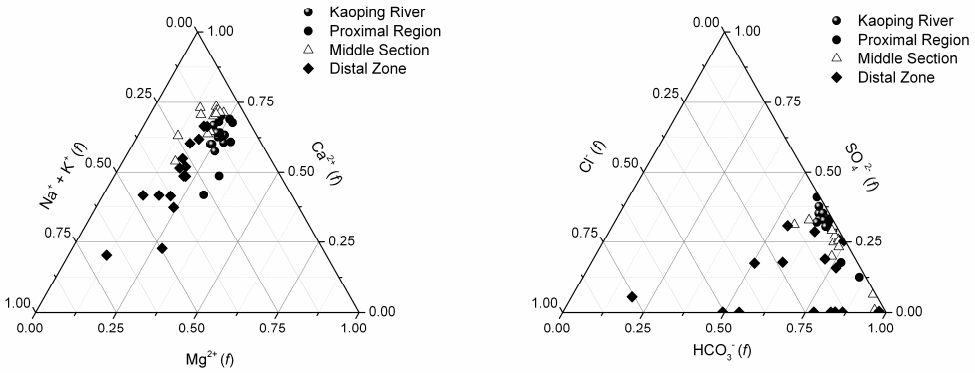

Figure 4.3. Triangular plots representing the relative equivalent fractions of major cation and anion charges in the Pingtung Plain groundwaters and the Kaoping River. Ca^{2+} is the dominant cation in the aquifer and the river, with Na^{+} + K^{+} becoming increasingly concentrated in the distal zone groundwaters. The anionic charge is dominated by HCO_3^{-} in both domains, with SO_4^{2-} representing greater than 30 % of the anionic charge of the river. Cl^{-} represents a maximum of 5 % of the anionic charge of the river, whereas it dominates some of the distal groundwaters accounting for up to 76 % of the equivalent charge.

Disproportionately high sulphide oxidation rates, related to the extreme physical erosion rates and intense rainfall in Taiwan, reported for the Kaoping River catchment (Das et al. 2012), explain the relatively enriched [SO_4^{2-}] in the river samples. The average Ba^{2+} and dissolved SiO_2 in the groundwaters, in theory both insensitive to passive seawater

mixing, were the most relatively enriched of all weathering species measured. For Ba^{2+}, substantial enrichment relative to the river concentration (142 nmol.L^{-1}) was observed in the middle section and distal zone, where mean concentrations were 290 and 883 nmol.L^{-1}, respectively (see Section 4.4.4 for discussion). For dissolved SiO_2, the entire aquifer was enriched relative to the river.

4.4.2 Seawater and groundwater mixing in the Pingtung Plain

The majority of samples, with chlorine concentrations of groundwater ($[Cl^-]_{gw}$) between 0.02 and 4.77 mmol.L^{-1}, lie on or slightly above the global meteoric water line (GMWL) in $\delta^{18}O/\delta D$ space, with some at the higher end of the Cl^- range trending towards a seawater end-member (Figure 4.4).

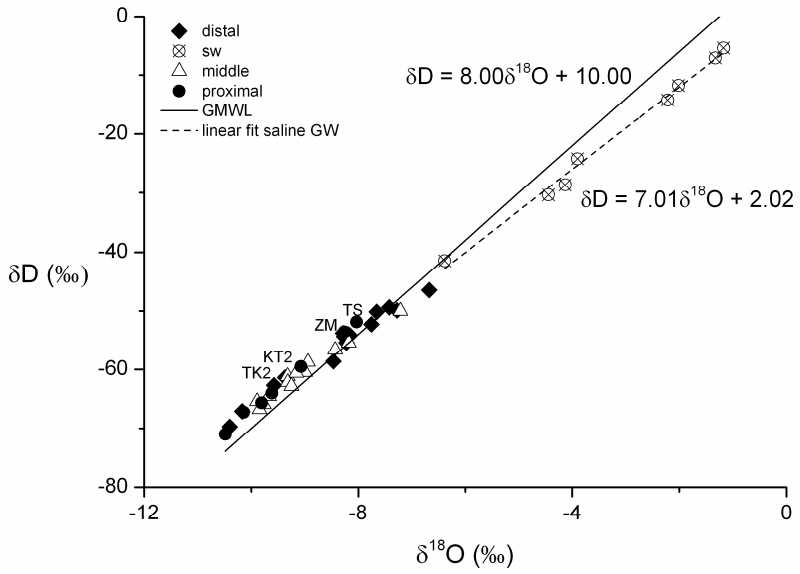

Figure 4.4. Distribution of stable isotopes of water from the Pingtung Plain in $\delta^{18}O$–δD mixing space. Groundwater with Cl^- concentrations between 0.02 and 4.77 mmol.L^{-1} (black circles, open triangles and closed diamonds) scatter around the GMWL. Eight samples with elevated Cl^- (217–487 mmol.L^{-1}) (crossed circles) lie on a mixing line between meteoric and seawater end-members.

Eight samples from the coastal zone, with $[Cl^-]_{gw}$ ranging from 217-523 mmol.L^{-1}, deviate strongly towards a seawater end-member (Figure 4.4). Because the seawater proportion in these samples is so high (for example, the concentration of sodium in these

eight coastal samples ranged from 31.71 to 76.04 % relative to the concentration in seawater), extracting the tiny-by-comparison groundwater chemical signature involves a large uncertainty. Therefore, the chemistry of these eight coastal samples, being dominated by seawater, was excluded from source-water calculations and major chemical trend interpretations.

4.4.3 Chlorine anomaly in the Pingtung Plain

The $[Cl^-]_{gw}$ for all samples was in excess of the rain Cl^- content adjusted for evapotranspiration ($[Cl^-]_{rain}$/ET), of 16.38 µmol.L^{-1} (see Section 4.6.1). A systematic increase in $[Cl^-]_{gw}$ was observed along the groundwater flow path, particularly at shallow and intermediate depths in the proximal region and middle section, and, with the exception of one well (HN2), at all depths in the distal zone (Figure 4.5A).

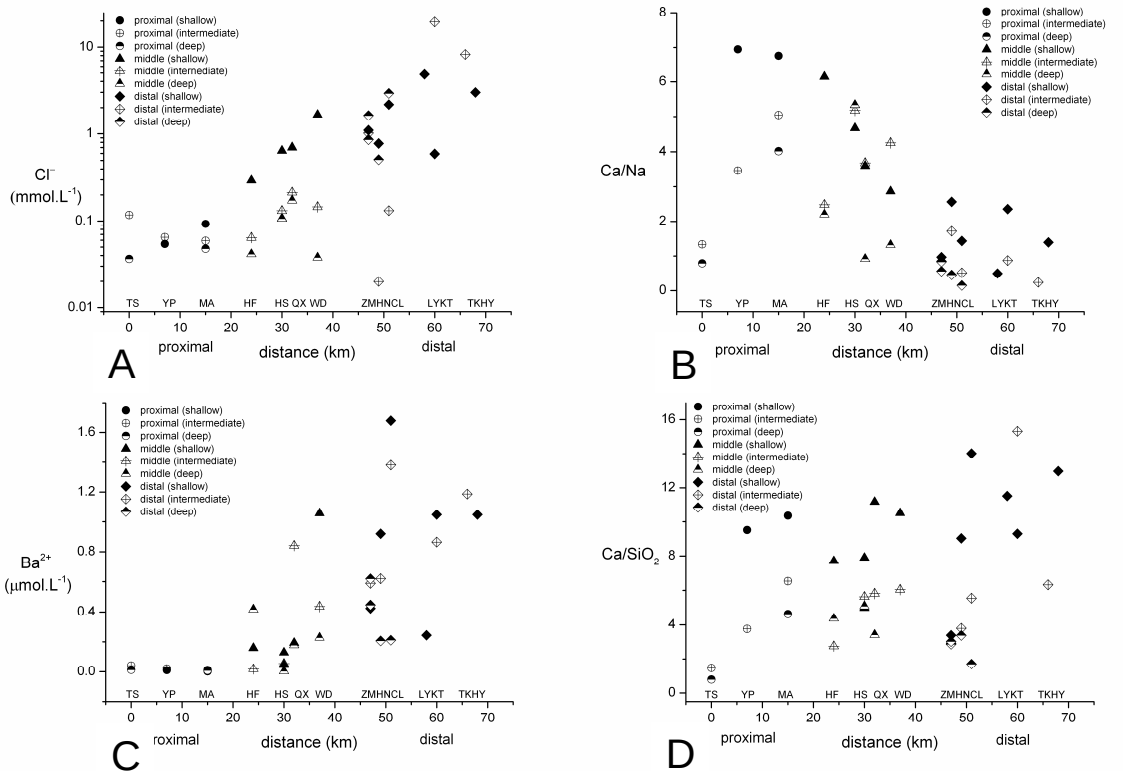

Figure 4.5A-D. Groundwater chemistry from the Pingtung Plain at three depth horizons (shallow: 6–60 m; intermediate: 61–140 m; deep: 141–237 m) along the subsurface flow path from the proximal foothills to the coast. Figures B and D show molar ratios.

The average $[Cl^-]_{gw}$ was 1.49 mmol.L^{-1}, requiring 1.47 mmol.L^{-1}, or ~ 99 % of the Cl^- to be sourced from hot-springs and/or seawater. Analysis of the Kaoping River time series showed that at 131.88 µmol.L^{-1}, the average Cl^- concentration of the river water

($[Cl^-]_{river}$) was more than eight times greater than $[Cl^-]_{rain}/ET$. A greater than ten-fold downstream systematic increase in chlorine concentrations was observed in the Kaoping River from headwaters to the river mouth by Chung et al. (2009). Our measurements of chlorine in the river samples were, on average, three times more concentrated than those reported by Chung et al. (2009). However, both data sets concur in the observation of there being chlorine enrichment in the river relative to the expected input via rainwater. It is possible that dry deposition of cyclic salts, undetected by rainwater sampling, could partly account for the trends observed in river chemistry, highlighting the need for improved constraints on rainwater chemistry.

4.4.4 Chemical trends in the Pingtung Plain

Groundwater chemistry was dominated by Ca^{2+}, which on average accounted for 56 % of the cationic charge (Figure 4.3), consistent with the abundance of carbonates in the hinterland and aquifer sediments and high dissolution rates of carbonates relative to silicate rock. Unlike absolute concentrations, any trends observed using Na-normalised ratios can be attributed to processes independent of dilution and evaporation. A rise in Ca/Na was seen along the groundwater flow path, most notably at shallow depths, until in the middle section at station HF, and particularly at depth, the ratio decreased (Figure 4.5B).

A further 22 % of the average cationic charge was represented by Na^+ (Figure 4.3), which was generally seen to increase relative to Ca^{2+} with depth and along the groundwater flow path in the middle section and the distal zone (Figure 4.5B). The behaviour of the Ca/Na ratio along the groundwater flow path implies that the weathering involves progressive silicate dissolution possibly combined with the precipitation of secondary calcite and/or the remobilisation of Ca^{2+} and Na^+ via ion exchange processes on clay sites. The indices of calcite saturation (*SI*) were calculated using the PHREEQC geochemical modelling package supplied by the USGS (http://wwwbrr.cr.usgs.gov/projects/GWC_coupled/phreeqc/) (Data Table F). Calculated *SI* values showed that all samples except proximal wells TS1 (*SI* = −2.63) TS2 (*SI* = −2.48) and YP2 (*SI* = −1.18) and middle well HF2 (*SI* = −1.22) were close to saturation (*SI* = 0) or supersaturated (*SI* > 0) with respect to calcite, with the highest *SI* value (*SI* = 0.55 – similar to that for seawater, which is 0.58) occurring in coastal well LY1 (Data Table F). The *SI* values support the likelihood that increasing Ca/Na ratios along the groundwater

flow path indicate some secondary calcite formation and some seawater mixing. The behaviour of Mg^{2+}, representing on average 20 % of the cationic charge (Figure 4.3), is similar to that of Ca^{2+} with elevated concentrations observed in proximal wells, and a decrease along the flow path, particularly at depth. The evolution of Ba^{2+} along the groundwater flow path showed that there was a significant increase in the middle section and the distal zone trending away from the bulk seawater composition (Figure 4.5C; Data Table F). Such enrichment of Ba^{2+} in coastal aquifers has been attributed to desorption of Ba^{2+} from aquifer solids induced by ionic strength changes upon seawater intrusion (Shaw et al. 1998).

The most proximal wells, TS1-2, located in the foothills of the central mountain range (Figure 4.1A), were at the highest topographic elevations in the sample set. Their concentrations of dissolved SiO_2 and $[Na^+]$ were greater by a factor of 1.5 than the next set of wells down-gradient (Figure 4.5B, D). This was in stark contrast to the concentrations of Ca^{2+} and Mg^{2+} in TS1-2, which were 3.3 and 2.1 times lower, respectively, than the next set of down-gradient wells (see Section 4.10 for discussion). The ratio of Ca/SiO_2 averaged 10.12 in shallow wells, whereas in intermediate to deep wells along the groundwater flow path the average ratio decreased to 5.86 (Figure 4.5D).

4.4.5 General characteristics of natural waters in the Choshui Plain

The results of chemical analyses of the 22 groundwater and 41 Choshui River samples, together with their physical and chemical parameters are presented in Data Table F. Total dissolved solids (TDS) in the groundwaters ranged from 243 to 5016 ppm. Excluding groundwater sample CP1 (5016 ppm TDS), found to have concentrations approaching bulk seawater values, brings the upper bound of the range in observed TDS to 1334 ppm. The temperature of the groundwaters (24.9-30.8 °C) systematically increased along the groundwater flow path, and with the exception of well station HL, increased with depth (Figure 4.6A). The pH values of the groundwaters ranged from slightly acidic to alkaline (6.7 to 7.7) and were relatively homogenous according to the spatial distribution of samples and the hydrological regime (Figure 4.6B).

The relative proportions of cations and anions in the groundwater and river water samples are shown in Figure 4.7. All major ions except SO_4^{2-} and K^+ were, on average, enriched to varying degrees in the groundwaters relative to the river. Respecting average Ca^{2+} concentrations, the proximal region and middle section were significantly enriched

relative to the river (2.06 and 2.09 versus 1.38 mmol.L^{-1}) and the distal zone broadly comparable (1.42 versus 1.38 mmol.L^{-1}). This was similar for Mg^{2+} with average

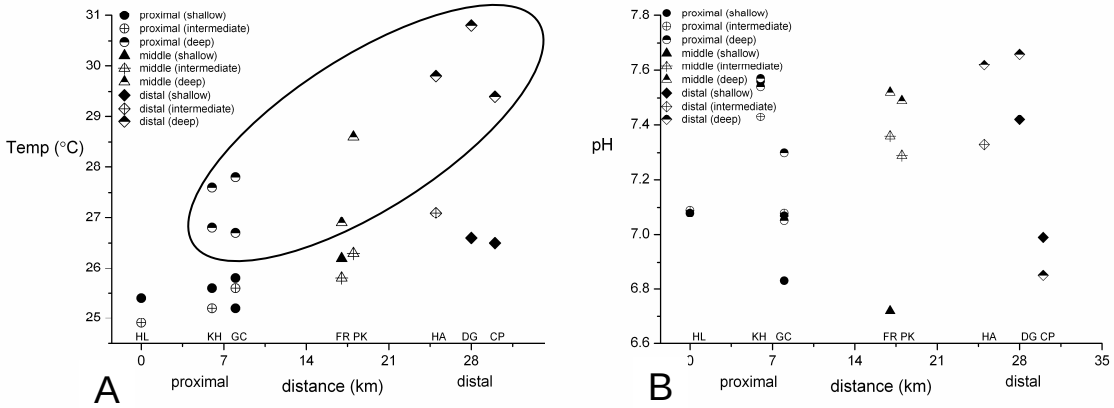

Figure 4.6. Temperature (A) and pH (B) according to distance along the groundwater flow path in the Choshui Plain. Systematic increases in temperature according to the spatial distribution of samples along the main direction of groundwater flow and with increasing depth were observed, whereas pH was relatively homogenous. All samples in the ellipse are 'deep'.

concentrations in the proximal region and middle section exceeding those in the river (0.83 and 0.92 versus 0.68 mmol.L^{-1}) but with a relative average decrease observed in the distal zone (0.53 versus 0.68 mmol.L^{-1}).

For Na^+, the average concentrations in all of the groundwater locations were enriched relative to the river, increasing from a factor of 3.0 in the proximal region to a factor of 6.6 in the distal zone (1.56 and 3.45 versus 0.52 mmol.L^{-1}, respectively). The relative enrichment of Na^+ in the distal zone is partly due to seawater mixing observed in one well (CP1) (see Section 4.6.4). Average K^+ concentrations in the proximal region (56.88 µmol.L^{-1}) and the middle section (47.71 µmol.L^{-1}) were depleted relative to the river (67.71 µmol.L^{-1}), whereas [K^+] in the distal zone (67.21 µmol.L^{-1}) had increased to comparable levels with the river (see Section 4.9.2 for discussion).

Unlike in the distal zone, where average sulphate concentrations (0.17 mmol.L^{-1}) were significantly depleted relative to the river (1.05 mmol.L^{-1}), the proximal region and middle section exhibited relative enrichment (1.12 and 1.14 mmol.L^{-1}, respectively), possibly indicating the dissolution of sulphur-bearing minerals in these locations. As will be investigated in Section 4.9.2, the low sulphate values in several distal wells possibly indicate sulphide formation in this location. The disproportionately high sulphate concentrations measured in 2004, 2009 and 2010 reported for the Kaoping River catchment (Das et al. 2012), are similar to the values measured in the Choshui River

during 2005-2006 for this study, suggesting that high rates of sulphide oxidation, possibly linked to high erosion rates, were occurring at the time of sampling in the Choshui Catchment.

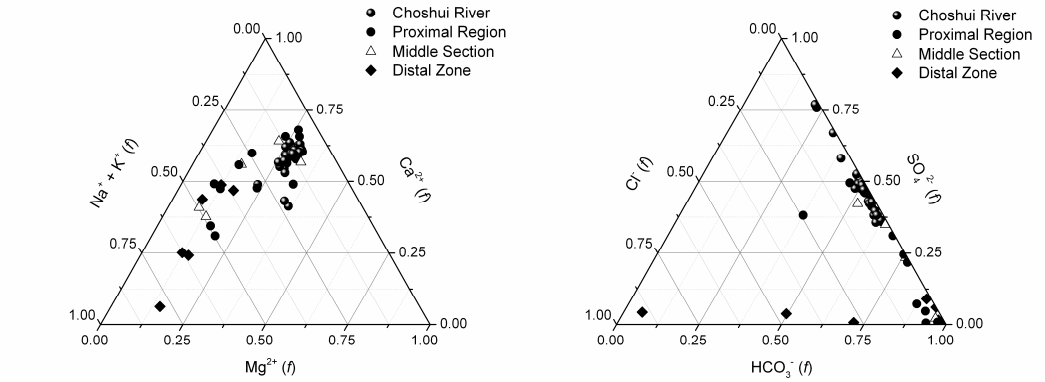

Figure 4.7. Triangular plots representing the relative equivalent fractions of major cation and anion charges in the Choshui Plain groundwaters and the Choshui River. Ca^{2+} is the dominant cation in the aquifer and the river, with Na+K becoming increasingly concentrated towards the distal zone groundwaters. The anionic charge is dominated by HCO_3^- and SO_4^{2-} in both domains, with SO_4^{2-} representing up to greater than 75 % of the anionic charge of the river. Cl^- represents a maximum of 4 % of the anionic charge of the river, whereas it dominates one of the distal groundwater samples accounting for up to 99 % of the equivalent charge.

4.4.6 Seawater infiltration and evapotranspiration in the Choshui Plain

The majority of samples, with chlorine concentrations of groundwater ($[Cl^-]_{gw}$) between 0.03-3.88 mmol.L^{-1}, lie on or slightly above the global meteoric water line (GMWL) in $\delta^{18}O$-δD space, with the exception of GC1, which lies below the GMWL signifying more evaporation to have occurred at this location relative to the other well sites (Figure 4.8). At 91.21 mmol.L^{-1} (bulk seawater = 545.84 mmol.L^{-1}), CP1 had the highest $[Cl^-]_{gw}$ of all waters sampled in the Choshui Plain, and given its proximity to the coastline, likely contained seawater (see Section 4.6.5).

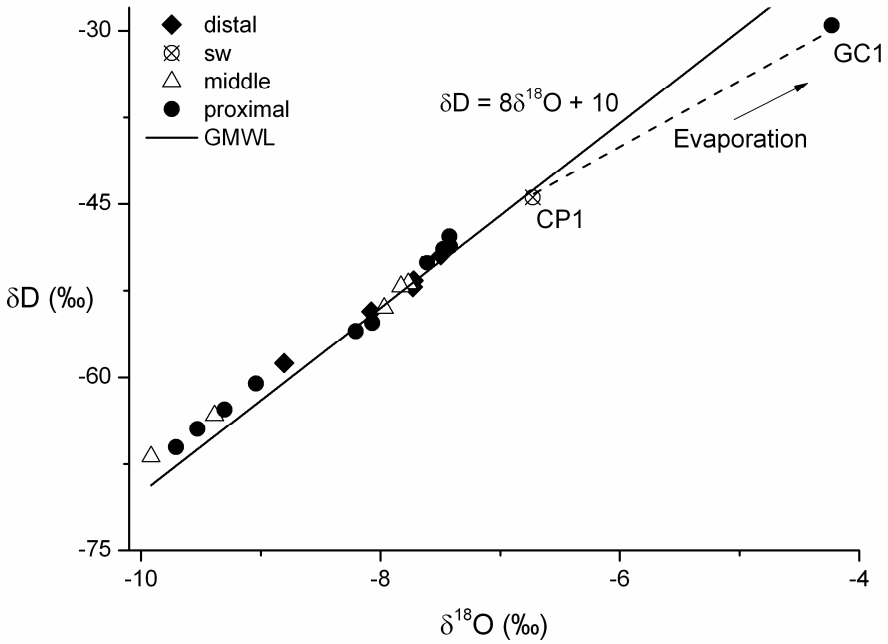

Figure 4.8. Distribution of stable isotopes of water from the Choshui Plain in $\delta^{18}O$–δD mixing space. Groundwater with Cl^- concentrations between 0.03 and 3.88 mmol.L^{-1} (black circles, open triangles and closed diamonds) scatter around the GMWL. Sample CP1, with elevated Cl^- (91.21 mmol.L^{-1}) (crossed circle), approaches a seawater end-member (0 ‰). One sample, GC1, which has a Cl^- concentration of 3.88 mmol.L^{-1}, in contrast to the remaining groundwater samples lies below the GMWL, indicating that a significant relative degree of evapotranspiration has occurred at this location.

4.4.7 Chlorine anomaly in the Choshui Plain

The $[Cl^-]_{gw}$ for all samples was in excess of the rain Cl^- content adjusted for evapotranspiration ($[Cl^-]_{rain}$/ET), of 16.38 µmol.L^{-1} (see Section 4.6.1). An increase in $[Cl^-]_{gw}$ was observed along the groundwater flow path, particularly at shallow depths in the proximal region and middle section, and, with the exception of two deep wells (HA2 and DG2), at all depths in the distal zone (Figure 4.9A). The average $[Cl^-]_{gw}$ was 4.74 mmol.L^{-1}, requiring 4.72 mmol.L^{-1}, or ~ 99 % of the Cl^- to be sourced from hot-springs and/or seawater.

Analysis of the Choshui River time series showed that significant seasonal variability occurred during the sampling period corresponding to a decrease in dissolved Cl^- in response to increased rainfall and river discharge during summer months and a likewise increase during the drier winter months (Figure 4.10).

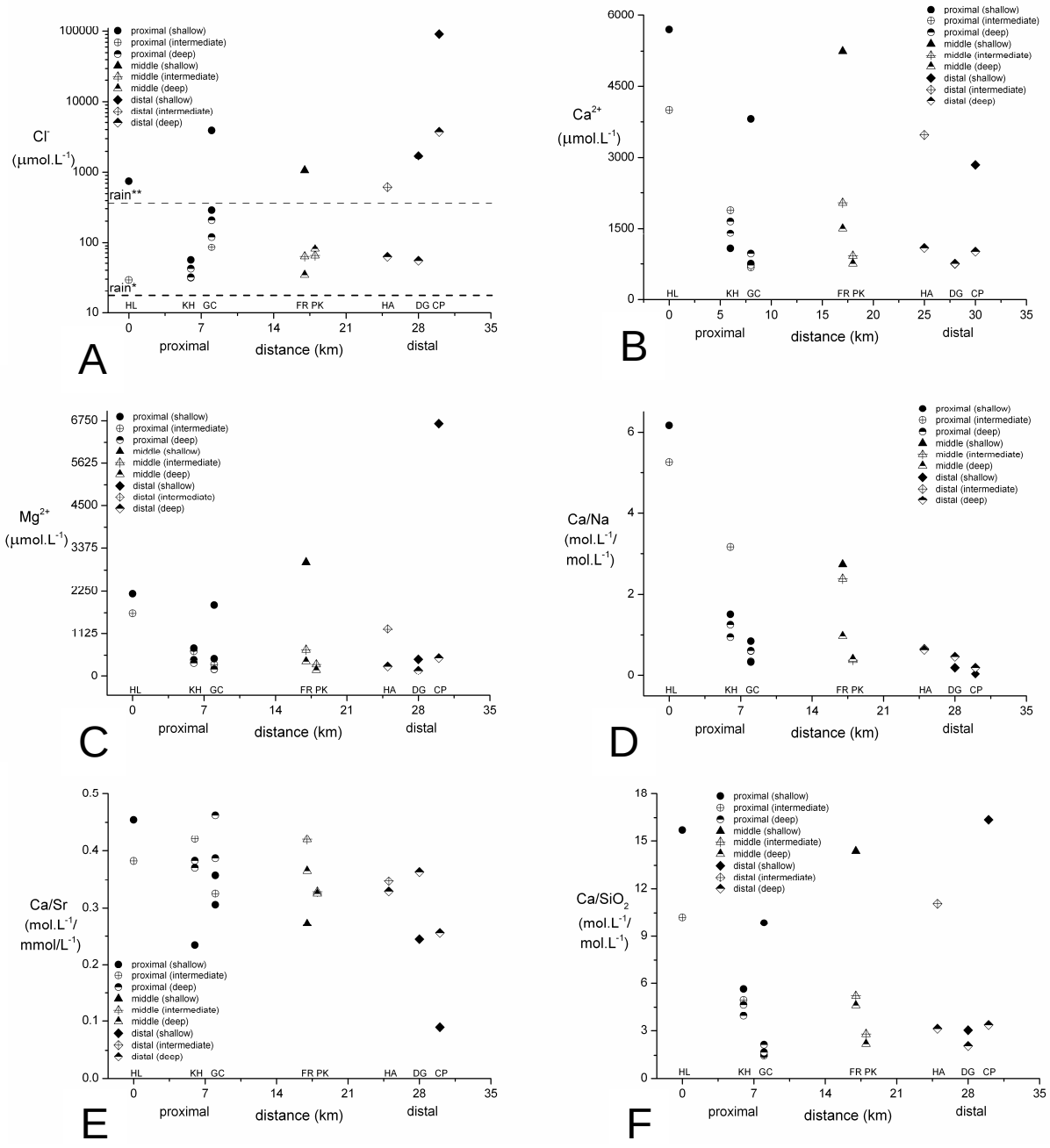

Figure 4.9A-F. Groundwater chemistry at three depth horizons (shallow: 10-74; intermediate (75-140; deep (141-294) along the subsurface flow path in the Choshui Plain from the proximal region to the coast. Rain is the evapotranspiration-corrected rainwater value. Rain** is the calculated Cl^- concentration after 100 % evapotranspiration. Figures C-F show molar ratios.*

This 'dilution effect' is commonly observed in riverine chemical hydrographs for most major elements (see section 5.6.2, Chapter 5 for discussion). However, at 72.99 $\mu mol.L^{-1}$, the average $[Cl^-]_{river}$ was more than four times greater than $[Cl^-]_{rain}$/ET. Up to 81 % evapotranspiration would be required to account for the average Cl^- concentration of the

river time series; an insupportable volume alongside a continually recharged aquifer. Therefore, the observation of chlorine enrichment in the river relative to the expected input via rainwater adjusted for evapotranspiration suggests that additional sources, such as hot-springs, were contributing to the dissolved riverine chemistry.

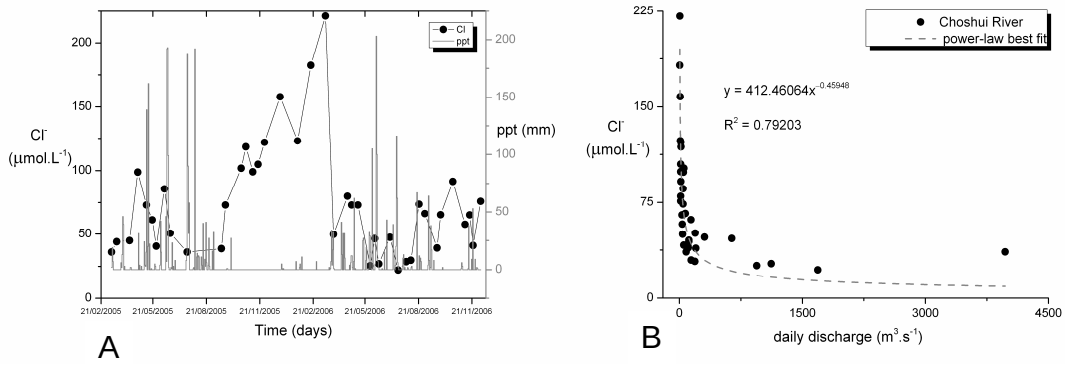

Figure 4.10. Variations in Cl^- concentrations as a function of time and precipitation (A) and daily discharge (B) in the Choshui River as seen throughout the annual hydrological cycle captured during sampling.

4.4.8 Chemical trends in the Choshui Plain

Groundwater chemistry was dominated by Ca^{2+}, which on average accounted for 47 % of the cationic charge (Figure 4.7), consistent with the abundance of carbonates in the hinterland and aquifer sediments and high dissolution rates of carbonates relative to silicate rock. Despite localised highs (e.g. at stations HL, GC and FR), however, Ca^{2+} was seen to generally decrease along the groundwater flow path, particularly at depth (Figure 4.9B), indicating its uptake by secondary mineral formation processes such as calcite formation and/or clay adsorption. The behaviour of Mg^{2+}, representing 18 % of the average cationic charge (Figure 4.7), was similar to that of Ca^{2+} with elevated concentrations observed in the proximal-most wells and a decrease along the flow path at depth (Figure 4.9C). At distal well CP1, Mg^{2+}, unlike Ca^{2+}, appears to be especially sensitive to seawater mixing (Figure 4.9C).

A further 35 % of the average cationic charge was represented by Na^+ (Figure 4.7), which was generally seen to increase relative to Ca^{2+} along the groundwater flow path as shown by the general decrease in the ratios of Ca/Na seen along the groundwater flow path at intermediate and deep wells in the proximal region and middle section and at all depths in the distal zone (Figure 4.9D). The behaviour of the Ca/Na ratio along the groundwater

flow path implied that the weathering involved progressive silicate dissolution, possibly combined with the precipitation of secondary calcite and/or the remobilisation of Ca^{2+} and Na^{+} via ion exchange processes on clay sites. Similar to the Pingtung Plain, saturation indices in the Choshui Plain groundwaters were close to zero (*SI* = −0.67 to 0.84), with the highest value occurring in coastal well HA1 (Data Table F), suggesting the possibility of secondary calcite formation and seawater mixing. Comparable to the behaviour of the Ca relative to Na was the decreasing ratio of Ca/Sr seen along the groundwater flow path at all depths, which is consistent with the secondary uptake of Ca^{2+} into carbonates (Figure 4.9E).

The ratio of Ca/SiO_2 remained high in the shallow wells along the groundwater flow path ranging from 8.18 in proximal region to an average peak of 14.37 in the middle section and declining to an average of 9.70 in the distal zone (Figure 4.9F). At depth, the Ca/SiO_2 ratio was 10.21 in the deepest proximal-most well, HL2, declining along the flow path to averages of 3.10, 2.20 and 2.85 in the deep wells of the proximal region, middle section and deep zone, respectively (Figure 4.9F), in accordance with increased silicate dissolution and the loss of Ca^{2+} via carbonate formation and/or clay uptake observed at depth (Figure 4.9F).

4.5 Residence times controlling groundwater chemistry: evidence from combined temperatures and major chemistry

Groundwater temperature has been shown to track hydraulic conductivity in the Choshui Plain, with significantly decreased temperatures having been associated with earthquake-induced permeability increases (Wang et al. 2012). Furthermore, this water released co-seismically into the Choshui Plain has been shown to have been derived from a mountain-bedrock source driven into the plain by high hydraulic pressures through bedrock fractures (possibly linked to the plain through increased permeabilities in the plain itself) (Wang et al. 2004b). The relationship between temperature and distance along the established groundwater flow paths in the Pingtung and Choshui Plains (see Figures 4.2A and 4.6A) should (if it is assumed that groundwater temperature is a function of residence time), therefore offer insight into the control of groundwater residence time (a function of hydraulic head and hydraulic conductivity) on groundwater chemistry.

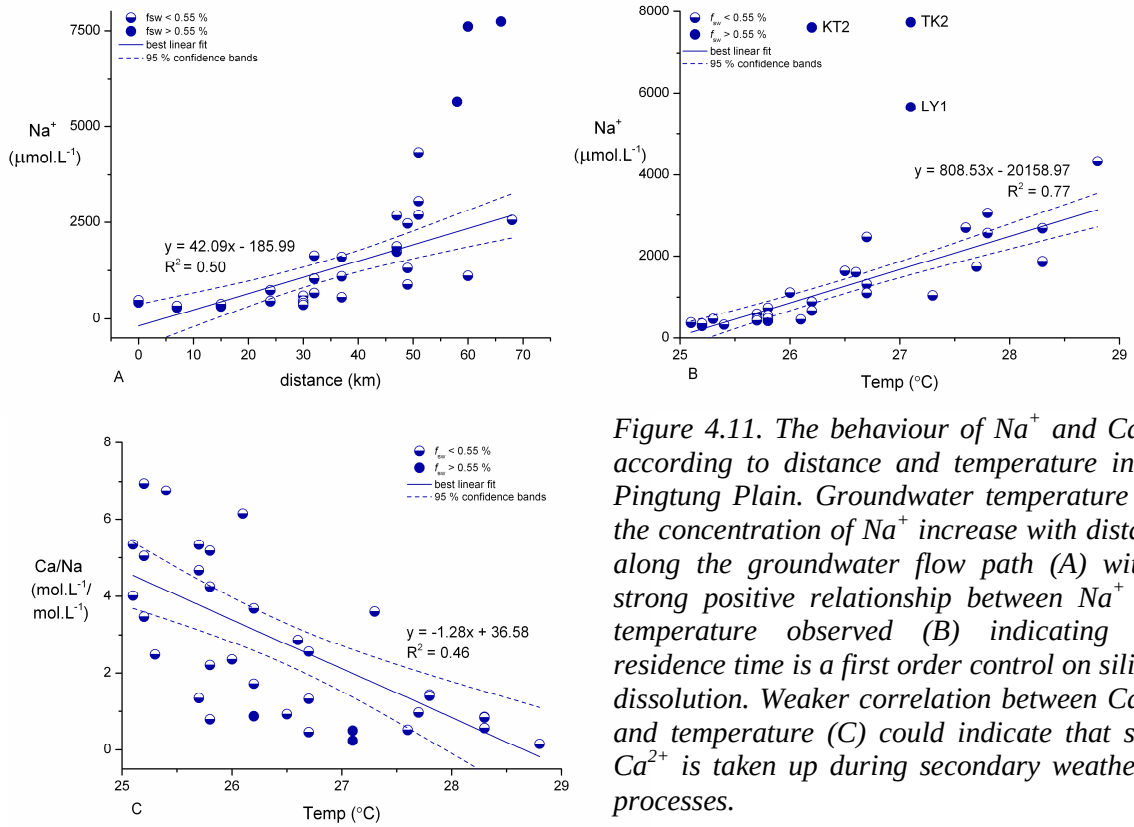

Figure 4.11. The behaviour of Na^+ and Ca/Na according to distance and temperature in the Pingtung Plain. Groundwater temperature and the concentration of Na^+ increase with distance along the groundwater flow path (A) with a strong positive relationship between Na^+ and temperature observed (B) indicating that residence time is a first order control on silicate dissolution. Weaker correlation between Ca/Na and temperature (C) could indicate that some Ca^{2+} is taken up during secondary weathering processes.

Similar to the evolution of temperature (Figure 4.2A), the concentration of dissolved Na^+ in the Pingtung Plain was seen to increase along the groundwater flow path, showing a good correlation with distance when excluding those coastal wells (LY1, TK2 and KT2) with relative seawater fractions greater than 0.55 % (see Section 4.6) (R^2 = 0.50) (Figure 4.11A). Excepting those wells with appreciable seawater concentrations, the relationship between Na^+ and temperature is strong (R^2 = 0.77) (Figure 4.11B), implying that the dissolution of silicate rock in the drilled depth of the Pingtung basin is to a first order controlled by groundwater residence times. In contrast, the Ca/Na ratios, the decline of which along the groundwater flow path having been attributed to silicate dissolution, calcite formation and/or ion exchange processes on clay sites (Figure 4.5B), display a weaker relationship with temperature than do Na^+ concentrations (Figure 4.11C), supporting the precipitation of secondary Ca^+ in explaining the Ca/Na ratios.

Using temperature as a proxy for residence time has a slightly different implication for the Choshui Plain groundwaters. Similar to the Pingtung Plain, temperatures generally increase with distance along the groundwater flow path, but in the case of the Choshui Plain, this distance-dependent temperature increase is most pronounced at depth (Figure

4.6A). Likewise, the evolution of Na^+ concentrations with distance appears to show partitioning of the shallow and intermediate wells relative to the deep wells (Figure 4.12A).

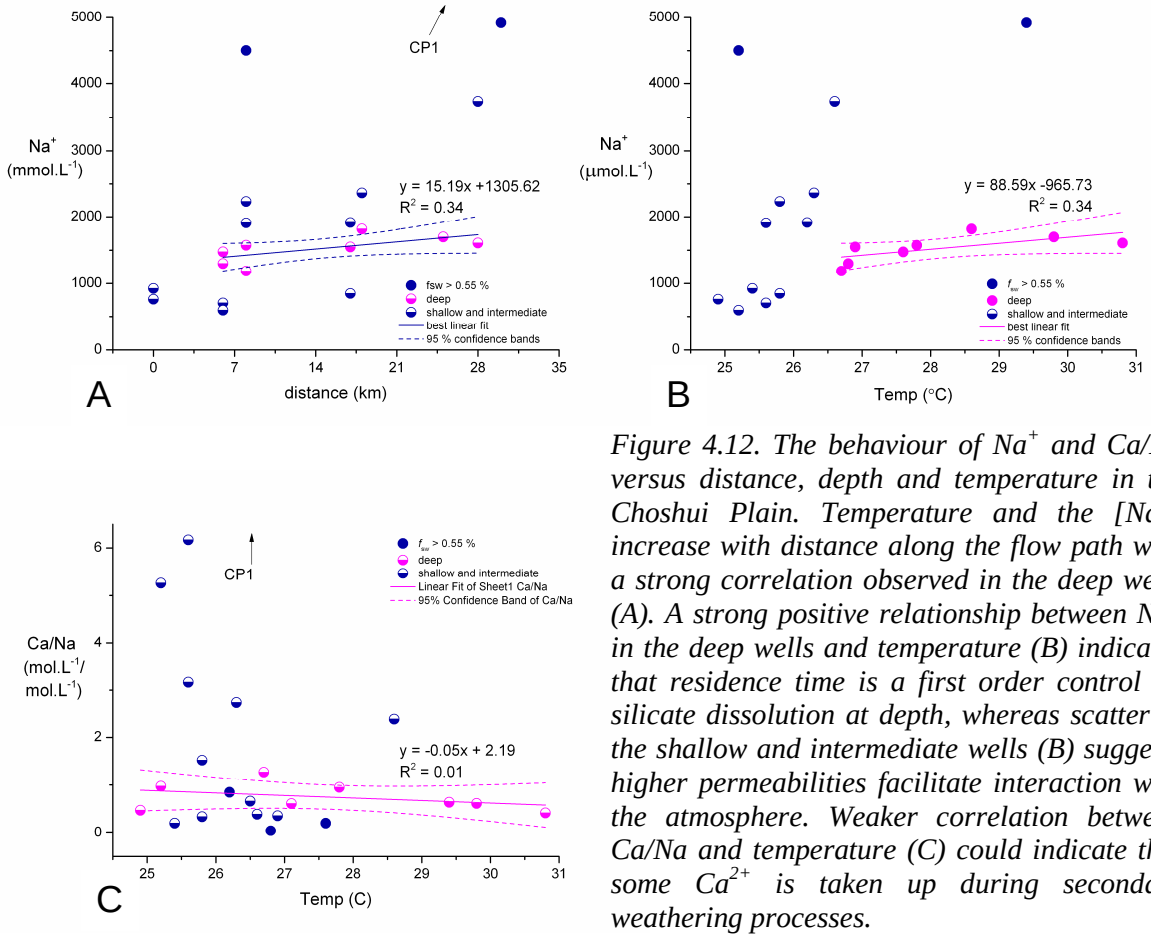

Figure 4.12. The behaviour of Na^+ and Ca/Na versus distance, depth and temperature in the Choshui Plain. Temperature and the [Na^+] increase with distance along the flow path with a strong correlation observed in the deep wells (A). A strong positive relationship between Na^+ in the deep wells and temperature (B) indicates that residence time is a first order control on silicate dissolution at depth, whereas scatter of the shallow and intermediate wells (B) suggests higher permeabilities facilitate interaction with the atmosphere. Weaker correlation between Ca/Na and temperature (C) could indicate that some Ca^{2+} is taken up during secondary weathering processes.

Plotting Na^+ versus temperature affirms this observation with the degree of silicate dissolution appearing to be controlled by groundwater residence times (Figure 4.12B). The scatter in the shallow and intermediate wells containing insignificant relative seawater fractions could be related to higher permeabilities in the upper reaches of the aquifer relative to the analogous portions of the Pingtung Plain aquifer, permitting enhanced seasonal forcing of the groundwater temperatures/residence times in the case of the Choshui Plain. As discussed in Section 2.2.2, Chapter 2, relatively high permeabilities in the upper reaches of the Choshui Plain could be a result of the shock caused by the 1999 Chi-Chi earthquake.

Similar to in the Pingtung Plain, the general decrease in Ca/Na ratios observed along the groundwater flow path in the Choshui Plain (Figure 4.9D) is attributed to silicate

dissolution, calcite formation and/or ion exchange processes on clay sites. Likewise, no relationship between Ca/Na ratios and temperature, even at depth (R^2 = 0.01) where the Na^+-temperature correlation is moderate (R^2 = 0.34), indicates that Ca^{2+} is preferentially taken up over Na^+ during secondary weathering processes (Figure 4.12C).

4.6 Source water characterisation and mixing

The chemical composition of groundwater in the Pingtung and Choshui Plains is potentially derived from four sources: rainwater (subject to some degree of evapotranspiration), hydrothermally-sourced water ('hot-spring'), seawater and solutes that derive from rock weathering processes in the plain and in the surrounding hills. Assuming that rock weathering processes in the plains will release negligible Cl^- and Li^+ (discussed in the following paragraph), their concentrations in the rain, hot-spring and seawater end-members were used to estimate the relative proportions of rainwater, hydrothermally-sourced water and seawater in each of the groundwater samples and in the river samples. Using this approach, the excess or deficit in solute concentrations outside of that derived from conservative mixing of the rain, hot-spring and seawater inputs can be attributed to rock weathering processes.

Given there are no known evaporite deposits within the drilled depth of the Pingtung and Choshui Plain sediments, Cl^- is assumed to be a conservative tracer. However, Li^+ is a non-conservative tracer of groundwater flow, but given its affinity with thermally-enhanced weathering (Kısakűrek et al. 2005) (here the measured Li^+ in the hot-spring end-member is 455 times greater than the average Li^+ concentration of the groundwater and river water samples) and relatively low reactivity during ascent to the surface from geothermal sources (Millot et al. 2010) it is appropriate for tracing hot-spring input (see Section 4.7 for discussion).

The first step in evaluating the sources of solutes to the groundwaters in the coastal plains was to correct the chemical concentrations of the major water source, rainwater, for any evapotranspiration it may have undergone before ultimate subsurface infiltration. The following section describes and illustrates the method used to estimate the degree of evapotranspiration to have affected the groundwater prior to and during recharge.

4.6.1 Evapotranspiration estimate

The Rayleigh Distillation of oxygen and deuterium isotope ratios was used to estimate the fraction of groundwater lost to evapotranspiration, as follows:

Linear regression through the groundwater data in $\delta^{18}O$-δD mixing space gave: $\delta D = 6.5\delta^{18}O - 1.7$ for the Pingtung Plain, and $\delta D = 6.8\delta^{18}O + 1.0$ for the Choshui Plain. The intersection of these lines with the global meteoric water line (GMWL) ($8.0\delta^{18}O + 10.0$ (Craig 1961)) gave estimated initial compositions for the sources of precipitation (δ_{rain}) of $\delta D = -69.8$ and $\delta^{18}O = -10.5$ for the Pingtung Plain, and $\delta D = -65.62$ and $\delta^{18}O = -9.76$ for the Choshui Plain. The GMWL was used to approximate a local meteoric water line as no isotope in precipitation data were available. The following exponential function describes the progressive partitioning of the heavier isotopes into the water reservoir as water is lost due to evapotranspiration:

$$R_{sample} = R_{rain} f_{residual}^{(\alpha-1)} \quad (4.1)$$

where R_{rain} is the initial isotope ratio of precipitation, given by:

$$((\delta_{rain} + 1000) \times R_{smow})/1000 \quad (4.2)$$

where R_{smow} is the isotopic ratio of Vienna Standard Mean Ocean Water (which for oxygen ($^{18}O/^{16}O$) is 2.0052×10^{-3} and deuterium ($^{2}H/^{1}H$) is 1.5576×10^{-4}) (IAEA 1983a). Equation 4.1 allows the isotopic ratio of the sample, (R_{sample}), to be related to the fraction of water that remains, $f_{residual}$, by R_{rain}, and by the equilibrium fractionation factor for evaporation, α, which in this case was calculated to be 0.9898 ($\delta^{18}O$) for the Pingtung Plain and 0.9920 ($\delta^{18}O$) for the Choshui Plain. To simplify the calculation, α values for δD were fixed at 0.9500 for both regions. The α values were derived from the calculated slopes in modelled $\delta^{18}O$-δD mixing space, which were selected to be lower than the spread of groundwater data (Figure 4.13A,B). As such, the selected values for α provide upper bounds on the degree of evapotranspiration to have affected the groundwaters (Figure 4.13A,B).

To convert the isotopic ratio of the sample (R_{sample}) into delta notation (δ_{sample}), the following equation was used:

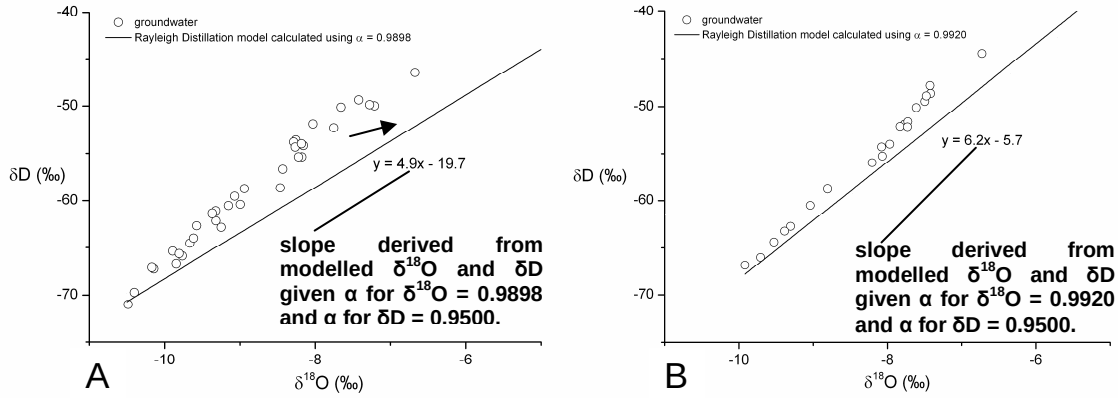

Figure 4.13. Rayleigh Distillation models and groundwaters in $\delta^{18}O$-δD mixing space. The open circles are Pingtung Pain (A) and Choshui Plain (B) groundwaters, respectively. The solid lines are calculated based on modelled estimates of $\delta^{18}O$ and δD, derived from selected α values to give a slope in $\delta^{18}O$-δD mixing space lower than the spread of the data. As such, the modelled values of $\delta^{18}O$ and δD reflect water compositions that have undergone more evapotranspiration than the samples. The arrow indicates the general direction that an evapotranspiration vector will take (exact slope dependent on the degree of evapotranspiration, with a decrease in slope indicating an increase in evapotranspiration).

$$\delta_{sample} = (R_{sample}/R_{smow} - 1) \times 1000 \quad (4.3)$$

where for the oxygen isotopic composition of the sample, becomes:

$$\delta^{18}O_{sample} = ({}^{18}O/{}^{16}O_{sample}/{}^{18}O/{}^{16}O_{smow} - 1) \times 1000 \quad (4.4)$$

Plotting $f_{residual}$ against calculated $\delta^{18}O_{sample}$, having used the starting compositions for source precipitation and the α values given above, gave the following expressions for the Pingtung and Choshui Plains, respectively (Figure 4.14A,B):

$$y = 0.3566e^{-0.0977x} \quad (4.5)$$

$$y = 0.29446e^{-0.1249x} \quad (4.6)$$

that were then used to model the $f_{residual}$ of the groundwater samples by substituting the oxygen isotopic value of the groundwater samples ($\delta^{18}O_{gw}$) for x.

Results show that on average, the groundwaters of the Pingtung and Choshui Plains underwent 15.10 % and 18.51 % evapotranspiration, respectively. The degree of evapotranspiration appears to have been underestimated for one sample, the most depleted well in the Choshui Plain, FR2, which was modelled to have undergone −1.61 % evapotranspirative loss (Figure 4.14B). However, the above method gives values that are broadly consistent with the range of previously published evapotranspirative estimates of 0 % to 25 % bounding the wet and dry seasons, respectively, in the Kaoping River catchment (Das et al. 2012).

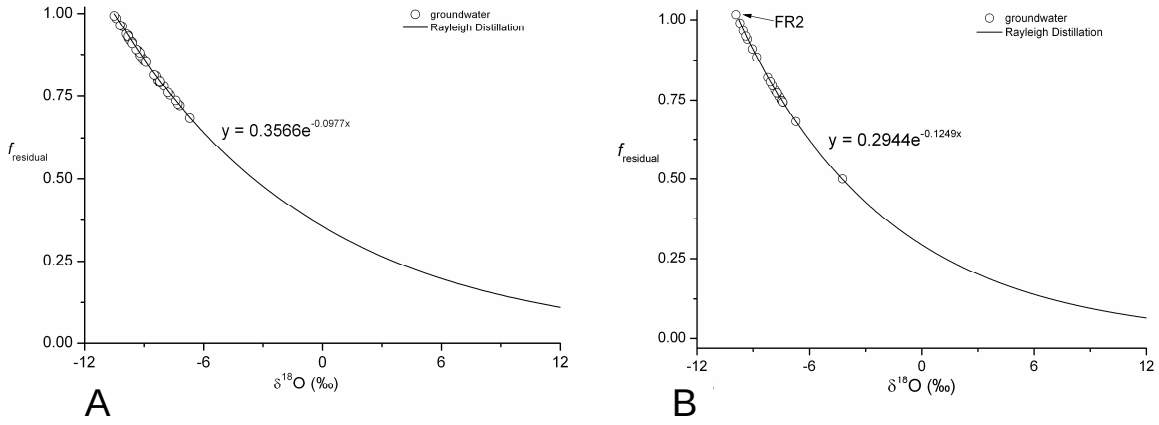

Figure 4.14. Rayleigh Distillation curves modelling the fractions of residual water after evapotranspiration given estimated isotopic starting compositions for precipitation and selected α values. The open circles are Pingtung Pain (A) and Choshui Plain (B) groundwaters, respectively.

4.6.2 Three end-member, two-tracer mixing model

The next step is to estimate the water fractions (*f*) from each component end-member (rainwater, hot-spring water and seawater). The mass balance equations used to estimate these water fractions are as follows:

$$f_1 + f_2 + f_3 = 1 \quad (4.7)$$

$$A_1f_1 + A_2f_2 + A_3f_3 = A_t \quad (4.8)$$

$$B_1f_1+B_2f_2 + B_3f_3 = B_t \quad (4.9)$$

where f_1, f_2, and f_3 are the fractions of rainwater, hot-spring and seawater, respectively, in the groundwater samples, and A_t and B_t are the Cl^- and Li^+ concentrations in the sample (i.e. t = total). The Cl^- and Li^+ concentrations in each of the three end-member components were taken from the spot sample measurement provided by Josh West (see Section 3.2.4, Chapter 3) for rainwater (A_1, B_1), analyses of Taiwanese hot-spring waters by Song and Liu (2006) (A_2, B_2), and Drever (1988) for bulk seawater (A_3, B_3) (Table 4.1). Given the likelihood of spatial and temporal variability of rainwater, and the probability that the sampling of rainwater omits detection of cyclic salts due to dry deposition, having only a single spot-sample measurement to represent the $[Cl^-]_{rain}$ limits the accuracy with which we can assess source-water contributions to the Pingtung Plain groundwaters. However, rainwater chemical contributions are typically minor, with temporal variations unlikely to drive the much larger variations observed in groundwater chemistry, and therefore uncertainties due to rainwater corrections are small. Solving Equations 4.7 to 4.9 gives:

$$f_1 = (A_t - A_3)(B_2 - B_3) - (A_2 - A_3)(B_t - B_3)/$$
$$(A_1 - A_3)(B_2 - B_3) - (A_2 - A_3)(B_1 - B_3) \quad (4.10)$$

$$f_2 = (A_t - A_3)/(A_2 - A_3) - [(A_1 - A_3)/(A_2 - A_3)]f_1 \quad (4.11)$$

$$f_3 = 1 - f_1 - f_2 \quad (4.12)$$

The proportion of Cl^- from each end-member ($[Cl^-]_{end\text{-}member}$) was then calculated and used to assign the contributions of rain, hot-spring and seawater to the concentrations of the other elements of interest, X_i, as follows:

$$[X_i]_{end\text{-}member} = [Cl^-]_{end\text{-}member} \times [X_i/Cl^-]_{end\text{-}member} \quad (4.13)$$

Knowing the end-member contributions for element X_i allows calculation of the contribution of dissolved chemistry from rock weathering processes in the plain ($[X_i]_{residual}$) from:

$$[X_i]_{sample} = [X_i]_{rain}/ET + [X_i]_{spring} + [X_i]_{sw} + [X_i]_{residual} \quad (4.14)$$

where ET is a factor of 0.85 and 0.81 for the Pingtung and Choshui Plains, respectively, used to correct the rainwater concentration for enrichment due to evapotranspiration. In the groundwater samples, the contribution of $[X_i]_{residual}$ is positive when weathering processes in the plains contribute to net enrichment of a given element X_i, such as mineral dissolution, ion exchange and biogeochemical activity, or negative when mineral formation ('reverse weathering') occurs.

4.6.3 Propagation of uncertainty in the mixing model

The end-member and input-error values for the uncertainty estimates in the mixing model are presented in Table 4.1. The residual values of water compositions ($[X_i]_{residual}$) corrected for rain, spring and seawater inputs using the three-end-member mixing model (Equations 4.7 to 4.14), contain compounded errors associated with uncertainty in each measured component. Given that the components of Equations 4.7 to 4.14 represent a non-linear set of combination variables (F), and assuming that the variances of measured components are independent, the total 1σ uncertainty in the calculated residual ($\sigma_{[xi]residual}$) for element X_i was estimated as:

$$\sigma_{[Xi]residual} = \Sigma((\delta F/\delta_{[Xi]})\sigma_{[Xi]})^2 \quad (4.15)$$

where the standard deviation (σ) (or the standard error (σ/√n) (SE), where appropriate) estimate relating to each variable in F is as follows: σ_{A1} (0.21 μmol.L^{-1}), SE_{A2} (1.12 mmol.L^{-1}), σ_{A3} (6.89 mmol.L^{-1}), σ_{B1} (0.02 nmol.L^{-1}), σ_{B2} (18.80 μmol.L^{-1}) and σ_{B3} (0.66 μmol/L^{-1}) are the uncertainties of chlorine (A) and lithium (B) concentrations in the rain (1), hot-spring (2) and seawater (3) end-members, respectively, and are all analytical uncertainties, with the exception of $SE_{A2,}$ which is the combined analytical and end-member variability uncertainties, where the latter is the standard error of the mean of the population (n = 21); SE_{At} and SE_{Bt} are the standard errors on the measurement of chlorine and lithium concentrations in the samples (t) that averaged, respectively 3.17 μmol.L^{-1} and 6.93 nmol.L^{-1} for groundwater samples in the Pingtung Plain, 0.50 μmol.L^{-1} and 12.79 nmol.L^{-1} for Kaoping River water samples, 1.66 μmol.L^{-1} and 19.2 nmol.L^{-1} for groundwater samples in the Choshui Plain and 0.14 μmol.L^{-1} and 6.34 nmol.L^{-1} for Choshui River water samples; $\sigma[Xi]_{[Xi/Cl]rain}$ (0.67 μmol.L^{-1} to 5.94 mmol.L^{-1}),

$SE[Xi]_{[Xi/Cl]spring}$ (18.80 μmol.L^{-1} to 2.72 mmol.L^{-1}) and $\sigma[Xi]_{[Xi/Cl]sw}$ (0.67 μmol.L^{-1} to 5.94 mmol.L^{-1}) are the uncertainties of element X_i in the ratios of X_i to chlorine in the rain, hot-spring and seawater end-members, respectively. Concentrations of major cations and sulphate and bicarbonate were not available for the rain water end-member; therefore, their concentrations in the rain end-member were calculated using the chlorine in the rain and seawater ratios normalised to chlorine, as follows: $[X_i]_{rain} = [Cl^-]_{rain} \times [X_i]/[Cl^-]_{sw}$. These are analytical uncertainties of X_i in the cases of rain and seawater end-members, and is the combined analytical and end-member variability uncertainty in the case of the hot-spring end-member; $SE_{[Xi]}$ is the standard error on the measurement of other elements of interest in the sample (see Table 3.1, Chapter 3). The analytical uncertainties on the measurement of elemental concentrations in rain, hot-spring and seawater end-members were assumed to be equivalent to those on the measurement of elemental concentrations in the samples.

Table 4.1. End-member and input-error values for the estimation of uncertainty in the three end-member, two-tracer mixing calculations used to ascertain the value of chemical residuals. All concentrations are in mol.L^{-1}.

	Na^+	K^+	Ca^{2+}	Mg^{2+}	Cl^-	SO_4^{2-}	HCO_3^-	Li^+
Rain[1] (*A1*)	1.40×10^{-5}	3.06×10^{-7}	3.08×10^{-7}	1.59×10^{-6}	1.64×10^{-5}	8.46×10^{-7}	6.98×10^{-8}	6.61×10^{-10}
σ Rain	1.78×10^{-7}	3.75×10^{-9}	3.57×10^{-9}	2.33×10^{-8}	2.07×10^{-7}	1.52×10^{-8}	3.49×10^{-9}	1.69×10^{-11}
Hot-spring[1,2] (*A2*)	2.22×10^{-2}	2.73×10^{-4}	3.92×10^{-4}	7.02×10^{-4}	3.49×10^{-3}	2.18×10^{-4}	1.49×10^{-2}	7.34×10^{-4}
σ/√n Hot-spring	2.72×10^{-3}	7.28×10^{-5}	1.32×10^{-4}	2.62×10^{-4}	1.12×10^{-3}	3.89×10^{-5}	1.82×10^{-3}	1.88×10^{-5}
Seawater[3] (*A3*)	4.68×10^{-1}	1.02×10^{-2}	1.03×10^{-2}	5.31×10^{-2}	5.46×10^{-1}	2.82×10^{-2}	2.33×10^{-3}	2.59×10^{-5}
σ Seawater	5.94×10^{-3}	1.25×10^{-4}	1.19×10^{-4}	7.78×10^{-4}	6.89×10^{-3}	5.08×10^{-4}	1.16×10^{-4}	6.65×10^{-7}

1. Data from Josh West (personal communication), comprising [Cl^-] and [Li^+] in rain and [Cl^-] in hot-springs. Concentrations of other solutes in rain are calculated (see text for discussion).
2. Hot-spring data ([Na^+], [K^+], [Ca^{2+}], [Mg^{2+}], [SO_4^{2-}] and [HCO_3^-]) from Song, Shen-Rong (personal communication).
3. Seawater data from Drever (1988).

For error estimates on the Sr^{2+}, SiO_2 and Ba^{2+} calculated concentrations in seawater – for which Equation 4.15 can not be used because there are no available concentration

values for these dissolved constituents in hot-spring water – the $\sigma_{[Na+]sw}$ as calculated using Equation 4.15, was used instead. The estimate of the concentration of sodium from seawater was the most sensitive to the error propagation out of all elements, and so using $\sigma_{[Na+]sw}$ should overestimate the uncertainty on Sr^{2+}, SiO_2 and Ba^{2+} derived from seawater.

4.6.4 End-members and their mixing in the Pingtung Plain

The results of three-end-member two tracer mixing (Equations 4.7 to 4.12) show that on average 99.52 % of the groundwater in the Pingtung Plain was meteoric in origin, 0.21 % was from hot-springs and 0.27 % was from seawater (Data Table G). The percentage of hot-spring water was positive in all samples, ranging between 0.04 and 0.61 %, with the highest values in middle-section deep well QX3 and in distal wells ZM1-4, shallow CL1 and shallow HY1 (Figure 4.15A). The percentage of seawater was positive in all samples except one well (HN2 had 0 % seawater), and was seen to increase along the groundwater flow path towards the coast, where in well KT2, it reached a maximum of 3.57 % (Figure 4.15B). Rainwater being relatively dilute, the average chemical input was small (Equation 4.13), amounting to < 1 % for Ca^{2+}, K^+, Sr^{2+}, Li^+, Ba^{2+}, Mg^{2+} and SiO_2, 1.9 % for Na^+ and 3.6 % for SO_4^{2-}.

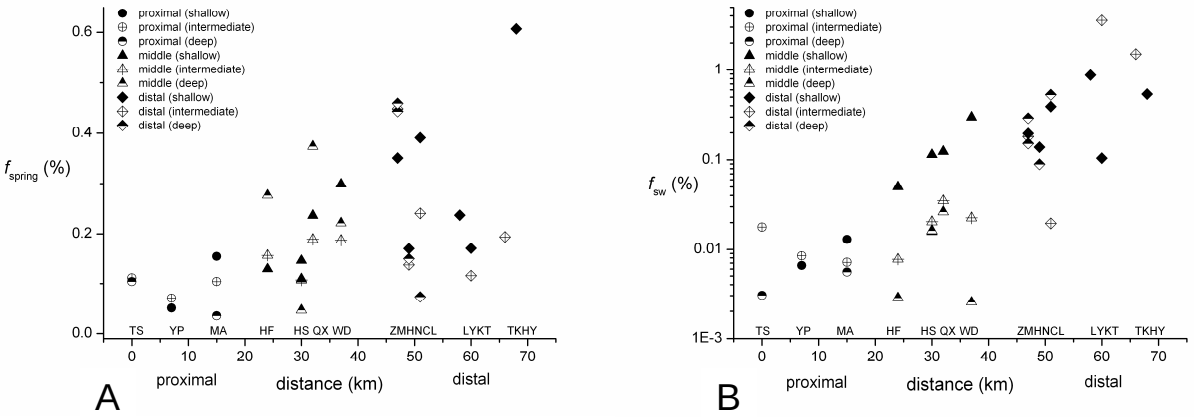

Figure 4.15. Fractions of hot-spring water (A), and seawater (B), in the Pingtung Plain groundwaters, calculated using ternary mixing proportions, as functions of distance along the subsurface flow path.

4.6.5 End-members and their mixing in the Choshui Plain

In the case of the Choshui Plain, the results of three-end-member two tracer mixing (Equations 4.7 to 4.12) show that on average 98.68 % of the groundwater was meteoric in origin, 0.46 % was from hot-springs and 0.86 % was from seawater (Data Table G). The percentage of hot-spring water was positive in all samples, ranging between 0.07 and 0.73 %, with the highest value in middle-section shallow well FR1. Excepting FR1, an overall decrease in the fraction of hot-spring water was seen along the groundwater flow path where it reached a relative minimum in the shallower well at station CP (Figure 4.16A). The percentage of seawater was positive in all samples excepting in one well (HL2 had 0 % seawater), and, excluding the well CP1, where it reached a maximum of 16.71 %, was relatively homogenous according to the spatial distribution of samples and the hydrological regime (Figure 4.16B). Rainwater being relatively dilute, the average chemical input was small (Equation 4.13), amounting to < 1 % for Ca^{2+}, Mg^{2+}, Na^{+}, K^{+}, Sr^{2+}, Li^{+}, Ba^{2+} and SiO_2 and 1.6 % for SO_4^{2-}.

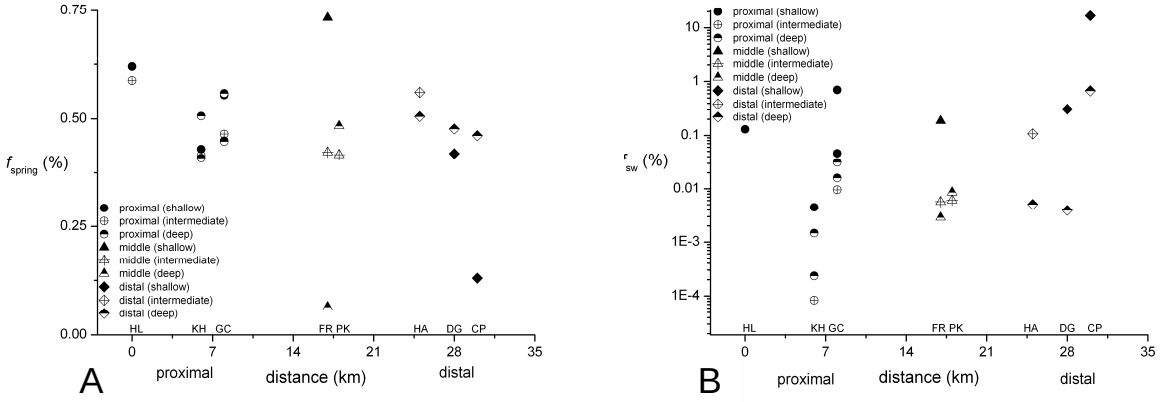

Figure 4.16. Fractions of hot-spring water (A), and seawater (B), in the Choshui Plain groundwaters, calculated using ternary mixing proportions, as functions of distance along the subsurface flow path.

4.7 Hydrothermal input

The chemistry of hot-spring water is related to the intensity of rock/water interaction in these geothermally-enhanced systems (Millot et al. 2010) and to the host mineralogy. These hydrothermally-sourced fluids migrate upward along faults and/or through permeable layers (e.g Gieskes et al. 1993). Song and Liu (2006) described the occurrence and chemistry of ~ 120 hot-springs in Taiwan, 21 of which develop along

tectonic structures in the Western Foothills zone and drain into the Pingtung Plain. The hot-springs draining into the Pingtung Plain display a range in dissolved Na^+ of 0.4 to 50.8 $mmol.L^{-1}$, and exhibit an average Na/Cl ratio of 6.36 (Song, Sheng-Rong, personal communication). Dissolved Cl^- ranged between 0.15 to 14.44 $mmol.L^{-1}$ (Song, Sheng-Rong, personal communication), the average of which (3.49 $mmol.L^{-1}$) was used to represent the hot-spring end-member here. The calculated percentage of hot-spring water varied significantly amongst the groundwater samples (Figures 4.15A and 4.16A) but, whilst it is probable that the chemistry of the hot-spring water also varied considerably, without samples and water flux estimates, a more precise representation of hot-spring chemistry is not possible.

4.8 Weathering and uplift history: evidence from the fraction of seawater input in the Pingtung Plain groundwater

Seawater intrusion in the Pingtung Plain has been described as occurring since pumping rates in the distal zone exceeded recharge rates in 1970 (Chiang and Wang 1998), which explains the high molarity of Cl^- in the near-coastal wells. The calculated groundwater flow rate in the distal zone was 23 $m.yr^{-1}$, which implies that reversals of hydraulic head of up to −42.57 m (minimum recorded hydraulic head at station TS) relative to sea level would have had to have occurred up to ~3043 years ago in order to explain the presence of seawater up to 70 km inland in the foothill wells.

Alternatively, about one third of the shortening across Taiwan is taken up on structures in the western foothills that extend southward to define the topographic boundaries of the Pintung Plain (Sella et al. 2002; Simoes et al. 2007). This shortening will drive significant, progressive uplift in the region surrounding the plain, which itself may still undergo subsidence. The uplifted sediments of the western foothills consist largely of coastal and shallow marine deposits, likely containing connate seawater. This water and laden chemistry may be flushed from uplifted sediments during modern weathering activity and enter the Pintung groundwater system. With conductivities much lower than those of the Pintung fill, it may take considerable time for this connate water to be drained, and it is likely that progressive uplift keeps elevating new water-rich rocks into positions where they can start to drain into the Pintung fill. Marine terrace uplift rates along Taiwan's eastern coastal range (Liew et al. 1993), and exhumation rates in the central

mountain range (Liu 1982) are ~ 5-7 $mm.yr^{-1}$, and are higher towards the southern regions of the island.

4.9 Chemical weathering in coastal plains

4.9.1 Weathering trends in the Pingtung Plain

Weathering yields in the Pingtung Plain groundwaters and in the Kaoping River are given by the concentrations of the residuals, $[X_i]_{residual}$ (Equation 4.14; Data Table G), which reflect the weathering processes within the aquifer sediments, and exhibit spatial trends along the groundwater flow path. The average estimated propagated uncertainties on the residual concentrations of Na^+, K^+, Ca^{2+}, Mg^{2+} and HCO_3^- ranged between 0.21 and 3.00 % for the groundwater samples, and between 0.35 and 2.11 % for the Kaoping River samples (Data Table G). The average uncertainty on $[SO_4^{2-}]_{residual}$ was −0.37 % for the groundwater samples and 0.55 % for the river samples. The negative uncertainty value for $[SO_4^{2-}]_{residual}$ is due to the significant formation of sulphate-bearing minerals in the distal zone.

As defined, the concentration of Li^+ in all groundwater samples could be explained by the mixing of rainwater, hot-spring water and seawater (Figure 14.17A). All of the proximal samples and several of the middle samples plot on a straight mixing line between rain and hot-spring end-members for chlorine and lithium (Figure 14.17A). The data points plotting off this line are clustered with and between samples from wells known to have experienced seawater reversals (KT1 and HY1) and are pulled towards the seawater end-member (opposing direction in three-end-member mixing space to positive residuals). Uptake of lithium via biological activity and/or clay adsorption/mineral formation are likely mechanisms, but if either were to occur to any significant degree, then those samples would skew towards the rain and seawater end-member mixing line, i.e. towards negative-residual space.

All groundwater samples showed positive residuals for Ca^{2+} and Mg^{2+} (Figure 4.17B, C), indicating that the weathering of carbonate mineral phases was a dominant process in the plain. All dissolved sodium residuals in the groundwater and river water is assumed to be derived from parent silicates, either directly by the dissolution of primary minerals, or secondarily via desorption from the surfaces of clays. Despite there being positive $[Na^+]_{residual}$ in all but two groundwater samples, seawater mixing was especially evident in the distal zone in all but two intermediate wells (CL2 where the $[Na^+]_{residual}$ was

2530±9 μmol.L^{-1} and HN2 where the $[Na^+]_{residual}$ was 848±4 μmol.L^{-1}) and in the middle section in all but three deep wells (WD3 where the $[Na^+]_{residual}$ was 1024±7 μmol.L^{-1}, QX3 where the $[Na^+]_{residual}$ was 1414±12 μmol.L^{-1} and HF3 where the $[Na^+]_{residual}$ was 650±8 μmol.L^{-1}) (Figure 4.17D).

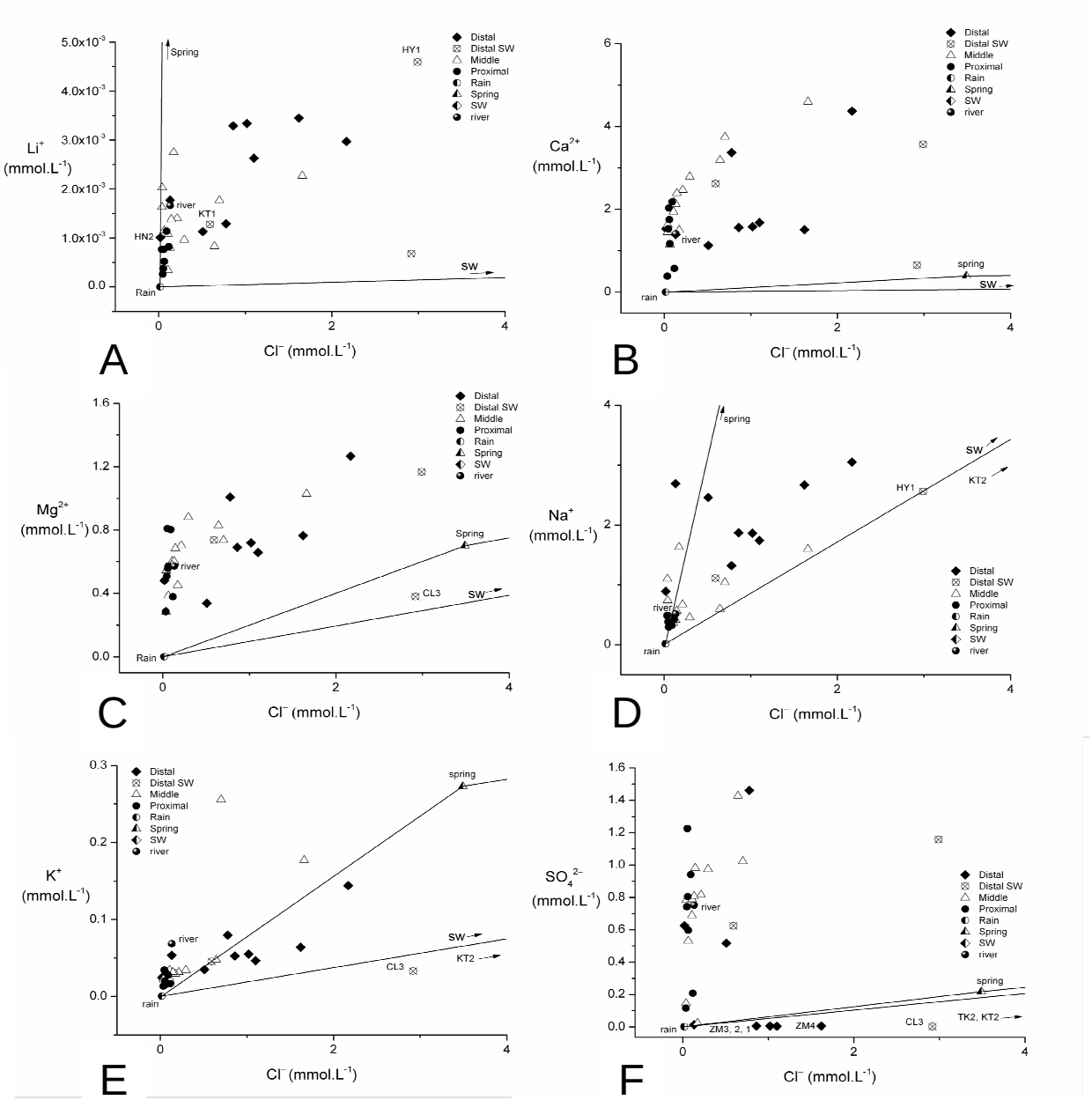

Figure 4.17. Ternary mixing plots showing conservative and non-conservative behaviour of Pingtung Plain groundwater and Kaoping River cations (A–E) and SO_4^{2-} (F). Crossed circles are near-coastal wells that experienced reversals of hydraulic head.

Likewise for $[K^+]_{residual}$ only distal samples plotted inside the mixing triangle (Figure 14.17E). With the exception of one well in the middle section, the river had, on average, higher $[K^+]_{residual}$ than the groundwaters, possibly reflecting that the source of

$[K^+]_{residual}$ in the river was easily mobilised material such as loose vegetation and top soil (Walling and Foster 1975). Given the high agricultural yields in the Pingtung Plain region, there is also the likelihood of there being local potassium-rich fertilizer sources infiltrating the surface water and groundwater systems.

Negative values of $[Na^+]_{residual}$, $[K^+]_{residual}$ and $[SO_4^{2-}]_{residual}$, indicate that 'reverse weathering', i.e. precipitation or adsorption of Na^+, K^+ and SO_4^{2-}, occurred in wells KT2 ($[Na^+]_{residual}$ = −9132±367 μmol.L^{-1}) and HY1 ($[Na^+]_{residual}$ = −122±59 μmol.L^{-1}) for Na^+ (Figure 4.17D), KT2 ($[K^+]_{residual}$ = −333±8 μmol.L^{-1}) and CL3 ($[K^+]_{residual}$ = −22±1 μmol.L^{-1}) for K^+ (Figure 4.17E), and KT2 ($[SO_4^{2-}]_{residual}$ = −300±29 μmol.L^{-1}), TK2 ($[SO_4^{2-}]_{residual}$ = −416±12 μmol.L^{-1}), CL3 ($[SO_4^{2-}]_{residual}$ = −148±4 μmol.L^{-1}) and ZM1-4 ($[SO_4^{2-}]_{residual}$ for ZM1 = −54±2 μmol.L^{-1}; ZM2 = −47±1 μmol.L^{-1}; ZM3 = −39±1 μmol.L^{-1}; ZM4 = −79±2 μmol.L^{-1}) for SO_4^{2-} (Figure 4.17F) (Data Table G). Clay formation is the likely mechanism of Na^+ and K^+ sequestration, as exchangeable ions, whereas the loss of SO_4^{2-} could imply bacterially-mediated sulphate reduction and the subsequent formation of pyrite.

4.9.2 Weathering trends in the Choshui Plain

Weathering trends in the Choshui Plain groundwaters and in the Choshui River are given by the concentrations of the residuals, $[X_i]_{residual}$ (Equation 4.14; Data Table G), which reflect the weathering processes within the aquifer sediments, and exhibit spatial trends along the groundwater flow path. The average estimated propagated uncertainties on the residual concentrations of Na^+, K^+, Ca^{2+}, Mg^{2+} and HCO_3^- ranged between 0.26 to 2.54 % for the groundwater samples, and between 0.18 to 1.64 % for the Choshui River samples (Data Table G). The average uncertainty on $[SO_4^{2-}]_{residual}$ was −1.72 % for the groundwater samples and 0.28 % for the river samples. The negative uncertainty value for $[SO_4^{2-}]_{residual}$ in the groundwater samples is due to the significant formation of sulphate-bearing minerals in the distal zone. The highest uncertainty estimated was for coastal well CP1 (Data Table G), which had an issue with its charge balance that may have been related to the precipitation of solids after collection (see Section 3.3.1, Chapter 3). Therefore, whilst its anion measurements are robust, the cation content is likely to be underestimated.

As defined, the concentration of Li^+ in all groundwater samples could be explained by the mixing of rainwater, hot-spring water and seawater (Figure 14.18A). All of the proximal wells excepting two, the shallow-most wells at stations GC and HL, plot on or

close to a binary mixing gradient between rain and hot-spring end-members for chlorine and lithium (Figure 14.18A), i.e. seawater is below detection in these samples.

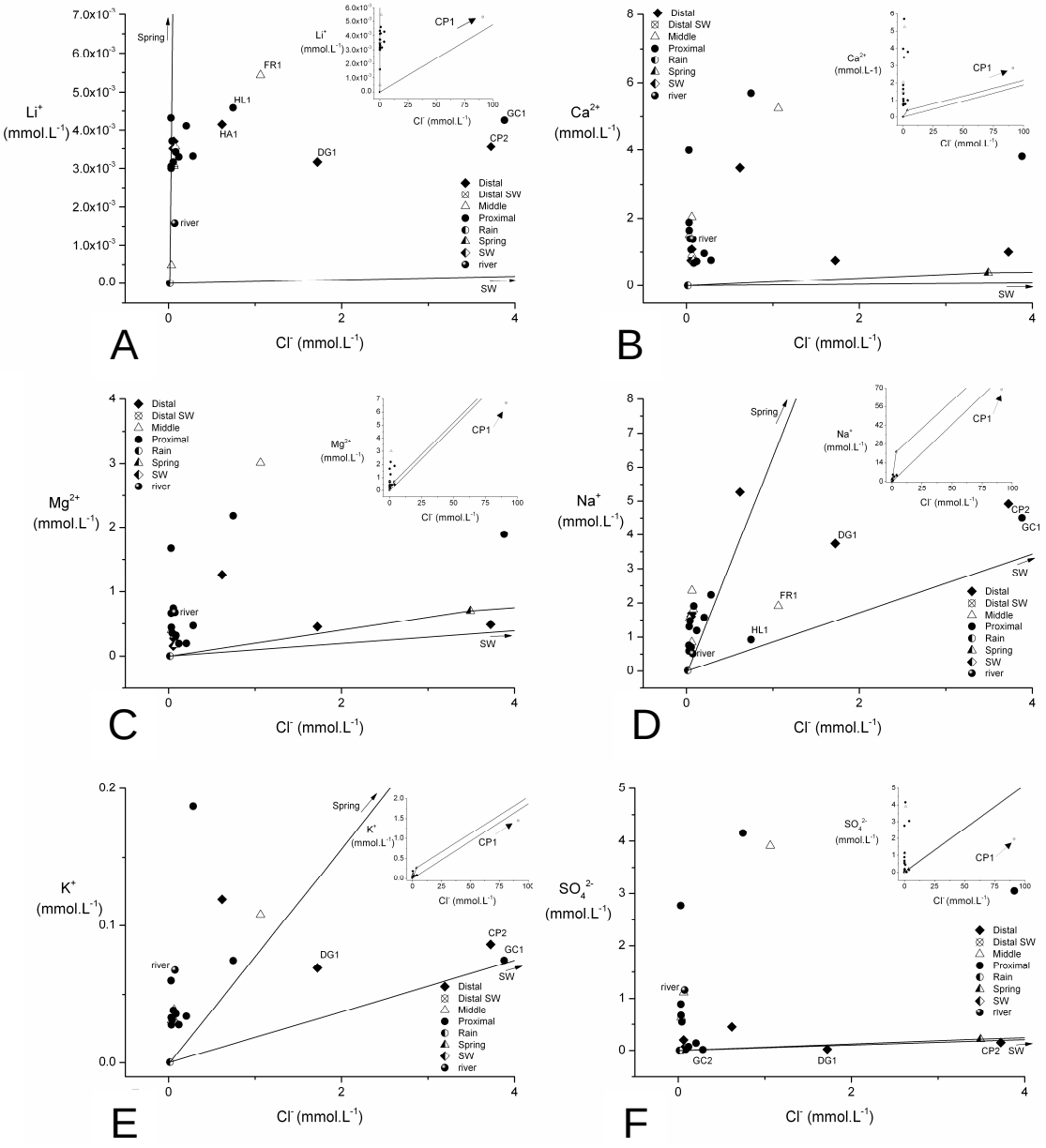

Figure 4.18. Ternary mixing plots showing conservative and non-conservative behaviour of Choshui Plain groundwater and Choshui River cations (A–E) and SO_4^{2-} (F). The insets show a greater extent of the mixing spaces than do the main graphs, to indicate where distal well CP1 plots.

Of all the wells, shallow proximal well GC1 had the highest relative fraction of seawater (0.70 %; $[Na^+]_{sw}$ = 3296±60 μmol.L^{-1}) after coastal well CP1 (Figure 14.18). Likewise shallow proximal well HL1 had a relatively high fraction of seawater (0.13 %;

$[Na^+]_{sw}$ = 607±12 μmol.L^{-1} (Figure 4.16B). All of the middle wells excepting shallow well FR1 plot on or about a binary mixing gradient between rain and hot-spring end-members for chlorine and lithium (Figure 14.18A). Middle shallow well FR1 had the highest relative fraction of hot-spring water (0.73 %; $[Na^+]_{spring}$ = 163±6) and had a relatively high seawater component (0.19 %; $[Na^+]_{sw}$ = 874±17), which explains its position in the mixing triangle (Figure 4.18A). In the distal zone, the two wells at station CP and the shallow wells at stations DG and HA, all with relatively high fractions of seawater (Figure 4.16B) were skewed towards the seawater end-member in chlorine and lithium mixing space (Figure 4.18A).

All groundwater samples showed positive residuals for Ca^{2+} and, with the exception of the two distal wells at coastal station CP, for Mg^{2+} (Figure 4.18B, C), indicating that despite there being evidence for secondary calcite formation (Section 4.4.8) the weathering of carbonate mineral phases was likely a dominant process in the plain. However, the highest Ca^{2+} concentrations occurred in proximal-most well HL1, which although situated several km from the mountain backdrop, may indicate that carbonate-derived inputs to the proximal region from the hillslopes are significant. Despite there being positive $[Na^+]_{residual}$ in all groundwater samples, there were significant seawater fractions evident in those groundwater samples positioned towards the seawater end-member in the ternary mixing plot (CP2 ($[Na^+]_{sw}$ = 3165±57 μmol.L^{-1}), GC1 ($[Na^+]_{sw}$ = 3296±60 μmol.L^{-1}), DG1 ($[Na^+]_{sw}$ = 1448±26 μmol.L^{-1}), FR1 ($[Na^+]_{sw}$ = 874±17 μmol.L^{-1}) and HL1 ($[Na^+]_{sw}$ = 607±12 μmol.L^{-1})) (Figure 4.18D). Likewise for potassium, all $[K^+]_{residual}$ values were positive with samples CP1, CP2 and GC1 plotting close to a binary mixing gradient between rain water and seawater end-members, and DG1 pulled towards the seawater domain (Figure 4.18E).

Negative values of $[SO_4^{2-}]_{residual}$ in proximal shallow well GC2 ($[SO_4^{2-}]$residual = −1.47±0.51 μmol.L^{-1}) and distal shallow and deep wells, DG1 ($[SO_4^{2-}]$residual = −67±3 μmol.L^{-1}) and CP2 ($[SO_4^{2-}]$residual = −40±5 μmol.L^{-1}), respectively (Figure 4.18F), indicate that the formation of sulphur-bearing minerals occurred in those portions of the aquifer. The loss of SO_4^{2-} could imply bacterially-mediated sulphate reduction and the subsequent formation of pyrite.

With the exception of two wells, proximal GC2 and distal HA1, the river had, on average, higher $[K^+]_{residual}$ than the groundwaters, and similar to what was observed in the Kaoping River, this possibly reflects that the source of $[K^+]_{residual}$ in the Choshui River was easily mobilised material such as loose vegetation and top soil or indeed, given the

agricultural activities in the Choshui Plain, there is also the likelihood of there being local potassium-rich fertilizer sources infiltrating the surface water and groundwater systems. In contrast to the Kaoping River, which had an average SO_4^{2-} concentration of 0.75 mmol.L^{-1}, the $[SO_4^{2-}]_{residual}$ in the Choshui River was 1.16 mmol.L^{-1}, and was only exceeded by those of the groundwaters in two proximal and one of the middle wells (Figure 4.18F).

4.9.3 Lithological controls on coastal plain groundwaters: carbonate versus silicate sources

There have been numerous studies done to estimate the proportion of carbonate to silicate-derived dissolved mass in natural waters (Garrels and Mackenzie 1967; Négrel et al. 1993; Gaillardet et al. 1999; Galy et al. 1999; Krishnaswami et al. 1999; Quade et al. 2003; Bickle et al. 2005). Dissolved major cation ratios normalised to Na are likely to indicate the variable proportions of silicate and carbonate dissolution. However, this use of cation ratios can be thwarted by the incongruent dissolution of parent silicates and carbonates, which is particularly likely in regions characterised by high erosion rates and weathering-limited regimes (such as Taiwan) (Stallard 1995). Especially important in such catchments is the precipitation of secondary carbonates (e.g Galy et al. 1999; English et al. 2000; Jacobsen et al. 2002; Bickle et al. 2005), which, if prevalent, will give rise to overestimations of the proportion of dissolved mass derived from silicate rock. Notwithstanding, using this approach can yield insight into the relative variation of silicate and carbonate dissolution along groundwater flow paths.

In $Mg_{residual}/Na_{residual}$-$Ca_{residual}/Na_{residual}$ (Mg^*/Na^*-Ca^*/Na^*) mixing space the Pingtung Plain groundwater and Kaoping River samples lie on a binary mixing array, the slope of which reflects the apparent Mg/Ca ratio of the carbonate end-member (Négrel et al. 1993), if there is no secondary calcite precipitation (Bickle et al. 2005). Increased silicate weathering (lower Ca^*/Na^* ratios) can be seen along the groundwater flow path towards the coast in the Pingtung Plain, with most of the distal samples plotting closes to the silicate end-member (Négrel et al. 1993; Gaillardet et al. 1999) (Figure 4.19) (see Section 4.10 for discussion). The inset in Figure 4.19 shows how two wells in the middle section of the Pingtung Plain, WD1 and HS1, contain a strong carbonate signature whereas distal well HY1 plots in negative mixing space due the uptake of Na^+.

In the case of the Choshui Plain groundwaters, 14 of the 21 wells with positive residuals (CP1 omitted from interpretation) plot close to the silicate end-member, with increasing silicate-derived content seen according to distance along the groundwater flow path (Figure 4.20, inset).

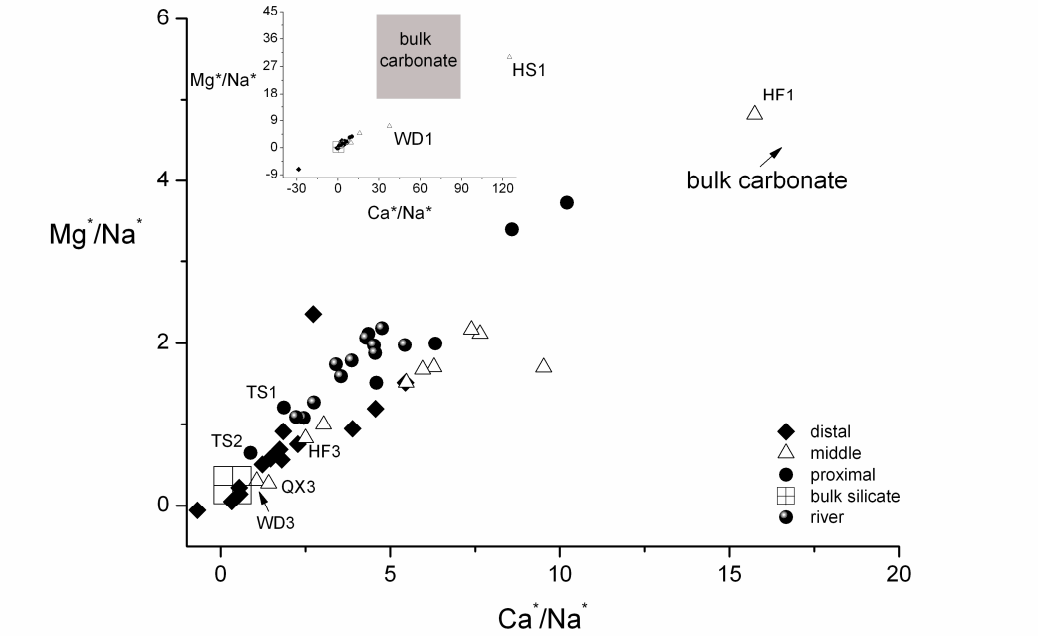

Figure 4.19. Mg^*/Na^*–Ca^*/Na^* mixing space using Na-normalised molar ratios of residual chemistry. The Pingtung Plain groundwater and Kaoping River water samples lie on a binary mixing array between silicate and carbonate end-members.

Proximal-most shallow well, HL1, plots closest to the carbonate end-member, with deeper HL2 also relatively carbonate-rich (Figure 4.20). In contrast, the intermediate and deep proximal wells at stations GC and deep wells at proximal station KH plot close to the silicate end-member, indicating both the loss of Ca^{2+} and the dissolution of Na^+-bearing phases in the deeper horizons (Figure 4.20, inset). All distal wells in the Choshui Plain plot close to the silicate end-member according to a groundwater flow regime increasing in carbonate formation and silicate dissolution with increased residence time (Figure 4.20, inset).

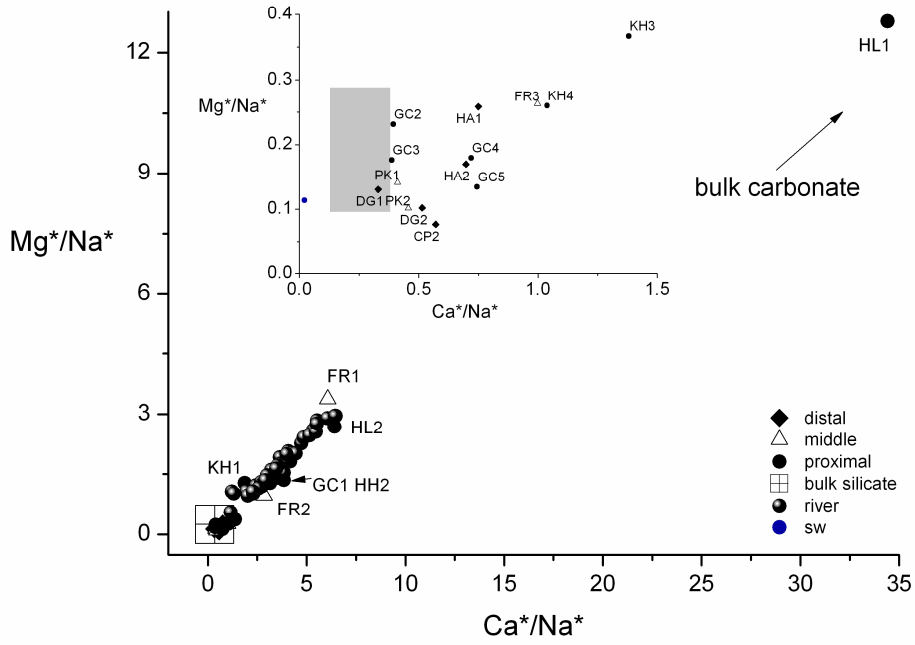

Figure 4.20. Mg^*/Na^*–Ca^*/Na^* mixing space using Na-normalised molar ratios of residual chemistry. The Choshui Plain groundwater and Choshui River water samples lie on a binary mixing array between silicate and carbonate end-members.

4.9.4 Carbonic versus sulphuric acid driving weathering reactions

As will be discussed in Chapter 6, knowing the type of acid involved in the breakdown of silicate and carbonate minerals has implications for assessing the impact of weathering reactions on the carbon, oxygen and sulphur cycles. The indiscriminate dissolution of silicate and carbonate minerals by varying proportions of carbonic acid derived from biological activity in the soil (−27 ‰ $\delta^{13}C_{DIC}$ for Taiwan (Hilton et al. 2010), which, after applying a +4.4 ‰ shift to distinguish between soil CO_2 and soil-respired CO_2 (Cerling et al. 1991), gives a dissolved inorganic carbon ($\delta^{13}C_{DIC}$) composition of −22.6 ‰) and sulphuric acid (which in weathering carbonate would give rise to resulting $\delta^{13}C_{DIC}$ of the carbonate end-member: −1.67± 0.18 ‰ (2σ, n = 4); see Table 6.1, Chapter 6) can be described by the covariations of X_{SO4} ($2 \times SO_4^{2-}/(2 \times SO_4^{2-}) + HCO_3^-$) and $\delta^{13}C_{DIC}$ (Galy and France-Lanord 1999).

The Pingtung and Choshui Plain groundwaters were characterised by shifting proportions of dissolved silicate and carbonate rock altered by varying mixtures of soil-respired carbonic acid and sulphuric acid (Figures 4.21 and 4.22). In the case of the Pingtung Plain, an overall shift from the predominantly higher degree of sulphuric-acid driven dissolution of carbonates in the proximal region to the principally soil-respired-

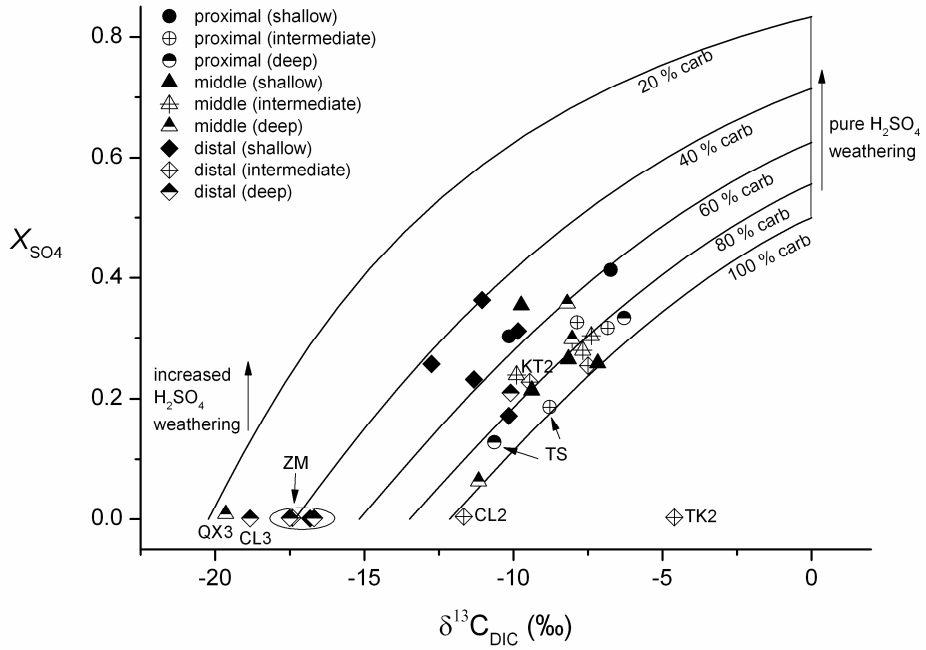

Figure 4.21. Isotopic composition of dissolved inorganic carbon ($\delta^{13}C_{DIC}$) versus the ratio of equivalent $SO_4^{2-}/(SO_4^{2-} + HCO_3^-)$ (X_{SO4}) for Pintung Plain groundwaters. The curves describe variable water mixtures of dissolved carbonate and silicate parent material, indiscriminately altered by various proportions of soil-respired carbonic acid and sulphuric acid.

carbonic-acid driven weathering of silicates in the distal zone was observed (Figure 4.21). An exception to this general trend were the foothill wells at station TS, which appear to have been exemplified by mainly carbonate weathering by carbonic acid, unlike the other proximal wells at stations YP and MA that were typified by higher relative proportions of sulphuric-acid driven dissolved carbonate (Figure 4.21).

Six of the seven wells in the Pingtung Plain (ZM1-4, CL3 and TK2) that had negative $[SO_4^{2-}]_{residual}$ (expecting well KT2 which had the highest relative fraction of seawater at 3.5 %) and an additional well from the deep horizon of the middle section (QX3) had depleted X_{SO4} values due to their low sulphur concentrations (Figure 4.21). Five of these X_{SO4}-depleted wells, from the deep horizons of the middle section and from all depths at distal well station ZM (indicated to be clay rich by relatively low measurements of hydraulic conductivity (2-38 $\mu m.s^{-1}$)) were characterised by high relative proportions of dissolved silicate mineralogy derived from the weathering action of soil-respired carbonic acid (Figure 4.21), whereas distal wells CL2 and TK2 were typified by predominantly

carbonate mineralogy altered by a heavier source of $\delta^{13}C_{DIC}$ than can be explained by soil-respired carbonic acid alone.

In the Choshui Plain, an overall shift from the predominantly higher degree of sulphuric-acid driven dissolution of silicates and carbonates in the proximal region to the principally soil-respired-carbonic-acid driven weathering of carbonates in the distal zone was observed (Figure 4.22). Three shallow and one intermediate proximal and middle wells (GC1, HL1, HL2 and FR1), with the highest dissolved SO_4^{2-} concentrations (2768–4151 µmol.L^{-1}) (Data Table F) and characterised by a higher relative degree of sulphuric acid-driven weathering, are distinguished from the deeper proximal wells at stations GC and KH, which have lower concentrations of SO_4^{2-} (72-675 µmol.L^{-1}) and are typified by biologically-mediated carbonic acid-driven weathering (Figure 4.22).

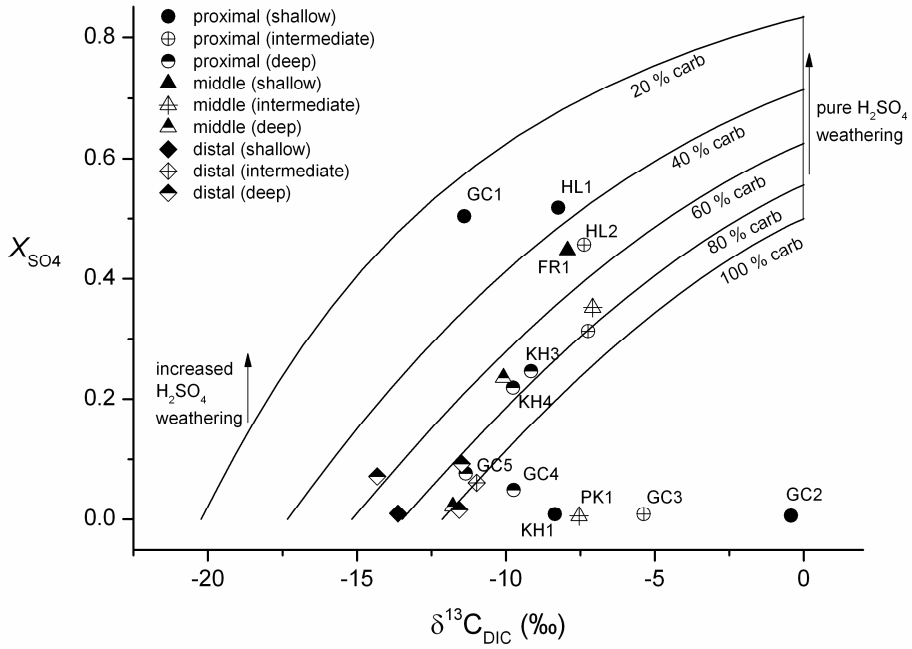

Figure 4.22. Isotopic composition of dissolved inorganic carbon ($\delta^{13}C_{DIC}$) versus the ratio of equivalent $SO_4^{2-}/(SO_4^{2-} + HCO_3^-)$ (X_{SO4}) for Choshui Plain groundwaters. The curves describe variable water mixtures of dissolved carbonate and silicate parent material, indiscriminately altered by various proportions of soil-respired carbonic acid and sulphuric acid.

Similar to in the Pingtung Plain, a shift towards heavier $\delta^{13}C_{DIC}$ values is seen in several of the wells with depleted SO_4^{2-} concentrations in the Choshui Plain (Figure 4.22).

It is possible that this shift towards relatively heavy $\delta^{13}C_{DIC}$ values in the absence of a SO_4^{2-} source for sulphuric acid (which in weathering carbonate would result in $\delta^{13}C_{DIC}$ close to −1.67 ‰) reflects the input from hydrothermally-sourced waters, which due to the production of CO_2 gas following dry CO_2 formation by metamorphic decarbonation at depth (Shieh and Taylor 1969; Friedman and O'Neil 1977) and subsequent dissolution of this gas in groundwaters (Mook et al. 1974), can display positive $\delta^{13}C_{DIC}$ values up to 16 ‰ enriched relative to the original rock. Additionally, the light $\delta^{13}C_{DIC}$ values characterising a cluster of the middle and distal wells in the Pingtung Plain (Figure 4.21) could be additionally influenced by a light pool of $\delta^{13}C_{DIC}$ resulting from the breakdown of organic matter by microbially-mediated reduction of SO_4^{2-}. As will be discussed in Chapter 6, the sulphur isotopic composition of aqueous sulphate can be used to fingerprint and quantify the magnitude of bacterially-mediated sulphate reduction.

4.10 Hydrological connectivity between bedrock and alluvial-fill domains: evidence from the Pingtung Plain aquifer system and implications for subsurface groundwater fluxes

Given its close proximity to the mountains, well station TS in the Pingtung Plain offered an insight into the hydrological transition between the bedrock and alluvial-fill domains. The samples from these wells, which plot close to the silicate end-member (Figure 4.19), were from intermediate TS1 and deep TS2, which were the highest of all the wells sampled, sitting in the foothills of the central mountain range. Their relatively silicate-rich chemistry reflected a different flow path to the groundwater collected from the other wells within the proximal region. These two proximal wells were also more evolved towards the silicate end-member than down-gradient wells in the middle section of the plain, with the exception of the deepest wells at stations QX, WD and HF (Figure 4.19). The distinctive chemistry of the two TS wells, given their proximity to the bedrock backdrop, implies that whilst some of the groundwater in the drilled depth of the Pingtung Plain comes from bedrock aquifers, another volume is rather derived from surface water infiltration within the plain.

It is possible that the two wells at proximal station TS could have been anomalous for some reason, such as contamination, and that as a result of some such cause they did not actually record the chemical character of the bedrock groundwater in the locality. However, the study of Calmels et al. (2011) showed that at least three water masses, each

with particularly distinct weathering signatures that reflected unique hydrological conditions, could explain the chemical variability of a six-year bi-weekly record of river chemistry in the elevated Liwu River catchment in the northeast region of Taiwan. Of especial significance was that one of these water masses, termed 'deep-groundwater', was of a meteoric source that had infiltrated the subsurface of the fractured bedrock, and that despite contributing to just 16 % of the 37-year river discharge, it accounted for >30 % of the silicate weathering flux. Given that the groundwater in fractured bedrock in the Liwu River catchment has been demonstrated to have a strong silicate signature, it is likely that other elevated catchments in Taiwan, such as the Kaoping River catchment feeding the Pingtung Plain, have similarly high silicate-derived compositions. Therefore, the chemistries of proximal wells TS1 and TS1 are more likely to have reflected the weathering signature of the deep fractured subsurface than they are to have been contaminated or otherwise unrepresentative. Of further significance, and as will be investigated more closely in Chapter 6, the Calmels et al. (2011) study shows that silicate weathering reactions in the deep fractured subsurface of Taiwan's bedrock appear to exert a major control on chemical fluxes from the orogen.

The Pingtung Plain is effectively a sedimentary basin, trapping relatively un-weathered material supplied from the bordering mountain areas. The similarity in the chemistry of the TS wells with those in the distal zone (Figure 4.19) either implies that isolated connectivity of groundwater flow paths existed between the two sets, or that they were hydrologically distinct, and that accumulative weathering along the groundwater flow path in the plain, of the same parent material as that in the bedrock system, resulted in the same dissolved product at the local terminus of each route.

Stable isotopes of water, $\delta^{18}O$ and δD, provide an additional constraint on the nature of groundwater flow paths from individual sources. Whilst the TS wells are distinct from the other proximal wells in $\delta^{18}O$-δD mixing space (Figure 4.4), plotting close to distal wells at stations ZM, some distal wells, e.g. TK2 and KT2, are shown to have similar stable isotope chemistry to the proximal wells MA and YP, ruling out an obvious direct path from station TS to the distal zone. Furthermore, chemical evolution along the groundwater path was observed for Ca/Na (Figure 4.5B).

This observation that there might be a terminus to solutes en route from the mountains at the transition between the bedrock and alluvial-fill domains suggests that the latter act as physical buffers initially impeding the chemical contribution potentially available for discharge to the ocean from the terrestrial subsurface. However, given the

observation of increased silicate dissolution with distance along the groundwater flow path, sufficient length scales across sedimentary basins may enable the progressive enrichment of silicate-derived solutes through alluvial fill deposits, and which may even enhance the significance of the subsurface silicate chemical weathering fluxes to the ocean in such regions.

4.11 Concluding remarks

Below is a summary of the findings presented in this chapter.

The groundwaters in the Pingtung and Choshui Plain alluvial-fill basins generally evolve along the groundwater flow paths from carbonate-rich chemistry in the proximal regions to silicate-dominated compositions in the distal zones. The processes involved are carbonate and silicate dissolution, calcite formation and clay uptake and desorption.

The groundwater chemistry in both plains is derived from four distinct sources. The first is rainwater, which provides a relatively insignificant proportion of dissolved solids, but which supplies the bulk of the water volume that falls directly onto the plain and that runs off the surrounding foothills. A second, chemically-distinct water source runs off and/or through the surrounding mountain bedrock and it has been shown that some of this latter supply intercepts water of an evolved chemical composition that has been hydrothermally sourced (e.g. hot-spring water). A third source of dissolved chemistry in the plains can be attributed to seawater, which in the case of the Pingtung Plain, is detectable in systematically increasing quantities from 70 km inland to the coast, where up to 3.5 % of the groundwater is shown to be derived from seawater. The uplift and exhumation of connate seawater-bearing sediments in the Western Foothills could explain the presence of seawater up to 70 km inland.

Ternary mixing calculations using the conservative tracer chlorine and the quasi-conservative tracer lithium, which give the fractions of the groundwaters derived from rain, hot-springs and seawater, indicate that a fourth source of dissolved chemistry is derived from the dissolution of minerals within the sediments of the alluvial fills and from the surrounding hillslopes. Mineral formation involving Na^+, K^+ and SO_4^{2-} is observed in localised regions of the aquifers, but most samples record increases in silicate-derived components (Na^+ and SiO_2) and a decrease in Ca^{2+}, reflecting positive chemical weathering of silicates and precipitation of secondary calcite along the groundwater flow paths.

The chemistry of the groundwaters in both plains arises from variable mixtures of silicate and carbonate source rocks that are largely altered by differing proportions of biologically-mediated carbonic acid and sulphuric acid. A general evolution from sulphuric acid-driven weathering of carbonates in the proximal regions to carbonic acid-driven dissolution of silicate minerals in the distal zones was observed. Two potential additional sources of dissolved inorganic carbon are an isotopically-depleted bacterially-mediated pool and a metamorphically-produced enriched pool.

It is suggested that relatively short distances between topographic highs and the coast, as exhibited by small mountain islands, maximise the hydraulic head gradients that drive large groundwater chemical fluxes to the ocean. In comparison to case study localities featuring this phenomenon, where groundwater discharge rates to the ocean are sometimes in excess of surface water fluxes, the Pingtung Plain in southwest Taiwan, despite having high permeabilities and being hydrologically connected to the surrounding steeply-elevated fractured bedrock where precipitation is typically in excess of three metres per year, acts initially as a physical buffer to the delivery of chemical weathering fluxes to the ocean. However, chemical evolution along the groundwater flow path in the Pingtung Plain suggests that with sufficient length scales, alluvial-fill deposits may be sources of significant dissolved subsurface chemical fluxes to the ocean.

Chapter 5

Chemical fluxes through Taiwan's coastal plains

5.1 Summary

This chapter presents calculated estimates of potential groundwater chemical fluxes to the ocean from two semi-confined sandy aquifers, the Pingtung and Choshui coastal plains in southwest and west Taiwan, respectively, and, for comparison, from the major river catchment in each setting. The potential subsurface fluxes are assessed relative to the estimates of local riverine chemical budgets with the objective of understanding the significance of groundwater in delivering solutes to the ocean in the context of total continental weathering. The methodologies used to constrain the hydraulic properties of the aquifers that govern groundwater flow are presented together with an evaluation of the errors involved in the chemical flux calculations. A summary of the main observations is given in the following section.

5.2 Aims, outline of methodology and summary of main findings

There are four principal aims of this chapter. Firstly, to compute robust estimates of subsurface major chemical fluxes that are available for ocean input through the drilled portions of the two major alluvial-fill aquifers in Taiwan. Only the proportion of these chemical fluxes attributable to relatively recent rock-water interactions will be considered so as to understand the contribution of this groundwater to the regional chemical weathering budget. To do this a compilation was made of measured hydraulic heads and conductivities from 43 wells in the Pingtung Plain in conjunction with published and measured details of the physical parameters governing groundwater flow in the Choshui Plain (Wang et al. 2005; Lin et al 2004). The outcomes of the compilation of the physical parameters governing groundwater flow in these aquifers were combined with the results of the major chemical analyses and the source-water mixing evaluations presented in Chapter 4, to calculate subsurface chemical fluxes. These chemical fluxes were specifically from shallow and deep chemical-weathering, that is, from low-temperature rock-water interactions within the aquifer sediments and the surrounding hillslopes

(chemical residuals), and from geothermal sources (hot-springs), and did not include solutes derived directly from rainwater or seawater (ancient or modern).

Secondly, to assess the relative significance of the subsurface chemical fluxes along the southwestern and western margins of Taiwan in the context of total chemical weathering fluxes, the two groundwater systems were compared to surface runoff across the two catchments. The Kaoping River, which flows across the Pingtung Plain and is the largest source of surface runoff to the ocean in the southwestern region, was compared to the subsurface chemical fluxes in the Pingtung Plain. For this purpose, a chemical time series gathered from analysis of 11 river water samples, collected during the period between March and August 2005, was combined with the 10-year average Kaoping River discharge value to represent a regional, long-term estimate of the riverine chemical fluxes. In the Choshui Plain, the Choshui River carries the largest surface runoff and was thus taken as a reference to assess the contribution of subsurface-delivered dissolved mass to the ocean along the studied portion of Taiwan's western margin (i.e. the southern portion of the Choshui Plain). For this purpose, a bi-weekly time series consisting of 41 river water samples collected during the period between March 2005 and December 2006 was combined with contemporaneous measurements of river discharge.

Thirdly, the potential ranges of subsurface chemical fluxes through these aquifers were assessed. In the case of the Pingtung Plain, published estimates of groundwater recharge, which were based on various water balance approaches and related offshore groundwater discharge measurements, (of which some are inferred to be associated with features exhibiting relatively large hydraulic conductivities that were bypassed during terrestrial sampling, such as bordering fault planes), were combined with the measurements of groundwater chemistry made as part of this study. For the Choshui Plain, detailed river discharge-concentration relationships were used to assess the range in seasonal variations of surface chemical fluxes. For the case of dissolved Na^+ in the Choshui River water samples, which exhibited a good anti-correlation with river discharge, it was possible to calculate comparatively precise estimates of regional riverine chemical fluxes over a range of discharges, and thus the seasonal variability of the Na^+ flux from the Choshui River was used to assess the relative significance of potential subsurface Na^+ fluxes to the ocean during different seasons.

Finally, efforts were made to consider the importance of these relative subsurface chemical fluxes in the contexts of other published regional and global estimates of the fresh fraction of submarine groundwater discharge, known in the literature as SFGD, that

is the fraction of submarine groundwater discharge (SGD) with a meteoric source, where SGD is defined as any and all flow of combined fresh and saline water on continental margins from the seabed to the coastal ocean, regardless of fluid composition or driving force (Burnett et al. 2003).

In the context of Taiwan, this chapter therefore demonstrates:

1. How, in computing groundwater chemical fluxes through the coastal plains, hydraulic conductivity measurements present the greatest source of uncertainty, but that good knowledge of the other parameters governing groundwater flow, combined with robust chemical analyses, can, notwithstanding, enable chemical fluxes to be calculated to within ± 24 % (1σ).
2. That subsurface chemical fluxes corrected for seawater through the Pingtung and Choshui coastal plains are generally small to modest in comparison to related estimates of solute delivery to the ocean by large rivers (1 % to 12 % for different elements).
3. How, depending on the chosen method for estimating groundwater discharge rates, chemical flux estimates vary significantly. Compared to offshore methods and to water balance approaches for quantifying fresh groundwater discharge, the combined use of direct measurements of hydraulic conductivities, gradients and groundwater chemistry provides relatively conservative estimates of subsurface chemical fluxes, with this study giving smaller values than all but one other terrestrial-based study.
4. That in comparing the long-term-average groundwater Na^+ flux of the Choshui Plain to that of the Choshui River, it can be shown that during periods of low surface runoff (winter) the relative seawater-corrected subsurface Na^+ flux is greatly enhanced (63 %).
5. How that in locations of high fresh water discharge offshore, such as deeply outcropping fault planes, subsurface chemical input to the ocean from the continent could be significant, but that sampling in these depths is challenging.
6. That the western and southwestern margins of the metasedimentary island of Taiwan, consisting of coastal plains fringing high-mountain topography, yields similar rates of shoreline-normalised groundwater flow to the ocean as analogous global estimates of submarine fresh groundwater discharge.

5.3 Background and motivation

Taiwan exhibits some of the highest values of physical erosion rates, over a variety of timescales, worldwide (Dadson et al. 2003). The link between physical erosion and chemical weathering discussed in Chapter 1 suggests that the solute fluxes permeating through the sedimentary basins that fringe the foothills of Taiwan's high mountain ranges will be at least to some degree positively related to the extensive exposure of fresh mineral surfaces that occur through rock-mass shattering and landsliding. The chemical effect of groundwater percolation through these wedges was demonstrated in Chapter 4, where it was shown that the sedimentary basins act initially as chemical buffers to the solutes that infiltrate the coastal plains from the fractured rock mass of the mountains, but that given sufficient groundwater residence times, these alluvial wedges promote the chemical breakdown of the accumulated debris from the hillslopes. A major question concerns the magnitude and composition of groundwater fluxes delivered through these alluvial-fill deposits available for direct input to the ocean, and the depth range over which these fluxes occur.

Calmels et al. (2011) estimated that 40 % of the silicate weathering flux carried by the Liwu River, east Taiwan, was derived from meteoric water that had circulated at depth within surrounding bedrock. In Chapter 4 it was shown that the potential importance of groundwater in modulating weathering fluxes is not restricted to bedrock environments and, furthermore, subsurface flow pathways to the ocean may bypass the surface drainage network entirely (Moore and Shaw 1998). In many places worldwide an alluvial wedge separates the bedrock and marine domains, where in the case of Taiwan (and elsewhere) there are widely distributed high porosities (e.g. Basu et al. 2001) facilitating high water fluxes and rendering large areas of reactive mineral surface areas available. In coastal regions groundwater may discharge directly to the oceans and this deeper groundwater, which can be enriched in certain elements by several orders of magnitude relative to surface waters, is a largely unknown contributor to global dissolved weathering fluxes (Zektzer et al. 1973).

It has been claimed that subsurface dissolved chemical fluxes can rival those of surface runoff in coastal regions (e.g. Li et al. 1999). However, there being a paucity of studies on subsurface delivery of dissolved mass to the ocean relative to published local, regional and global estimates of riverine chemical fluxes, and there being uncertainties and disagreement as to the fluxes of groundwater, it is currently difficult to measure the importance of groundwater processes within global geochemical cycles. Furthermore, to

assess the significance of groundwater as a chemical weathering agent, quantitative estimates of weathering fluxes from a variety of subsurface environments are needed.

The natural force in coastal aquifers driving net discharge of groundwater to the oceans is the positive hydraulic gradient between high-ground in the hinterland and the shoreline (Johannes 1980; Simmons 1992), modulated by the pumping action of the tides (Riedhl et al. 1972) and seasonal oscillations (Holly et al., 2005). As fresh water fluxes through the subsurface increase with increasing hydraulic head, the freshwater/seawater interface moves seaward (Sanford and Konikow 1989a,b) resulting in freshwater discharge far offshore (Essaid 1990a,b). Humid regions with high mountain topography near the coastline, such as tropical and sub-tropical ocean islands like Taiwan, are particularly prone to this effect (Burnett et al. 2003). In comparison to the well-studied subsurface chemical fluxes through volcanic island arcs, for example, where high weathering rates in basaltic and andesitic lithologies promote rapid groundwater infiltration (Hahn et al. 1997) and subsequent chemical discharges to the ocean sometimes in excess of surface runoff (Church 1996; Kim et al. 2003; Rad et al. 2007; Schopka and Derry 2012), the metasedimentary island of Taiwan offers an opportunity to measure subsurface weathering fluxes to the ocean from an analogous mountain-island setting that differs in lithology and in terms of its drainage patterns.

A network of well-established rivers route water, sediment and solutes from the mountain ranges in Taiwan in contrast to the poorly developed drainage paths in many of the well-studied volcanic ocean islands. Additionally, Mulligan et al. (2007), using combined numerical simulation modelling and marine geophysical data, showed that submarine freshwater discharge off the coast of North Carolina is promoted by the focusing of subsurface flow through *palaeochannels*, which breach permeable sediments in confining aquifer units and therefore act as conduits for the exchange of groundwater with seawater. Of especial importance is that the surface drainage systems on Taiwan have been delivering sediment to the coastal plains and ocean throughout the Neogene and thus relict fluvial channels, or *palaeochannels*, in high-stand intervals terminate within extensive deep canyons offshore of Taiwan (see Figure 2.1, Chapter 2).

There are difficulties with extending offshore observations of groundwater discharge due to poor accessibility and with distinguishing the freshwater component in seawater-dominated samples. It is therefore useful to have counterpart studies onshore where the direct sampling of groundwater through a range of depths is relatively straightforward.

5.4 Evaluation of the parameters governing groundwater flow

The values of the physical parameters used in calculating the chemical fluxes through the Pingtung and Choshui coastal plains are presented in Table 5.1, where δh is the change in hydraulic head across the drilled depths of the basins, δl is the length of the groundwater flow path and k is the hydraulic conductivity. The approach taken in determining the relevant quantities of these physical parameters is discussed in the following subsections.

Table 5.1. Summary of the physical parameters used in calculating subsurface chemical fluxes. Section 5.5.2 presents a discussion of the uncertainties in these parameters.

Region	δh (m)	δl (m)	$\delta h/\delta l$	width (m)	depth (m)	Area (m^2)	k ($m.s^{-1}$)
Pingtung	52.62	38500	1.37×10^{-3}	35561	237	8427957	5.06×10^{-4}
Plain	±0.14	±0		±0	±0	±0	$\pm 1.09 \times 10^{-4}$
Choshui	40.74	25716	1.58×10^{-3}	32875	294	9665250	4.16×10^{-4}
Plain	±0.00	±0		±0	±0	±0	$\pm 1.43 \times 10^{-4}$

5.4.1 Hydraulic head time series in the Pingtung Plain

A daily hydraulic head time series covering the period November 1998 to May 2003 (WRA data) was used to understand the direction and slope of groundwater flow in the Pintung Plain. The previous subdivisions of the plain into a coarse-grade gravel-rich 'proximal region' a medium-grade sand-rich 'middle section' and a fine-grade 'distal zone' with sands, silts and intercalated clays (Ting et al. 1988a) corresponded to a decreasing hydraulic head gradient (averaged at each of the 14 stations), broadly contouring the topographic slope along a southwest groundwater flow path (Figure 5.1A-C). Due to its proximity to the coast, the distal zone was considered to be the optimum portion of the aquifer to best represent the potential chemical flux to the ocean. And thus, the seven coastal and near-coastal stations (HN, CL, ZM, HY, KT, TK and LY), comprising 23 wells, were chosen to define the distal zone (Figure 5.1C), through which the chemical fluxes were estimated.

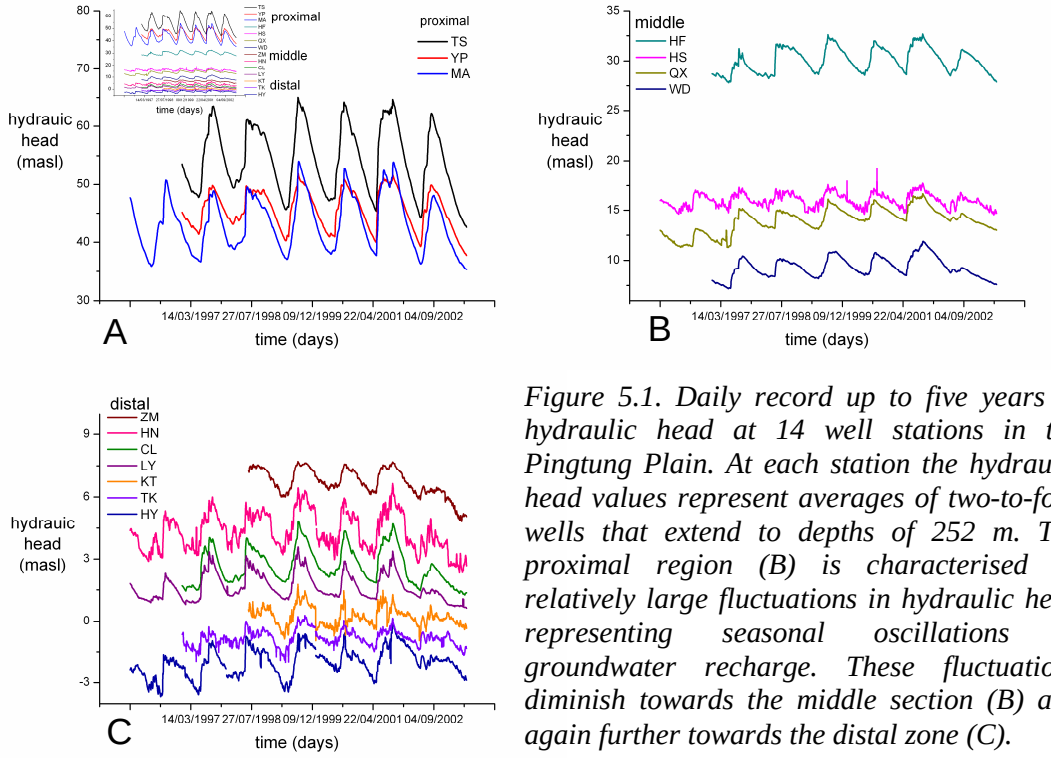

Figure 5.1. Daily record up to five years of hydraulic head at 14 well stations in the Pingtung Plain. At each station the hydraulic head values represent averages of two-to-four wells that extend to depths of 252 m. The proximal region (B) is characterised by relatively large fluctuations in hydraulic head representing seasonal oscillations of groundwater recharge. These fluctuations diminish towards the middle section (B) and again further towards the distal zone (C).

In contrast to previous descriptions of the hydraulic properties of the Pingtung Plain in which only the uppermost horizon (~ 60 m) was described as being fully unconfined (Wang et al. 2003), analysis of the hydraulic head time series here showed that significant hydrological connectivity across the sampling depth (237 m) between each of the wells at a given station was observed (Figure 5.2A-N). In the proximal region, all of the wells at each station (TS1&2, YP1&2 and MA1-3) showed significant connectivity (deduced by their exhibiting very similar hydraulic head time-series responses) (Figure 5.2A-C). In the middle section, hydraulic heads increased with depth at station HS (Figure 5.2E) indicating the presence of a localised confining unit. Higher hydraulic heads at middle well HF2 also shows that there are confining portions of the plain in the middle section (Figure 5.2D). In the distal zone, where chemical fluxes are calculated, all of wells except at station LY displayed significant hydraulic connectivity (Figure 5.2H-N). The two deeper wells at station LY (LY2&3) exhibited isolation from the shallow-most (LY1) demonstrating the presence of a discrete confining unit giving rise to higher hydraulic pressures in this location (Figure 5.2K). Notwithstanding there being indication of discrete partial connectivity, the scatter in hydraulic head differences with depth in the distal zone was slight: at ZM, the average daily hydraulic head difference between each of the four wells comprising the station was 0.27 ± 0.19 m (2σ, n = 1786); the average daily hydraulic

head differences for the other distal stations were, HN = 1.45 ± 1.67 m (2σ, n = 2716); CL = 0.35 ± 0.46 m (2σ, n = 2340); TK = 2.02 ± 0.65 m (2σ, n = 2285); KT = 1.49 ± 0.94 m (2σ, n = 1788); HY = 0.98 ± 1.25 m (2σ, n = 2313); LY = 1.10 ± 0.42 m (2σ, n = 2758).

Detailed investigation of the hydraulic head time series shows that the average hydraulic head fluctuation over all the sampled stations was ± 6.97 m, with summer highs and winter lows and has remained relatively stable over the five-year time period of daily records (Figure 5.1A-inset). Most proximal to the foothills at stations TS, YP and MA, average hydraulic head ranged from 54.28 m to 43.26 m (Figure 5.1A), decreasing to between an average high of 30.06 m and an average low of 9.32 m in the four wells (HF, QX, HS and WD) comprising the middle section of the plain (Figure 5.1B), and culminating in the distal zone where the range in average hydraulic head was from −2.01 m at station HY to 6.71 m at station ZM (Figure 5.1C).

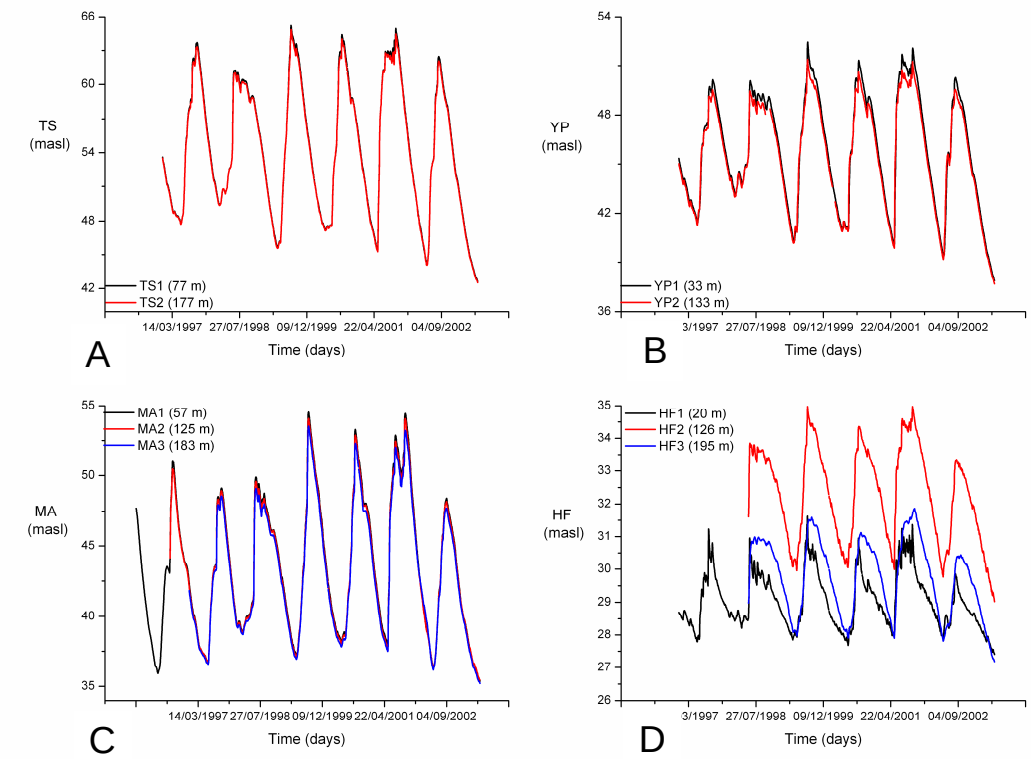

Figure 5.2. Detailed daily record up to five years of 43 individual wells, comprising 14 stations, in the Pingtung Plain. Most wells at a given station experience significant hydrological connectivity. The values in parentheses represent the average screen depth below the surface for the given well.

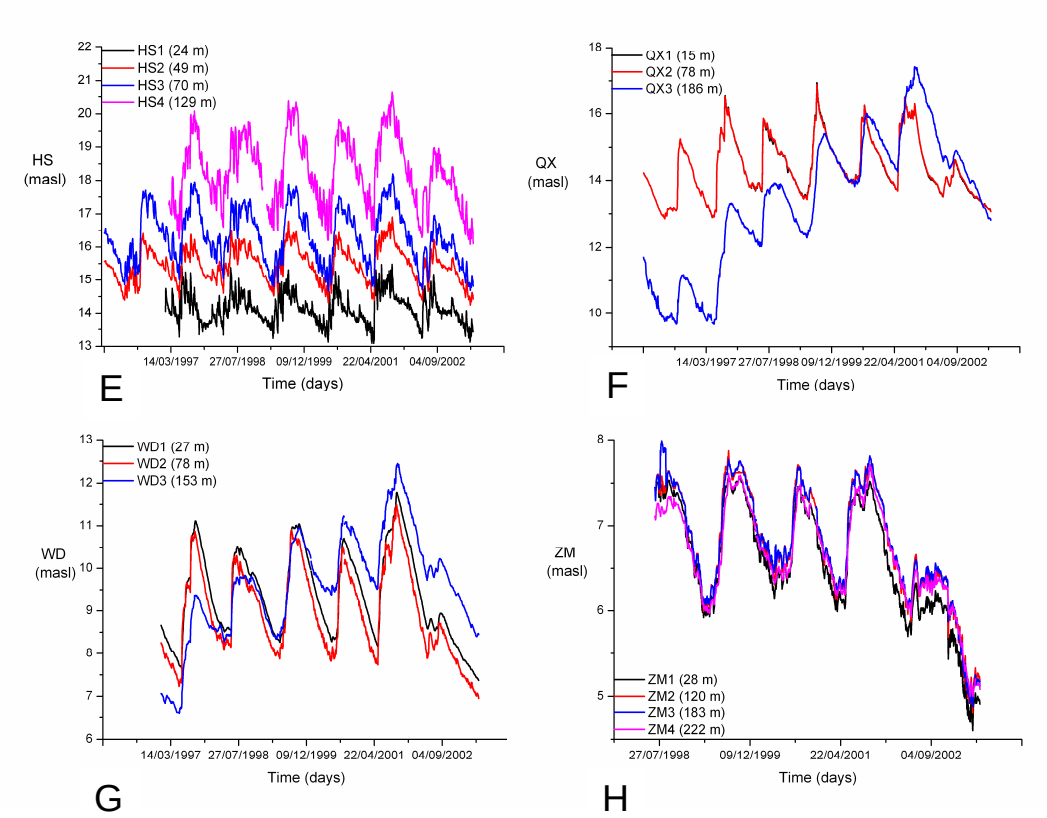

Figure 5.2 continued

5.4.2 Reversal of hydraulic head in the Pingtung Plain

The hydraulic head time series was used to investigate the magnitude of hydraulic head reversal responsible for the seawater intrusion into the coastal Pingtung Plain groundwaters as discussed in Chapter 4. The purpose of doing so was to constrain an hydraulic gradient that accounted for intermittent head reversals. Hydraulic head reversals were indicated by the episodic negative gradients, relative to the long-term background levels, observed between the wells comprising the distal zone. The three wells at coastal station LY, two of which, LY2 and LY3 had chlorine concentrations in excess of 266 mM (Data Table F), had periodically higher hydraulic head values than all wells at near-coastal CL (Figure 5.3A-C) facilitating seawater and groundwater mixing.

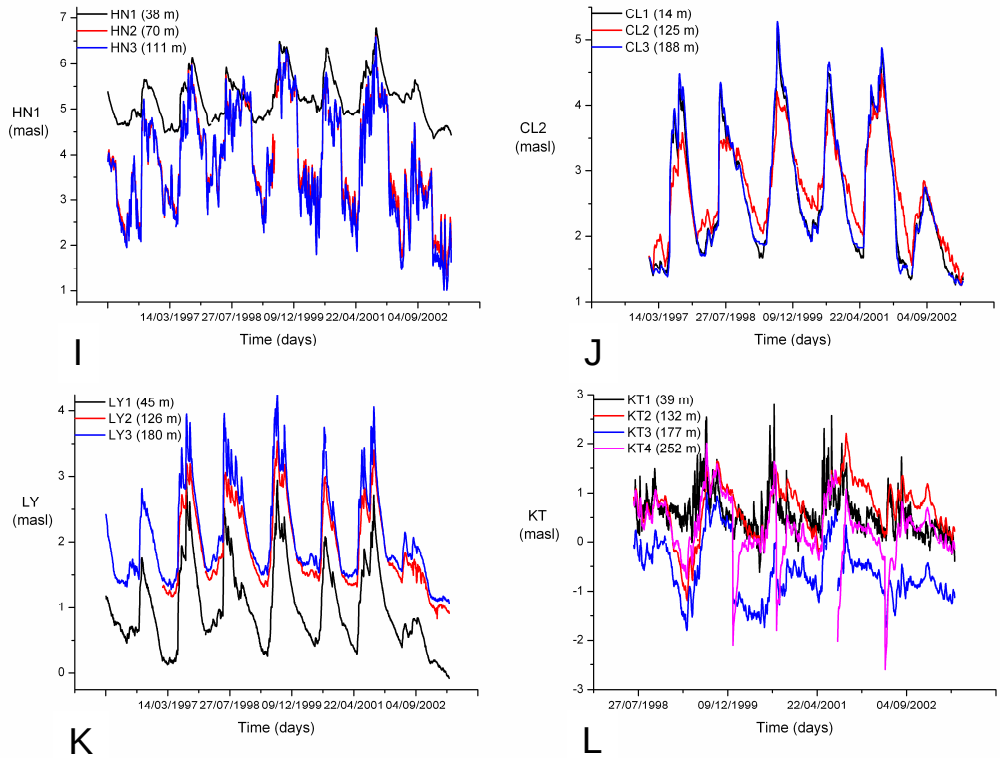

Figure 5.2 continued

Shallow well CL1 experienced six discrete periods of hydraulic head reversal lasting between 3 and 74 days; five with respect to LY3, where the difference in hydraulic head ranged between −0.33 m and −0.01 m and one with respect to LY2, where the difference in hydraulic head ranged between −0.22 m and −0.01 m (Figure 5.3A). Middle-depth well CL2 experienced five discrete episodes of hydraulic head reversal; four with respect to LY3 lasting between three and 126 days, where the difference in hydraulic head ranged between −0.24 m and −0.01 m, and one with respect to LY2 lasting 60 days (coinciding with the period of 126 days of hydraulic head reversal between CL2 and LY3), with a range in hydraulic head difference of −0.10 m to −0.01 m (Figure 5.3B). Deep well CL3 underwent six discrete phases of hydraulic head reversal, all with respect to LY3, lasting between five and 41 days and had a range in magnitude of −0.59 m to −0.01 m (Figure 5.3C).

Wells at station LY were supplied with seawater from down-gradient wells at stations KT, where chlorine concentrations in the two deepest wells exceeded 405 mM (Data Table F) and, to a lesser degree from station TK, where the concentration of chlorine in three of the wells (all except TK2) was greater than 216 mM (Data Table F; Figures 5.4A-C and 5.5). The magnitude of the hydraulic head reversals into the wells at station LY ranged from between −0.12 m (from KT2 into LY2) (Figure 5.4B) and −1.48 m (from KT1 into LY1) (Figure 5.4A).

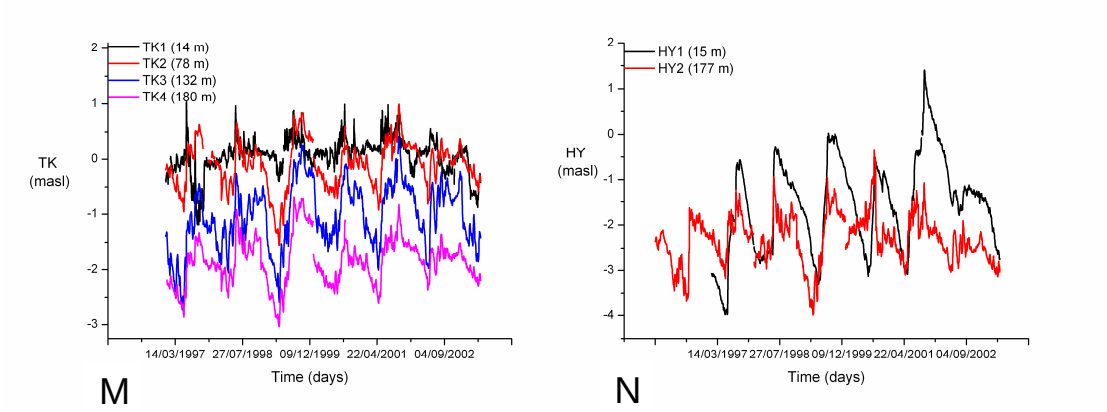

Figure 5.2 continued

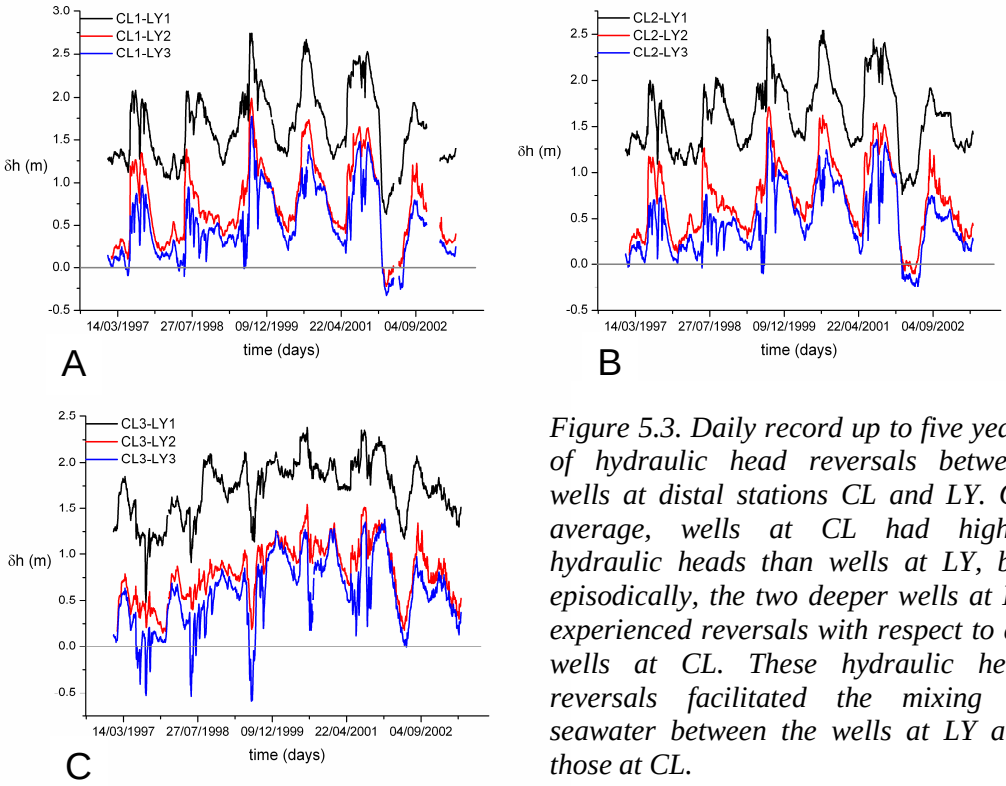

Figure 5.3. Daily record up to five years of hydraulic head reversals between wells at distal stations CL and LY. On average, wells at CL had higher hydraulic heads than wells at LY, but episodically, the two deeper wells at LY experienced reversals with respect to all wells at CL. These hydraulic head reversals facilitated the mixing of seawater between the wells at LY and those at CL.

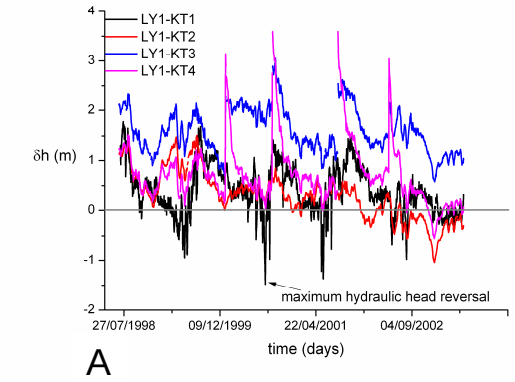

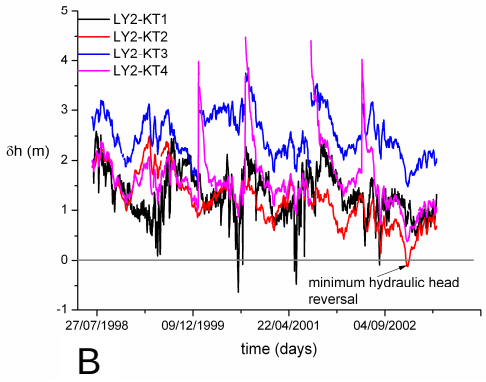

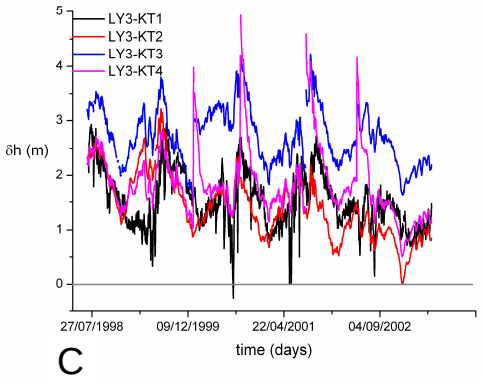

Figure 5.4. Daily record up to five years of hydraulic head reversals between wells at distal stations LY and KT. On average, wells at LY had higher hydraulic heads than wells at KT, but episodically, all wells at KT except KT3 experienced significant reversal with respect to the shallow-most well at LY (A), and the two shallow-most wells at KT experienced reversals into the two deeper wells at LY (B and C).

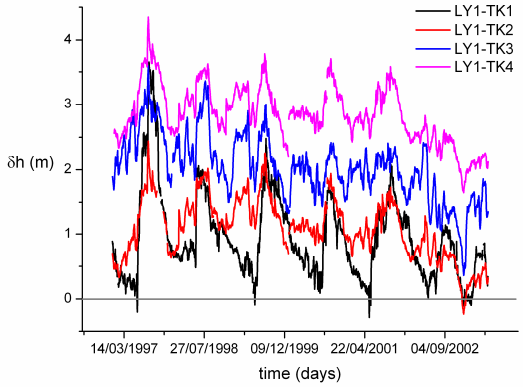

Figure 5.5. Daily record up to five years of hydraulic head reversals between the shallow-most well at distal station LY and wells at station TK. On average, the wells at LY had higher hydraulic heads than all wells at TK, but episodically, the shallow-most well at TK, and to a lesser degree TK2, experienced reversals with respect to LY1.

In turn, wells at station KT were supplied with seawater from down-gradient wells at stations TK (Figure 5.6A-D) and at HY, where the concentration of chlorine was greater than 480 mM in HY2 (Data Table F; Figure 5.7A-C). All four wells at coastal station TK had persistently higher hydraulic head values than the deepest well at near-coastal station KT (Figure 5.6D), whereas only the shallow-most well at station HY displayed hydraulic

head reversal with respect to station KT (Figure 5.7A-C). The magnitude of hydraulic head reversal into the wells at station KT ranged from between −0.34 m (from TK2 into KT1) (Figure 5.6A) to −2.79 (from TK1 into KT4) (Figure 5.6D).

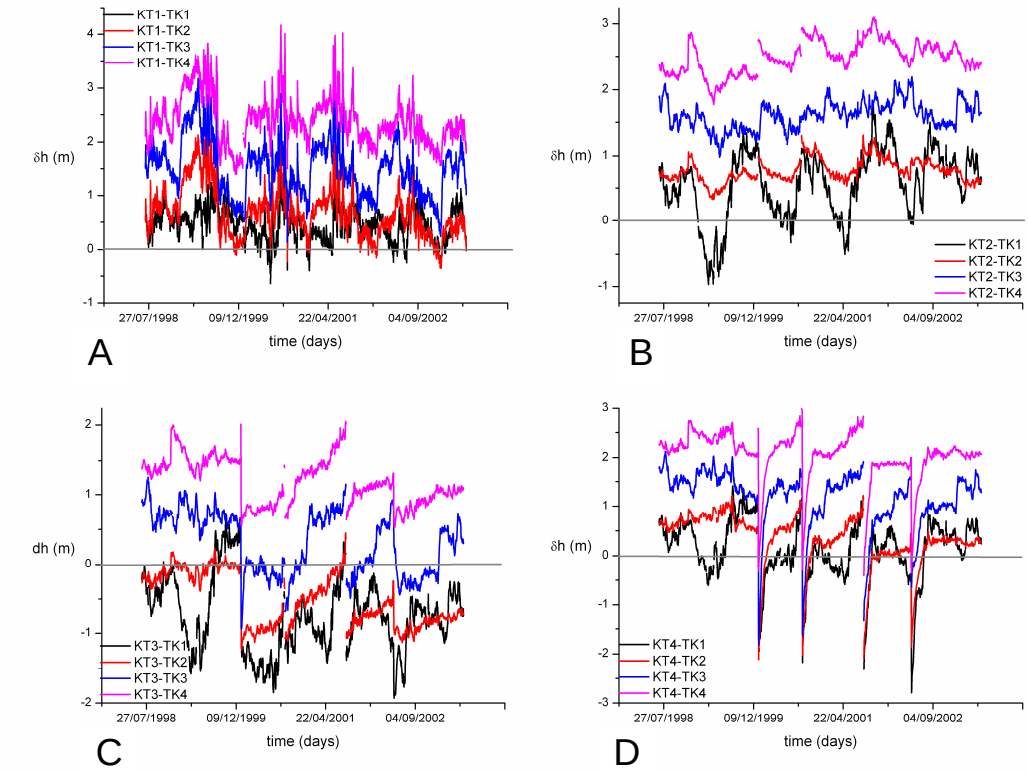

Figure 5.6. Daily record up to five years of hydraulic head reversals between wells at distal stations KT and TK. On average, wells at KT had higher hydraulic heads than wells at TK, but episodically, the shallow-most well at TK experienced reversals with respect to all wells at KT, TK2 experienced reversals with respect to all wells at KT other than KT2, TK3 experienced reversals into KT3 and KT4 and TK4 experienced reversals into KT4.

Supplying wells at station TK with seawater were down-gradient wells at station HY (Figure 5.8A-D) where the magnitude in hydraulic head reversal ranged from −0.5 m (from HY1 into TK2) (Figure 5.8B) to −2.38 m (from HY1 into TK4) (Figure 5.8D).

Unlike at station LY, where the greatest reversals in hydraulic head occurred in the deepest wells, hydraulic head reversals from HY, TK and KT into up-gradient reaches of the alluvial fill were observed to be greatest out of the most shallow wells at each of these stations, likely indicating that withdrawal from the near-surface aquifer in the distal zone for agricultural purposes was the most significant cause of groundwater depletion in the region, exceeding the rate of groundwater recharge during several episodes encompassed by the hydraulic head time series.

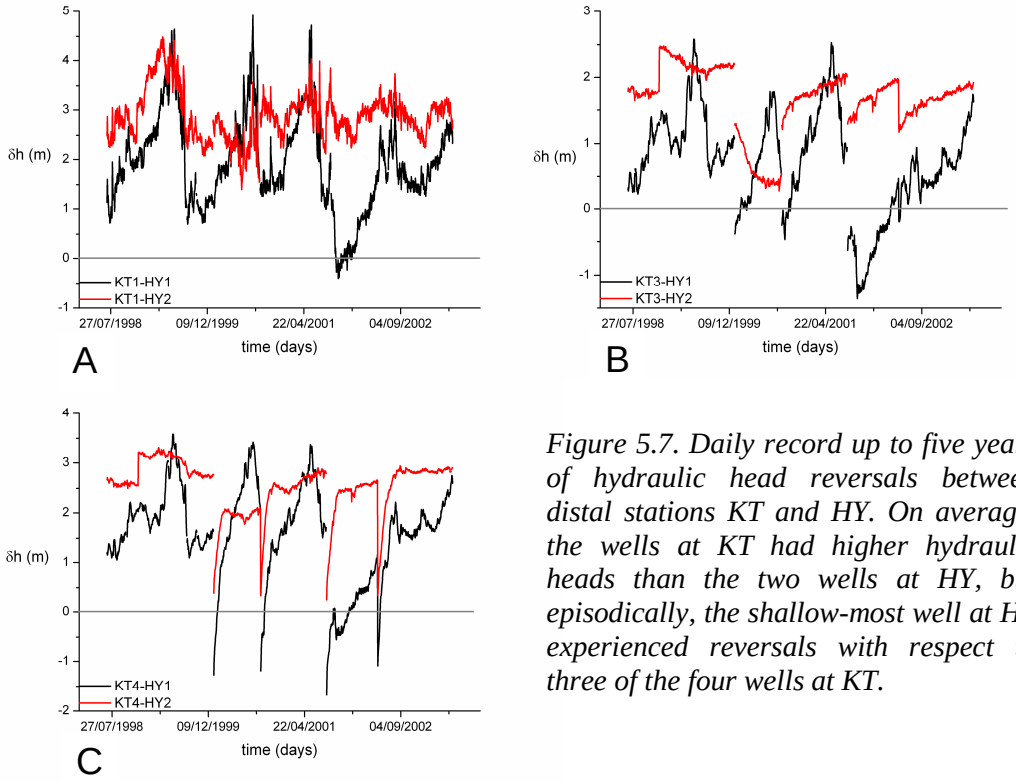

Figure 5.7. Daily record up to five years of hydraulic head reversals between distal stations KT and HY. On average, the wells at KT had higher hydraulic heads than the two wells at HY, but episodically, the shallow-most well at HY experienced reversals with respect to three of the four wells at KT.

5.4.3 Defining the hydraulic gradient in Pingtung Plain

The chemical fluxes through the distal zone of the Pingtung Plain were calculated by combining the groundwater chemistry and permeabilities (see Section 5.4.4) from 15 of the coastal and near-coastal wells with the average hydraulic gradient across the plain, calculated as the difference between the average hydraulic head at proximal station TS and an adjusted average hydraulic head at distal station HY1 (Table 5.1). The adjustment of the hydraulic head at station HY1 involved subtracting its negative hydraulic head values from zero, to ensure that the hydraulic gradient used for chemical flux calculations accounted for the loss of hydraulic driving force due to the seawater intrusion. Furthermore, the mixing model developed in Chapter 4 to distinguish seawater from solutes derived from rock-water interactions was thus used to ensure that only solutes resulting from rock-water interactions were incorporated into the chemical flux calculations.

The physical and chemical properties of the eight coastal wells with concentrations of chlorine approaching that of bulk seawater (Data Table F) were not considered in estimating the fluxes. It is the case that the omitted wells from stations TK and LY, in particular, are closer to the coastline than most other distal stations, and therefore if included in the source-water and chemical-flux calculations, might offer a more accurate

representation of groundwater weathering fluxes to the ocean than the fluxes based on the well sub-selection. However, that that would be gained regarding further insight into the magnitude and nature of the groundwater chemical fluxes discharging to the ocean would be lost due to propagated uncertainty when calculating the groundwater proportion in these seawater infiltrated samples.

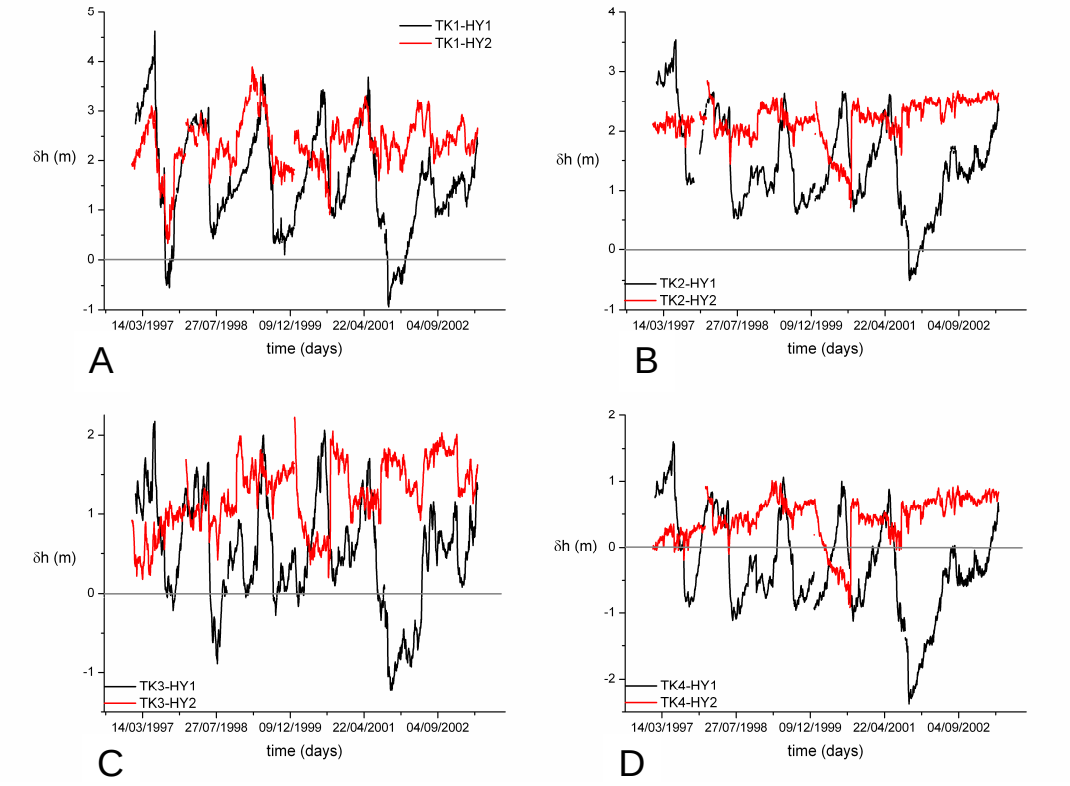

Figure 5.8. Daily record up to five years of hydraulic head reversals between wells at distal stations TK and HY. On average, wells at TK had higher hydraulic heads than wells at HY, but episodically, the shallow-most well at HY experienced significant reversals with respect to all wells at TK, and the deeper well at HY experienced reversal with respect to the deepest well at TK (D).

The average hydraulic head difference between stations TS and HY1 was 55.76±0.11 m (1σ, n = 1795), which, when divided across the distance between the two (38,500 m), gave an hydraulic gradient of 1.45×10^{-3}. After subtracting the magnitudes of the negative hydraulic heads at station HY1 from zero, the hydraulic head difference between stations TS and HY was reduced to 52.62±0.14 m (1σ, n = 1795), giving an adjusted hydraulic gradient for the plain of 1.37×10^{-3}.

5.4.4 Hydraulic conductivity in the Pingtung Plain

In a similar manner to the diminishing hydraulic head fluctuations seen along the groundwater flow path of the Pingtung Plain, the range in hydraulic conductivity (*k*) (WRA data) in the 43 sampled wells across the Pingtung Plain broadly corresponded to the subdivisions from coarse to fine grained moving towards the coast (Figure 5.9A; Data Table A). The hydraulic conductivities spanned over four orders of magnitude, ranging from 1.79 × 10^{-6} m.s^{-1} to 2.68 × 10^{-3} m.s^{-1} and with a mean value of 5.65 × 10^{-4} m.s^{-1} (Figure 5.9B) and exhibited a general decrease from the topographically highest station, TS, to the distal zone (Figure 5.9A), where the average hydraulic conductivity, which was used for chemical flux calculations (see Section 5.5), was 5.06 × 10^{-4} m.s^{-1} (Figure 5.10; Table 5.1). Superimposed on this decreasing gradient was a localised average high of 1.10 × 10^{-3} m.s^{-1} at distal station CL (Figure 5.9A).

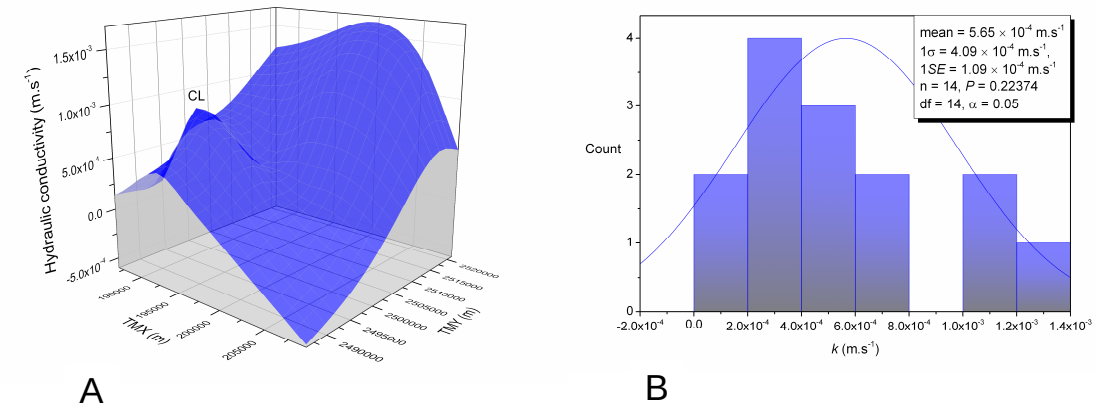

Figure 5.9. Hydraulic conductivity surface for the sampled portion of the Pingtung Plain (A) and probability distribution of hydraulic conductivities for the 14 wells representing the distal zone (B).

The results of a Shapiro-Wilk test (Shapiro and Wilk 1965) show that distribution of the hydraulic conductivity values in the subset of seven stations comprising the 15 wells used for chemical flux calculations in the distal zone was consistent with a normal distribution (P = 0.96, df = 7, α = 0.05, where P is the probability of obtaining a normal distribution at 95 % confidence (α = 0.05) and n − 1 degrees of freedom (df), i.e. at P > 0.05, the distribution is likely normal) (Figure 5.10). The rationale for averaging the distal zone hydraulic conductivities was based on there being significant hydrological connectivity across the sampling depth (237 m) between each of the wells at a given station, as shown in the previous sections by the hydraulic head time series. The true flow

field will have a range of fluxes due to variations in hydraulic conductivity, but the aim is to estimate the average flux. Therefore, the cumulative flux for flow along a set of channels of differing permeability but with equal driving heads being equal to the sum of the conductivities times the driving pressure gradient, the average hydraulic conductivity is just the arithmetic mean (and the uncertainty in hydraulic conductivity is the standard error on this mean) (see Section 5.5.2).

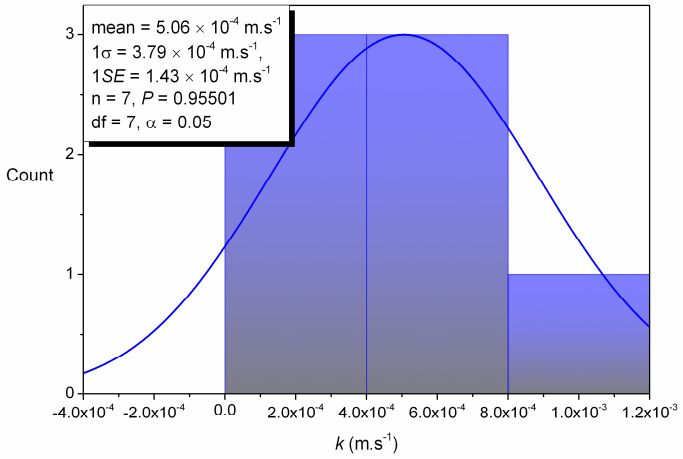

Figure 5.10. Probability distribution for the average hydraulic conductivity value at each of the seven stations comprising the 14 wells in the distal zone of the Pingtung Plain, illustrating normality of the population.

When analysed against well-screen depth, hydraulic conductivity displayed a poor negative correlation (Figure 5.11), suggesting that the sediments comprising the drilled depth of the Pingtung Plain basin are largely unconsolidated, supporting the hydraulic connectivity demonstrated by the hydraulic head time series.

5.4.5 Defining the hydraulic gradient in the Choshui Plain

The chemical fluxes through the Choshui Plain were calculated by combining the groundwater chemistry and permeabilities (see Section 5.4.5) from 21 coastal and near-coastal wells with the estimated hydraulic gradient across the length of the sampling transects. The total set of wells comprising the proximal, middle and distal sections of the aquifer were chosen for water and chemical flux estimates in the case of the Choshui Plain because of the relative proximity of the combined region to the coast (see Figure 2.8,

Chapter 2). The static water levels in each of the 21 wells used for the chemical flux estimates (Data Table A), which were measured in November 2008 at the time of sampling, were subtracted from the well stations' elevations giving a discrete snapshot of the hydraulic head difference between proximal-most station HL and coastal stations DG and CP (Figure 5.12).

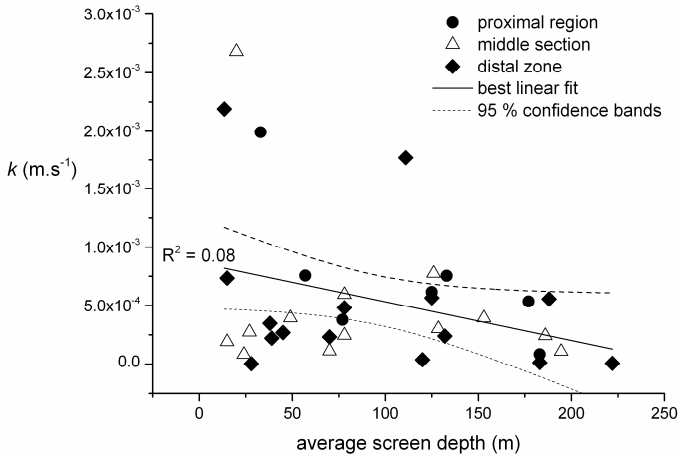

Figure 5.11. Hydraulic conductivity (k) in the Pingtung Plain plotted against depth (average well screen depth). The very weak correlation between k and depth supports the hydraulic connectivity observed between wells at a given station, as shown by the daily hydraulic head time series.

This hydraulic head snapshot represents the winter gradient, when water levels are relatively low. However, as was shown using the more detailed hydraulic head data set in the case of the Pingtung Plain (Figure 5.1A), seasonal oscillations, whilst important near the foothills, become diminished towards the middle and distal reaches of the groundwater flow network, which are analogous to the sampled portion of the Choshui Plain. Thus, the representative hydraulic gradient was calculated as the average hydraulic head difference, at the time of sampling, between the two wells at proximal station HL and the three wells comprising distal stations CP and DG (Figure 5.12), divided by the flow path distance between the two sets (Table 5.1). The average hydraulic head difference between stations HL and CP/DG was 40.74 m, which when divided across the distance between the two (32,875 m) gave an average hydraulic gradient of 1.58×10^{-3}.

The mixing model developed in Chapter 4 to distinguish seawater from solutes derived from rock-water interactions was used to ensure that only solutes resulting from

rock-water interactions in the Choshui Plain were incorporated into the chemical flux calculations. Distal well CP2, which had a concentration of chlorine approaching that of bulk seawater (91.21 mmol.L^{-1}; Data Table F) and issues with its charge balance (see Section 4.9.2, Chapter 4), was excluded from the chemical flux estimates.

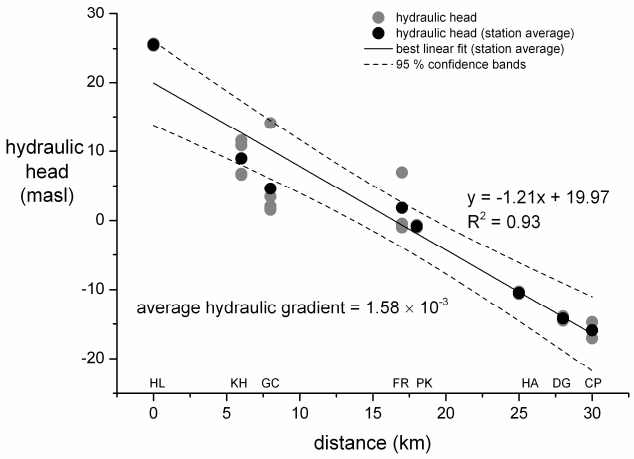

Figure 5.12. Static water levels for each of the 22 wells in the Choshui Plain at the time of sampling (November). The hydraulic gradient reflects the winter position of the water table.

5.4.6 Hydraulic conductivity in the Choshui Plain

Hydraulic conductivity measurements were not available for the 22 wells sampled in the Choshui Plain. Therefore, the permeability in the Choshui Plain was taken from the average of eight hydraulic conductivity measurements ascertained by pump testing that were available in the literature (WRA data after Lin et al. 2004) (Figure 5.13; Table 5.1). These hydraulic conductivity measurements were not from the wells sampled as part of this study, but provide a suitable estimate of the permeability range in the near-coastal section of the Choshui Plain.

The range in hydraulic conductivity, taken from these eight measurements, spanned from 1.34×10^{-4} m.s^{-1} to 7.77×10^{-4} m.s^{-1}, with an average of 4.16 m.s^{-1} (Figure 5.14A; Table 2.1, Chapter 2). The results of a Shapiro-Wilk test (Shapiro and Wilk 1965) show that the distribution of the hydraulic conductivity values from these eight wells, the average of which was used for chemical flux calculations in the Choshui Plain, could not be distinguished from a normal population (P = 0.39, df = 8, α = 0.05) (Figure 5.14B).

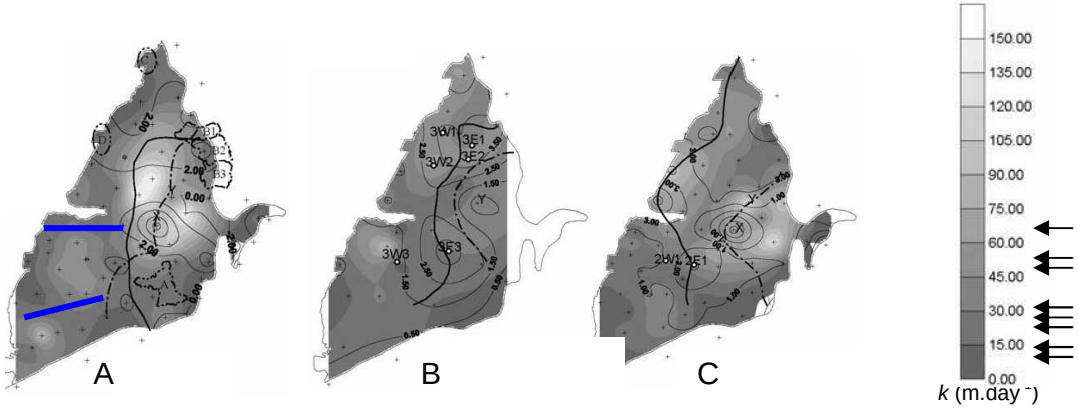

Figure 5.13. Hydraulic conductivity distribution maps at three depth horizons in the Choshui Plain. Modified after Lin et al. (2004). Layers (A), (B) and (C) correspond to maximum depths of 80 m, 160 m and 270 m, respectively. Blue lines show the transects along which the 22 wells sampled for this study were distributed. Arrows show the hydraulic conductivity values measured at wells 2E1, 2W1, 3E1, 3W1, 3E2, 3W2, 3E3 and 3W3 (see Table 2.1, Chapter 2), the average of which, 4.16 × 10−4 m.s^{-1}, was used for chemical flux calculations here.

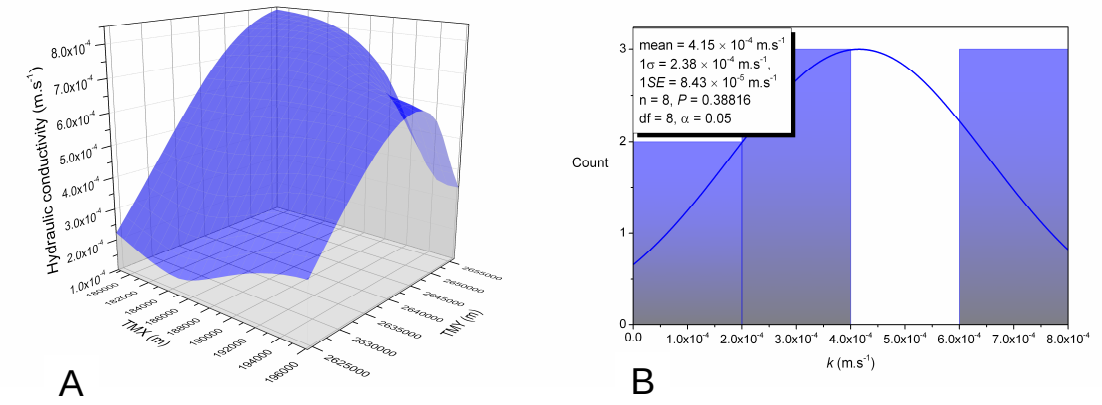

Figure 5.14. Hydraulic conductivity surface for the sampled portion of the Choshui Plain (A) and probability distribution of hydraulic conductivities for the 8 wells representing the near-coastal zone (B).

5.5 Calculation of chemical fluxes

5.5.1 Methodology

The hydraulic heads and conductivities constrained from field measurements were used to model groundwater flow in the Pingtung Plain, defined by a flow-path length of 39 km, width of 36 km and depth of 237 m (Table 5.1), the properties of which were

combined with the chemistry from 15 coastal and near-coastal wells comprising the distal zone to estimate the average chemical flux. Likewise, groundwater flow through the Choshui Plain, defined by a flow-path length of 26 km, width of 33 km and a depth of 294 m (Table 5.1), was constrained using hydraulic head and conductivity data, which together with chemistry data from 21 coastal and near-coastal wells comprising the sampled section of the Choshui Plain were used to calculate the chemical fluxes. These flow-path widths and depths were chosen as the regions most likely to capture the potential groundwater chemistry flux available for discharge into the ocean. Combining these physical parameters and chemical compositions gives dissolved fluxes through the distal zones after Darcy (1856), as follows:

$$Q_{gw} = kA\delta h/\delta l \times [X_i]_{\mathrm{gw}} \quad (5.1)$$

where Q_{gw} is the chemical groundwater flux (mol.yr^{-1}), k is the hydraulic conductivity (m.s^{-1}), A = cross sectional area of groundwater flow through the drilled depth of the basin (m^2), δh = change in hydraulic head along the groundwater flow path, δl = length of groundwater flow path and $[X_i]_{\mathrm{gw}}$ is the average concentration of a given element X_i in the given flow-path sampled. The Q_{gw} is then expressed as a percentage relative to total runoff using the dissolved chemical fluxes of the Kaoping and Choshui Rivers to approximate the total surface chemical fluxes in the respective regions:

$$Q_{\mathrm{gw}}/(Q_{\mathrm{river}} + Q_{\mathrm{gw}}) \times 100 = \textit{\% of total runoff} \quad (5.2)$$

To calculate the total relative chemical flux derived from rock-water interactions (residual plus hot-spring chemistry), the seawater contribution was removed from the bulk flux calculations by first subtracting $[X_{\mathrm{i}}]_{\mathrm{sw}}$ from the $[X_{\mathrm{i}}]_{\mathrm{sample}}$ (Equation 4.12 (Chapter 4)) parameter for all samples. The average of the seawater-corrected samples for each element was then used as input for $[X_{\mathrm{i}}]_{\mathrm{gw}}$ (Equations 5.1 and 5.2) to estimate the % of total runoff derived from rock-water interactions. Dissolved mass derived from rainwater was not removed from the chemical flux calculations as rainwater contributions are similarly common to both groundwater and river water samples and thus are cancelled each out in Equation 5.2.

5.5.2 Propagation of errors in the chemical flux estimates

For net weathering fluxes calculated using combined groundwater chemistry and water fluxes (Equation 1), there are compounded errors associated with uncertainty in each measured component. Given that the components of Equation 5.1 represent a linear set of combination variables, and assuming that the variances of measured components are independent, the total 1σ uncertainty ($SE_{Q[xi]}$) in the chemical weathering flux for element X_i was estimated as:

$$SE_{Q[Xi]} = [(Q[X_i])^2 \times (SE_{\delta h}^2/\delta h^2 + SE_{\delta l}^2/\delta l^2 + SE_A^2/A^2 + SE_k^2/k^2 + SE_{[Xi]}^2/[X_i]^2 + {}^*\sigma/SE_{[Xi]SW}^2)]^{1/2} \quad (5.3)$$

where $SE_{\delta h}$, $SE_{\delta l}$, SE_A and SE_k are the standard errors associated with the average change in hydraulic head (δh) across the groundwater flow path length, the change in length of groundwater flow path (δl), the cross sectional area of groundwater flow (A), and the average of hydraulic conductivity (k) measurements, respectively, and $SE_{[Xi]}$ is the analytical uncertainty on dissolved chemistry. The additional term ${}^*\sigma/SE_{[Xi]sw}$ is the uncertainty on the calculation of the seawater contribution (see Section 4.6.3 (Chapter 4)), which becomes a further source of uncertainty when calculating chemical fluxes corrected for the seawater component.

The standard error in the average change of hydraulic head was possible to calculate in the case of the Pingtung Plain ($SE_{\delta h}$ = 0.14), which was taken as the ($\sqrt{\Sigma}\sigma_{\delta h}^2/n-1)/\sqrt{n}$, where n = 1795 is the number of individual measurements in the daily five-year hydraulic head time series and σ^2 is the natural variance of that population. Only one set of static water-level measurements were available for estimating the hydraulic gradient in the Choshui Plain, but given that the measurements were made in the dry season (November 2008), they should represent a minimum gradient. Uncertainties in the measurements of δh are assumed to be insignificant. Given that one unidirectional flow path was assumed, there are no uncertainties associated with $SE_{\delta l}$ and SE_A. For estimating the uncertainty associated with permeability, the average conductivities for each of the seven stations comprising the fifteen wells representing the distal zone in the Pingtung Plain, and for each of the eight wells representing the Choshui Plain were chosen, giving seven and eight discrete hydraulic conductivities, respectively (Sections 5.4.4 and 5.4.6). The standard error in hydraulic conductivity (SE_k) was calculated on the average k values (Table 5.1),

where σ^2 is the natural variance of those populations, giving values of 1.09×10^{-4} m.s^{-1} (n = 7) for the Pingtung Plain and 1.43×10^{-4} m.s^{-1} for the Choshui Plain (n = 8).

The relative standard deviation on the chemical analytical measurements ranged from 1.23 to 3.35 %, giving a range in average $SE_{[Xi]}$ of 0.20 to 0.85 % for n = 35 (Pingtung) and 22 (Choshui) groundwater samples, and 0.35 to 1.51 % for n = 11 (Kaoping) and 41 (Choshui) river water samples. Temporal variations in groundwater chemistry determined by the spatial averaging of spot samples is not considered to be a significant source of error, as the time-variations in the elements of interest for weathering budgets are attenuated relative to the variability of surface conditions in alluvial fill aquifers with hydraulic conductivities in the measured range.

5.6 Chemical fluxes

5.6.1 Chemical fluxes from the Kaoping River

The average annual discharge for the Kaoping River during the period 1981–1990 was 7.40×10^{12} L.yr^{-1} (Ting et al. 1998a). Average monthly discharges during the same period ranged from 0.03×10^{12} L.month^{-1} in February 1984 to 3.30×10^{12} L month^{-1} in September 1990. The results of the chemical analyses of the 11 Kaoping River water samples are presented in Data Table F and a summary of the chemical characteristics of the Kaoping River water samples and a comparison with the nearby groundwater chemistry is discussed in Section 4.4.1 (Chapter 4). Combining the average annual river discharge with the average chemical concentrations for major and trace ions gave chemical flux estimates ranging from 1.05×10^{6} μmol.yr^{-1} (Ba^{2+}) to 1.04×10^{10} μmol.yr^{-1} (Ca^{2+}). The full suite of chemical fluxes is presented in Table 5.2.

Table 5.2 Average annual chemical flux estimates for the Kaoping River

	Na^+	K^+	Ca^{2+}	Mg^{2+}	SO_4^{2-}	Sr^{2+}	Li^+	Ba^{2+}	SiO_2
mol.yr^{-1}	3.80 × 10^9	5.06 × 10^8	1.04 × 10^{10}	4.23 × 10^9	5.57 × 10^9	3.00 × 10^7	1.22 × 10^7	1.05 × 10^6	1.07 × 10^9

As was discussed in Section 2.4.1.1 (Chapter 2), sampling bias due to most river water samples having been collected during the dry period likely resulted in an overestimate of the chemical flux estimates for the Kaoping River, which likely render the relative groundwater chemical fluxes through the Pingtung Plain, calculated using Equation 5.2, to be lower-than-average estimates.

5.6.2 Chemical fluxes from the Choshui River

The Choshui River had an annual discharge rate, calculated daily during the period March 2005 to December 2006 of 9.18×10^{12} L.yr^{-1} (WRA data; Data Table C). Average monthly discharges during the same period ranged from 1.23×10^{10} L.month^{-1} in Feb 2006 to 1.06×10^{13} L.month^{-1} in July 2005. The results of the chemical analyses of the 41 Choshui River water samples (collected approximately biweekly during the same period as the discharge measurements were made) are presented in Data Table F and a summary of the chemical characteristics of the Choshui River water samples and a comparison with the nearby groundwater chemistry is discussed in Section 4.4.5 (Chapter 4).

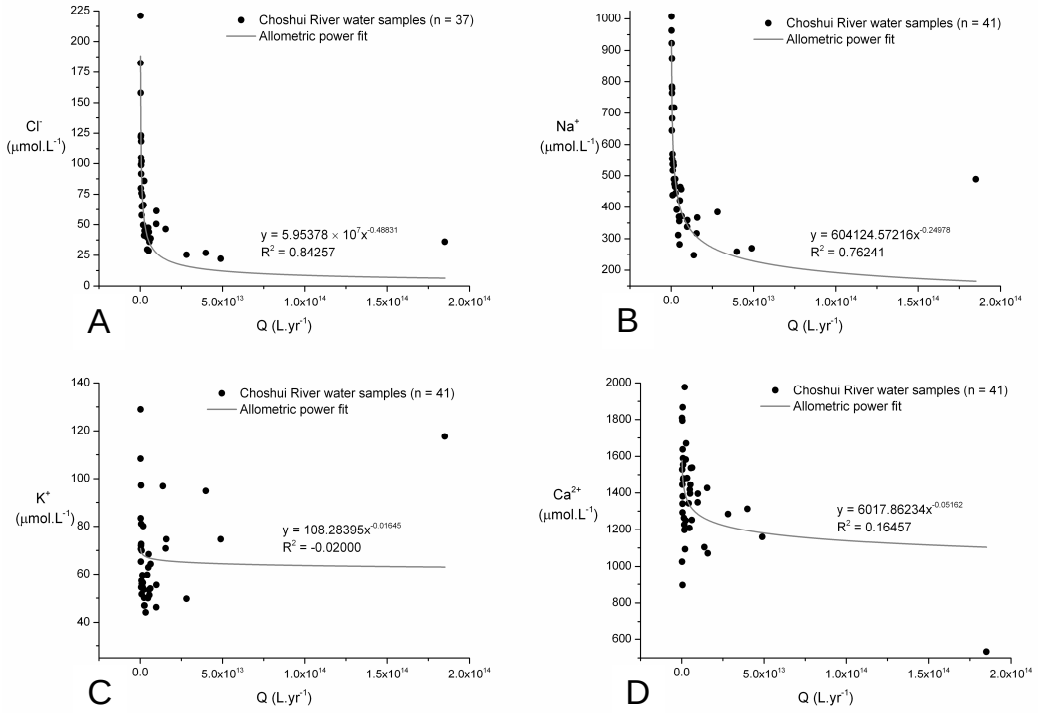

Figure 5.15. Relationships between selected solute concentrations and discharge for the 22-month record of the Choshui River. The curves correspond to power-law best fits of the data. Strong correlations with discharge were observed for Cl^- (A) and Na^+ (B), whereas other elements showed modest to weak correlations with discharge (C-H). The lack of strong fits with most of the solutes suggests that processes other than dilution by rainwater were operating.

In addition to daily discharge data, hourly discharge measurements were calculated and collected at the time of water sampling. Discharge-concentration relationships for major and trace ions were thus established using best-fit power functions (Figure 5.15A-H). In the case of [Cl^-] and [Na^+], strong anti-correlations with river discharge, over the range of hourly discharges measured, were exhibited (Figure 5.15A&B). Periods of low

surface runoff are characterised by higher rates of evapotranspiration than during high-intensity rainfall episodes. Therefore, in regions such as the Choshui River catchment where there are no instances of Cl-bearing evaporite minerals, a strong negative correlation between river discharge and [Cl^-] is expected. The main source of Na^+ to the river is from plagioclase feldspar, but given the relatively sluggish rates with which Na^+ is released from plagioclase during weathering, its concentrations in river water typically become diluted during high discharge events. However, Calmels et al. (2011) showed that depending on the hydrological conditions different groundwater flow paths can be preferentially activated each with a unique chemical signature that will be detected in river-water chemistry if sampling is opportune. Normal recharge conditions result in river chemistry that exhibits binary mixing as is shown to be largely the case for Na^+ and Cl^- over the sampling period of the Choshui River (Figure 5.15A&B). The Calmels et al. (2011) study showed using high-frequency river-flood sampling (sub daily for 25 days during Typhoon Mindulle, which made landfall in Taiwan on 1/7/04, and up to every four hours for 12 days during Typhoon Krosa, which passed over Taiwan during the period from 1-8/10/07) of the Liwu River in east Taiwan that during typhoons ternary mixing is observed in molar ratio mixing space (Sr/Ca versus Na/Ca) of the river-water samples. This mixing relationship reflects the activation of a third and distinct hydrological pathway that responds only to high-energy flushing of the subsurface. The highest hourly discharge by a factor of four recorded during sampling of the Choshui River (1.85×10^{14} $L.yr^{-1}$) was on the 19/7/05, when Typhoon Haiting reached west Taiwan. Similar to the chemistry recorded in the Liwu River water samples during the two typhoon events documented by Calmels et al. (2011), the single sample collected from the Choshui River during Typhoon Haiting exhibits lower Sr^{2+} and Ca^{2+} and higher Na^+ then would be predicted by binary mixing alone (Figure 5.15B,D,G & 5.16). Likewise, K^+, which like Na^+ is silicate-derived, exhibits a higher concentration during Typhoon Haiting than that which would be predicted by binary mixing (Figure 5.15C). However, K^+ in river water is also derived from vegetation and thus easily mobilised K-rich organic matter can lead to high [K^+] during periods of high discharge. Most of the Ca^{2+} in surface waters in the Choshui River catchment is derived from carbonate rock. Because of the relatively high solubility of carbonate, [Ca^{2+}] can remain high during periods of high surface runoff. This relative stability of [Ca^{2+}] during a large range of discharges can be seen in the Choshui River sample set (Figure 15.15D), where the correlation between [Ca^{2+}] and discharge is poor.

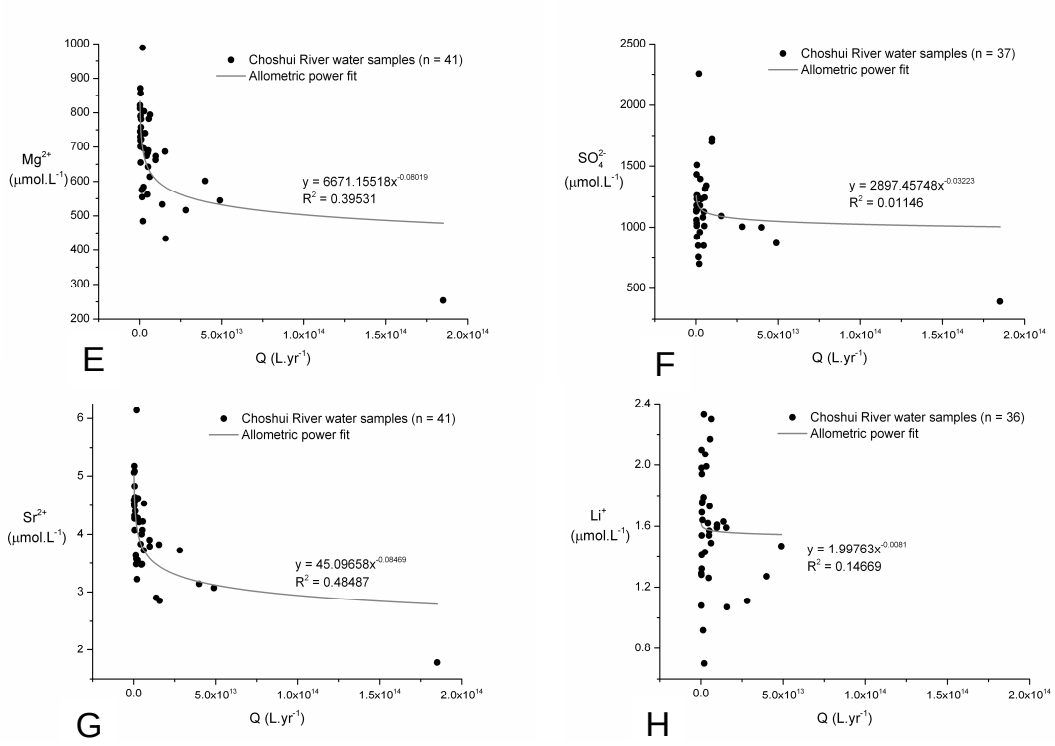

Figure 5.15 continued

The relationships between Mg^{2+} and Sr^{2+} concentrations and river discharge are moderately good (Figure 5.15E&G), suggesting both silicate and carbonate sources to the river of these elements. Relatively high [SO_4^{2-}] during increased river discharges resulted in a poor correlation between the two measurements (Figure 5.15F). The oxidation of pyrite contributes most of the SO_4^{2-} to the Kaoping River (Das et al. 2012). In Chapter 6, it is shown that the oxidation of pyrite during landsliding is rapid. Given the positive correlation between landsliding and surface runoff in Taiwan (Dadson et al. 2003), it is reasonable to expect relatively high [SO_4^{2-}] in surface waters during bouts of high discharge. The concentrations of dissolved Li^+ exhibited a poor correlation with discharge over the sampled range (Figure 5.15H). In Chapter 4 it is shown that the most significant source of Li^+ to surface waters in the Choshui River catchment is from hot-springs. One possible explanation for the relatively high [Li^+] observed during periods of high discharge could be that hydrological purging of hot-springs occurs during high surface runoff, which may result in increased Li^+ to surface waters at these times.

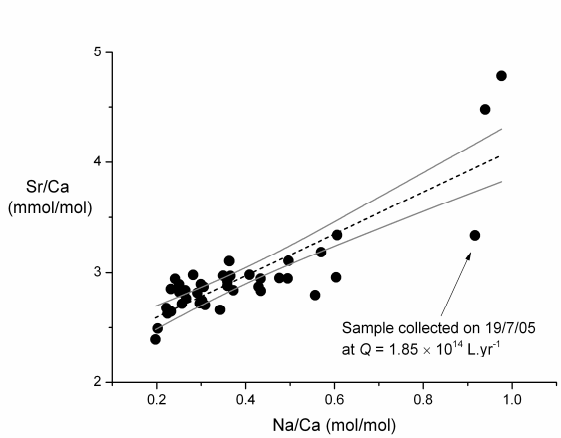

Figure 5.16. Variation in the ratio of Sr/Ca relative to the ratio of Na/Ca for the 22-month time series of the Choshui River. The dashed line is a linear best fit (R^2 = 0.70, grey lines are 95 % confidence limits) through the data showing that most samples can be generally explained by binary mixing. The arrow indicates the sample collected on 19/7/05 during Typhoon Haiting, which exhibits a similar mixing relationship to those of the two typhoon sample sets from the Liwu River (Calmels. et al. 2011), with low Ca^{2+} and Sr^{2+} relative to Na^+.

Given the large range in solute concentrations obtained for the Choshui River (Data Table F) over a variety of discharges (sample collection covered two full summer seasons and one-and-a-half winter seasons), the average chemistry of all samples measured was combined with the average annual discharge of the sampling period in computing a likely long-term chemical flux estimate for the Choshui River (Table 5.3). However, the particularly good relationship between [Na^+] and discharge for both the rising and falling limbs of the river hydrograph (Figure 5.17), allowed for relatively precise estimates of [Na^+] at given selected discharges. Therefore, Na^+ fluxes were calculated for selected low-flow discharge (1.84×10^{11} L.yr^{-1}), to represent a winter flux, and peak-flow discharge (4.89×10^{13} L.yr^{-1}), corresponding to a summer flux, using the power-law relationships between [Na^+] and discharge to calculate [Na^+]. The power law representing the falling limb of the hydrograph was chosen to calculate the low-flow Na^+ flux because there were a greater number of representative samples on the falling limb at low discharge values (Figure 5.17). Likewise, the only samples above 2×10^{13} L.yr^{-1} were on the rising limb of the river hydrograph, and thus the power law for the rising limb was used to estimate the likely peak-flow Na^+ flux (Figure 5.17). The highest discharge measurement in the data set (19/07/05, 1.85×10^{14} L.yr^{-1}), which was collected during Typhoon Haiting, was a factor of 4 higher than the next highest discharge (17/07/06, 4.89×10^{13} L.yr^{-1}) and was omitted from the power law fit of the rising limb of the hydrograph. The [Na^+] calculated at this high discharge would be a large under estimate based on the otherwise good relationship between [Na^+] and discharge (Figure 5.15B) and would result in a large uncertainty in the chemical flux estimate for [Na^+], and would therefore likely result in an over estimate of the relative subsurface flux (Equation 5.2). The calculated [Na^+] at selected low-flow and

peak-flow discharges gives an estimate of the seasonal variability of riverine chemical fluxes for this element (Table 5.3), with low-flow characteristic of intermittently dry winter conditions and peak-flow typifying the wetter summers.

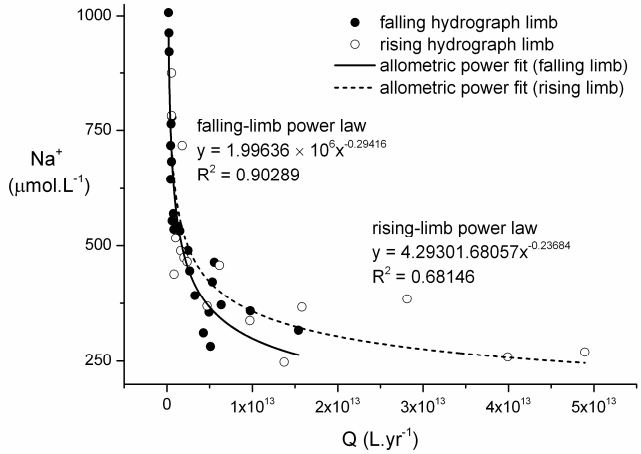

Figure 5.17. Relationships between [Na^+] and discharge for the 22-month record of the Choshui River with power law lest-fits through the data for both the falling (solid line) and rising (dashed line) limbs of the river hydrograph.

Table 5.3 Chemical flux estimates for the Choshui River. Fluxes are in mol.yr^{-1}.

	Na^+	K^+	Ca^{2+}	Mg^{2+}	SO_4^{2-}	Sr^{2+}	Li^+
average annual	4.79 × 10^9	6.22 × 10^8	1.27 × 10^{10}	6.24 × 10^9	1.06 × 10^{10}	3.72 × 10^7	1.45 × 10^7
peak-flow	1.20 × 10^{10}	-	-	-	-	-	-
low-flow	1.78 × 10^8	-	-	-	-	-	-

5.6.3 Subsurface chemical fluxes through the Pingtung Plain

The estimated average water flux Q_{gw} (Equation 5.1), through the distal zone of the Pingtung Plain was 1.84 × 10^{11} L.yr^{-1}. The elemental contributions of groundwater to total chemical fluxes from the Pingtung Plain, expressed as relative percentages of combined surface and subsurface discharges for bulk fluxes (% $_{total\text{-}runoff}$) and for fluxes corrected for

a seawater component (% $_{total\text{-}runoff\ (fresh)}$) (Equations 5.1, 5.2 and 4.14 (Chapter 4)), are presented in Table 5.4. The relative groundwater fluxes corrected for seawater of Na^+, SiO_2 and Ba^{2+} were modest at 5.03, 6.06 and 11.78 %, respectively. In comparison, the relative groundwater fluxes corrected for seawater of Ca^{2+}, SO_4^{2-}, Li^+, K^+, Sr^{2+} and Mg^{2+} were small. The very low value for SO_4^{2-} can be explained by the precipitation of sulphate-bearing compounds (e.g. pyrite), which is indicated by negative residual values for SO_4^{2-} (Equation 4.13, Chapter 4) in a number of distal wells (Data Table G). The formation of minerals such as pyrite in these localised zones could be due to bacterially-mediated sulphate reduction. Positive fluxes, however, imply that overall SO_4^{2-} is a net weathering product across the plain and likely results from the oxidation of pyrite.

Table 5.4 Groundwater chemical fluxes (where the standard error at 1σ on the fluxes is ± 28.3 %) in the distal zone of Pingtung Plain. Fluxes are in mol.yr^{-1}.

	Na^+	K^+	Ca^{2+}	Mg^{2+}	SO_4^{2-}	Sr^{2+}	Li^+	SiO_2	Ba^{2+}
Q_{gw} (mol.yr^{-1})	5.82 × 10^8	2.67 × 10^7	4.44 × 10^8	1.87 × 10^8	1.06 × 10^8	1.35 × 10^6	4.04 × 10^5	6.94 × 10^7	1.41 × 10^5
% $_{total\text{-}runoff}$	13.29	5.01	4.09	4.24	1.88	4.31	3.19	6.07	11.79
% $_{total\text{-}runoff\ (fresh)}$	5.03	3.81	3.99	3.01	1.42	4.02	2.98	6.06	11.78

5.6.4 Subsurface chemical fluxes through the Choshui Plain

The estimated average water flux Q_{gw} (Equation 5.1), through the near-coastal zone of the Choshui Plain was 2.01 × 10^{11} L.yr^{-1}. The elemental contributions of groundwater to total chemical fluxes in the Choshui Plain, expressed as relative percentages of combined surface and subsurface discharges for bulk fluxes (% $_{total\text{-}runoff}$) and for fluxes corrected for a seawater component (% $_{total\text{-}runoff\ (fresh)}$) (Equations 5.1, 5.2 and 4.14), are presented in Table 5.5.

Table 5.5 Groundwater chemical fluxes (standard error at 1σ on the fluxes is ± 20.3 %) in the Choshui Plain. For relative fluxes, blue is based on the average annual river flux and purple and yellow, respectively on selected low-flow peak-flow discharges.

	Na^+	K^+	Ca^{2+}	Mg^{2+}	SO_4^{2-}	Sr^{2+}	Li^+	SiO_2	Ba^{2+}
Q_{gw} (mol.yr^{-1})	4.10 × 10^8	1.15 × 10^7	3.84 × 10^8	1.56 × 10^8	1.81 × 10^8	1.10 × 10^6	7.07 × 10^5	7.27 × 10^7	9.78 × 10^4
% $_{total\text{-}runoff}$ (average annual)	7.89	1.81	2.94	2.44	1.67	2.87	4.63	-	-
% $_{total\text{-}runoff\ (fresh)}$ (average annual)	6.07	1.47	2.92	2.27	1.61	2.82	4.60	-	-
% $_{total\text{-}runoff}$ (low-flow)	69.71	-	-	-	-	-	-	-	-
% $_{total\text{-}runoff\ (fresh)}$ (low-flow)	63.45	-	-	-	-	-	-	-	-
% $_{total\text{-}runoff}$ (peak-flow)	3.30	-	-	-	-	-	-	-	-
% $_{total\text{-}runoff\ (fresh)}$ (peak-flow)	2.51	-	-	-	-	-	-	-	-

The seawater-corrected groundwater fluxes of Na^+ and Li^+, calculated relative to the average annual Choshui River fluxes, were modest at 6.07 and 4.60 %, respectively, and slightly exceeded those relative to the Kaoping River. In comparison, and similar to seawater-corrected chemical fluxes for the Pingtung Plain, the relative seawater-corrected groundwater fluxes of K^+, Ca^{2+}, Mg^{2+}, SO_4^{2-} and Sr^{2+}, calculated relative to the average annual Choshui River flux are small.

The range in discharges for the Choshui River (up to a factor of 267) greatly exceeds that of groundwater chemistry for all solutes except SO_4^{2-} (Data Table C). Owing to this, the high chemical concentrations in river water during low-flow discharges are not sufficient to compensate for the large reduction in water volume observed during these times, and chemical fluxes thus rapidly decline. Therefore, the seawater-corrected subsurface chemical flux of Na^+ (which represents the average flux during winter hydrological conditions (Section 5.4.5)) relative to the flux of Na^+ based on the selected low-flow discharge of the Choshui River (% $_{total\text{-}runoff\ (fresh)}$), at 63.45 %, is exceptionally high. Likewise, the relative subsurface flux of Na^+ during peak-flow discharge is low (Figure 5.17). These show that for estimating chemical weathering fluxes the time-averaging of river chemical fluxes (probably for all elements) is essential. Despite long-term relative

subsurface chemical fluxes being low, the seasonal range indicated by the variety of Na^+ fluxes, could potentially have a bearing on processes that are sensitive to short-term changes, such as nutrient delivery to the coastal ocean, which would impact on coastal ecology.

5.6.5 Using other estimates of groundwater recharge and water fluxes

Estimations of groundwater recharge using soil-moisture water budget and chloride mass balance approaches (Ting 1996; Ting et al. 1998b), numerical modelling (MODFLOW: (McDonald and Harbaugh 1988) (Ting et al. 1998a)), and estimations of submarine fresh groundwater discharge (SFGD) from offshore sampling of open ocean (Lin et al. 2010, 2011) give a range in derived groundwater throughput in the Pingtung Plain spanning two orders of magnitude (Table 5.6).

Table 5.6 Various estimates of groundwater fluxes in the Pingtung Plain region

Source	Estimate Type	Method	Water flux
Lin et al. (2011)	SFGD	binary mixing	4.50×10^{12} L.yr^{-1}
Ting et al. (1998a)	recharge	MODFLOW[1]	9.56×10^{11} L.yr^{-1}
Ting et al. (1996)	recharge	soil water-budget	6.69×10^{11} L.yr^{-1}
Ting et al. (1998b)	recharge	Cl mass balance	4.00×10^{11} L.yr^{-1}
Ting et al. (1998b)	recharge	mixing-cell method	1.32×10^{11} L.yr^{-1}
Peng et al. (2008)	SFGD	binary mixing	34164–42048 L.m^{-2}.yr^{-1}
This study[2]	discharge	Darcy[3] approach	1.84×10^{11} L.yr^{-1}

[1]McDonald and Harbaugh (1988); [2]See Section 5.6.3; [3]Darcy (1856)

In addition, SFGD estimates via seepage meters gave average localised flow rates of 42.05 m^3.m^{-2}.yr^{-1} for August (2004) and 34.16 m^3.m^{-2}.yr^{-1} for October (2005) at 8-m water depth along 150 m shore-parallel and 300 m shore-normal transects off the southern-most region along the Pingtung Plain coastline (Peng et al. 2008; Table 5.6). Mass balance calculations using the salinity and isotope characteristics of the pore waters associated with these seepage meters and of related terrestrially-sampled groundwaters imply that the fresh fraction of submarine groundwater discharge at this location was 26-99 %. The average fraction of fresh water was 76±40 % (2σ, n = 16), which exceeded the estimates made at the 17 other sites where SFGD was measured around the coast of Taiwan (0-59 %) (Peng et al. 2008), and likewise too was greater than the range of the global estimates (0-35 %) (Hussain et al. 1999; Taniguchi and Iwakawa 2004; Taniguchi et al. 2005). In addition, the seepage velocities (34-42 m.yr^{-1}; Peng et al. (2008)) exceeded most of the worldwide

reported values, which are typically less than 36 $m.yr^{-1}$ and usually highest in volcanic island settings (Kim et al. 2003).

As discussed in Section 2.3, Chapter 2, the high fraction of meteoric water measured offshore along the southern-most Pingtung coastline is likely due to the seepage meters' proximity to the major high-angle active oblique-slip Chaochou Fault (Figure 2.1, Chapter 2). Since it is one of the major faults in Taiwan and given its proximity to the Pingtung Plain, it is useful to single this fault out and to assess potential chemical fluxes related to it. The Chaochou Fault potentially continues to depths of ~ 2 km where it is interpreted as either splaying from, or being a rotated version of, a younger and deeper thrust fault (Wiltschko et al. 2010). The Chaochou Fault therefore has the potential to facilitate submarine fresh groundwater discharge into the depths of the offshore Kaoping Canyon (Figure 2.1, Chapter 2). Extrapolating the average fault-related freshwater flow rates from the seepage meter measurements (38.11 $m^3.m^{-2}.yr^{-1}$ × 0.76 = 28.96 $m^3.m^{-2}.yr^{-1}$) across the 150 m shore-parallel transect over the depth range of the Chaochou Fault (2000 m) allows for augmented groundwater chemical flux estimates (Table 5.7), whereby the water flux calculated using hydraulic heads and hydraulic conductivities (measurements that would have bypassed the fault zone) is added to the water flux based on the average seepage meter measurements and the extrapolated depth range (150 m × 2000 m = 300,000 m^2), giving a combined water flux (1.84×10^{11} $L.yr^{-1}$ + 8.69×10^9 $L.yr^{-1}$ = 1.92×10^{11} $L.yr^{-1}$) with which to calculate the augmented chemical fluxes. This chemical flux extrapolation is obviously speculative, with just 16 seepage meter measurements at 8 m water depth, each covering a surface area of 0.11 m^2 (Peng et al. 2008), representing the 150 m of measured shoreline and the 2000 m of extrapolated depth. However, the extrapolated water volume is only 5 % of the groundwater flux estimate based on hydraulic heads and hydraulic conductivities and such has little impact on the relative subsurface fluxes.

It is likely that groundwater discharge occurs to varying degrees along the entire continental shelf below the drilled depth of the Pingtung basin, which if taken into account would allow for further augmentation of the chemical fluxes. However, without knowledge of the hydraulic properties for the deeper portions of the plain (~2 km depth), extrapolating the range of chemical fluxes into these deeper regions would yield very speculative SFGD estimates.

The results of combining the selected estimates of groundwater recharge and SFGD with the average chemical composition of the groundwater in the distal zone of the

Pingtung Plain are presented in Table 5.7. Relative groundwater flux estimates vary considerably depending on the water flux value used, with the highest seawater-corrected chemical fluxes based on the SFGD estimate of Lin et al. (2011). In their study of SFGD off the coast of the Pingtung Plain, Lin et al. (2011) used salinity and environmental isotope tracers to estimate the fresh fraction of their sampled offshore (open ocean) waters, and used these fractions to calculate a SFGD flux representing groundwater discharge along the Kaoping Canyon. It appears from their study that they extrapolated the salinity and isotope characteristics of the 83 open ocean samples, collected at different depths (0 m-1600 m) from two sampling transects, (one shore normal from the coast to 25 km offshore and one shore parallel at water depths of 800 m, together comprising 10 stations in total), to represent the chemistry of the volume of seawater in the sampled portion of the canyon observed to have any fresh water (1.5×10^{14} L), and then used the fraction of this volume estimated to be fresh water (3 %) to derive their SFGD flux of 4.50×10^{12} L.yr^{-1}. How they estimated the annual flux is unclear. Furthermore, taking the volume of seawater, of which they estimated 3 % to be fresh, and dividing that volume by the number of samples representing it (1.5×10^{14} L ÷ 83) apportions a volume of 1.8×10^{12} L to one sample, the chemistry of which sample to define the apportioned volume. This volume of 1.8×10^{12} L is greater than all of the other groundwater recharge and discharge estimates (other than that of Lin et al. 2011) and almost a factor of ten greater than the Darcy-based flux estimated here (Table 5.6). Also of importance is potential topologically-driven variability of subsurface groundwater discharge along geologically and hydraulically heterogeneous submarine canyons (Charette et al. 2008). However, the advantage of the Lin et al. (2011) study is that it covers potential groundwater discharge depths far greater than those sampled onshore. Therefore, if their extrapolation is conservative and their consideration of the residence times of the chemical species used to estimate their annual flux is robust, then presumably the subsurface solute delivery to the ocean off the southwest coast of Taiwan amounts to more than half that of the Kaoping River chemical flux for many solutes (Table 5.7). Large hydraulic pressures related to a combination of potentially extensive confining units at depth and head pressures from the mountain range could potentially give rise to greater SFGD fluxes at depths below the well window.

Table 5.7 Sea water-corrected groundwater chemical fluxes (Q_{gw}*) using selected estimates of recharge, in the distal zone of Pingtung Plain. The blue rows are bulk chemical fluxes and the yellow rows are groundwater chemical fluxes relative to the average annual chemical flux of the Kaoping River (% $_{total\text{-}runoff\ (fresh)}$). Fluxes are in mol.yr^{-1}.

	Na^+	K^+	Ca^{2+}	Mg^{2+}	SO_4^{2-}	Sr^{2+}	Li^+	SiO_2	Ba^{2+}
Lin et al. (2011)	4.93 × 10^9	4.91 × 10^8	1.06 × 10^{10}	3.22 × 10^9	1.97 × 10^9	3.08 × 10^7	9.22 × 10^6	1.70 × 10^9	3.44 × 10^6
Ting et al. (1998a)	1.05 × 10^9	1.04 × 10^8	2.26 × 10^9	6.84 × 10^8	4.19 × 10^8	6.54 × 10^6	1.96 × 10^6	3.60 × 10^8	7.32 × 10^5
Ting et al. (1996)	7.33 × 10^8	7.30 × 10^7	1.58 × 10^9	4.79 × 10^8	2.93 × 10^8	4.58 × 10^6	1.37 × 10^6	2.52 × 10^8	5.12 × 10^5
Ting et al. (1998b)[1]	4.38 × 10^8	4.37 × 10^7	9.44 × 10^8	2.86 × 10^8	1.75 × 10^8	2.74 × 10^6	8.20 × 10^5	1.51 × 10^8	3.06 × 10^5
Ting et al. (1998b)[2]	1.45 × 10^8	1.44 × 10^7	3.11 × 10^8	9.45 × 10^7	5.78 × 10^7	9.03 × 10^5	2.71 × 10^5	4.97 × 10^7	1.01 × 10^5
Darcy[3] + Peng et al. (2008)	2.11 × 10^8	2.10 × 10^7	4.54 × 10^8	1.38 × 10^7	8.42 × 10^7	1.32 × 10^6	3.94 × 10^5	7.25 × 10^7	1.47 × 10^5
Lin et al. (2011)	56.47	49.25	50.46	43.21	26.14	50.63	42.96	61.24	76.59
Ting et al. (1998a)	21.60	17.09	17.79	13.91	6.99	17.89	13.79	25.13	41.00
Ting et al. (1996)	16.17	12.61	13.15	10.16	5.00	13.23	10.07	19.02	32.72
Ting et al. (1998b)[1]	10.34	7.94	8.30	6.33	3.05	8.36	6.27	12.31	22.53
Ting et al. (1998b)[2]	3.67	2.77	2.90	2.18	1.03	2.92	2.16	4.43	8.76
Darcy[3] + Peng et al. (2008)	5.25	3.98	4.17	3.15	1.49	4.20	3.12	6.33	12.27

[1]Cl mass balance method; [2]Mixing cell method; [3]Darcy (1856)

5.6.6 Global context

The calculated groundwater fluxes of 1.84 × 10^{11} L.yr^{-1} (14.15 m^3.m^{-1}.day^{-1}) in the drilled depths of the Pintung Plain, and 2.01 × 10^{11} L.yr^{-1} (16.73 m^3.m^{-1}.day^{-1}) in the sampled portion of the Choshui Plain are comparable to the global average shoreline-normalised groundwater flux estimate to the ocean of 11 m^3.m^{-1}.day^{-1} (Zektzer 2000),

which was calculated from combined hydrological and hydrogeological terrestrial-based modeling. One of the yet-to-be explained features of inter-comparison submarine groundwater discharge studies is that the fluxes tend to correlate positively with the scale of the studies, even in cases where local and regional flux estimates are derived for the same location or where coastal geologies are similar. For example, the average shoreline-normalised regional (10-300 km) submarine groundwater discharge fluxes in clastic settings, estimated by other authors and summarised by Charette et al. (2008), are significantly greater than analogous smaller-scale local studies. For example, estimates for submarine groundwater discharge fluxes to the ocean are 660-6600 $m^3.m^{-1}.day^{-1}$ for the Bay of Bengal (Moore 1997). If 5 % of this flux was derived from fresh groundwater then the shoreline-normalised flux for the Bay of Bengal would be 33-330 $m^3.m^{-1}.day^{-1}$, at least double the flux estimated for the Choshui Plain and at least three times the global average groundwater flux of Zektzer (2000). One reason put forward by Charette et al. (2008) to explain this discrepancy between regional and local-scale studies is that the former are conducted out on the continental shelf where the effects of sub-tidal pumping are greater, whereas the latter flux estimates would include only direct and intertidally-forced submarine groundwater discharge. In relation to the above issue, Moore and Wilson (2005) point out that locally-based, nearshore studies are usually conducted during calm ocean conditions whereas open-ocean large-scale regional studies would capture the effects of storms.

Thus the outstanding questions pertaining to estimates of submarine fresh groundwater discharge concern the depth ranges over which this form of solute delivery to the ocean occurs, the local and global magnitude of this dissolved mass that bypasses the surface drainage network entirely and the potential impact of this under-sampled source of dissolved mass on our understanding of ocean geochemical budgets.

5.7 Conclusions and further work

Groundwater chemical fluxes representing solutes derived from chemical weathering have been calculated using hydraulic head and hydraulic conductivity data together with chemical analyses of groundwater for two locations along Taiwan's coastline; the Pingtung Plain in southwest Taiwan and the Choshui Plain in the central west. The groundwater weathering fluxes from the Pingtung Plain range between 1 % and 4 % for Ca^{2+}, Mg^{2+}, K^+, $SO_4^{2-,}$ Sr^{2+} and Li^+, between 5 % and 6 % for Na^+ and SiO_2, and

are 12 % for Ba^{2+} of total runoff, (combined surface (Kaoping River) and subsurface chemical fluxes), demonstrating that subsurface weathering fluxes, at least in the drilled depth of the Pingtung basin (~237 m), are modest. Likewise, for the drilled depth of the Choshui Plain, subsurface chemical fluxes relative to the estimated annual average chemical flux from the Choshui River range between 1 % and 5 % for Ca^{2+}, Mg^{2+}, K^{+}, $SO_4^{2-,}$ Sr^{2+} and Li^{+} and are 6 % for Na^{+}, again suggesting that the fresh fraction of submarine groundwater discharge, at least in the top ~300 m of the alluvial fill sediments, is modest in comparison to solute delivery to the ocean via surface runoff. However, submarine groundwater discharge has been observed by other authors offshore of the Pingtung Plain, as deep as 1200 m into the Kaoping Canyon. It is likely that the relatively short distances between the high mountain topography and the coast exhibited in Taiwan would result in large hydraulic head gradients that are likely to drive groundwater chemical fluxes to the ocean deep into the offshore environment, which could be potentially significant.

Further work that could be done to explore the potential significance of submarine fresh groundwater discharge in Taiwan should involve the development of deep (>500 m) onshore boreholes in the alluvial-fill deposits close to the coast, which would enable direct measurement of the physical properties of these aquifers at depth and determination of the groundwater chemistry that is likely to represent deep submarine groundwater discharge. The use of deep terrestrial boreholes to categorise the physical properties of the aquifers and to ascertain the groundwater chemistry would greatly complement offshore studies that, whilst do serve to extend the depth range of submarine groundwater discharge observation, are limited by poor spatial resolution and by the difficulty of extracting the fresh signal in seawater-dominated samples. In addition, further work to characterise and quantify the subsurface chemical weathering budget in Taiwan should involve exploration along the east coast of the island where silicate weathering fluxes are known to have circulated along meteoric pathways through the fractured bedrock. In contrast to the western margin of Taiwan, where the steep mountain topography grades into the gently sloping uplifted East Asian continental margin, sedimentary deposition along the east coast of Taiwan is limited and debris from the hillslopes mainly accumulates as thin gravel beaches. Thus, the east coast of Taiwan is characterised by steeply dipping fractured bedrock slopes that grade at high angles directly into the ocean where they continue to outcrop to >7000 m water depth. Groundwater flow rates associated with the Chaochou Fault offshore of the Pingtung Plain were found to be in excess of global rates. Thus,

driven by high hydraulic gradients and uninterrupted by alluvial-fill deposits, bedrock-derived groundwater chemical fluxes to the ocean along the fracture planes characterising the east margin of Taiwan could be shown to be especially significant.

Seasonal variations in the groundwater chemical fluxes from the Choshui Plain, relative to those from the Choshui River, were assessed using the example of dissolved Na^+, the concentration of which showed a good correlation with river discharge and which therefore allowed for a robust estimate of the average low-flow river concentrations. The seawater-corrected Na^+ flux from the Choshui Plain, relative to that from the low-flow Na^+ flux estimate of the Choshui River was 63.45 %. Despite the long-term average relative subsurface flux being low, this range in seasonal variation could have significant implications for shorter scale phenomenon, such as nutrient delivery and coastal ecology.

The shoreline-normalised groundwater chemical fluxes for both plains compare well to global estimates of submarine fresh groundwater discharge along clastic coastlines. However, in comparison to other case studies, particularly of volcanic ocean island settings where groundwater discharge rates to the ocean are sometimes in excess of surface water fluxes, chemical fluxes from analogous regions in Taiwan are low. These comparatively low relative fluxes occur despite subsurface chemical enrichment of most elements relative to surface waters and that the plains exhibit high permeabilities and are surrounded by steeply-elevated fractured bedrock where precipitation is typically in excess of three metres per year and where hydraulic pressures are high. However, estimates of subsurface chemical fluxes are sensitive to the method used for calculating groundwater fluxes. For the Pingtung Plain region alone, several different estimates of effective groundwater recharge and groundwater discharge have been calculated spanning greater than two orders of magnitude. The discharge estimate calculated here for the Pingtung Plain, using hydraulic heads and hydraulic conductivities, is lower than all but one previous estimate of effective recharge for the region, highlighting the advantage of having direct physical measurements of aquifers' properties towards calculating conservative estimates of subsurface groundwater discharge and chemical fluxes.

Chapter 6

Insights from bedrock aquifers

"*Few tasks in hydrogeology are more difficult than locating drilling sites for water wells in igneous and metamorphic rocks.*" Davis, S.N. and DeWiest, R.J.M. (1966).

6.1 Summary

Thus far the data presented in this thesis has been representative of groundwaters and surface waters from alluvial-fill sedimentary basins along Taiwan's western margin. This chapter presents major and trace chemistry and isotopic compositions of groundwaters and related surface waters from bedrock catchments in two different locations. The groundwaters were sampled from tunnels in two distinct bedrock aquifers, Tunnels 1, 6 and 8 of the Bayyang Tunnel Trail located in Taroko Gorge National Park in the Liwu River catchment in east Taiwan (see Figure 2.10, Chapter 2), and Tunnel 28 located in the Fenchihu township between the upper reaches of the Choshui and Tsengwen River catchments in central west Taiwan (see Figure 2.12, Chapter 2). Details of the chemical variability within and between tunnels are related generally to the physical properties of the overlying rock-mass, such as thickness and dip of the bedding, and more specifically to lithology, weathering agent and, in the case of Tunnel 1, surface processes. The methodology and main observations are summarised in the following section.

6.2 Aims, outline of methodology and summary of main findings

There are two primary aims of this chapter. The first aim is to investigate further the previous identification and description by Calmels et al. (2011) of two groundwater types in Taiwan that, together with surface runoff, can explain the full chemical hydrograph of the Liwu River over 37 years of river discharge measurements (see Section 4.10 Chapter 4 and Section 5.6.2, Chapter 5 for previous discussion of these groundwater types). These two groundwater end-members were established using two and three groundwater samples, respectively, from Tunnel 1. In order to investigate whether other groundwater end-members might be present in the catchment that might highlight different

types of weathering in the Liwu River drainage basin, an additional 43 groundwater samples were collected from the Bayyang Tunnel Trail, 38 of which were from Tunnel 1 and five in total from Tunnel 6 and Tunnel 8 (see Figures 2.10 and 2.11, Chapter 2). A further nine groundwater samples were collected from Tunnel 28 (see Figures 2.12 and 2.13, Chapter 2) to observe if similar hydrogeochemical mixing relationships to those in the Liwu River catchment were active in a second catchment.

The second aim is to understand some of the main controls on chemical fluxes in elevated uplifted regions so as to identify aspects of the climate/atmosphere-erosion feedback taking place in active mountain belts, such as the primary weathering agents and weathering reactions in deep bedrock aquifers and to what extent are they controlled by physical erosion. To achieve this aim, the chemical variability of groundwaters sampled along a 520 m transect within Tunnel 1 is presented and discussed and some of the important weathering reactions that are predominantly occurring within fractured bedrock in Taiwan are described. An assessment of the controls on the chemical variability of the groundwaters is presented with particular focus on the interplay of landslides with chemical weathering activity in deep fractured bedrock. The importance of this interplay between physical and chemical denudation in mediating portions of the carbon, sulphur and oxygen biogeochemical cycles is addressed.

All groundwater samples were collected from drip sites along the ceilings of the tunnel interiors. Care was taken to ensure that these waters were uncontaminated by selecting only those tunnels or portions of tunnels that had been bored through bedrock and which had had no cement or other artificial casing put in place for support. The groundwater samples were collected over a range of seasonal conditions. In the case of the Bayyang Tunnel Trail, the samples were collected over four years (2007 to 2010) during late winter (April 2009), early summer (May 2010) and summer periods (September 2007, September 2009 and June to August 2010). Groundwater samples were recovered from Tunnel 28 during summer 2009 and early summer (May) 2010. Also collected were four surface runoff samples from Bayyang, two in September 2009 at a distance of 14 km from Tunnel 1 within the same lithological units as the tunnels and two from September 2010 from off of the landslide scar above the entrance to Tunnel 1. Three surface runoff samples were collected from near Tunnel 28 in September 2009, including one from a small stream approximately 2 km from Tunnel 28, one from the valley slope adjacent to the stream and one from what appeared to be an old landslide scar within 100 m of the tunnel. Published

water data from the Liwu River (Calmels et al. 2011) and the Choshui River (WRA data) are also presented.

In particular, over the course of the four-year sampling campaign at Bayyang, 40 groundwater samples were recovered along a ~520 m sampling transect in Tunnel 1 (see Figure 2.11, Chapter 2). This sample set is of particular importance because it has enabled background chemical variability in a fractured bedrock aquifer to be established that, as will be discussed in Section 6.5.2, to a first order appears to be related to the dip direction of the bedding and the slope/thickness of the rock-mass above the tunnel. Furthermore, a landslide (surface area = ~10,000 m^2, depth = ~10 m) that removed approximately 10 metres of bedrock from the entire 200 m ridge face above the tunnel entrance occurred in October 2009 (approximately two months after Typhoon Morakot made landfall in Taiwan), shortly after the September 2009 sampling period and prior to the final sampling expeditions in 2010. As will be demonstrated later in this chapter, this major physical disruption of the overlying bedrock had a significant impact on chemical weathering processes in the deep fractured aquifer that highlights some important features of the climate/atmosphere-erosion feedback.

In the context of Taiwan, this chapter therefore demonstrates:

1. How by analysing an additional 43 groundwater samples together with the previously published set of 5 groundwater samples from the Liwu River drainage basin, it can be shown qualitatively that rather than two groundwater end-members defining the hydrogeochemical mixing in bedrock aquifers a continuum of at least four groundwater end-members can now be described.
2. That geological structure rather than thickness of overburden appears to be a primary control on groundwater chemistry.
3. That the October 2009 landslide induced the rapid oxidation of pyrite, generating an excess of sulphuric acid, which then acted as the main weathering agent, causing a weathering pulse of silicate and, to a relatively lesser degree, carbonate dissolution within the disrupted bedrock mass.
4. How the landslide resulted in significant disruption of previously systematic chemical trends observed in the fractured-bedrock hosted groundwater in the vicinity of Tunnel 1, which implicates the importance of the biogeochemical cycling of carbon, sulphur and oxygen in active mountain belts.

5. How, in the months following the landslide, most solutes were returned to background concentrations by the mechanisms of bacterial sulphate reduction, CO_2 degassing and clay formation.
6. That the chemical and hydrological impact of the landslide was largely restricted to the zone directly below the ruptured surface consisting of approximately 200 m of overburden, with post-landslide solutes in the tunnel interior largely akin to those reflecting background physical conditions.

6.3 Background and motivation

Outcrops of crystalline (igneous and metamorphic) and consolidated sedimentary rocks cover more than 20 % of Earth's continental near-surface and they dominate in upland areas where most major rivers have their headwaters. However, the aquifers in these fractured bedrock zones are complex, anisotropic hydrogeological environments that exhibit irregular groundwater flow pathways (Krásný and Sharp 2007). Difficulties thus arise in constraining groundwater flow paths and also in accessing groundwater in fractured bedrock, and therefore comparatively little is known regarding hydrogeochemical interactions in these settings. In serving to overcome the latter of these difficulties, the disused transport tunnels in Taiwan provide a rare opportunity for gathering information about groundwater chemistry in fractured bedrock. And whilst delineating groundwater flow paths in fractured bedrock remains a difficult task, it will be shown later in this chapter that knowledge of groundwater chemistry in these settings affords important insights into the chemical weathering of active mountain belts.

As was discussed in Chapter 2 (Section 2.3), most of the studies conducted on groundwater chemistry in Taiwan have been concerned with the mitigation of various hazards to drinking water, and little work has been carried out on chemical weathering. One of the most important exceptions to this situation is the study by Calmels et al. (2011), who used chemical hydrograph separation methods to quantify the proportion of silicate- and carbonate-derived dissolved mass, from two different groundwater end-members, contributing to the long-term flux of the Liwu River. One of the two groundwater end-members was termed 'shallow-groundwater' and the other 'deep-groundwater' with each reflecting the activity of distinct hydrological flow paths. Given the lack of understanding of groundwater flow properties in fractured bedrock and also of chemical weathering in these settings, the Calmels et al. (2011) study provided unique insight into the

hydrogeochemistry of active mountain belts. However, the limited number of groundwater samples used by Calmels et al. (2011) to define both end-members (five) prompts further questions as to the extent of chemical variability in fractured bedrock. The Calmels et al. (2011) paper was not specific about the hydrology of the shallow- and deep-groundwater, leaving questions about flow paths and their separation and the reasons for their activation under specific meteorological and physical conditions.

Of central concern in this chapter is the particular role that combined physical erosion and chemical weathering plays in the redistribution of carbon, sulphur and oxygen between the atmosphere and solid Earth. As was discussed in Chapter 1, the cycling of carbon and sulphur in hydrogeochemical pathways has implications for understanding both the negative (carbonic-acid dissolution of silicate rock) and the positive (sulphuric-acid weathering of carbonate rock) climate-erosion feedbacks. Oxygen is also an important element in biogeochemical cycles, and is linked to the cycling of carbon and sulphur via the burial (atmospheric oxygen (O_2) release) and oxidation (O_2 consumption) of organic carbon (Bolton et al. 2006), which controls O_2 levels over geologic time, and via the oxidative weathering of pyrite, which provides a negative feedback against excessive O_2 variation (Garrels and Perry 1974). A key feature of the carbon, sulphur and oxygen combined cycle is that the rapid oxidative weathering of pyrite can lead to significant production of sulphuric acid (Williamson and Rimstidt 1994; Calmels et al. 2007), which in weathering carbonate rock, returns ancient sedimentary CO_2 to the atmosphere (Walker et al. 1981; Berner et al. 1983). Also of importance in the climate-erosion feedback is the link between physical erosion and the chemical dissolution of silicate rock, which as will be shown later in this chapter, is enhanced in the presence of excess sulphuric acid.

The action of landslides, associated with extreme rainfall and earthquakes (Dadson et al. 2003), readily replenishes mineral surfaces in Taiwan (Das et al. 2012), exposing them to acid dissolution. Furthermore, extensive metasedimentary settings such as the Himalayan mountain chain, containing lithological units with large modal abundances of sulphides (Bordet et al. 1971) and characterised by intense rainfall bouts and frequent landslides (Burbank et al. 1996), typically display variable but overall high rates of pyrite oxidation (Galy and France-Lanord 1999; Turchyn et al. 2013). Together with gypsum dissolution, pyrite oxidation is the main process giving rise to sulphate enrichment in natural waters. Independently implicated in modulating sulphate concentrations in natural waters are the roles of physical erosion, which promotes pyrite oxidation by enhancing connectivity with the atmosphere and by increasing mineral surface area (Calmels et al.

2007; Das et al. 2012), and of a deep biosphere in which bacteria reduce aqueous sulphate that was liberated via pyrite oxidation before it reaches the ocean (Turchyn et al. 2013). Any link between physical erosion and a deep biosphere has thus far eluded observation, but as will be shown later in this chapter, the samples collected from Tunnel 1 show that bacterial sulphate reduction is promoted by the high sulphate concentrations derived from rapid pyrite oxidation following a major landslide.

6.4 General characteristics of natural waters in the Liwu and Choshui catchments

The results of chemical analyses of the groundwater and surface water samples from both settings, together with their basic physical and chemical parameters (temperature, pH and relative drip rates) are presented in Data Table D. Temperature and pH measurements were made on all samples upon collection excepting those from the September 2007 and summer 2010 sample sets. In order to assess chemical gradients that might be related to the physical features of the overlying rock masses, the drip-water samples from the two main tunnels, Tunnel 1 and Tunnel 28, were collected in linear sample arrays distributed in both cases east to west along the length of the tunnel interiors (see Figures 2.11 and 2.13, Chapter 2). In both cases the overlying rock mass was thicker and had a slightly steeper topographical gradient on the east-facing slopes than on the west-facing ridge slopes (see Figures 2.11 and 2.13, Chapter). Additional samples from Tunnel 6 and Tunnel 8, situated approximately 1.5 to 2.0 km from Tunnel 1 along the Bayyang Tunnel Trail and each overlain by approximately 40-50 m of overburden, were collected from approximately midway through these tunnels. It is important to highlight that whilst the tunnels themselves run parallel to topographic contours with less than 200 m between the interiors and the surface, they are situated on steep hillslopes with approximately 2000 m of topographic relief above them.

6.4.1 Temperature and pH of the groundwaters

The temperature of the groundwaters from the Bayyang Tunnel Trail ranged from 20.6 °C to 24.3 °C, and from Tunnel 28 ranged from 18.9 °C to 24.0 °C. The temperatures of the groundwater samples collected from Tunnel 1 in Bayyang slightly decreased along the sampling transect from east to west, but exhibited a lot of scatter (Figure 6.1A). If seasonal atmospheric signals in recharge waters were to some degree attenuated with time/depth in the overlying rock mass, the related temperatures would display a smoothed

variability. Thus, the variability in temperatures rather suggests a strong heterogeneity related to the geological structure and that furthermore, the fracture network is too

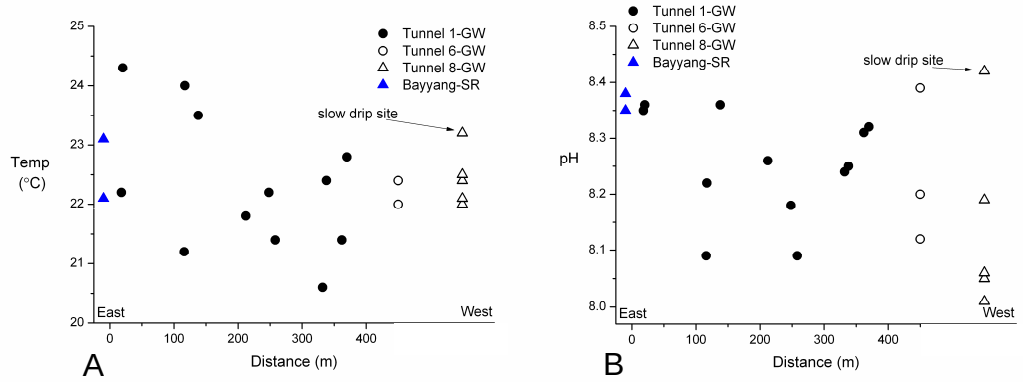

Figure 6.1. Temperature (A) and pH (B) according to tunnel-transect distance in Tunnel 1. Also shown are temperature and pH measurements from Tunnel 6 and Tunnel 8. Note, there is no tunnel-transect distance scale for Tunnels 6 and 8 as these samples were collected 1.5-2 km from Tunnel 1 from approximately midway through the tunnels. A general decrease in temperature was observed with distance in Tunnel 1, possibly reflecting the shorter groundwater residence time in the west portion of the tunnel associated with a decrease in overlying rock-mass thickness. The temperature values of the Tunnel 6 and Tunnel 8 drip-waters were within the range of those from Tunnel 1. One sample from Tunnel 8, which was from a relatively slow drip site, had a somewhat high temperature value. The pH values showed no systematic trends along the sampling transects.

complex for groundwater flow paths to be related directly to rock-mass thickness. Groundwater temperatures from Tunnel 6 and Tunnel 8 were within the range of those from Tunnel 1, with the highest value from the only relatively slow drip (similar drip rate to Tunnel 1) site (Tunnel 8) (Figure 6.1A). In contrast, the temperature of the samples collected in September 2009 (wet season) from Tunnel 28 (19.0±0.2 °C; 2σ, n = 5) were systematically lower than the samples collected there in May 2010 (end of the dry season) (23.4±0.8 °C; 2σ, n = 4) (Figure 6.2A), indicating that the drip waters were influenced by seasonal atmospheric changes, which suggests that the rock mass experiences relatively rapid flushing during recharge. That the groundwater temperatures in Tunnel 28 were lower in September 2009 than they were in May 2010, suggests that the intense rainfall which had characterised the late summer period in 2009 lead to rapid flushing of the rock mass above the tunnel. The relatively elevated temperatures characterising the drip-waters in May 2010 might therefore reflect increased groundwater residence times during the drier winter interval.

In both settings, the pH values were alkaline reflecting solutions buffered by carbonate (both 8.1 to 8.4 for Bayyang and for Tunnel 28). The indices of calcite

saturation (*SI*) were calculated using the PHREEQC geochemical modelling package supplied by the USGS (http://wwwbrr.cr.usgs.gov/projects/GWC_coupled/phreeqc/) (Data Table D). Calculated saturation indices of calcite showed that all samples were super saturated ($SI > 0$), with values ranging from 0.8 to 1.3 in Bayyang and from 0.3 to 0.9 in Tunnel 28. In Tunnel 1, the pH values were relatively homogenous according to the spatial distribution of the sampling transect and the apparent hydrological regime (Figure 6.1,B).

Groundwater pH values from Tunnel 6 and Tunnel 8 were comparable to those from Tunnel 1, and as was the case with the inter-tunnel comparison of temperatures, the only 'slow-drip' water (Tunnel 8) recovered from Tunnels 6 and 8 was similar to the highest values observed in Tunnel 1 (Figure 6.1B). In Tunnel 28, pH systematically decreased as the overlying rock mass decreased, with the highest values similar to that of the spot sample of surface runoff collected 100 m from the tunnel exit (Figure 6.2B). This decreasing trend in pH along the sampling transect in Tunnel 28 corresponded to a similar decrease in the saturation index of calcite (Data Table D), and therefore could indicate an associated decrease in the carbonate buffering of the waters. In both tunnels, the highest pH values correspond to the greatest rock-mass thicknesses and are similar to the surface-water values in the respective vicinities.

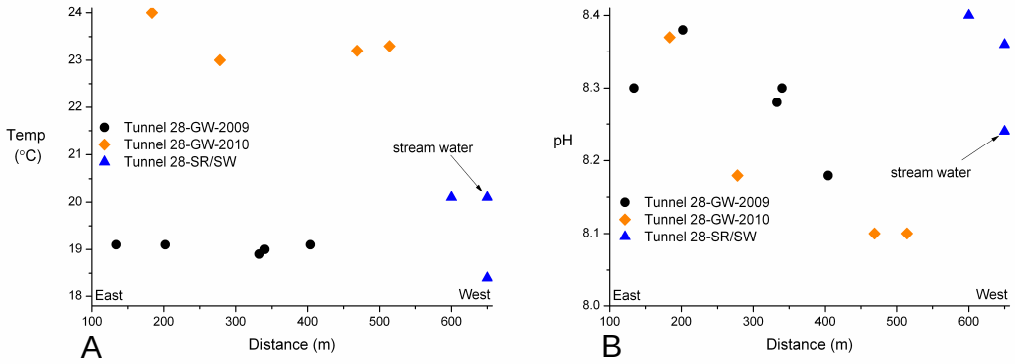

Figure 6.2. Temperature (A) and pH (B) according to tunnel-transect distance in Tunnel 28. The temperatures of the drip-waters sampled in September 2009 were systematically lower than those collected in May 2010 suggesting a seasonal influence and significant hydrological connectivity between the surface and the rock mass. A systematic decrease in pH of the drip-waters was observed from east to west with the highest values similar to that of surface runoff.

6.4.2 Major ion chemistry of the groundwaters

Total dissolved solids (TDS) ranged from 83 ppm to 1,739 ppm along the Bayyang Tunnel Trail, and from 64 ppm to 234 ppm in Tunnel 28. The relatively high values in Bayyang are associated mainly with sulphate concentrations in Tunnel 1, which reached

12,082 µmol.L^{-1} (1,161 ppm), compared to a maximum [SO_4^{2-}] of 1,318 µmol.L^{-1} (127 ppm) in Tunnel 6 and 631 µmol.L^{-1} (61 ppm) in Tunnel 8. The relative proportions of major cations and anions in the groundwater and surface water samples from both locations are shown in Figure 6.3. Major cation chemistry was dominated by Ca^{2+}, which accounted for 42 % to 89 % (average = 69±28%; 2σ, n = 48) of the cationic charge in Bayyang and 56 % to 67 % (average = 63±8 %; 2σ, n = 9) of the cationic charge in Tunnel 28 (Figure 6.3), consistent with the abundance of carbonate bedrock in both settings and the high dissolution rates of carbonates relative to silicate rock (Meybeck 1987; White et al. 1999). Displaying a greater range than Ca^{2+}, Mg^{2+}, which could be derived from primary carbonates and silicates, represented a further 6 % to 54 % (average = 21±24 %; 2σ, n = 48) of the cationic charge in Bayyang (Figure 6.3). In contrast to the large range in Mg^{2+} charge representation in Bayyang, in Tunnel 28, Mg^{2+} represented 27 % to 34 % (average = 30±4 %; 2σ, n = 9) of the cationic charge (Figure 6.3). Also exhibiting a large range in equivalent charge representation in Bayyang was Na^+, the only source of which in this setting is silicate rock, and which accounted for 1 % to 34 % (average = 10±16 %; 2σ, n = 48) of the cationic charge (Figure 6.3). In contrast, Na^+ accounted for just 4 % to 14 % (average = 6±6 %; 2σ, n = 9) of the cationic charge in Tunnel 28 (Figure 6.3). The remainder of the cationic charge in both settings was dominated by K^+, which accounted for up to 3 % in Bayyang and 1 % in Tunnel 28.

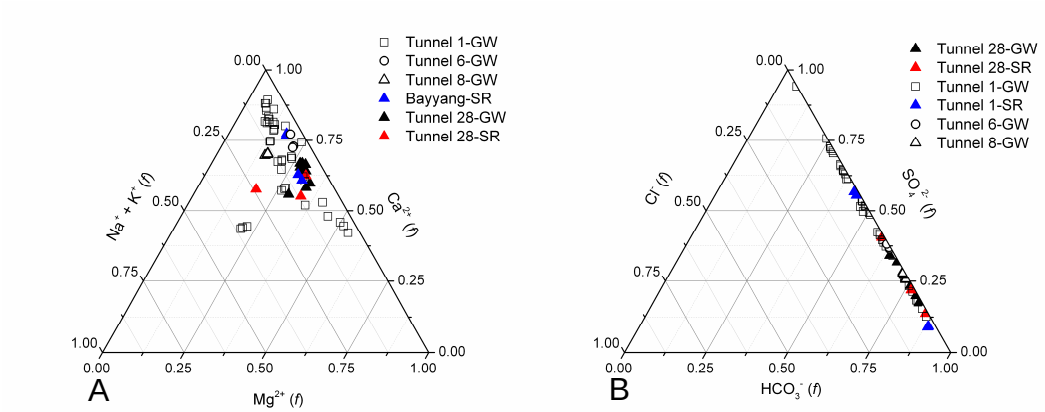

Figure 6.3. Triangular plots showing the relative equivalent fractions of major cation (A) and anion (B) charges of the groundwaters and surface waters from the tunnels at Bayyang and from Tunnel 28 in Fenchihu. In both settings the dominant cation was Ca^{2+}, followed by varying fractions of Mg^{2+} and Na^+. The anionic charge is dominated by varying proportions of HCO_3^- and SO_4^{2-}, with insignificant fractions of Cl^-, in both settings.

In both settings, the anionic charge was dominated by HCO_3^- and/or SO_4^{2-}, with no greater than 2 % of the equivalent negative charge of either set of groundwaters represented by Cl^- (Figure 6.3). There is abundant pyrite present in both settings and there have been no reported occurrences of evaporite minerals. Thus it follows that the dominant presence of SO_4^{2-} in both settings is from the oxidation of pyrite (Yoshimura et al. 2001; Das et al. 2012). With 13 % to 94 % (average = 47±38 %; 2σ, n = 48) of the anionic charge accounted for by SO_4^{2-}, the groundwaters in Bayyang record highly variable rates, and in some samples very high rates, of pyrite oxidation. This is in somewhat of a contrast to Tunnel 28, where [SO_4^{2-}] is less variable, accounting for 18 % to 40 % (average = 27±14 %; 2σ, n = 9) of the anionic charge.

6.5 Mixing of groundwater chemical end-members

As was discussed in Chapter 1, the proportion of carbonate to silicate-derived dissolved mass in natural waters is of central interest in the climate-erosion feedback debate (Garrels and Mackenzie 1967; Négrel et al. 1993; Gaillardet et al. 1999; Galy et al. 1999; Krishnaswami et al. 1999; Quade et al. 2003; Bickle et al. 2005). Major cation ratios normalised to Ca, such as Sr/Ca and Na/Ca can be used in conjunction with knowledge of these ratios in the host rocks to partition Ca between silicate and carbonate sources and thus can resolve variable proportions of altered silicate and carbonate giving rise to natural solutions. However, it is important to consider that the interpretation of trends in cation ratio plots can be complicated by incongruent dissolution and precipitation processes involving parent silicates and carbonates (Bickle et al. 2005), which is particularly likely in regions characterised by high erosion rates and weathering-limited regimes such as Taiwan (Stallard 1995). Notwithstanding, when plotted against each other, the ratios of Sr/Ca and Na/Ca describe the mixing relationships of chemically distinct water masses, water masses which may or may not record incongruent dissolution and precipitation processes.

6.5.1 Molar ratios from Tunnel 1 and the Liwu River

It was discussed in Chapter 5 (Section 5.6.2) how during two typhoons, a discrete hydrological pathway was demonstrated to be activated in the Liwu River catchment, and that the distinct groundwater end-member associated with this activation (‘shallow groundwater’) was apparent in the Sr/Ca and Na/Ca molar ratios of Liwu River water

samples that were collected at high-frequency (up to every four hours) during the two flood events (Calmels et al. 2011). The chemical composition of the shallow-groundwater end-member (Sr/Ca = 1.49; Na/Ca = 0.10) was represented by the mean of two drip-water samples that were collected in 2007 at tunnel-transect distances of 340 m and 380 m, respectively (near the west portion), inside Tunnel 1 (Figure 6.4; see Figure 2.11, Chapter 2).

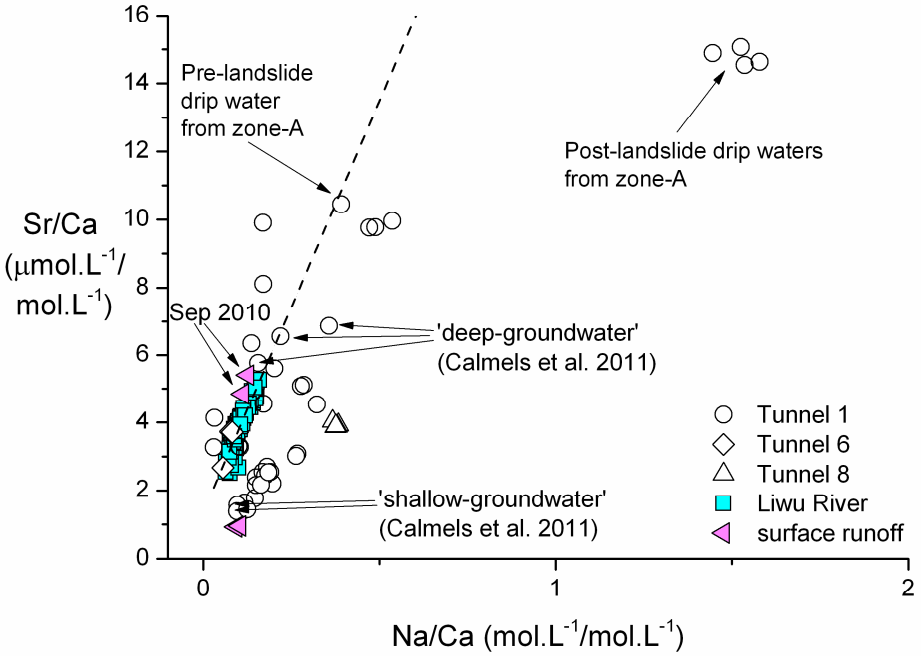

Figure 6.4. Variation of the Sr/Ca ratio as a function of the Na/Ca ratio for the groundwater from Tunnel 1 (open circles), Tunnel 6 (open diamonds), Tunnel 8 (open triangles), surface runoff (pink triangles) and water samples from the Liwu River (blue squares). The dashed line is a best linear fit (R^2 = 0.87) through the 138 samples from the 2002-2008 Liwu River time series (Calmels et al. 2011). The plot shows that the river water samples can largely be explained by the mixing of two previously-defined water masses; surface runoff and deep groundwater. (Not shown are the typhoon samples, which plot close to the shallow-groundwater end-member). Also shown are two new end-members; a very silicate-rich component (zone-A) and a more-evolved shallow-groundwater type (open triangles).

The shallow-groundwater end-member was described as reflecting a slow surface runoff process, i.e. surface runoff that had percolated somewhat through the soil and bedrock, but not to any considerable depth, but which had a significant residence time and thus an altered chemistry relative to a more typically rapid surface runoff.

It is shown in Figure 6.4 that both of the shallow-groundwater samples plot off a binary mixing line between a ‘deep groundwater’ end-member, characterised by a

relatively silicate-rich composition and a 'rapid-surface-runoff' end-member, with a higher calcium component due to its having predominantly reacted rapidly with the more soluble carbonate phase. The binary mixing line is a best linear fit through 138 water samples collected approximately bi-weekly from the main channel of the Liwu River during the period September 2002 to February 2008 (Figure 6.4). The two representative shallow-groundwater samples defined by Calmels et al. (2011) have similar Na^{+}, Ca^{2+} and Sr^{2+} to 14 of the 18 other drip-water samples collected from the western portion of Tunnel 1 and to one drip-water sample collected from 34 m inside the east entrance. These 15 samples consist of four drip-waters from the April 2009 sample set, collected from tunnel-transect distances of 203 m to 342 m; three drip-waters collected in September 2009 from tunnel-transect distances of 248 m to 370 m; three drip-waters collected in May 2010 from tunnel-transect distances of 258 m to 362 m; and five drip-waters from the summer 2010 sample set (Figure 6.4), four of which were collected from tunnel-transect distances of 334 m to 517 m. Also of similar Na^{+}, Ca^{2+} and Sr^{2+} composition to the shallow groundwater end-member were two surface runoff samples (Figure 6.4) that were collected in the Liwu River catchment in September 2009, approximately 14 km from Tunnel 1. The two surface runoff samples that were collected in September 2010 directly off the scar of the October 2009 landslide surface plot along the binary mixing line closer to the silicate end-member in Sr/Ca-Na/Ca mixing space (Figure 6.4).

It was quantified in the Calmels et al. (2011) study that greater than 30 % of the total silicate weathering flux from the Liwu River drainage basin could be attributed to weathering reactions taking place deep in the bedrock. This 'deep groundwater' end-member was defined using three drip-water samples collected from near the east entrance inside Tunnel 1 (Figure 6.4) from tunnel-transect distances of 11 m to 125 m. The deep-groundwater end-member was more enriched in silicate-derived cations (Sr/Ca = 6.39±0.93, Na/Ca = 0.24±0.17; 2σ, n = 3) than were the shallow-groundwater and surface runoff components (Figure 6.4) and was described as being likewise of meteoric origin yet unlike the shallow-groundwater end-member not simply typified by a chemistry reflecting rapid near-surface weathering reactions, such as those dominated by soil-respired CO_2.

The three representative deep-groundwater samples define the silicate-enriched region of the binary mixing array between it and the carbonate-enriched rapid surface runoff end-member (Figure 6.4). These three groundwater samples have similar chemistry to eight of the 17 other drip-waters collected from the east portion of Tunnel 1. These eight other drip-waters similar to the deep-groundwater end-member were collected at tunnel-

transect distances ranging from 13 m to 172 m. They lie on or close to the binary mixing line and each of them exhibits higher Sr/Ca and/or Na/Ca ratios than the representative deep groundwater sample with the lowest Sr/Ca and Na/Ca ratio (Figure 6.4). Of the nine other samples collected from the east portion of Tunnel 1, four lie on the binary mixing line closer to the carbonate end-member and one sample, at 34 m inside the east entrance, plots close to the shallow-groundwater end-member. The remaining four samples that were collected in the east portion of Tunnel 1 plot uniquely off the binary mixing line and have a distinctively silicate-rich chemistry (Sr/Ca = 14.78±0.42, Na/Ca = 1.52±0.10; 2σ, n = 4) (Figure 6.4). These four samples were collected from the same clustered drip site (zone-A) at approximately 15 m inside the east entrance of Tunnel 1 during May to August 2010, and, as will be explored in subsequent sections, record the most dramatic chemical shifts observed in post-landslide groundwater in Tunnel 1.

6.5.2 Rock-mass thickness, primary fabric and the fracture network as controls on groundwater chemistry

That the drip-waters in the western portion of Tunnel 1 were predominantly similar to the shallow-groundwater end-member previously described by Calmels et al. (2011) suggests that hydrological mixing with surface runoff is relatively rapid in this section of Tunnel 1 when compared to mixing between the deep groundwater end-member and rapid surface runoff. The shallow-groundwater end-member might be simply viewed as a stage in the mixing process between rapid surface runoff and deep-groundwater (Calmels et al. 2011), but given that the deep system yields water at all times and that shallow subsurface periodically runs dry, there must be periods of hydrological separation between the two. Such hydrological separation would suggest that different chemical reactions occur in each hydrologically distinct zone. In considering the topographic profile of the ridge through which Tunnel 1 is bored (see Figure 2.11, Chapter 2), the steeper slope of the east-facing ridge side corresponds to a thicker rock mass, through which groundwater could potentially percolate, than the shallower-sloping west-facing ridge portion, which offers a relatively reduced rock-mass thickness for groundwater infiltration and percolation. This potential increase in groundwater residence time associated with rock-mass thickness in the east portion of Tunnel 1 might explain the more evolved chemistry of the groundwater typifying the section (Figure 6.4). Also of potential significance in controlling groundwater residence times in the fractured rock mass above Tunnel 1 is the dip and dip direction of

the primary bedding/fracture planes (52° N/NW). The N/NW dip of the primary fabric might favour a more direct routing of surface runoff from the surface into the west portion of the tunnel. Likewise, percolation through from the surface to the east section of the tunnel would be largely facilitated by secondary fractures, which would potentially be narrower and less well-connected than the factures associated with the primary fabric.

Some of the drip-waters from the respective east and west portions of Tunnel 1 contradict a straightforward hydrological model of decreasing groundwater residence times from east to west. The four drip-water samples from the west portion of Tunnel 1 that plot closer to the deep-groundwater end-member than do the other 14 samples from the west portion of Tunnel 1, the one drip-water sample from 34 m inside the east entrance that plots close to the shallow-groundwater end-member and the four drip-water samples from the east portion of Tunnel 1 that plot close to the surface runoff component, all reflect hydrological heterogeneity of the fracture network and suggest that rock-mass thickness is somewhat a crude proxy for groundwater residence times in fractured bedrock aquifers.

Two of the four-drip water samples from the east portion of Tunnel 1 that plot close to the surface runoff component were collected from drip sites that had conspicuous features associated with them suggestive of their having a relatively direct connection with the surface. The first of these was collected from the nearest drip site inside the east entrance, at a tunnel-transect distance of just 7 m and thus potentially reflected a short fracture network between the surface and the tunnel interior. The second was collected in September 2009 from a small solution cavity, which was approximately 1 m^3 in size with deposits of weathered rock fragments and clay deposits accumulated inside and had surrounding walls that were draped in secondary calcite curtain formations (see Plate 1: DSCF3469, Chapter 2). Upon return to this solution cavity in May 2010, the drip site was dry, suggesting that the percolation of groundwater at this fracture zone is sensitive to rapid changes in recharge. This is in contrast to many of the other drip sites, which, at least as far as can be told from these incidental observations, exhibited no seasonal changes in drip rates.

In addition to the hydrogeochemical mixing trends observed in Tunnel 1, Tunnel 6 and Tunnel 8 along the Bayyang Tunnel Trail exhibited distinctive chemical compositions in molar ratio mixing space that give insight into how the fracture network may control groundwater chemistry. The three drip-water samples from Tunnel 6, one from September 2009 and two from May 2010, plot on the binary mixing line between deep-groundwater and surface runoff in Sr/Ca-Na/Ca mixing space (Figure 6.4). The drip-waters from Tunnel

6 were collected from a large solution cave, which was approximately 20 m long and 4-5 m deep and exhibited both relatively slow and fast-dripping groundwater discharge along several fractures during the entire sampling campaign. The cave was located approximate halfway through Tunnel 6, where the overlying topography was thickest (~40 m). That the drip waters from Tunnel 6 plot on the binary mixing line close to the carbonate end-member in Sr/Ca-Na/Ca mixing space indicates the rapid flushing of the bedrock with a predominant surface runoff component, and indeed explains the presence of the relatively extensive cave, which would be prone to forming during periods of high recharge given rapid connectivity between the tunnel interior and the surface.

In contrast to Tunnel 6, the chemistry of the five drip-waters from Tunnel 8, three collected in September 2009 and two in May 2010, define a unique position in Sr/Ca-Na/Ca mixing space (Sr/Ca = 3.92±0.12, Na/Ca = 0.38±0.01; 2σ, n = 5) (Figure 6.4). These five groundwaters plot off the binary mixing line midway between the shallow-groundwater and deep-groundwater end-members defined by Calmels et al. (2011). As was described in Chapter 2 (Section 2.4.2.5), Tunnel 8 exhibited a continual gushing of groundwater through into the tunnel interior from the surrounding rock mass at a much faster rate than groundwater percolation in Tunnel 6 (or indeed than any of the tunnels), but unlike in Tunnel 6, no cave had developed in Tunnel 8. Also of note in Tunnel 8 was that the rate of groundwater discharge did not appear to diminish at all over the course of the sampling period, which contrasts the transience of the groundwater percolation that led to the small solution cavity in Tunnel 1. Given the rapid discharge of the groundwater in Tunnel 8, the groundwater chemistry might be expected to reflect that of surface runoff, provided that recharge was concurrent with discharge, which was not the case in Tunnel 8 in May 2010. That the chemistry is similar to, yet more evolved than the shallow-groundwater end-member indicates that storage of the groundwater after initial recharge, presumably in a complex network of fractures in the ridges above Tunnel 8, must be important, and that the reason for the rapid groundwater percolation at the point of discharge could reflect an abrupt change in the fracture network, such as would be introduced by a larger fault.

6.5.3 At least two new groundwater end-members

In addition to the ‘shallow’ and ‘deep’ groundwater end-members identified by Calmels et al. (2011), two other components of the hydrogeochemistry in the Liwu River

drainage basin have been established. The first is the most silicate-rich end-member indicated by the four post-landslide drip-water samples from the east portion of Tunnel 1 that plot significantly off the binary line in Sr/Ca-Na/Ca mixing space (Figure 6.4). This post-landslide silicate-rich end-member had greater than four times the Na^+ concentration ($[Na^+]$ = 3248±271 μmol.L^{-1}; 2σ, n = 4) of the deep-groundwater end-member of Calmels et al. (2011) ($[Na^+]$ of 763±390 μmol.L^{-1}; 2σ, n = 3). The second is the more evolved shallow-groundwater-type component found in Tunnel 8 (Figure 6.4), which appears to indicate a longer residence time than the shallow-groundwater end-member described by Calmels et al. (2011). This new shallow-groundwater end-member had greater than three times the Na^+ ($[Na^+]$ = 563±65 μmol.L^{-1}; 2σ, n = 5) of the shallow-groundwater of Calmels et al. (2011) ($[Na^+]$ of 171±62 μmol.L^{-1}; 2σ, n = 2). These two additional groundwater end-members suggest that rather than a binary mixing between two distinct components, a more complex continuum between at least four groundwater end-members characterises the hydrogeochemistry of the rapidly eroding fractured bedrock in Taiwan.

It has been possible here to qualitatively relate the chemistry of these end-members to aspects of the structural confines, but without groundwater flux information, it is not at present possible to quantify the importance of the chemical weathering activity associated with these two new end-members in terms of chemical fluxes. However, as will be fully investigated in Section 6.6, the more silicate-rich end-member, which was specifically related to the effects of landsliding on the hydrogeochemistry, reveals important aspects of the carbon, sulphur and oxygen biogeochemical cycles occurring in fractured bedrock at depth.

6.5.4 Molar ratios from Tunnel 28 and the Choshui River

The variation in Sr/Ca ratios as a function of Na/Ca ratios of the nine drip-water samples from Tunnel 28, of the three nearby surface runoff samples and of the 41 water samples from the Choshui River display a similar pattern to that of the water samples from the Liwu River catchment (Figure 6.5). The river samples, two of the surface runoff samples and three of the groundwater samples plot on a binary mixing trend between carbonate- and silicate-dominated end-members (Figure 6.5). The surface runoff sample that plots below the binary mixing line was from a small stream approximately 2 km from Tunnel 28, whereas the surface sample nearer to the carbonate end-member was runoff from the valley slope adjacent to the stream and the other surface sample that plots closer

to the silicate end-member was runoff from what appeared to be an old landslide scar 100 m from Tunnel 28. This is similar to the trends displayed by surface runoff in the Liwu River catchment, where two of the four surface runoff samples, which were collected off the scar of the October 2009 landslide, plot closer to the silicate end-member than the other two surface runoff samples that were collected from nearby valley slopes. It is likely that the disrupted surfaces in both settings had relatively high abundances of fresh silicate mineral surfaces, which would more readily dissolve than *in situ* silicate bedrock.

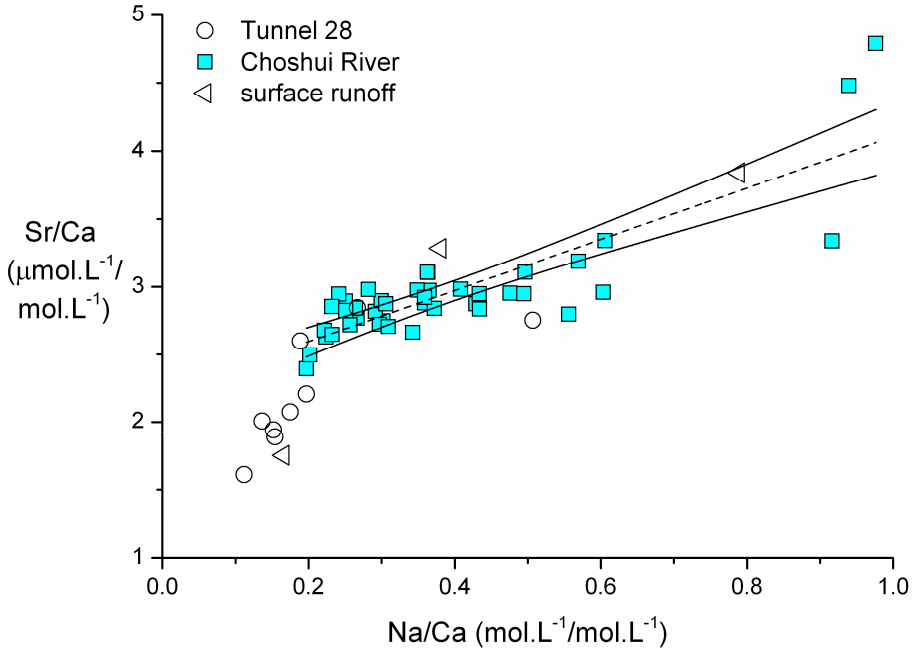

Figure 6.5. Variation of the Sr/Ca ratio as a function of the Na/Ca ratio for the groundwater from Tunnel 28 (open circles), surface runoff (open triangles) and water samples from the Choshui River (blue squares). The dashed line is a best linear fit (R^2 = 0.70) through the 41 samples from the 2005/6 Choshui River time series. The plot shows that the river water samples can largely be explained by the mixing of two water masses similar to those that describe the mixing of the Liwu River water samples. Also similar to the Liwu River catchment is the cluster of groundwater samples close to a shallow-groundwater component.

The groundwater trends in Sr/Ca-Na/Ca mixing space exhibited no direct relationship to the thickness of the overlying rock-mass, indicating the importance of the fracture network in determining groundwater residence times and hence groundwater chemistry. Three of the groundwater samples plot on or close to the binary mixing line (Figure 6.5). Two of these with the highest indices of calcite saturation (0.8 and 0.9) plot close to the carbonate end-member and were collected in September 2009 and May 2010

from tunnel-transect distances of 202 m and 278 m, respectively, in the east portion of the tunnel where pH values were similar to that of surface runoff (8.4 and 8.2 versus 8.3) (Figure 6.2B), reflecting a relatively high degree of carbonate buffering. The third, with an index of calcite saturation of 0.3, plots slightly below the binary mixing line closer to the silicate end-member and was collected at a tunnel-transect distance of 404 m in the west portion of the tunnel where pH values were lower (Figure 6.2B). The remaining six groundwater samples plot in a similar relative position to the shallow-groundwater end-member from the Liwu River catchment.

Based on the presented data-set, the only candidate for a deep groundwater end-member in the Choshui River catchment was the average composition of the three river water samples that plot at the silicate-enriched end of the binary mixing line in Sr/Ca-Na/Ca mixing space (Figure 6.5). Two of these samples were collected during the driest period of the time series, on the 25th of January and the 17th of February 2006, at relatively low discharges (5.38 × 10^{11} L.yr^{-1} (17.06 m^3.s^{-1}) and 2.33 × 10^{11} L.yr^{-1} (7.39 m^3.s^{-1}), respectively; see Figure 5.15, Chapter 5), and the third sample was collected on the 19th of July 2005, during the highest discharge of the time series (1.85 × 10^{14} L.yr^{-1} (5866.65 m^3.s^{-1})) on the day that Typhoon Haiting reached west Taiwan. Approaching these three samples in Sr/Ca-Na/Ca mixing space is the surface runoff sample collected from the landslide scar adjacent to Tunnel 28. However, missing from the groundwater data set from Tunnel 28 are the additional two end-members observed along the Bayyang Tunnel Trail, namely that revealed in the post-landslide samples in Tunnel 1 and that associated with the persistent high discharge in Tunnel 8. The reasons for this must include the differences in rock-mass thickness and structure above the tunnels. The rock mass above Tunnel 28 peaks in thickness at approximately 70 m, which is almost three times less than that above Tunnel 1 (~200 m) and which might explain the absence of the landslide-related silicate-rich end-member from Tunnel 28. The dip and dip direction of the primary fabric in Tunnel 28 (48° N/W), relative to the E/W trend of the tunnel, displays a similar structural juxtaposition to the trend of Tunnel 1 and in both tunnels, the highest pH values were associated with the east-facing ridges (Figure 6.1B and Figure 6.2B). Additionally, the very high drip-water discharges, (as might indicate the rapid release of groundwater that had been previously stored for a significant period of time such as appears to have been the case in Tunnel 8), were not observed in Tunnel 28 during either sampling period, which possibly explains why the more-evolved shallow groundwater end-member that was established in Tunnel 8 was not found in Tunnel 28.

6.6 Landslide-enhanced bacterial activity and CO_2 release

This section documents the weathering responses in the fractured bedrock above Tunnel 1 to the Oct 2009 landslide. The sequence of events surrounding the landslide are summarised in Figure 6.6 and discussed in detail in the following sub-sections.

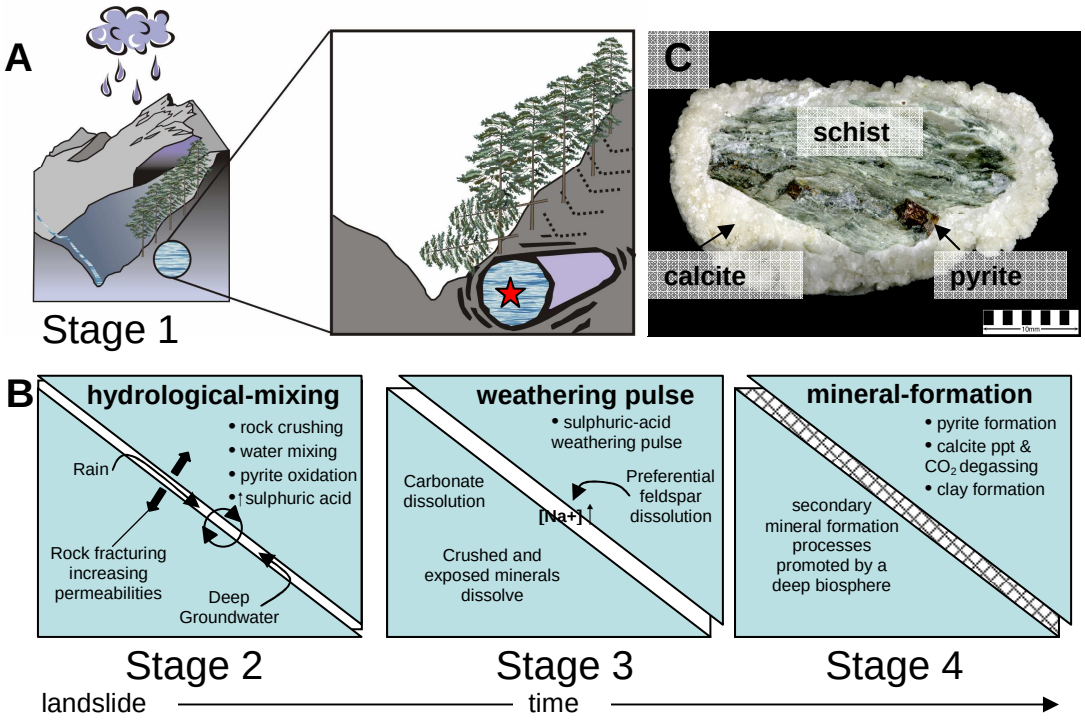

Figure 6.6. Schematic overview of the events surrounding the landslide (A and B) with accompanying photograph of a rock sample from the tunnel surround exhibiting the main mineral phases (B). The landslide (Stage 1) caused rupturing of the underlying fracture network, increasing permeabilities and leading to rapid hydrological flushing and the mixing of meteoric and deep-groundwater fluids (Stage 2). Likewise, the rock crushing effect of the landslide caused the exposure and oxidation of pyrite (see Section 6.6.5 for a discussion based on oxygen isotopes of sulphate), forming sulphuric acid, and increased the fresh mineral surface area of the host lithologies, leading to a carbonate and silicate weathering pulse driven by sulphuric acid (Stage 3). Also, secondary mineral formation processes ensued returning most solutes to near background concentrations, which were measured during Stage 4.

It is concluded that the evolution of the groundwater compositions can be described in terms of four stages, each referring to a specific period in the sequence of the events surrounding the landslide and each characterised by a specific groundwater composition, either measured or inferred. In summary, these are 1) Stage 1, which refers to pre-landslide conditions with a measured groundwater chemistry, 2) Stage 2, which refers to the period immediately after the landslide when groundwaters are inferred to have been significantly

diluted by mixing with meteoric waters, 3) Stage 3, which is inferred to comprise a period of mineral dissolution immediately after Stage 2 driven by pyrite oxidation and 4) Stage 4, which produced the waters sampled eight to eleven months after the landslide by modification of Stage 3 waters by biologically-driven sulphate reduction, calcite precipitation and clay formation (Figure 6.6).

To assess the landslide-induced chemical changes, the average pre-landslide (Stage 1) chemistry of groundwater at zone-A (15 m inside the tunnel entrance tens of metres below the ruptured surface and focused along a 2 m-wide fracture cluster exhibiting drip rates of ~250 mL hr^{-1} at the time of sampling), was ascertained by investigating pre-landslide (Stage 1) chemical trends along the length of the tunnel. As will be shown in Sections 6.6.2 and 6.6.3 there was a good correlation between the concentration of solutes and distance observed along the sampling transect and so best-linear fits between concentration and distance were used to estimate the average pre-landslide (Stage 1) compositions at zone-A. The next step (Stage 2) explains the marked reduction in [Cl^-] from Stage 1 to Stage 4 by mixing the pre-landslide (Stage 1) groundwater with rain (see Section 6.6.1) to define a groundwater composition representing Stage 2. (Cl^-, assumed to be a conservative tracer of groundwater flow, has the same concentration in Stages 2, 3 and 4). Stage 3 is discussed in Section 6.6.2 and represents a groundwater composition that, for all solutes excepting Na^+, reflects an inferred mineral dissolution pulse (and/or solute release pulse). The magnitude of the mineral dissolution pulse is inferred from the observed change in [Na^+] from Stage 2 to Stage 4 (see Section 6.6.2).

The chemical compositions of all groundwater samples collected from Tunnel 1 are presented in Data Table D and a summary of the important groundwater compositions representing the various stages surrounding the landslide is presented in Table 6.1. The following subsections show that systematic chemical organisation of weathering products related to distance through the tunnel before the landslide (Stage 1) was followed by varying degrees of disruption of these trends by Stage 4, with the most notable observed changes seen in [Na^+] (Section 6.6.2), the oxygen isotopic composition of aqueous sulphate ($\delta^{18}O_{SO4}$, Section 6.6.5) and the sulphur isotopic composition of aqueous sulphate ($\delta^{34}S_{SO4}$, Section 6.6.6).

Table 6.1 Chemical compositions of groundwaters from zone-A, at various pre-and post-landslide stages. Ions are in μmol L^{-1}. Isotopes are in ‰. Uncertainties are 2 standard errors (see Section 6.6.1.1).

	Na^+	K^+	Ca^{2+}	Mg^{2+}	SO_4^{2-}	Cl^-	Sr^{2+}	HCO_3^-	SiO_2	$^{87}Sr/^{86}Sr$	$\delta^{13}C_{DIC}$	$\delta^{34}S_{SO4}$	$\Delta^{18}O_{SO4}$ [b]
average before (Stage 1)	827± 86	217± 35	3569± 262	2738± 501	4636± 578	74± 11	27± 3	4341± 427	204± 60	0.707625± 0.000944	−1.63± 2.89	−12.01± 4.05	10.6± 4.4
average post-hydrological-mixing (Stage 2) (Inferred)	305± 55	80± 22	1307± 166	1001± 318	1700± 367	31± 3	10± 2	1585± 271	74± 38	-	−7.87± 2.89	-	-
average after (Stage 4)	2573± 595	136± 3	2660± 460	1257± 201	2668± 129	31± 3	32± 1	5177± 481	222± 1	0.709001± 0.000103	−2.77± 0.55	4.83± 6.26	18.3± 1.0
Rain [a]	4	1	7	3	13	6	trace	trace	trace	-	-	-	-

a, Calmels et al. (2011)
b, $\Delta^{18}O_{SO4} = \delta^{18}O_{SO4} - \delta^{18}O_{H2O}$ (see Section 6.6.5 for discussion)

6.6.1 Post-hydrological-mixing (Stage 2)

The $58.5\pm^{11.7}_{8.6}$ % (see Section 6.6.2.1 for calculation of upper- and lower-bound error estimates) drop in zone-A [Cl^-] (Figure 6.7) is inferred to reflect mixing of the existing groundwaters with Stage 1 compositions with water from a meteoric source that had undergone negligible evapotranspiration. It is thought that the landslide increased permeabilities causing hydrological flushing of underlying bedrock fractures and the rapid through-flow of meteoric water (Figure 6.6). Similar hydrological changes in the upper crust following earthquakes have been attributed to co-seismic permeability increases (Rojstaczer et al. 1995).

During this initial response to the landslide, it seems most probable that the dilution of the pre-landslide groundwater was by rain with the mixture containing 64 % of its water from rain and 36 % from the average pre-landslide zone-A groundwater. If the dilutant had had the composition of rapid surface runoff or shallow-groundwater, unrealistically large contributions from these end-members would be required. The Stage 2 water compositions are thus calculated (see Section 6.6.1.1) by mixing 36 parts of Stage 1 waters (the average pre-landslide solute concentrations from zone-A) with 64 parts of rain water (Table 6.1).

6.6.1.1 Post-hydrological-mixing calculation

Calculated estimates of post-hydrological-mixing compositions (Stage 2) for a given element X_i ($[X_i]_{post\text{-}mix}$) are given by:

$$[X_i]_{post\text{-}mix} = [[X_i]_{before} \times (1 - f)] + ([X_i]_{rain} \times f) \quad (6.1)$$

where $[X_i]_{before}$ is the average concentration of element X_i in pre-landslide (Stage 1) groundwater (Table 6.1; see Section 6.6.2), $[X_i]_{rain}$ is the concentration of element X_i in rain (Calmels et al. 2011) and f is the fraction of rain in the pre-landslide (Stage 1) groundwater. The post-hydrological-mixing (Stage 2) compositions are given when 64 % rain is mixed with the pre-landslide (Stage 1) end-member, which reflects the difference between pre- and post-landslide (Stage 1 and Stage 4) [Cl^-] (Table 6.1). The uncertainty in $[X_i]_{post\text{-}mix}$ at 2 mean standard errors (*SE*) $((\sqrt{\sum}\sigma^2[X_i]/(n - 1))/\sqrt{n})$, is therefore given by $0.64 \times SE_{[Xi]before}$, where $SE_{[Xi]before}$ is the respective uncertainty in $[X_i]_{before}$ given by the 95 % confidence banding around the best-fit linear fits through all pre-landslide (Stage 1) samples versus distance along the tunnel interior (see Sections 6.6.2 and 6.6.3).

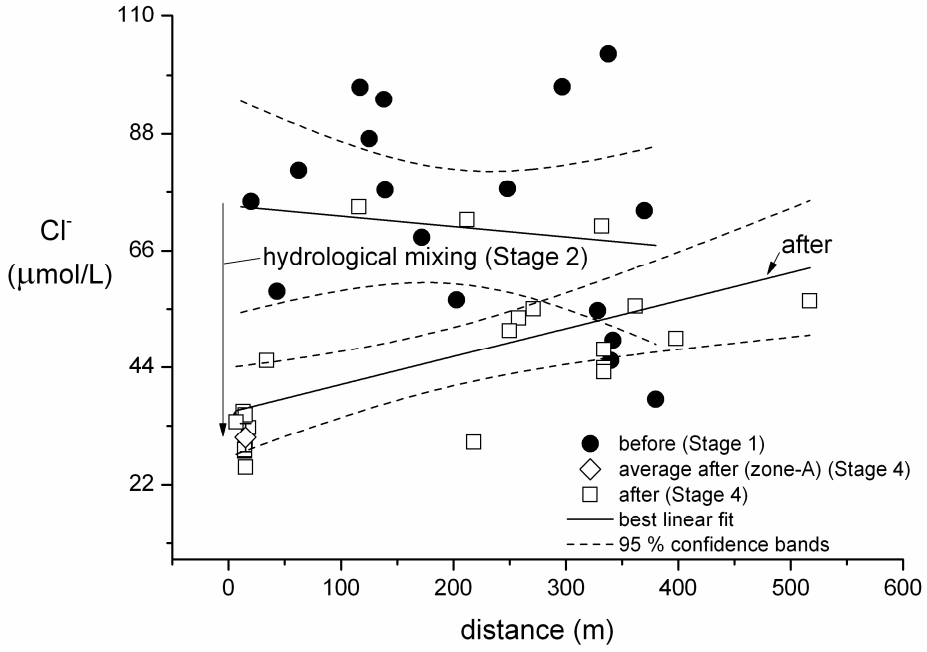

Figure 6.7. Behaviour of Cl^- in pre- and post-landslide groundwater versus distance along the tunnel interior. The [Cl^-] drop in post-landslide (Stages 2-4) groundwater shows how the increased permeabilities in zone-A following the landslide permitted the rapid influx of meteoric water into the fracture network. Error bars are 2SE of the population means.

6.6.2 Mineral dissolution pulse indicated by Na^+ enrichment

A striking feature of the inferred change (Stage 2 to Stage 4) in groundwater chemistry resulting from the October 2009 landslide is the factor of $8.44 \pm^{4.23}_{2.94}$ rise in zone-A $[Na^+]$ ($[Na^+]_{after}/[Na^+]_{post\text{-}mix}$, where $[Na^+]_{after}$ and $[Na^+]_{post\text{-}mix}$ are the respective concentrations of sodium in post-landslide (Stage 4) and post-hydrological-mixing (Stage 2) compositions) (Figure 6.8). The 0.2±0.1 % increase in the $^{87}Sr/^{86}Sr$ ratio and a shift from an 8 % to a 26 % silicate-derived solution ($(Na^+ + K^+)/\sum$cations + anions) (Table 6.1), indicate that the landslide stimulated a pulse of Na-bearing silicate dissolution, the proceeds of which continued to issue from the ruptured fracture network over the series of months following the event. Any potential later recovery in $[Na^+]$ compared to pre-landslide (Stage 1) values to have occurred was not seen within the sampling period. Thus, for the purpose of estimating the degree of mineral dissolution to have occurred as a result of the landslide, it is assumed that Na^+, which is least likely to have been incorporated into secondary minerals over the timescales involved, behaved conservatively.

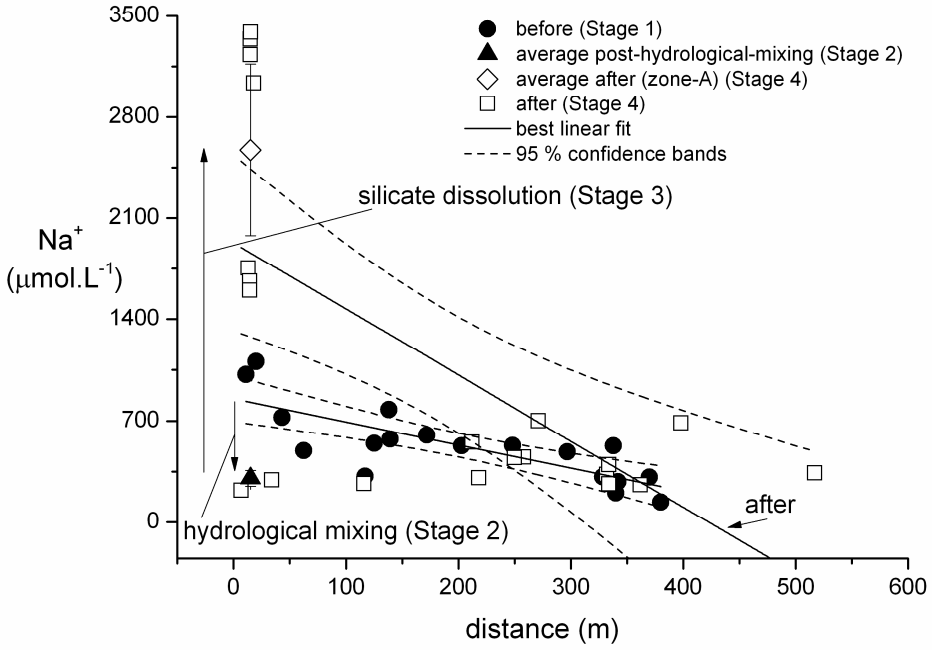

Figure 6.8. Behaviour of Na^+ in pre- and post-landslide groundwater versus distance along the tunnel interior. The surplus sulphuric acid generated by the oxidation of pyrite caused the dissolution of Na-bearing mineral phases by a factor of 8.44 relative to the post-hydrological-mixing (Stage 2) concentration in zone-A (Table 1). It is assumed that during secondary mineral formation processes, $[Na^+]$ behaved conservatively. Error bars are 2SE of the population means.

As will be shown using the carbon isotopic composition of dissolved inorganic carbon ($\delta^{13}C_{DIC}$) in Section 6.6.4, sulphuric acid was the main weathering agent, which would presumably indiscriminately attack silicate and carbonate phases. This implies that the $8.44 \pm^{4.23}_{2.94}$ rise in [Na^+], or the 'weathering factor' (*WF*), should represent the minimum degree of alteration to have been incurred by all mineral phases present. To test this, post-hydrological-mixing (Stage 2) concentrations for a given element X_i were multiplied by $8.44 \pm^{4.23}_{2.94}$ to give calculated 'post-weathering' compositions (Stage 3) (see Section 6.6.2.1), which were then compared to measured post-landslide compositions (Stage 4). As will be shown in Section 6.6.3, most measured post-landslide (Stage 4) solutes appear to indicate significantly less cumulative enrichment than [Na^+].

Similar absolute increases in solutes derived from the seismically-related temperature-driven alteration of albite were reported in brecciated horizons at >1 km-depth along active zones of the Chelungpu Fault, Taiwan (Ishikawa et al. 2008), but it is shown by the change in [Na^+] here that at relatively shallower depths, significant silicate dissolution is triggered by the action of landslides.

6.6.2.1 Post-weathering (Stage 3) composition calculation

Calculated estimates of post-weathering (Stage 3) compositions for a given element X_i ($[X_i]_{post\text{-}weath}$) are based on the change observed between post-hydrological-mixing (Stage 2) and post-landslide (Stage 4) Na^+ concentrations, assuming all phases are congruently dissolved:

$$[X_i]_{post\text{-}weath} = [X_i]_{post\text{-}mix} \times ([Na^+]_{after}/[Na^+]_{post\text{-}mix})^* \quad (6.2)$$

where the * denotes the weathering factor of $8.44 \pm^{4.23}_{2.94}$ discussed above. Although all the solutes except Mg^{2+} are significantly enriched in measured post-landslide (Stage 4) compositions compared to inferred post-hydrological-mixing (Stage 2) compositions (Table 6.1), the magnitudes of these enrichments are significantly less than that of Na^+. The calculated post-weathering (Stage 3) compositions, for all solutes other than Na^+, are greater than the measured post-landslide (Stage 4) compositions. However, the signal-to-noise ratios relating the differences between post-hydrological-mixing (Stage 2) and measured post-landslide (Stage 4) compositions ($([X_i]_{post\text{-}landslide} - [X_i]_{post\text{-}mix})/(SE_{post\text{-}landslide}$

+ $SE_{\text{post-mix}}$)) are all, excepting Mg^{2+}, greater than one, ranging from 1.95 in the case of SO_4^{2-} to 8.34 in the case of Sr^{2+} (Table 6.1). These significant signal-to-noise ratios indicate that all solutes excepting Mg^{2+} were enhanced by the weathering pulse (Stage 3) following the landslide.

A Max-Min method was used to calculate upper- and lower-bound error estimates on the observed weathering factors for a given element X_i ($[X_i]_{\text{after}}/[X_i]_{\text{post-mix}}$) at 2 mean standard errors (SE) ($(\sqrt{\sum}\sigma^2[X_i]/(n-1))/\sqrt{n}$), as follows:

$$\text{upper bound } SE_{WF} = ([X_i]_{\text{after}} + SE_{[Xi]\text{after}})/([X_i]_{\text{post-mix}} - SE_{[Xi]\text{post-mix}}) \quad (6.3)$$

$$\text{lower bound } SE_{WF} = ([X_i]_{\text{after}} - SE_{[Xi]\text{after}})/([X_i]_{\text{post-mix}} + SE_{[Xi]\text{post-mix}}) \quad (6.4)$$

6.6.3 Other solutes versus distance in Tunnel 1

This section assesses the comparison between calculated post-weathering compositions (Stage 3) (Equation 6.2) and measured post-landslide (Stage 4) compositions. Despite the $8.44 \pm^{4.23}_{2.94}$ increase in $[Na^+]$ and carbon isotopic evidence suggesting that the weathering pulse was driven by the action of sulphuric acid (see Section 6.6.4 and Figure 6.11), which would readily dissolve the carbonate mineral phases present, the behaviours of $[SO_4^{2-}]$ and $[Ca^{2+}]$, although less organised than that of $[Na^+]$, suggest that most SO_4^{2-} and Ca^{2+} concomitantly released was recaptured by sulphate reduction and calcite formation during the months following the landslide (Figure 6.9A,B).

In the case of the sulphuric acid-driven dissolution of a Na-bearing silicate mineral, SO_4^{2-} and Na^+ will be released in a 1:2 molar ratio, as shown by the following simplified stoichiometric formula:

$$2NaAlSi_3O_8 + H_2SO_4 \rightarrow 2Na^+ + SO_4^{2-} + 6SiO_{2(aq)} + 2AlOOH \quad (6.5)$$

and likewise in the case of the sulphuric acid-driven dissolution of a carbonate mineral, SO_4^{2-} and Ca^{2+} are expected to be released in a 1:2 molar ratio:

$$2CaCO_3 + H_2SO_4 \rightarrow 2Ca^{2+} + 2HCO_3^- + SO_4^{2-} \quad (6.6)$$

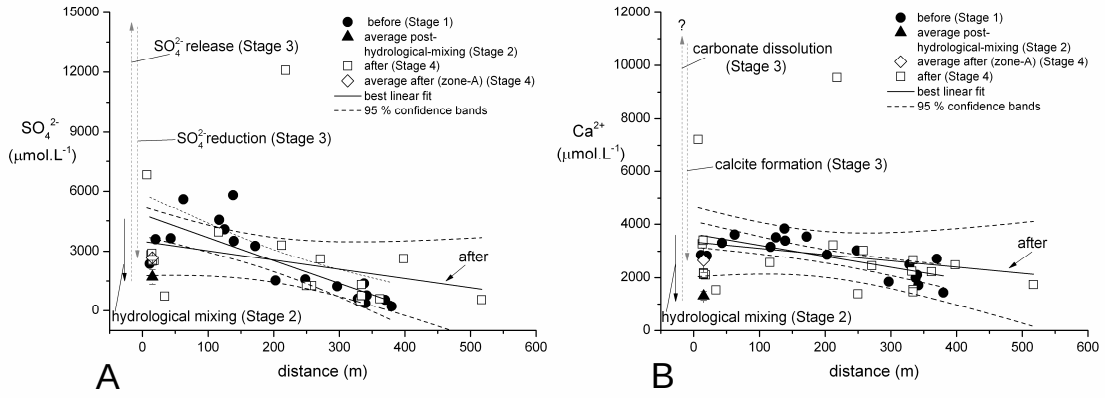

Figure 6.9. The behaviour of SO_4^{2-} (A) and Ca^{2+} (B) in pre- and post-landslide groundwaters as a function of distance along the sampling transect in Tunnel 1. Carbon isotopes (Figure 6.11) implicate the role of sulphuric acid in driving the weathering pulse evidenced by the [Na^+] spike, but post-landslide (Stage 4) zone-A [SO_4^{2-}] shows that secondary sulphide formation occurred in the months following the landslide, depleting surplus SO_4^{2-} to below background concentrations. Some degree of carbonate dissolution was likely to have occurred during the sulphuric acid-driven weathering pulse, but any liberated Ca^{2+} was returned to near background concentrations during secondary calcite precipitation driven by CO_2 degassing and pH changes (see Figure 6.11). Error bars are 2SE of the population means.

Therefore, the $1.57 \pm^{0.53}_{0.34}$ observed increase in SO_4^{2-} and the $2.03 \pm^{0.70}_{0.54}$ observed increase in Ca^{2+} (from Stage 2 to Stage 4), when compared to the $8.44 \pm^{4.23}_{2.94}$ increase in [Na^+], indicate that a significant degree of secondary SO_4^{2-} uptake followed the weathering pulse (Stage 3) and that, unless 100 % incongruent dissolution of silicate relative to carbonate mineral phases occurred, some degree of secondary Ca^{2+} uptake also ensued. As will be shown below in Section 6.6.4, the excess acidity produced by the oxidation of pyrite was buffered, at least in part, by the dissolution of carbonate, yet stoichiometric considerations demand some degree of incongruent dissolution favouring silicate over carbonate weathering.

The behaviour of other solutes (Mg^{2+}, K^+, Sr^{2+}, SiO_2) was also disrupted to varying degrees by the landslide (Figure 6.10A-D; Table 6.1). However, as was the case for SO_4^{2-} and Ca^{2+}, near-background concentration levels in other solutes at zone-A were observed during post-landslide (Stage 4) sampling.

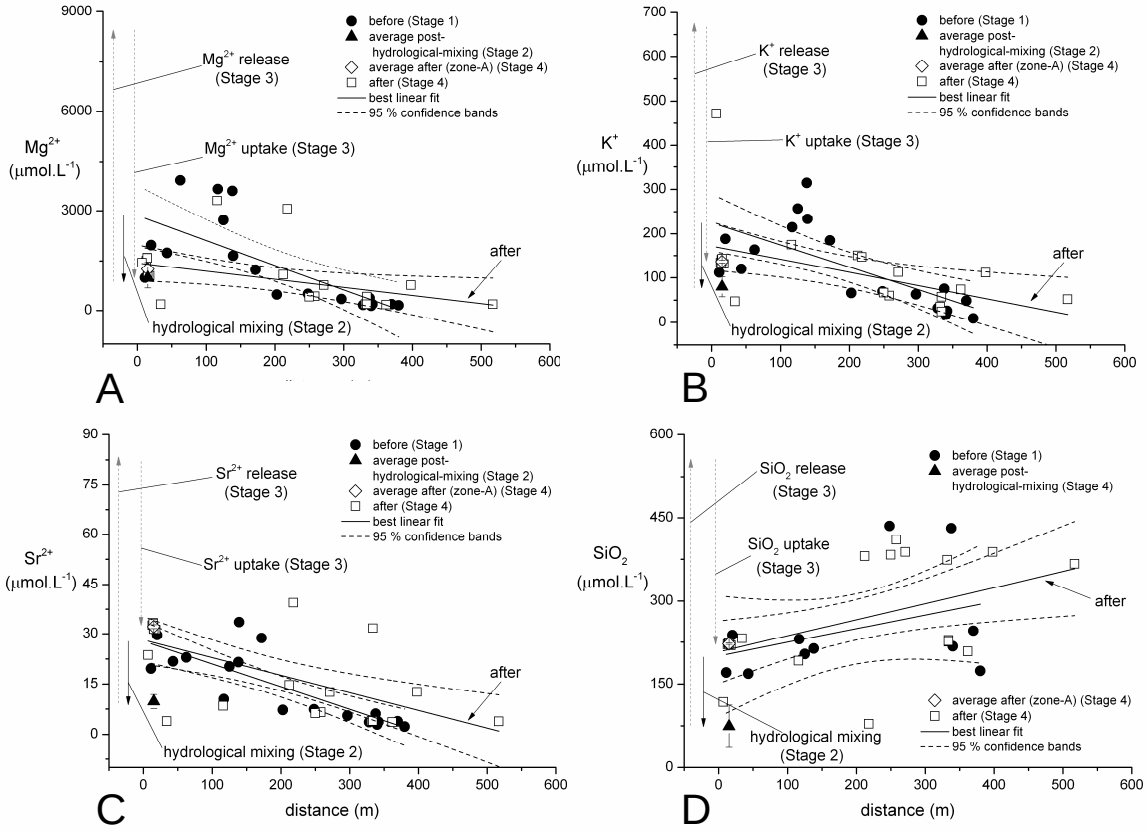

Figure 6.10. The behaviour of Mg^{2+} (A), K^{+} (B), Sr^{2+} (C) and SiO_2 (D) in pre- and post-landslide groundwaters as a function of distance along the sampling transect in Tunnel 1. The weathering pulse evidenced by the post-landslide (Stage 4) observed increase in Na^{+} was not seen in other solutes, suggesting that their post-landslide (Stage 4) compositions had been returned to background concentrations by secondary mineral formation processes.

Dissolved silica exhibited little change after the landslide, perhaps due to the formation of kaolinite following Na^{+} release from albite. In taking up the excess aluminium following albite dissolution, the formation of kaolinite is compatible with the concentrations of SiO_2 (average = 258±186 μmol.L^{-1}; 2σ, n = 32; max = 435 μmol.L^{-1}, min = 79 μmol.L^{-1}) (Drever 1988, Figure 16.2). The cations Mg^{2+}, K^{+} and Sr^{2+} would be equally as likely to dissolve as would Na^{+}, yet will more readily form and/or adsorb to clay minerals than will Na^{+} (and Ca^{2+}). Thus, the mechanisms of clay formation and adsorption can be invoked here to explain the relative depletion of these elements following the landslide (Table 6.1). For example, the excess Mg^{2+}, likely to have been released during the weathering pulse from the primary chlorites that are abundant in the schist formations in the region, and K^{+}, presumably from K-feldspar, would have formed, or have been incorporated into, phases such as smectite and vermiculite, the common solid products of

schist weathering. For this to have been the case, clay mineral formation would have had to have occurred predominantly within the fracture network before the outflow of water.

6.6.4 Sulphuric acid and incongruent dissolution

This section details the modelling of the changes in dissolved inorganic carbon ($\delta^{13}C_{DIC}$) and Ca^{2+} related to pyrite oxidation, SO_4^{2-} reduction and calcite dissolution/precipitation. Rock alteration by sulphuric acid produces water with a carbon isotopic composition of dissolved inorganic carbon ($\delta^{13}C_{DIC}$) reflecting that of the host carbonate, whereas the involvement of carbonic-acid in mineral dissolution imparts the combined isotopic fingerprint of the carbon bound by the acid (a product of atmospheric CO_2 and soil-respired CO_2) (for Taiwan = −22.6 ‰ (Hilton et al. 2010; Cerling et al. 1991)) and the rock (Galy and France-Lanord 1999). A useful way to look at the co-variation of sulphuric and carbonic acids in aqueous solutions is to plot $\delta^{13}C_{DIC}$ against the equivalent ratio of sulphate to bicarbonate $[SO_4^{2-}]/([SO_4^{2-}] + [HCO_3^-]$, termed X_{SO4} (Galy and France-Lanord 1999) (Figure 6.11).

The $\delta^{13}C_{DIC}$ of the carbonate end-member of the tunnel lithology, ascertained by first leaching whole rock carbonate (Section 3.3.8.2, Chapter 3) is −1.67±0.18 ‰ (2σ, n = 4), indistinguishable from the average pre-landslide groundwater value (−1.63±2.89 ‰) (Figure 6.11) and significantly heavier than the product of carbonic-acid dissolution, demonstrating that carbonate dissolution by sulphuric acid is a dominant background (Stage 1) process. Still dominated by sulphuric-acid driven alteration of carbonate is the average post-landslide (Stage 4) groundwater ($\delta^{13}C_{DIC}$ = −2.77±0.55 ‰) (Figure 6.11), but the change in cation ratios suggest a shift from at least 8 % to a minimum of 26 % derived from silicate minerals (($Na^+ + K^+$)/∑cations + anions) following the landslide (Table 6.1). The initial (Stage 2) $\delta^{13}C_{DIC}$ prior to any calcite precipitation would have reflected a mixture between the deep-groundwater end-member, meteoric water and soil-respired HCO_3^- sources, introduced together by the landslide-driven increase in permeability.

Secondary calcite precipitation may be driven by 1) degassing of CO_2, 2) pH changes driven, for example, by silicate dissolution and/or SO_4^{2-} reduction or 3) by a combination of the two. The different mechanisms can be distinguished by $\delta^{13}C_{DIC}$ changes. To assess the mechanism of secondary calcite formation, the behaviour of $\delta^{13}C_{DIC}$ was modelled by adjusting the post-hydrological-mixing (Stage 2) $\delta^{13}C_{DIC}$ composition ($\delta^{13}C_{DIC\text{-}post\text{-}mix}$) so that the Stage 3 chemical pathway described by Rayleigh distillation

would lead to the target $\delta^{13}C_{DIC}$ value of the observed mean post-landslide (Stage 4) zone-A groundwater ($\delta^{13}C_{DIC\text{-}post\text{-}landslide}$) (−2.77±0.55 ‰) (Figure 6.11). For the simple Rayleigh model a combined degassing and precipitation equilibrium fractionation factor (α) (0.9950) (average of 0.9980 and 0.9920) was used based on the following simplified stoichiometric formula:

$$Ca^{2+} + 2HCO_3^- \leftrightarrow CO_2 + CaCO_3 + H_2O \quad (6.7)$$

where α = 0.9920 for the left-hand side of Equation 6.7 reflects degassing and α = 0.9980 for the right-hand side of Equation 6.7 represents precipitation (Mook et al. 1974). The following equation describes the behaviour of $\delta^{13}C_{DIC}$ accordingly:

$$\delta^{13}C_{DIC\text{-}remain} = \delta^{13}C_{DIC\text{-}post\text{-}mix} + 1000 \times (f^{(\alpha - 1)} - 1) \quad (6.8)$$

where $\delta^{13}C_{DIC\text{-}remain}$ is the stable carbon isotopic composition of the remaining fluid after fractional secondary calcite precipitation driven by degassing.

An initial post-weathering (Stage 3) X_{SO4} value of 0.68, based on $[SO_4^{2-}]_{post\text{-}weath}$ = 14360 μmol.L^{-1} (Equation 6.2) and $[HCO_3^-]_{post\text{-}weath}$ = 13382 μmol.L^{-1} (Equation 6.2) would reflect the input of surface runoff (high HCO_3^-/SO_4^{2-} ratios (Calmels et al. (2011)) and would require up to 81 % secondary sulphide formation to transform the calculated post-weathering (Stage 3) compositions to the measured post-landslide (Stage 4) compositions (discussed below in Section 6.6.6) (Table 6.1). Decreasing the degree of carbonate dissolution assumed to have occurred during the weathering pulse, and thereby the amount of secondary carbonate formation, would result in having to increase the inferred isotopic value of post-hydrological-mixing (Stage 2) $\delta^{13}C_{DIC}$ and thus reduce the amount of soil-derived HCO_3^- ($\delta^{13}C_{DIC}$ = −22.6 ‰, Hilton et al. 2010; Cerling et al. 1991) in surface fluids inferred to have been mixed with the average pre-landslide (Stage 1) end-member (Figure 6.11).

Taking the simplest of scenarios, whereby the magnitude of Na^+ increase is equal to that of HCO_3^-, (if the reactions described in Equations 6.5 and 6.6 had occurred to equal degrees), a post-hydrological-mixing (Stage 2) $\delta^{13}C_{DIC}$ composition of −7.87 ‰ would require up to 61 % HCO_3^- incorporation into secondary calcite to transform calculated post-weathering (Stage 3) compositions to the measured post-landslide (Stage 4) compositions (Table 6.1; Figure 6.11). The expected $\delta^{13}C_{DIC}$ value for rain fully

equilibrated with the atmosphere would be ~0 ‰, so the inferred $\delta^{13}C_{DIC}$ value of post-hydrological-mixing (Stage 2) groundwater (−7.87 ‰) reflects that this groundwater had equilibrated with/incorporated carbon derived from organic matter. However, during secondary calcite formation one mole of Ca^{2+} is incorporated into the solid for every two moles of HCO_3^- (Equation 6.7) and so given the 1:1 Ca^{2+}:HCO_3^- molar ratio resulting from the sulphuric acid-driven dissolution of carbonate (Equation 6.6), an excess of Ca^{2+} would be expected in the post-landslide (Stage 4) drip-waters if silicate and carbonate dissolution had been congruent.

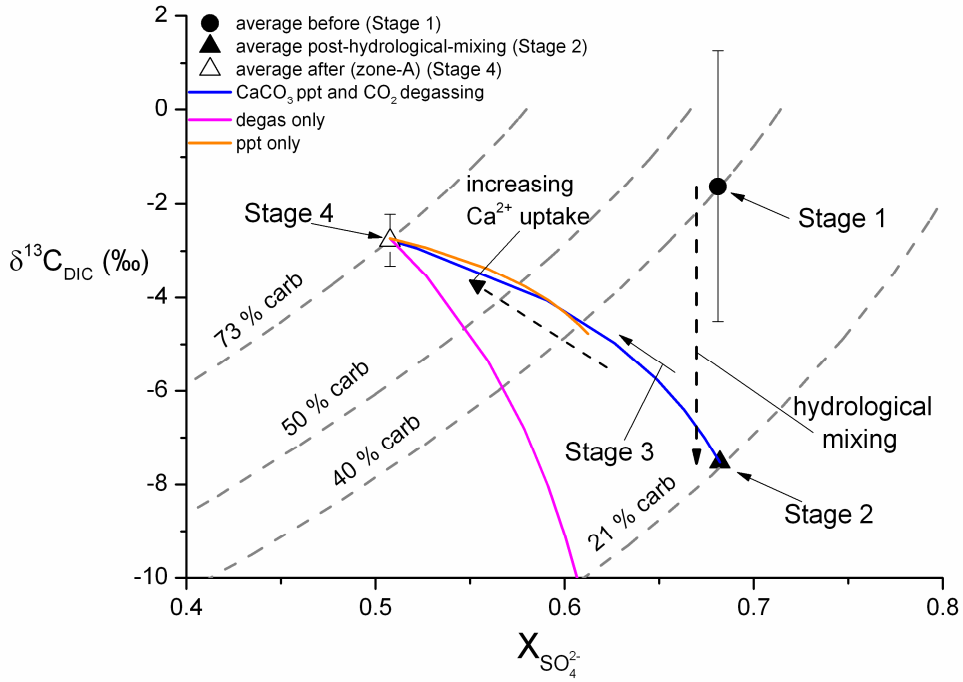

Figure 6.11. The covariation of X_{SO4} ($[SO_4^{2-}]/([SO_4^{2-}] + [HCO_3^-])$) and $\delta^{13}C_{DIC}$ in zone-A drip-waters. The mixing space describes water composition according to the relative indiscriminate alteration of silicate and carbonate rock by varying proportions of biologically-mediated-carbonic and sulfuric acids. Dashed curves represent mixtures that have not undergone any secondary mineral formation (Galy and France-Lanord 1999). The $\delta^{13}C_{DIC}$ of soil CO_2 in Taiwan is −22.6 ‰ (Hilton et al. 2010; Cerling et al. 1991). The $\delta^{13}C_{DIC}$ of the secondary-calcite end-member is −1.67±0.18‰ close to the pre-landslide groundwater value (−1.63±2.89 ‰), which is characteristic of carbonate dissolution by sulphuric acid. Post-landslide hydrological mixing (Stage 2) of surface and deep end-members causes an immediate drop in $\delta^{13}C_{DIC}$, reflecting dissolved carbon input from the surface. The solid lines describe HCO_3^- incorporation into secondary calcite driven by CO_2 degassing (pink), precipitation (orange) and combined degassing + precipitation (blue).

Shown in Figure 6.11 are three model curves (solid lines) that describe the secondary uptake up HCO_3^- into calcite based on 1) CO_2 degassing with no carbonate precipitation, 2) carbonate precipitation with no CO_2 degassing and 3) combined CO_2 degassing and carbonate precipitation. The first of these models would imply an excess of Ca^{2+} in post-landslide (Stage 4) zone-A drip-waters unsupported by observation or by stoichiometric considerations. Furthermore, given the pervasive development of secondary calcite observed inside the tunnel's fractured surround it is unlikely that CO_2 degassing was unaccompanied by carbonate formation. The second model is possible, but all drip-waters appeared to be degassed at the time of collection. The third model, carbonate precipitation driven by CO_2 degassing (and potentially by SO_4^{2-} reduction (Garrels and Lerman 1984)), is thus preferred.

Therefore, given the stoichiometric considerations outlined in Equations 6.5, 6.6 and 6.7, the $\delta^{13}C_{DIC}$-Ca^{2+}-X_{SO4} modelling suggests that incongruent dissolution of the host lithology occurred, that is, preferential silicate over carbonate weathering, despite the readiness with which sulphuric acid will attack carbonate mineral phases. This inference is supported by there being large (> 1 mm) euhedral crystals of pyrite, generally found with rusted surfaces, and a finer-grained anhedral pyrite mass both abundantly embedded in the schist surrounding the tunnel (Figure 6.6). Presumably localised zones (with respect to the rock) associated with this silicate-hosted pyrite mass underwent rapid oxidation following the landslide with the liberated sulphate forming sulphuric acid, which then preferentially dissolved the silicate phases as they were in the immediate vicinity of the redox zones.

6.6.5 Insight from oxygen isotopes

A useful tool for assessing the mechanisms of oxidative weathering of pyrite in natural waters is the oxygen isotopic composition of aqueous sulphate ($\delta^{18}O_{SO4}$), which is set during the formation of aqueous SO_4^{2-} and which does not undergo subsequent oxygen isotope exchange with water (Lloyd 1968). The oxidative weathering of pyrite can proceed in an oxic environment using atmospheric oxygen (O_2) as the oxidant or in a reducing environment where oxidation is usually coupled to iron reduction. The various sources of sulphate resulting from different weathering pathways plot in distinct sulphur-oxygen isotope (sulphur isotopic composition of aqueous ($\delta^{34}S_{SO4}$) versus $\delta^{18}O_{SO4}$) space (Figure 6.12A). In an oxic environment, such as would be expected in the fractured subsurface of Tunnel 1 following the October 2009 landslide, the oxidative weathering of pyrite produces $\delta^{18}O_{SO4}$ derived from a mixture of the oxygen atoms in the atmosphere ($\delta^{18}O_{atm}$ =

23.5 ‰) and those in meteoric water ($\delta^{18}O_{H2O}$). Thus, when normalised to the isotopic composition of the water, ($\delta^{18}O_{SO4} - \delta^{18}O_{H2O}$, termed $\Delta^{18}O_{SO4}$), the post-landslide zone-A drip-waters should record a shift towards higher $\Delta^{18}O_{SO4}$ values, which would reflect that pyrite oxidation proceeded using an increased proportion of atmospheric oxygen (O_2) due to the opening up of the fracture network.

The average $\delta^{18}O_{H2O}$ for Tunnel 1 drip-waters from which the $\delta^{18}O_{SO4}$ was measured was −11.5±2.6 ‰ (2σ, n = 15) and the range in $\Delta^{18}O_{SO4}$ in Tunnel 1 was from 3.2 to 19.2 ‰ (Figure 6.12B). The average pre-landslide (Stage 1) $\Delta^{18}O_{SO4}$ and $\delta^{34}S_{SO4}$, both estimated using linear best fits of each versus distance along the sampling transect in Tunnel 1 with error bars based on 95 % confidence banding, were 10.6±4.4 ‰ (2σ, n = 9) and −12.0±4.0 ‰ (2σ, n = 13), respectively. When compared to pre-landslide (Stage 1) values, significant positive shifts in both $\Delta^{18}O_{SO4}$ and $\delta^{34}S_{SO4}$ (Section 6.6.6) were observed in post-landslide (Stage 4) zone-A drip-waters, which for each isotopic composition was calculated as the average of the seven post-landslide (Stage 4) zone-A drip-waters. The average post-landslide (Stage 4) $\Delta^{18}O_{SO4}$ at zone-A was 18.3±1.0 ‰ (2σ, n = 7), which records a $1.7\pm^{1.4}_{0.6}$ increase compared to average pre-landslide (Stage 1) values (Figure 6.12B).

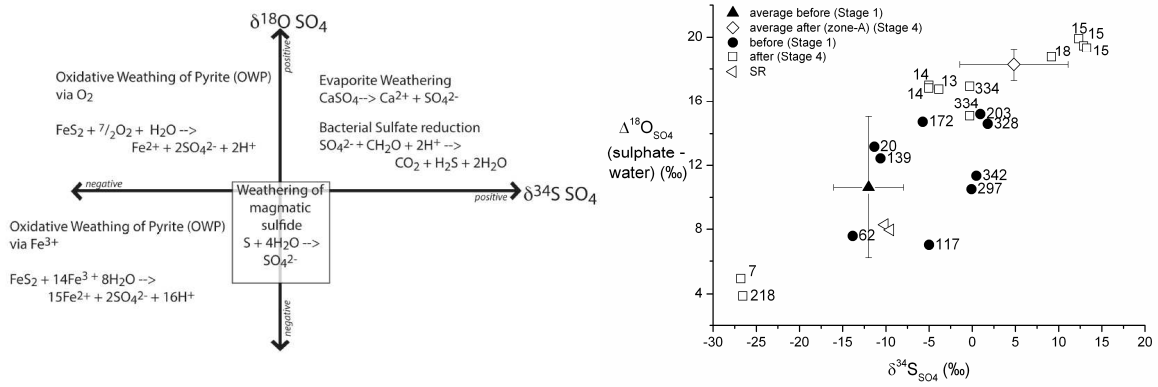

Figure 6.12. Schematic of sulphur and oxygen isotope space showing isotopically-distinct sulphate resulting from weathering and reduction of different minerals (A) (after Turchyn et al. 2013), and the covariation of $\Delta^{18}O_{SO4}$ ($\delta^{18}O_{SO4} - \delta^{18}O_{H2O}$) and $\delta^{34}S_{SO4}$ in Tunnel 1 drip-waters. Numbers refer to tunnel-transect distances. See text for discussion.

This significant positive shift in $\Delta^{18}O_{SO4}$ is inferred to result from the landslide opening up connectivity between the atmosphere and the deep biosphere. This enhanced connectivity shifted the pathway of pyrite weathering towards the consumption of a greater relative proportion of atmospheric O_2 than during pre-landslide conditions.

6.6.6 Bacterial sulphate reduction

The $8.44 \pm^{4.23}_{2.94}$ increase in $[Na^+]$ from Stage 2 to Stage 4 was accompanied by a $1.57 \pm^{0.53}_{0.34}$ increase in SO_4^{2-} indicating that a significant degree of secondary SO_4^{2-} uptake followed the weathering pulse (Stage 3). Therefore, to complete the sequence of events depicted in Figure 6.6, a mechanism is required to explain the post-landslide (Stage 3) secondary uptake of SO_4^{2-}. Less then 1 ‰ sulphur isotope fractionation occurs during pyrite oxidation (Balci et al. 2007) and thus the sulphur isotopic composition of aqueous sulphate ($\delta^{34}S_{SO4}$) corresponds closely to the sulphur isotopic composition of the initial sulphide ($\delta^{34}S_S$). The average $\delta^{34}S_S$ measured in eight hand-picked pyrite crystals was 14.05±0.46 ‰ (2σ, n = 8) whereas bulk sulphide extracted from the schist (see Section 3.3.9, Chapter 3) gave $\delta^{34}S_S$ of 6.44±1.50 ‰ (2σ, n = 2), indicating the presence of an isotopically lighter, disseminated fine-grained sulphide pool associated with silicate mineral phases.

When compared to the average pre-landslide (Stage 1) $\delta^{34}S_{SO4}$ value (−12.01±4.05 ‰), calculated using a linear best fit through $\delta^{34}S_{SO4}$ versus distance along the sampling transect in Tunnel 1 with error bars based on 95 % confidence banding, a significant 16.8±7.5 ‰ positive excursion in zone-A $\delta^{34}S_{SO4}$ was observed in post-landslide (Stage 4) zone-A drip-waters (4.83±6.86 ‰, 2σ, n = 7, calculated as the average of the seven post-landslide (Stage 4) zone-A drip-waters).

During anaerobic metabolic pathways, bacteria using SO_4^{2-} as electron acceptors produce sulphide depleted in ^{34}S relative to the fluid, which consequently becomes isotopically enriched (Jones and Starky 1957). Two possibilities thus exist with which to explain the 16.8±7.5 ‰ positive excursion in zone-A $\delta^{34}S_{SO4}$ following the landslide (Stage 1 to Stage 4) (Figure 6.13). First, during rock alteration (Stage 3), sulphuric acid resulting from the oxidation of the euhedral crystals would impart a relatively heavy isotopic fingerprint to the resulting SO_4^{2-}. Second, the isotopically lighter disseminated sulphide pool, upon oxidation, provides the source of excess sulphuric acid and the surplus SO_4^{2-} released during weathering is returned to sulphide by bacterially-mediated

reduction, driving the $\delta^{34}S_S$ in a positive direction. Simultaneously negating the former and supporting the latter possibility is the observation that up to 81 % secondary SO_4^{2-} uptake from Stage 3 to Stage 4 is required to balance the pre- and post-landslide SO_4^{2-} budget (Table 6.1). This upper-bound estimate of SO_4^{2-} uptake is based on equivalent post-landslide release of HCO_3^- and Na^+ (Equations 6.5 and 6.6), the plausibility of which is supported by the post-landslide (Stage 4) SO_4^{2-} at 218 m inside the tunnel, which is 12082 μmol.L^{-1} (Figure 6.9A). Furthermore, the isotopically lighter disseminated sulphide pool would exhibit far greater surface area-to-volume ratios than the euhedral crystal mass, rendering it easier to dissolve, and further still, many of the larger pyrite crystals would have been prevented from oxidising given their pre-existing rusted surfaces (Figure 6.6C). Therefore, the mechanism of bacterially-mediated sulphate reduction directed the groundwater chemical shift facilitated by the landslide in which a 16.8±7.5 ‰ positive excursion in $\delta^{34}S_{SO4}$ accompanied up to 81 % secondary SO_4^{2-} uptake into sulphide (Figure 6.13).

To assess the mechanism of secondary pyrite formation, the behaviour of $\delta^{34}S_{SO4}$ was modelled by testing different α values based on an expected range (Turchyn et al. 2013) for bacterially-mediated sulphate reduction, by substituting $\delta^{34}S_{SO4}$ for $\delta^{13}C_{DIC}$ into Equation 6.8. The results of this modelling are illustrated in Figure 6.13, where $\delta^{34}S_{SO4}$ is plotted against Ca^{2+}/SO_4^{2-} and fractionation curves are drawn based on epsilon values (the per mil equivalent of α values) of 20.0, 15.0 and 9.6 ‰. The curves are drawn for two scenarios. The first illustrates 81 % sulphate reduction in the absence of secondary carbonate formation, i.e. the initial (Stage 3) Ca^{2+}/SO_4^{2-} value is 0.48, which is derived from Ca^{2+} = 6936 μmol.L^{-1} and $SO_4^{2-} = [SO_4^{2-}]_{post\text{-}weath}$ (14360 μmol.L^{-1}). The 6936 μmol.L^{-1} value for Ca^{2+} is derived from the assumption that Ca^{2+} uptake would be half of the HCO_3^- uptake:

$$Ca^{2+}\ \text{uptake} = [Ca^{2+}]_{post\text{-}weath} - (([HCO_3^-]_{post\text{-}weath} - [HCO_3^-]_{after})/2) \quad (6.9)$$

and thus 6936 μmol.L^{-1} of Ca^{2+} should be in the fluid after Stage 3. The second illustrates 81 % sulphate reduction after carbonate formation has completed, i.e. sulphate reduction begins at Ca^{2+}/SO_4^{2-} = 0.48 as above, but the second step in the model jumps to a constant Ca^{2+} of 2660 μmol.L^{-1} (i.e. Stage 4 or $[Ca^{2+}]_{after}$) and the $SO_4^{2-} = 0.9 \times [SO_4^{2-}]_{post\text{-}weath}$ (12924 μmol.L^{-1}), or 0.9 × 14360 μmol.L^{-1} (Equation 6.2). Also shown is a third scenario where 61 % carbonate formation is decoupled from SO_4^{2-} uptake (Figure 6.13). The

models suggest that bacterially-mediated sulphate reduction occurred concurrently with secondary carbonate formation at an epsilon value of 9.6 ‰. This epsilon value would increase (i.e. the curves would shift to the right thus intercepting the post-landslide composition at higher epsilon values) with decreasing carbonate formation (increasing $[Ca^{2+}]_{after}$) depending on the degree of incongruent dissolution to have occurred.

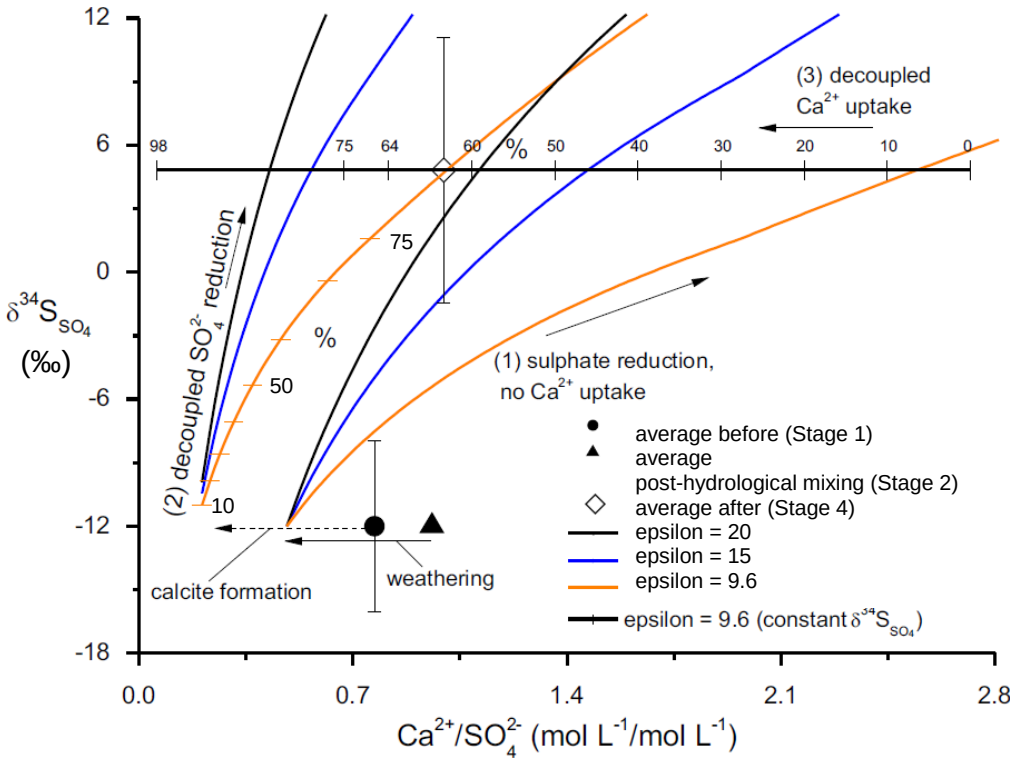

Figure 6.13. The ratio of Ca^{2+}/SO_4^{2-} versus $\delta^{34}S_{SO4}$ in zone-A drip-waters. Curves describe Rayleigh fractionation of sulphur isotopes at different epsilon (ε) values for scenarios (1), assuming sulphate reduction in the absence of carbonate formation, (2), decoupled sulphate reduction following carbonate formation and (3), decoupled carbonate formation following the sulphate reduction. Bacterially-mediated sulphate reduction explains both the 16.8±7.5 ‰ rise in $\delta^{34}S_{SO4}$ in zone-A and the relative loss of SO_4^{2-} during post-landslide conditions.

6.6.7 Concluding remarks, discussion and further work

Landsliding is the dominant hillslope erosion process in Taiwan (Hovius et al. 2011) and it is pervasive in the Liwu River catchment. At any time, a significant number of landslide affected locations must exist in the catchment and this must propagate into the weathering mechanisms described here. Also of potential importance is the weathering activity likely to be occurring within landslide debris piles, which are more fragmented,

aerated and drained than underlying rock mass. The weathering enhancement shown here to follow landslides could be greatly augmented following large earthquakes. For example, greater than 20,000 soil and bedrock landslides (surface area >3600 m^2) in Taiwan's Western Foothills were triggered by the 1999 Chi-Chi earthquake (M_w 7.6), and an increase in the rate of landsliding was observed for more than six years following the event (Hovius et al. 2011b).

This study shows that pyrite oxidation (under oxic conditions) and bacterially-mediated sulphate reduction are potentially important mechanisms during landslides in the cycling of atmospheric carbon and oxygen. Landslides being a frequent phenomenon in this setting, it is likely that calcite formation following past disruptions is to some degree represented among the abundance of secondary carbonates found inside the tunnel. Therefore, net CO_2 release by carbonate formation following landslide-induced weathering pulses driven by sulphuric acid poses as a largely unknown converter of ancient sedimentary carbon into atmospheric CO_2. Being unable to constrain the chemical fluxes issuing from the landslide-disrupted crust, the atmospheric CO_2 and O_2 budgets in this case remain unresolved, but this study highlights the need for more work in order to quantify the net direction and significance of carbon and oxygen transfer between the atmosphere and the solid Earth during these brief but prevalent and pervasive physical erosion events.

The spatial restriction of the landslide-induced chemical changes to zone-A implies that any wider-reaching fracture connectivity as a result of failure is transient and that it is the weathering processes in the immediate vicinity of the ruptured surface that will be most profoundly influenced. Secondary calcite precipitation, in sealing post-landslide fractures, could play a role in constraining the size of the region to be affected. Notwithstanding, in regions of high landslide frequency and high surface runoff, the magnitude of locally-restricted weathering pulses and the responses of a deep biosphere, are likely to play a pivotal role in controlling the fluxes of major solutes from an orogen and have significant bearings on the carbon, sulphur and oxygen cycles.

6.6.7.1 Sulphate variability in groundwater: insights from river water

The highly variable SO_4^{2-} concentrations in fractured bedrock groundwaters and the link between SO_4^{2-} enrichment and physical erosion demonstrated to exist in the Liwu River catchment can be further assessed in analysing SO_4^{2-} in river waters. The analysis of

longer-term records of sulphate concentrations in the Liwu River (Calmels et al. 2011) associated with Tunnels 1, 6 and 8, the Choshui River (WRA data), which drains the lithological units of Tunnel 28 in Fenchihu, and the Kaoping River (Das et al. 2012; WRA data), which drains the same lithology as that associated with Tunnel 28 (Sections 6.4 and 6.5.4), shows that SO_4^{2-} concentrations in surface waters are likewise variable and not simply related to first-order processes, such as dilution by rain water, which would give higher concentrations at lower discharges well described by classic power-law fits (see Cl^- versus discharge plot, Figure 5.15A, Chapter 5).

The range in SO_4^{2-} concentrations recorded bi-weekly in the Liwu River during the period September 2002 to February 2008 was 526 to 1383 $\mu mol.L^{-1}$, with an average value of 1014±394 $\mu mol.L^{-1}$ (2σ, n = 138) (Calmels et al. 2011). Overall a higher average [SO_4^{2-}] (1159±628 $\mu mol.L^{-1}$; 2σ, n = 37) and greater than twice the dynamic range in [SO_4^{2-}] measured in the Liwu River was recorded approximately bi-weekly in the Choshui River during the period March 2005 to December 2006 (WRA data). Two other data sets, by Das et al. (2012), record similarly variable [SO_4^{2-}] during different sampling periods in the tributaries and main channel of the Kaoping River. The first is comprised of river water samples collected during the wet season in August 2004, which displayed a range in SO_4^{2-} of 561-778 $\mu mol.L^{-1}$ (average = 690±137; 2σ, n = 11). The second is comprised of river water samples collected during the dry period December 2009 to January 2010, which exhibited a range in SO_4^{2-} of 437-1767 $\mu mol.L^{-1}$ (average = 1090±597; 2σ, n = 26).

It was shown in Chapter 5 that a poor correlation between [SO_4^{2-}] and discharge was observed for the Choshui River during the 2005/6 sampling period (see Figure 5.15F, Chapter 5). Although a moderate negative correlation between [SO_4^{2-}] and discharge was observed for the Liwu River 2002-2008 data set (R^2 = 0.50) (Figure 6.14), the scatter in the data plot indicates that processes other than simple dilution, such as physical erosion, are taking place. Das et al. (2012) suggest that the high concentrations of SO_4^{2-} in the Kaoping River time series must be linked to the high physical erosion rates observed in the Kaoping River drainage basin, as such high rates would lead to the rapid oxidation of the abundant pyrite in the surrounding lithology.

It has been concluded by Bolton et al. (2006) that physical erosion rates as opposed to the level of atmospheric O_2 limits the rate of drawdown of atmospheric oxygen due to the oxidation of pyrite (and organic matter).

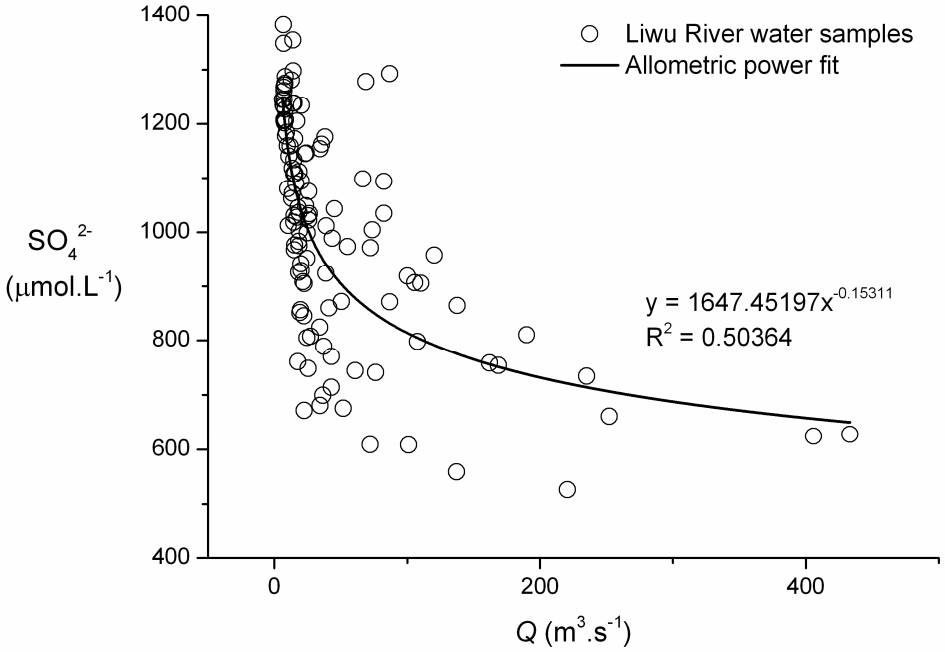

Figure 6.14. Relationship between SO_4^{2-} and discharge for the 2002-2208 bi-weekly Liwu River sample set. A moderate correlation described by a power-law fit was observed (R^2 = 0.50364) but significant scatter was evident suggesting that processes other then first-order dilution during heavier discharges were at play.

Although highly speculative at this stage, it might be that variability in physical erosion rates, such as episodic periods of landsliding, have given rise to the disparate SO_4^{2-} concentrations in the respective river-water sample sets. Likewise, due to the coupling between physical erosion and pyrite oxidation rates demonstrated using the groundwater chemistry time series from Tunnel 1, it is possible that the disparity in the magnitudes and dynamic ranges of the SO_4^{2-} concentrations in the groundwaters from the Bayyang Tunnel Trail and from Tunnel 28 in Fenchihu reflect the local rates of physical erosion near the time of sampling.

6.7 Conclusions

This chapter has investigated two aspects of groundwater chemistry in a fractured bedrock setting. Hydrogeochemical mixing relationships were shown to be more complex than previously suggested for the Liwu River drainage basin. Rather than simple binary mixing between two distinct groundwater end-members, as has previously been described, the identification of two additional geochemical components, each reflecting distinct

hydrological pathways, suggests that a more complex continuum between at least four groundwater end-members better describes the hydrogeochemistry in fractured bedrock.

An assessment of tunnel drip-waters collected before and after the October 2009 landslide shows that in rapidly-eroding regions like Taiwan, chemical fluxes from orogenic belts are tightly controlled by geomorphic processes. Significant chemical shifts were observed for Cl^-, Na^+ and isotopes of sulphur and oxygen and were inferred for other solutes and stable isotopes of carbon. The chemical changes demonstrate that the landslide resulted in the opening up of hydrological pathways and the rapid flushing of meteoric water through the fractured subsurface. An excess of sulphuric acid was produced and released into the rock surround due to the rapid oxidative weathering of pyrite. As evidenced by the spike in Na^+ concentrations, silicate weathering was significantly enhanced in the aftermath of the landslide. The excess sulphuric acid was to some degree buffered by carbonate dissolution, but stoichiometric considerations indicate that incongruent mineral dissolution favoured the weathering of silicate over carbonate rock. The incongruent dissolution was likely owing to the pyrite in the specific location of Tunnel 1 being hosted by the schist, which is largely composed of silicate phases.

A combination of stoichiometric considerations and the positive shift observed in isotopes of sulphur indicate that most of the sulphate released during pyrite oxidation was subsequently returned to sulphide by bacterially-mediated sulphate reduction. The observed rise in oxygen isotopes of aqueous sulphate shows that the landslide caused a shift in the oxidative weathering of pyrite that resulted in the enhanced drawdown of atmospheric oxygen.

This interplay between biogeochemistry and geomorphology is likely to exert an important control on the fluxes of major solutes from active mountain belts.

Chapter 7

Conclusions

7.1 Chapter summary

This chapter provides summaries of the main findings of the thesis and the avenues of future research that should be explored in light of the findings presented in detail in Chapters 4, 5 and 6. In doing so, it briefly returns to the questions outlined in Section 1.2 of the thesis Introduction (Chapter 1) and summarises the progress made in addressing them.

7.2 A summary of the main findings of the thesis

7.2.1 Alluvial-fill coastal plains

The chemistry of the groundwaters from the drilled depths of the Pingtung and Choshui alluvial-fill coastal plains in western and southwestern Taiwan arises from variable mixtures of silicate and carbonate source rocks that have been altered by differing proportions of biologically-mediated carbonic acid and sulphuric acid. A general evolution from sulphuric acid-driven weathering of carbonates in the proximal regions near the mountains to carbonic acid-driven dissolution of silicate minerals in the distal zones near the coastlines was observed. Thus, the groundwaters in both coastal plains generally evolve along the groundwater flow paths from carbonate-rich chemistry in the proximal regions to silicate-dominated compositions in the distal zones. Increasing silicate-derived dissolved mass (Na^+ and SiO_2) was also observed with depth in the basins.

One important outstanding question raised from these observations of chemical variability in alluvial-fill coastal plains pertains to the depth range over which increasing silicate dissolution occurs. Presumably, at some depth horizon a limit to silicate dissolution would be observed, but deeper boreholes are needed in order to explore this line of investigation in Taiwan.

The main processes involved in determining the groundwater chemistry in the coastal plains are carbonate and silicate dissolution, calcite formation, clay uptake and desorption and sulphate reduction. The main controls on groundwater chemistry are lithology, groundwater residence times and type of weathering agent.

Three-end-member, two-tracer mixing relationships, using the conservative tracer chlorine and the quasi-conservative tracer lithium, have revealed that the groundwater chemistry in both coastal plains is derived from four distinct sources: rainwater, hydrothermally-sourced water (e.g. hot-spring water), seawater (ancient and modern) and from the dissolution of minerals within the sediments of the alluvial fills and from the surrounding hillslopes. The results of three-end-member two-tracer mixing calculations show that on average 99.52 % of the groundwater in the Pingtung Plain was meteoric in origin, 0.21 % was from hot-springs and 0.27 % was from seawater. In the case of the Choshui Plain, the results of ternary mixing calculations show that on average 98.68 % of the groundwater was meteoric in origin, 0.46 % was from hot-springs and 0.86 % was from seawater.

Based on the ternary mixing relationships, the percentage of seawater was found to be positive in all samples from both coastal plains with the exception of one well from each basin (coastal well HN2 (Pingtung) and distal well HL2 (Choshui) each had 0 % seawater). Whereas the proportion of seawater in the Choshui Plain was relatively homogenous according to the spatial distribution of samples and the hydrological regime, in the Pingtung Plain it was seen to increase along the groundwater flow path from 70 km inland towards the coast. The significant presence of seawater as far inland as 70 km can be explained by the observation that the uplifted sediments of the western foothills bordering the Pingtung Plain consist largely of coastal and shallow marine deposits, which likely contain connate seawater. This water and laden enriched chemistry may be flushed from uplifted sediments during modern weathering activity and enter the Pintung groundwater system.

Long-term average groundwater chemical weathering fluxes have been calculated using hydraulic head and hydraulic conductivity data together with chemical analyses of groundwater for the Pingtung and Choshui coastal plains. Relative to the chemical fluxes from the major rivers along Taiwan's western and southwestern margins, the groundwater weathering fluxes from both plains range between 1.4 % and 4.6 % for Ca^{2+}, Mg^{2+}, K^{+}, $SO_4^{2-,}$ Sr^{2+} and Li^{+}, between 5.0 % and 6.1 % for Na^{+} and SiO_2, and are 11.8 % for Ba^{2+}, demonstrating that relative subsurface weathering fluxes in the drilled depth of Taiwan's

coastal plains (~300 m) are modest. However, the Na^+ flux from the Choshui Plain, relative to that from the low-flow Na^+ flux estimate of the Choshui River was 63.45 %. Therefore, despite the long-term average relative subsurface fluxes being low, this range in seasonal variation evidenced by the relative Na^+ fluxes calculated at low river discharge could have significant implications for shorter scale phenomenon, such as nutrient delivery and coastal ecology.

The shoreline-normalised groundwater chemical fluxes for the drilled depths of the Pingtung (14.15 $m^3.m^{-1}.day^{-1}$) and Choshui (16.73 $m^3.m^{-1}.day^{-1}$) coastal plains compare well to global estimates of submarine fresh groundwater discharge along clastic coastlines (11 $m^3.m^{-1}.day^{-1}$). However, in comparison to other case studies, particularly of volcanic ocean island settings where groundwater discharge rates to the ocean are sometimes in excess of surface water fluxes, chemical fluxes from analogous regions in Taiwan are low.

The outstanding questions pertaining to estimates of submarine fresh groundwater discharge across clastic shorelines concern the depth ranges over which this form of solute delivery to the ocean occurs, the local and global magnitude of this dissolved mass that bypasses the surface drainage network entirely and the potential impact of this under-sampled source of dissolved mass on our understanding of ocean geochemical budgets. In order to address these issues, future researchers would need to implement deep (>500 m) onshore boreholes in alluvial-fill deposits close to the coast, which would enable direct measurement of the physical properties of these aquifers at depth and determination of the groundwater chemistry that is likely to represent deep fresh submarine groundwater discharge. If the depth ranges over which fresh submarine groundwater discharge occur could be constrained and partnered to onshore-assessed quantitative estimates of subsurface chemical fluxes, then there would be great potential for augmenting current estimates of solute delivery from the continents to the ocean.

7.2.2 Fractured bedrock aquifers

The collection of drip-waters from two distinct series of disused transport tunnels has enabled detailed assessments of the chemical variability of groundwaters in fractured bedrock and of the relationship between physical erosion and chemical weathering in active mountain belts.

In assessing the chemical variability of groundwaters from steeply-elevated bedrock aquifers, hydrogeochemical mixing relationships were shown to be more complex

than has previously been suggested for the example of the Liwu River drainage basin. The identification of two additional geochemical components in the Liwu River catchment, each reflecting distinct hydrological pathways, suggests, as opposed to simple binary mixing between two previously identified distinct groundwater end-members, that a more complex continuum between at least four groundwater end-members better describes the hydrogeochemistry in fractured bedrock.

An assessment of tunnel drip-waters collected before and after a major landslide had disrupted one of the ridges above Tunnel 1 in Bayyang has shown that in rapidly-eroding regions like Taiwan chemical fluxes from orogenic belts are tightly controlled by geomorphic processes. Relative to drip waters collected prior to the landslide, a $58.5\pm^{11.7}_{8.6}$ % drop in Cl^-, a factor of $8.44\pm^{4.23}_{2.94}$ rise in Na^+, a factor of $1.7\pm^{1.4}_{0.6}$ increase in the oxygen isotopic composition of aqueous sulphate and a 16.8±7.5 ‰ positive excursion in the sulphur isotopic composition of aqueous sulphate all lead to the conclusions that the landslide resulted in 1) the opening up of hydrological pathways and the rapid flushing of meteoric water through the fractured subsurface, 2) a significant silicate weathering pulse, 3) a shift towards the oxidation of pyrite being driven by a greater proportion of atmospheric oxygen than during pre-landslide conditions and 4) the recapturing of excess sulphate that was released during the weathering pulse by bacterially-mediated sulphate reduction. These results strongly suggest that in regions of high landslide frequency and high surface runoff the magnitude of locally-restricted weathering pulses and the responses of a deep biosphere are likely to play a pivotal role in controlling the fluxes of major solutes from an orogen and to have significant bearings on the carbon, sulphur and oxygen cycles.

Through investigations of riverine chemical fluxes and soil weathering profiles, in many settings, a positive link between the rates of physical erosion and chemical weathering has been shown to exist, but it has also been shown that these processes can become decoupled at extremely high physical erosion rates, such as are displayed in Taiwan. However, this study has shown that important weathering processes in the deep biosphere for the cycling of atmospheric carbon and oxygen are coupled to physical erosion processes (landsliding) characteristic of rapidly-eroding terrain. A lack of groundwater flux constraint has prevented a quantitative estimate of carbon and oxygen transfer in this instance. It is therefore important to have a greater number of groundwater samples from fractured bedrock aquifers in a variety of settings reflecting a range of

physical erosion rates together with robust assessments of groundwater flow in fractured bedrock in order to quantify the net direction and significance of carbon and oxygen transfer between the atmosphere and the solid Earth during landslides which are brief but prevalent and pervasive physical erosion events globally.

In this thesis, chemical weathering processes have been identified and groundwater chemical fluxes have been calculated for the west coast of Taiwan, where alluvial-fill sediments fringe the high mountain topography. In addition, chemical weathering processes, together with their controls, have been identified in the deep bedrock aquifers of Taiwan's Central Range and Western Foothills. To add substantially to the picture of chemical weathering in Taiwan, and to quantify the total dissolved subsurface chemical load from the active orogen, needed will be quantitative estimates of chemical weathering fluxes issuing directly from the mountains to the ocean. The optimum location to constrain this latter groundwater chemical flux is along Taiwan's eastern margin (both onshore and offshore groundwater sampling would be most favourable), where the high mountain topography continues uninterrupted to submarine depths of greater than 4000 m. The deep fractures and faults along the eastern margin of Taiwan presumably act as conduits for submarine groundwater discharge, which would be driven by up to 9000 m of steeply-dipping orographic relief.

Bibliography

Anderson, S.P., Drever, J.I., Frost, C.D. and Holden, P. 2000. Chemical weathering in the foreland of a retreating glacier. *Geochim. Cosmochim. Acta* **64**, 1173-1189.

Anderson, S.P. 2012. How deep and how steady is Earth's surface? *Geology* **40**, 863-864.

Aumont, O., Orr, J.C., Monfray, P., Ludwig, W., Amiotte-Suchet, P. and Probust, J-C. 2001. Riverine-driven interhemispheric transport of carbon. Global Biogeochem. Cycles **15**, 393-405.

Balci, N., Shanks, W.C., Mayer, B. and Mandernack, K.W. 2007. Oxygen and sulphur isotope systematics of sulphate produced by bacterial and abiotic oxidation of pyrite. *Geochim. Cosmochim. Acta* **71**, 3796-3811.

Basu, A. R., Jacobsen, S. B., Poreda, R. J., Dowling, C. B. and Aggarwal, P. K. 2001. Large groundwater strontium flux to the oceans from the Bengal Basin and the marine strontium isotope record. *Science* **293**, 1470-1473.

Becker, J.A., Bickle, M.J., Galy, A. and Holland, T.J.B. 2008. Himalayan metamorphic CO_2 fluxes: Quantitative constraints from hydrothermal springs. *Earth Planet. Sci. Lett*. **265**, 616-629.

Berner, R.A., Lasaga, A.C. and Garrels, R.M. 1983. The carbonate-silicate geochemical cycle and its effect on atmospheric carbon dioxide over the past 100 million years. *American Journal of Science* **283**, 641-683.

Berner, E.K and Berner, R.A. 1996. Global Environment: Water, Air and Geochemical Cycles, 376 p. Prentice Hall, Upper Saddle River, New Jersey.

Berner, R.A. and Caldeira, K. 1997. The need for mass balance and feedback in the geochemical carbon cycle. *Geology* **25**, 955-956.

Berner, R.A. 1999. A new look at the long-term carbon cycle. *GSA Today* **9**, 1-6.

Bickle, M.J. 1998. The need for mass balance and feedback in the geochemical carbon cycle: Comment. *Geology* **26**, 477-478.

Bickle, M.J., Bunbury, J., Chapman, H.J., Harris, N.B.W., Fairchild, I. and Ahmad, T. 2003. Fluxes of Sr into the Headwaters of the Ganges. *Geochim. Cosmochim. Acta* **67**, 2567-2584.

Bickle, M., Chapman, H.J., Bunbury, J., Harris, N.B.W., Fairchild, I.J., Ahmad, T. and Pomiès, C. 2005. Relative contributions of silicate and carbonate rocks to riverine Sr fluxes in the headwaters of the Ganges. *Geochim Cosmochim Acta* **69**, 2221-2240.

Birkeland, P. 1999. Soils and Geomorphology, third ed. Oxford University Press, New York.

Bluth, G.J.S. and Kump, L.R. 1994 Lithologic and Climatologic Controls of River Chemistry. *Geochimica et Cosmochimica Acta* **58**, 2341–2359.

Bolton, E.W., Berner, R.A. and Petsch, S.T. 2006. The weathering of sedimentary organic matter as a control on atmospheric O_2: 11. Theoretical modelling. *American Journal of Science* **306**, 575-615.

Bordet, P., Colchen, M., Krummenacher, D., Le Fort, P., Mouterde, R. and Remy, M. 1971. Recherches Géologiques dans l'Himalaya du Ne´pal, Re´gion de le Thakkhola. Centre National de la Recherche Scientifique.

Bowin, C., Lu, R.S., Lee, C.S. and Schouten, H. 1978. Plate convergence and accretion in the Taiwan-Luzon region. *Am. Assoc. Petrol. Geol. Bull*. **62**, 1645-1672.

Burbank, D.W., Leland, J., Fielding, E., Anderson, R.S., Brozovic, N., Reid, M.R. and Duncan, C. 1996. Bedrock incision, rock uplift and threshold hillslopes in the northwest Himalayas. *Nature* **379**, 505-510.

Burnett, W. C., Bokuniewich, H., Huettel, M., Moore, W. S. and Taniguchi, M. 2003. Groundwater and pore water inputs to the coastal zone. *Biogeochemistry* **66**, 3-33.

Caldeira, K. and Berner, R.A. 1998. The need for mass balance and feedback in the geochemical carbon cycle: Comment. *Geology* **26**, 478.

Calmels, D., Gaillardet, J., Brenot, A. and France-Lanord, C. 2007. Sustained sulphide oxidation by physical erosion processes in the Mackenzie River basin:Climatic perspectives. *Geology* **35**, 1003-1006.

Calmels, D., Galy, A., Hovius, N., Bickle, M., West, J.A., Chen, M-C. and Chapman, H. 2011. Contribution of deep groundwater to the weathering budget in a rapidly eroding mountain belt, Taiwan. *Earth Planet. Sci. Lett*. **303**, 48-58.

Carey, A.E., Gardner, C.B., Goldsmith, S.T., Lyons, W.B. and Hicks, D.M. 2005. Organic Carbon Yields from Small, Mountainous Rivers, New Zealand. *Geophysical Research Letters* **32**: L15404. doi:10.1029/2005GL023159.

Carson, M. A. and Kirkby, M. J. 1972. *Hillslope Form and Process.* Cambridge Geographical Studies No. 3. Cambridge University Press, New York.

Cerling, T.E., Solomon, D.K., Quade, J. and Bowman, J.R. 1991. On the isotopic composition of carbon in soil carbon dioxide. *Geochim. Cosmochim. Acta* **55**, 3403-3405.

Chai, B.H.T. 1972. Structure and tectonic evolution of Taiwan. *Am. J. Sci*. **272**, 389-442.

Charette, M.A., Moore, W.S. and Burnett, W.C. 2008. Uranium- and thorium-series nuclides as tracers of submarine groundwater discharge, in: Krishnaswami, S., Cochran, J.K. (Eds.), U-Th Series Nuclides in Aquatic Systems, Elsevier, Amsterdam, pp. 155-92.

Chen, K.P. and Wu, H.Y. 1962. Epidemiologic studies on blackfoot disease: 2. A study of source of drinking water in relation to the disease. *J. Formosan Med. Assoc.* **61**, 611-618.

Chen, S-L., Dzeng, S.R., Yang, M-H., Chiu, K-H., Shieh, G-M. and Wai, C.M. Arsenic Species in Groundwaters of the Blackfoot Disease Area, Taiwan. 1994. *Environ. Sci. Technol*. **28**, 877-881.

Chen, C.H., Ho, H.C., Shea., K.S., Lo, W., Lin, W.H., Chang, H.C., Huang, C.S., Lin, C.W., Chen, G.H., Yang, C.N. and Lee, Y.H. 2000. Geological map of Taiwan, 1:500,000. Central Geological Survey, Ministry of Economic Affairs, Taiwan.

Chen, W.S., Ridgeway, K.D., Horng, C.S., Chen, Y.G., Shea, K.S. and Yeh, M.G. 2001. Stratigraphic architecture, magnetostratigraphy, and incised-valley systems of the Pliocene-Pleistocene collisional margin foreland basin of Taiwan. *Geological Society of America Bulletin* **113**, 1249-1271.

Chen, K-Y. and Liu, T-K. 2007. Major Factors Controlling Arsenic Occurrence in the Groundwater and Sediments of the Chianan Coastal Plain, SW Taiwan. *Terr. Atmos. Ocean. Sci*. **18**, 975-994.

Chia, Y., Wang, Y.S., Chiu, J.J. and Liu, C.W. 2001. Changes of Groundwater Level due to the 1999 Chi-Chi Earthquake in the Choshui River Alluvial Fan in Taiwan. *Bulletin of the Seismological Society of America* **91**, 1062-1068.

Chiang, C.J. and Wang, C.H. 1998. Seawater intrusion in the Pingtung Plain, in: Hsu, S.K. (Ed.), Groundwater and Hydrogeology of the Pingtung Plain Symposium, Taipei pp 297-315.

Chiang, C-S., Yu, H-S. and Chou, Y-W. 2004. Characteristics of the wedge-top depozone of the southern Taiwan foreland basin system. *Basin Res*. **16**, 65-78.

Chou, C-H., Huang, T-J., Lee, Y-P., Chen, C-Y., Hsu, T-W. and Chen, C-H. 2011. Diversity of the alpine vegetation in central Taiwan is affected by climate change based on a century of floristic inventories. *Botanical Studies* **52**, 503-516.

Chung, C-H., You, C-F. and Chu, H-Y. 2009. Weathering sources in the Gaoping (Kaoping) river catchments, southwestern Taiwan: Insights from major elements, Sr isotopes, and rare earth elements. *J. Mar. Syst*. **76**, 433-443.

Church, T. M. 1996. An underground route for the water cycle. *Nature* **380**, 579– 580.

Claypool, G.E., Holser, W.T., Kaplan, I.R, Sakai, H. and Zak, I. 1980. The Age Curves of sulfur and oxygen isotopes in marine sulphate and their mutual interpretation. *Chem Geo*. **28** 199-260.

Craig, H., 1961. Isotopic variations in meteoric waters. *Science* **133**, 1702-1703.

Dadson, S.J., Hovius, N., Chen, H., Dade, W.B., Hsieh, M-L., Willett, S.D., Hu, J-C., Horng, M-J., Chen, M-C., Stark, C.P., Lague, D. and Lin, J-C. 2003. Links between erosion, runoff variability and seismicity in the Taiwan orogen. *Nature* **426**, 648-651.

Dadson, S.J., Hovius, N., Chen, H., Dade, B.W., Lin, J-C., Hsu, M-L., Lin, C-W., Horng, M-J., Chen, T.C., Milliman, J. and Stark, C.P. 2004. Earthquake triggered increase in sediment delivery from an active mountain belt. *Geology* **32**, 733-736.

Darcy, H.P.G. 1856. Les fontaines publiques de la Ville de Dijon.Victor Dalmont, Paris.

Das, A., Chung, C.H. and You, C.F. 2012. Disproportionately high rates of sulphide oxidation from mountainous river basins of Taiwan Orogeny. *Geophysical Research Letters* **39**, L12404, doi:10.1029/2012GL051549.

Davis, S.N. and DeWiest, R.J.M. 1966. Hydrogeology. John Wiley and Sons, Inc.

Dixon, J.L., Hartshorn, A.S., Heimsath, A.M., DiBiase, R.A. and Whipple, K.X. 2012. Chemical weathering response to tectonic forcing: A soils perspective from the San Gabriel Mountains, California. *Earth Planet. Sci. Lett*. **323-324**, 40-49.

Drever, J.I., 1988. The Geochemistry of Natural Waters. Prentice Hall, New Jersey.

Ebelmen, J. 1845. Sur les produitsde la décomposition des especes minérales da famille des silicates. *Ann. Mines* **7**, 3-66.

English, N., Quade, J., DeCelles, P. and Garzione, C. 2000. Geologic control of Sr and major element chemistry in Himalayan rivers, Nepal. *Geochim. Cosmochim. Acta* **64**, 2549-2566.

Environment Canada. 1998. HYDAT Version 98-1.05.8, Surface water and sediment data: Atmospheric Environment Program, Water Survey of Canada, CD-ROM.

Essaid, H. I. 1990a. The computer model SHARP, a quasi-three-dimensional finite-difference model to simulate freshwater and saltwater flow in layered coastal aquifer systems. U.S. Geological Survey ; Books and Open-File Reports Section [distributor], Water-Resources Investigations Report 90-4130, xi, 181 p.

Essaid, H. I. 1990b. A multilayered sharp interface model of coupled freshwater and saltwater flow in coastal systems: Model development and application: *Water Resources Research*, **26**, 1431-1454.

Evans, M.J., Derry, L.A. and France-Lanord, C. 2004. Geothermal fluxes of alkalinity in the Narayani river system of central Nepal. *Geochem. Geophys. Geosyst*. **5**, 1-21.

Faye, S., Maloszewski, P., Stichler, W., Trimborn, P., Faye, S.C. and Gaye, C.B. 2005. Groundwater salinization in the Saloum (Senegal) delta aquifer: minor elements and isotopic indicators. *Sci. Total Environ*. **343**, 243-259.

France-Lanord, C. and Derry, L.A. 1997. Organic carbon burial forcing of the carbon cycle from Himalayan erosion. *Nature* **390**, 65-67.

Friedman, I. and O'Neil, J.R. 1977. Compilation of stable isotope fractionation factors of geochemical interest. In: Fleischer, M. (Ed). Data of Geochemistry, Vol. 440-K.K., Geological Survey, pp. 1-114.

Gaillardet, J., Dupré, B., Louvat, P. and Allègre, C. J. 1999. Global silicate weathering and CO_2 consumption rates deduced from the chemistry of large rivers. *Chemical Geology* **159**, 3-30.

Galy, A., France-Lanord, C. and Derry, L.A. 1999. The strontium isotopic budget of Himalayan Rivers in Nepal and Bangladesh. *Geochim. Cosmochim. Acta* **69**, 1905-1925.

Galy, A. and France-Lanord, C. 1999. Weathering processes in the Ganges-Brahmaputra basin and the riverine alkalinity budget. *Chemical Geology* **159**, 31-60.

Garrels, R.M. and Lerman, A. 1984. Coupling of the sedimentary sulphur and carbon cycles. *American Journal of Science* **284**, 989-1007.

Garrels, R. and Mackenzie, F. 1967. Origin of the chemical compositions of some springs and lakes. *American Chemical Society Advances in Chemistry Series* **67**, 222-242.

Garrels, R. M. and Mackenzie, F. T. 1971. *Evolution of Sedimentary Rocks*. Norton, New York.

Garrels, R. M., and Perry, E. A. 1974, Cycling of carbon, sulfur and oxygen through geologic time, *in* Goldberd, E. D., editor, The Sea—Ideas and Observations on Progress in the Study of the Seas: New York, Wiley, Marine Chemistry, **5**, 303–316.

Gat, J.R. 2000. Atmospheric water balance−the isotopic perspective. *Hydrological Processes* **14**, 1357-1369.

Gieskes, J.M., Gamo, T. and Kastner, M. 1993. Major and minor element geochemistry of interstitial waters of Site 808, Nankai Accretionary Prism: an overview, in: Hill, i.a.,

Taira, A., Firth, J.V. (Eds.), Proc. Ocean Drilling Program, Scientific Reports 131. Ocean Drilling program, College Station, Texas, pp. 387-396.

Gilbert, G.K. 1877. Report on the Geology of the Henry Mountains, US Geographical and Geological Survey of the Rocky Mountain Region, Washington, DC: Government Printing Office.

Gislason, S. R., Oelkers, E.H., Eiriksdottir, E.S., Kardjilov, M.I., Gisladottir, G., Sigfusson, B. and Snorrason, A. 2009. Direct Evidence of the Feedback Between Climate and Weathering. *Earth Planet. Sci. Lett.* **277**, 213-222.

Gonfiantini, R. 1978. Standards for stable isotope measurements in natural compounds. *Nature* **271**, 534-536.

Hahn, J., Lee, Y., Kim, N., Hahn, C. and Lee, S. 1997. The groundwater resources and sustainable yield of Cheju volcanic island, Korea. *Environmental Geology* **33**, 45-53.

Hanshaw, B.B. and Back, W. 1980. Chemical mass-wasting of the northern Yucatan Peninsula by groundwater dissolution. *Geology* **8**, 222-224.

Hart, R. 1970. Chemical exchange between sea water and deep ocean basalts. *Earth and Planetary Science Letters* **9**, 269-279.

Heermance, R.V. and Evans, J. P. 2006. Evolution of the of the Chelungpu fault, Taiwan: The mechanics of frontal ramps and fault imbrication, *J. Struct. Geology* **28**, 929-938.

Hebenstreit, R., Böse, M. and Murray, A. 2006. Late Pleistocene and Early Holocene Glaciations in Taiwanese Mountains. *Morphodynamics and Climate in Taiwan since the Late Pleistocene* **147**, 76–88.

Hilton, R.G., Galy, A., Hovius, N., Horng, M-J. and Chen, H. 2010. The isotopic composition of particulate organic carbon in mountain rivers of Taiwan. *Geochim. et Cosmochim. Acta* **74**, 3164-3181.

Hilton, R.G., Galy, A., Hovius, N., Kao, S-J., Horng, M-J. and Chen. H. 2012. Climatic and Geomorphic Controls on the Erosion of Terrestrial Biomass from Subtropical Mountain Forest. *Global Biogeochemical Cycles* **26**, GB3014. doi:10.1029/2012GB004314.

Ho, C.S. 1988. An introduction to the geology of Taiwan: explanatory text of the geological map of Taiwan (2nd ed.). *Taipei, Centr. Geol. Surv. Min. Econ. Affairs* 192p.

Hodell, D., Mead, G.A. and Mueller, P.A. 1990. Variation in the strontium isotopic composition of seawater (8 Ma to present): Implications for chemical weathering rates and dissolved fluxes to the oceans. *Chemical Geology (Isotope Geoscience Section)* **80**, 291-307.

Hodell, D. A., Mueller, P.A. and Garrido. J.R. 1991. Variations in the Strontium Isotopic Composition of Seawater During the Neogene. *Geology* **19**, 24 –27.

Holland, G., Lollar, B.S., Li, L., Lacrampe-Couloume, G., Slater, G.F. and Ballentine, C.J. 2013. Deep fracture fluids isolated in the crust since the Precambrian era. *Nature* **497**, 357-360.

Holly A.M, Mulligan, A.E. and Harvey, C.F. 2005. Seasonal oscillations in water exchange between aquifers and the coastal ocean. *Nature* **436**, 1145-1148.

Holser, W.T., Kaplan, I.R., Sakai, H. and Zak, I. 1979. Isotope geochemistry of oxygen in the sedimentary sulphate cycle. *Chemical Geology* **25**, 1-17.

Holser, W.T., Maynard, J.B. and Cruikshank, K.M. 1989. Modelling the natural cycle of sulphur through Phanerozoic time. In *Evolution of the Global Biogeochemical Sulphur Cycle*. Brimblecombe, P. and Lein, A.Y. (Eds). SCOPE John Wiley and Sons Ltd.

Hovius, N., Stark, C.P., Chu, H-T. and Lin, J-C. 2000. Supply and Removal of Sediment in a landslide-Dominated Mountain Belt: Central Range, Taiwan. The *Journal of Geology* **108**, 73-89.

Hovius, N., Galy, A., Hilton, R.G., Sparkes, R., Smith, J., Kao, S-J., Hongey, C., Lin I-T., and West., A.J. 2011a. Erosion-driven Drawdown of Atmospheric Carbon Dioxide: The Organic Pathway. *Applied Geochemistry* **26**, S285-S287.

Hovius, N., Meunier, P., Lin, C-W., Chen, H., Chen, Y.-G., Dadson, S., Horng, M-J. and Lines, M. 2011b. Prolonged Seismically Induced Erosion and the Mass Balance of a Large Earthquake. *Earth and Planetary Science Letters* **304**, 347–355.

Hsu, T.L. 1961. The artesian water system beneath the Pingtung valley, southern Taiwan. *Proc. Geol. Soc. China* **4**, 73-81.

Hsu, L.M. 1984. Pleistocene formation with dissolved-in-water type gas in the Chianan plain, Taiwan. *Petroleum Geology of Taiwan* **20**, 199-213.

Hsu, S-K. 1998. Plan for a groundwater monitoring network in Taiwan. *Hydrogeology Journal* **6**, 405-415.

Hussain, N., Church, T.M. and Kim, G. 1999. Use of ^{222}Rn and ^{226}Ra to trace groundwater discharge into Chesapeak Bay. *Mar. Chem*. **65**, 127–134.

IAEA (International Atomic Energy Agency). 1983a. *Guidebook on Nuclear Techniques in Hydrology.* IAEA, Vienna, Tech. Rept. Ser. No. 91.

IAEA. 1983b. *Isotope Techniques in the Hydrogeological Assessment of Potential Sites for the Disposal of High Level Radioactive Wastes.* IAEA, Vienna, Tech. Rept. Ser. No. 228.

Ishikawa, T., Tanimizu, M., Nagaishi, K., Matsuoka, J., Tadai, O., Sakaguchi, M., Hirono, T., Mishima, T., Tanikawa, W., Lin, W., Kikuta, H., Soh, W. and Song, S.-R. 2008.

Coseismic fluid–rock interactions at high temperatures in the Chelungpu fault. *Nature Geoscience* **1**, 679-683.

Jacobson, A.D., Blum, J.D. and Walter, L.M. 2002. Reconciling the elemental and Sr isotope composition of Himalayan weathering fluxes: Insights from the carbonate geochemistry of stream waters. *Geochim. Cosmochim. Acta* **66**, 3417-3429.

Jacobson, A.D. and Blum, J.D. 2003. Relationship between mechanical erosion and atmospheric CO_2 consumption in the New Zealand Southern Alps. *Geology* **31**, 865-868.

Jean, J.S. 1992. Investigations on infiltrability and grain size analysis in Pingtung Plain. *National Cheng Kung University, Technical Report, Taiwan, ROC* 450pp (in Chinese).

Johannes, R. E. 1980. The ecological significance of the submarine discharge of groundwater. *Mar. Ecol. Prog. Ser*. **3**, 365-373.

Jones, G.E. and Starky, R.J. 1957. Fractionation of stable isotopes of sulfur by micro organisms and their role in deposition of native sulfur. *J. Appl. Microbiol.* **5**, 111–115.

Kao, T.M. and Kao, S.R. 1954. Studies on the cause of a particular dry gangrene. *J. Formosan Med. Assoc*. **53**, 272 (abstract).

Kao, S.J. and Liu, K.K. 1996. Particulate organic carbon export from a subtropical mountainous river (Lanyang His) in Taiwan. *Limnology and Oceanography* **41**, 1749-1757.

Karim, A. and Veizer, J. 2000. Weathering processes in the Indus River Basin: implications from riverine carbon, sulphur, oxygen and strontium isotopes. *Chemical Geology* **170**, 153-177.

Kasting, J.F. 1984. Comments on the BLAG model: The carbonate-silicate geochemical cycle and its effect on atmospheric carbon dioxide over the past 100 million years. *American Journal of Science* **284**, 1175-1182.

Kasting J.F. 1987. Theoretical constraints on oxygen and carbon dioxide concentrations in the Precambrian atmosphere. *Precambrian Res*. **34**, 205-229.

Kay, A. E., Lau, L.S., Stroup, E.D., Dollar, S.J., Fellows, D.P. and Young, R.H.F. 1977. Hydrological and ecological inventories of the coastal waters of West Hawaii. Univ. Hawaii, Water Resources Research Center Technical Report, 105, 94 pp.

Keeling, C.D., Piper, S.C., Bacastow, R.B., Wahlen, M., Whorf, T.P., Heimann, M. and Meijer. H.A. 2001. Exchanges of atmospheric CO2 and 13CO2 with the terrestrial biosphere and oceans from 1978 to 2000. I. Global aspects, SIO Reference Series, no. 01-06, San Diego, CA: Scripps Institution of Oceanography.

Kendall, C. and McDonnel, J.J. 1998. In *Isotope Tracers in Catchment Hydrology*. Elsevier Science B.V., Amsterdam. pp. 51-86.

Kim, G., Lee, K.K., Park, K.S., Hwang, D.W. and Yang, H.S. 2003. Large submarine groundwater discharge (SGD) from a volcanic island. *Geophysical research letters* **30**, doi:10.1029/2003GL018378.

Kısakűrek, B., James, R.H. and Harris, N.B.W. 2005. Li and δ^7Li in Himalayan rivers: Proxies for silicate weathering? *Earth Planet. Sci. Lett*. **237**, 387−401.

Kopf, A., Klaeschen, D. and Mascle, J. 2001. Extreme efficiency of mud volcanism in dewatering of accretionary prisms. *Earth Planet. Sci. Lett*. **189**, 295-313.

Kopf, A., Dehyle, A., Lavrushun, V.Y., Polyak, B.G., Gieskes, J.M., Buadnidze, G.I., Wallmann, K. and Eisenhauer, A. 2003. Isotopic evidence (He, B, C) for deep fluid and mud mobilization from mud volcanoes in the Caucasus continental collision zone. *Int. J. Earth Sci. (Geol. Rund.)*, **92**, 407-425.

Krásný, J. and Sharp, J.M., Eds. 2007. Introductory paper: Hydrology of fractured rocks from particular fractures to regional approaches: State-of-the-art and future challenges (1-30). In Groundwater in Fractured Rocks: Selected papers from the Groundwater in Fractured Rocks Conference, Prague, 2003. Taylor & Francis Group, London, UK.

Krishnaswami, S., Singh, S. and Dalai, T. 1999. Silicate weathering in the Himalaya: Role in contributing to major ions and radiogenic Sr to the Bay of Bengal. In Ocean Science, Trends and Future Directions. Ed. B.L.K. Somayajulu. Indian National Science Academy and Akademia International, New Delhi, pp 23-51.

Kuo, C-H., Wang, C-H. and Huang, C-C. 2003. Declination of groundwater levels in recharge areas and its impact on the hydrological environment in the Pingtung Plain, Taiwan. *Western Pacific Earth Sciences* **3**, 9-20.

Laaksoharju, M., Gascoyne, M. and Gurban, I. 2008. Understanding Groundwater Chemistry Using Mixing Models. *High-level Radioactive Waste Disposal in Sweden: Hydrogeochemical Characterisation and Modelling of Two Potential Sites* **2**3, 1921–1940.

Langmuir, D., and Mahoney, J.J. 1984. Chemical equilibrium and kinetics of geochemical processes in ground water studies: in Hitchon, B., and Wallick, E., eds., Practical Applications of Ground Water Geochemistry, National Water Well Association, Dublin, Ohio.

Lasaga, A.C., Soler, J.M., Ganor, J., Burch, T.E. and Nagy, K.L. 1994. Chemical weathering rate laws and global geochemical cycles. *Geochimica et Cosmochimica Acta* **58**, 2361–2386.

Lee, C.H., Chen, W.P. and Lee, R.H. 2002. Estimate groundwater recharge of Taiwan from base-flow-record method. *J. Taiwan Water Conservancy* **50**, 69-80 (in Chinese with English abstract).

Lee, C.H., Chen, W.P. and Lee, R.H. 2006. Estimation of groundwater recharge using water balance coupled with base-flow-record estimation and stable-base-flow analysis. *Environ. Geol*. **51**, 73-82.

Lerman, A. and Wu., L. 2006. CO_2 and sulphuric acid controls of weathering a river composition. *J. Geochem. Explor*. **88**, 427-430.

Lerman, Abraham, Lingling Wu, and Fred T. Mackenzie. 2007. CO_2 and H_2SO_4 Consumption in Weathering and Material Transport to the Ocean, and Their Role in the Global Carbon Balance. *Special Issue: Dedicated to the Memory of Professor Roland Wollast* **106**, 326–350.

Li, L., Barry, D.A., Stagnitti, F. and Parlange, J.Y. 1999. Submarine groundwater discharge and associate chemical input to a coastal sea. *Water Resour. Res*. **35**, 3253-3259.

Li, S-L., Calmels, D., Han, G., Gaillardet, J. and Liu, C-Q. 2008. Sulphuric acid as an agent of carbonate weathering constrained by $^{13}C_{DIC}$: Examples from Southwest China. *Earth Planet. Sci. Lett*. **270**, 189-199.

Liew, P.M., Hsieh, M.L. and Lai, C.K. 1990. Tectonic significance of Holocene marine terraces in the Coastal Range, eastern Taiwan. *Geodynamic Evolution of the Eastern Eurasian Margin* **183**, 121–127.

Liew, P.M., Pirazzoli, P.A., Hsieh, M.L., Arnold, M., Barusseau, J.P., Fontugne, M. and Giresse, P. 1993. Holocene tectonic uplift deduced from elevated shorelines, eastern Coastal Range of Taiwan. *Tectonophys*. **222**, 55-68.

Liew, P.M., C.M. Kuo, S.Y. Huang, and M.H. Tseng. 1998. Vegetation Change and Terrestrial Carbon Storage in Eastern Asia During the Last Glacial Maximum as Indicated by a New Pollen Record from Central Taiwan. *Global and Planetary Change* **16–17**, 85–94.

Lin, C.C. 1957. *Geomorphology of Taiwan*. Taiwan Province Archives, Taipei, Taiwan 244pp. (in Chinese).

Lin, K-C., Horng, F-W., Yu, H-M. and Ma, F.C. 1994. Biomass and leaf area index estimates of broadleaf forests in Fu-shan forest. *Bulletin of Taiwan Forestry Research Institute* **9**, 299-315.

Lin, A. T., and Watts, A.B. 2002. Origin of the West Taiwan Basin by Orogenic Loading and Flexure of a Rifted Continental Margin. *Journal of Geophysical Research: Solid Earth* **107**, B9 2185. doi:10.1029/2001JB000669.

Lin, K-C., Hamburg, S.P., Tang, S. Hsia, Y-J. and Lin, T.C. 2003. Typhoon effects on litterfall in a subtropical forest. *Canadian Journal of Forest Research-Revue Canadienne De Recherche Forestiere* **33**, 2184-2192.

Lin, Y-B., Tan, Y-C., Yeh, J.T-C., Liu, C.W. and Chen, C-H. 2004. Aviscoelastic model for groundwater level changes in the Cho-Shui River alluvial fan after the Chi-Chi earthquake in Taiwan. *Water Resources Research* **40**, W04213, doi:10.1029/2003WR002412.

Lin, I-T., Wang, C-H., You, C-F., Lin, S., Huang, K. F. and Chen, Y-G. 2010. Deep submarine groundwater discharge indicated by tracers of oxygen, strontium isotopes and barium content in the Pingtung coastal zone, southern Taiwan. *Mar. Chem*. **122**, 51-58.

Lin, I-T, Wang, C-H., Lin, S. and Chen, Y-G. 2011. Groundwater–seawater Interactions off the Coast of Southern Taiwan: Evidence from Environmental Isotopes. *Journal of Asian Earth Sciences* **41**, 250–262.

Liu, T.K. 1982. Tectonic implications of fission track ages from the Central Range, Taiwan. *Proceedings of the Geological Society of China* **25**, 22-37.

Liu, C.S., Liu, S.Y., Lallemand, S.E., Lundberg, N. and Reed, D. 1998. Digitial elevation model offshore Taiwan and its tectonic implications. *Terrestrial Atmospheric and Oceanic Sciences* **9**, 705-738.

Liu, C.S., Schnürle, P., Wang, Y., Chung, S-H., Chen, S-C. and Hsiuan, T-H. 2006. Distribution and Characters of Gas Hydrate Offshore of Southwestern Taiwan. *Terr. Atmos. Ocean. Sci*. **17**, 615-644.

Liu, K.K., Kao S.J., Wen, L.S. and L., C.K. 2007. Carbon and nitrogen isotopic compositions of particulate organic matter and biogeochemical processes in the eutrophic Danshuei Estuary in northern Taiwan. *Science of the Total Environment* **382**, 103-120.

Liu, T-K., Chen, K-Y., Yang, T.F., Chen, Y-G., Chen, W-F., Kang, S-C. and Lee, C-P. 2009. Origin of Methane in High-arsenic Groundwater of Taiwan – Evidence from Stable Isotope Analyses and Radiocarbon Dating. *Journal of Asian Earth Sciences* **36**, 364–370.

Lo, C-H. and Onstott, T.C. 1995. Rejuvenation of KAr Systems for Minerals in the Taiwan Mountain Belt. *Earth and Planetary Science Letters* **131**, 71–98.

Lloyd, R.M. 1968. Oxygen isotope behavior in the Sulfate-Water System. *J. Geophys. Res.* **73**, 6099–6110.

Lu, S.Y., Cheng, J.D. and Brooks, K.N. 2001. Managing forests for watershed protection in Taiwan. *Forest Ecology and management* **143**, 77-85.

Lyons, W.B., Carey, A.E., Kicks, D.M. and Nezat, C.A. 2005. Chemical weathering in high-sediment-yielding watersheds, New Zealand. *Journal of Geophysical Research* **110**, F01008, doi:10.1029/2003JF000088.

Martin, C.E.A., Galy, A., Hovius, N., Bickle, M., Lin, I.-T., Horng, M.-J., Calmels, D. and Chen, H. 2013. The sources and fluxes of dissolved chemistry in a semi-confined,

sandy coastal aquifer: The Pingtung Plain, Taiwan. *Applied Geochemistry* **33**, 222-236.

McDonald, M.G. and Harbaugh, A.W. 1988. A modular three-dimensional finite-difference ground water flow model. *U.S. Geological Survey Open File Report* 83-875, Book 6.

Meizner, O.E. 1923. The occurrence of ground water in the United States, with a discussion of principles, 321p. USGS Water Supply Paper 489.

Meybeck, M. 1987. Global chemical weathering of surficial rocks estimated from river dissolved loads. *Am. J. Sci*. **287**, 401–428.

Milkov, A.V. 2000. Worldwide distribution of submarine mud volcanoes and associated gas hydrates. *Mar. Geol*. **167**, 29-42.

Miller, W.A. 1865. Chemical examination of a hot spring containing caesium and lithium in Wheal Clifford, Cornwall. In *Report of the British Association* 34th meeting, pp. 35-36.

Milliman, J.D. and Syvitski, J.P.M. 1992. Geomorphic/Tectonic Control of Sediment Discharge to the Ocean: The Importance of Small Mountainous Rivers. *The Journal of Geology* **100**, 525–544.

Millot, R., Scaillet, B. and Sanjuan, B. 2010. Lithium isotopes in island arc geothermal systems, Guadeloupe, Martinique (French West Indies) and experimental approach. *Geochem. Cosmochim. Acta* 74, 1852-1871.

Misra, S. and Froelich, P.N. 2012. Lithium isotope history of Cenozoic seawater: changes in silicate and reverse weathering. *Science* **335**, 818-823.

Mook, W.G., Bommerson, J.C. and Staverman, W.H. 1974. Carbon isotope fractionation between dissolved bicarbonate and gaseous carbon dioxide. *Earth and Planetary Science Letters* **22**, 169-176.

Moore, W. S. 1996. Large groundwater inputs to coastal waters revealed by ^{226}Ra enrichments. *Nature* **380**, 612– 614.

Moore, W.S. 1997. High fluxes of radium and barium from the mouth of the Ganges-Brahmaputra River during low river discharge suggest a large groundwater source. *Earth and Planetary Science Letters* **150**, 141-150.

Moore, W.S. 2010. The effect of submarine groundwater discharge on the ocean. *Annual Review of Marine Science* **2**, 59-88.

Moore, W. S. and Shaw, T. J. 1998. Chemical signals from submarine fluid injection onto the continental shelf. *J. Geophys. Res.-Oceans* **103**, 21543-21552.

Moore, W.S and Wilson, A.M. 2005. Advective flow through the upper continental shelf driven by storms, buoyancy, and submarine groundwater discharge. *Earth Planet. Sci. Lett.* **235**, 564–76.

Mulligan, A.E., Evan, R.L. and Lizarralde, D. 2007. The role of paleochannels in groundwater/seawater exchange. *Journal of Hydrology* **335**, 313-329.

Négrel, P., Allègre, C.J., Dupré, B. and Lewin, E. 1993. Erosion sources determined by inversion of major and trace element ratios and strontium isotopic ratios in river water: The Congo Basin case. *Earth Planet. Sci. Lett*. **120**, 59-76.

Niewöhner, C., Hensen, C., Kasten, S., Zabel, M. and Schulz, H.D. 1998. Deep sulfate reduction completely mediated by anaerobic methane oxidation in sediments of the upwelling area off Namibia. *Geochim. Cosmochim. Acta* **62**, 455-464.

Nordstrum, D.K. and Munoz, J.L. 1986. Geochemical thermodynamics. Palo Alto, California. Blackwell Scientific Publications 477p.

Nordstrom, D.K., Ball, J.W., Donahoe, R.J. and Whittemore, D. 1989. Groundwater chemistry and water-rock interactions at Stripa. *Geochimica et Cosmochimica Acta* **53**, 1727-1740.

Palmer, M.R. and Edmond, J.M. 1989. The strontium isotope budget of the modern ocean. *Earth and Planetary Science Letters* **92**, 11–26.

Pawellek, F., Frauenstein, F. and Veizer, J. 2002. Hydrochemistry and isotope geochemistry of the upper Danube River. *Geochim. Cosmochim. Acta* **66**, 3839-3854.

Peng, T.R., Chen, C.T.A., Wang, C.H., Zhang, J. and Lin Y.J. 2008. Assessment of terrestrial factors controlling the submarine groundwater discharge in water shortage and highly deformed island of Taiwan, Western Pacific Ocean. *Journal of Oceanography* **64**, 323-337.

Quade, J., English, N. and DeCelles, P.G. 2003. Silicate versus carbonate weathering in the Himalaya: a comparison of the Arun and Seti River watersheds. *Chemical Geology* **202**, 276-296.

Rad, S.D., Allègre, C.J. and Louvat, P. 2007. Hidden erosion on volcanic islands. *Earth Planet. Sci. Lett*. **262**, 109-124.

Raymo, M.E. and Ruddiman, W.F. 1992. Tectonic forcing of late Cenozoic climate. *Nature* **359**, 117-122.

Raymo, M.E., Ruddiman, W.F. and Froelich, P.N. 1988. Influence of late Cenozoic mountain building on ocean geochemical cycles. *Geology* **16**, 649-653.

Riedhl, R.J., Huang, N. and Machan, R. 1972. The subtidal pump: a mechanism of interstitial water exchange by wave action. *Mar. Biol*. **13**, 210-221.

Rojstaczer, S., Wolf, S. and Michel, R. 1995. Permeability enhancement in the shallow crust as a cause of earthquake-induced hydrological changes. *Nature* **373**, 237-239.

Salmon, C.D., Walter, M.T., Hedin, L.O. and Brown, M.G. 2001. Hydrological controls on chemical export from an undisturbed old-growth Chilean forest. *Journal of Hydrology* **253**, 69-80.

Sanford, W. E., and Konikow, L. F. 1989a. Simulation of calcite dissolution and porosity changes in saltwater mixing zones in coastal aquifers: *Water Resources Research*, **24**, 655-667.

Sanford, W. E., and Konikow, L. F. 1989b, Porosity development in coastal carbonate aquifers. *Geology*, **17**, 249-252.

Sayles, F.I. and Mangelsdorf, P.C. 1977. The equilibration of clay minerals with seawater: exchange reactions. *Geochim. Cosmochim. Acta* **41**, 951-960.

Schopka, H.H. and Derry, L.A. 2012. Chemical weathering fluxes from volcanic islands and the importance of groundwater: The Hawaiian example. *Earth Planet. Sci. Lett*. **339-340**, 67-78.

Sella, G.F., Dixon, T.H. and Mao, A. 2002. REVEL: a model for recent plate velocities from space geodesy. *J. Geophys. Res*. **107**, 2081. doi:10.1029/2000JB000033.

Seno, T., Moriyama, T., Stein, S., Woods, D.F., Demets, C., Argus D. and Gorgon R. 1987. Redetermination of Philippine Sea plate motion (abstr.). *EOS: Trans. Am. Geophys. Union* **68**, 474.

Seno, T. 1993. Tectonics of the Taiwan region. *J. Seismol. Soc. Jpn*. **46**, 461-477.

Shapiro, S.S. and Wilk, M.B. 1965. An analysis of variance test for normality (complete samples)†. *Biometrika* 52, 591-611.

Sharp, R.P. 1982. Landscape evolution (A review). *Proceedings of the National Academy of Sciences of the United States of America* **79**, 4477–4486.

Shaw, T.J., Moore, W.S., Kloepfer, J., Sochaski, M.A., 1998. The flux of barium to the coastal waters of the southeastern USA: the importance of submarine groundwater discharge. Geochim. Cosmochim. Acta 62, 3047-3054.

Shieh, Y.N. and Taylor, H.P. 1969. Oxygen and carbon isotope studies of contact metamorphism of carbonate rocks. *Journal of Petrology* **10**, 307-331.

Shih, T.T. 1967. A survey of the active mud volcanoes in Taiwan and a study of their types and the character of the mud. *Petrol. Geol. Taiwan* **5**, 259-311.

Shin, T.C. and Teng, T.L. 2001. An overview of the 1999 Chi-Chi, Taiwan, earthquake. *Bulletin of the Seismological Society of America* **91**, 895-913.

Sibuet, J-C., Hsu, S-K., Le Pichon, X., Le Formal, J.P., Reed, D., Moore, G. and Liu, C-S. 2002. East Asia plate tectonics since 15 Ma: Constraints from the Taiwan region. *Tectonophysics* **344**, 103–134.

Simmons, G. M. Jr., 1992. Importance of submarine groundwater discharge (SGWD) and seawater cycling to material flux across sediment/water interfaces in marine environments. *Mar. Ecol. Prog. Ser.* **84**, 173-184.

Simoes, M., Avouac, J.P. and Chen, Y.G. 2007. Slip rates on the Chelungpu and Chushiang thrust faults inferred from a deformed strath terrace along the Dungpuna river, West Central Taiwan. *J. Geophys. Res.* **112**, BO3510. doi:10.1029/2005JB004200.

Song, Y.C. and Xu, G-S. 2003. A Scheme of Vegetation Classification of Taiwan, China. *Acta Botanica Sinica* **45**, 883-895.

Song, S-R. and Liu, C-M. 2006. Distributions and chemical characteristics of the hot springs in Taiwan. *Jour. Eng. Env.* **17**, 93-104.

Slomp, C.P. and Van Cappellen, P. 2004. Nutrient Inputs to the Coastal Ocean Through Submarine Groundwater Discharge: Controls and Potential Impact. *Journal of Hydrology* **295**, 64–86.

Stallard, R. F., and Edmond, J.M. 1983. Geochemistry of the Amazon: 2. The Influence of Geology and Weathering Environment on the Dissolved Load. *Journal of Geophysical Research: Oceans* **88**, 9671–9688.

Stallard, R.F. 1995. Relating chemical and physical erosion. *Rev. Min. Geochem*. **31**, 543-564.

Su, H.J. 1984. Studies on the climate and vegetation types of natural forests in Taiwan: 1. analysis of the variation in climatic factors. *Quarterly Journal of Chinese Forestry* **17**, 1-14.

Suppe, J. 1976. Décollement folding in southwestern Taiwan. *Petroleum Geology of Taiwan* **13**, 25-35.

Taniguchi, M., Burnett, W.C., Cable, J.E. and Turner, J.V. 2002. Investigation of submarine groundwater discharge. *Hydrol. Process*. **16**, 2115–2129.

Taniguchi, M. and Iwakawa, H. 2004. Submarine groundwater discharge in Osaka Bay, Japan. *Limnol*. **5**, 25–32.

Taniguchi, M., Ishitobi, T. and Saeki, K.I. 2005. Evaluation of Terrestrial Factors Controlling the SGD in Taiwan 337 time-space distributions of submarine groundwater discharge. *Ground Water* **43**, 336–342.

Teng, L.S. 1987. Tectonostratigraphic facies and geologic evolution of the Coastal Range, eastern Taiwan. *Geol. Soc. China Mem*. **8**, 229-250.

Teng, L.S. 1990. Geotectonic evolution of late Cenezoic arc-continent collision in Taiwan. *Tectonphys* **183**, 57-76.

Thode, H.G., Monster, J. and Dunford, H.D. 1961. Sulphur isotope geochemistry. *Geochim. Cosmochim. Acta* **25**, 159-174.

Ting, C.S. 1993. Groundwater Resources and Management Evaluation Studies for the Pingtung Plain, Taiwan. National Science Council, National Pingtung Polytechnic Institute and Faculty of Earth Sciences, Free University, Amsterdam.

Ting, C.S. 1996. Groundwater recharge estimation using soil moisture budgeting and chloride mass balance methods in the Pingtung Plain. In: Tiingsanchali T, Wileyewickrema AC, (eds) Proceedings International Conference on Urban Engineering in the 21st Century, Bangkok, Thailand. AIT, pp F212–F217.

Ting, C.S., Zhou, Y., de Vries, J.J. and Simmers, I. 1998a. Development of a Preliminary Ground Water Flow Model for Water Resources Management in the Pingtung Plain, Taiwan. *Ground Water* **36**, 20-36.

Ting, C.S., Kerh, T. and Liao, C-J. 1998b. Estimation of groundwater recharge using the chloride mass balance method, Pingtung Plain, Taiwan. *Hydrogeol. J.* **6**, 282-292.

Turchyn, A.V., Brüchert, V., Lyons, T.W., Engel, G.S., Balci, N., Schrag, D.P. and Brunner, B. 2010. Kinetic Oxygen Isotope Effects During Dissimilatory Sulfate Reduction: A Combined Theoretical and Experimental Approach. *Geochimica et Cosmochimica Acta* **74**, 2011–2024.

Turchyn, A., Tipper, E., Galy, A., Lo, J-K. and Bickle, M. 2013. Isotope evidence for secondary sulphide precipitation along the Marsyandi River, Nepal, Himalayas. *Earth Planet. Sci. Lett*. **374**, 36-46.

Vance, D., Teagle, D. A. H. and Foster, G. L. 2009. Variable Quaternary chemical weathering fluxes and imbalances in marine geochemical budgets. *Nature* **458**, 493-496.

Vasconcelos, C. and McKenzie, J.A. 1997. Microbial mediation of modern dolomite precipitation and diagenesis under anoxic conditions (Lagoa Vermelha, Rio de Janeiro, Brazil). *Journal of Sedimentary Research* **67**, 378-390.

von Blanckenburg, F., Hewawasam, T. and Kubik, P.W. 2004. Cosmogenic nuclide evidence for low weathering and denudation in the wet, tropical highlands of Sri Lanka. *J. Geophys. Res*. **109**, F03008, doi:10.1029/2003JF000049.

von Blanckenburg, F. and Dixon, J.L. 2012. Do Mountains Withdraw CO_2? *Mineralogical Magazine*, **76(6)** 2500.

von Damm K.L., Edmond J.M., Grant B., and Measures C.I. 1985. Chemistry of submarine hydrothermal solutions at 21°N, East Pacific Rise. *Geochim. Cosmochim. Acta* **49**, 2197-2220.

Walker, J.C.G., Hays, P.B., Kasting, J.F. 1981. A negative feedback mechanism for the long-term stabilization of earth's surface temperature. *J. Geophys. Res*. **86**, 9776-9782.

Walker, J.C.G. 1986. Global geochemical cycles of carbon, sulphur and oxygen. *Marine Geology* **70**, 159-174.

Walling, D.E. and Foster, I.D.L. 1975. Variations in the natural chemical concentration of river water during flood flows and the lag effect: some further comments. *J. Hydrol.* **26**, 237–244.

Wang, J. and Wang, P. 1980. Relation between sea-level changes and climatic climactic fluctuations in eastern China in late Pleistocene. *Acta Geographica Sinica* **35**, 299-312 (in Chinese).

Wang, S., Shu, M. and Yang, C. 1988. Morphological study of mud volcanoes on land in Taiwan. *J. Nat. Taiwan Museum* **31**, 31-49.

Wang, C-H., Kuo, C-H., Peng, T-R., Chen, W-F., Liu, T-K. and Chiang, C-J. 2003. Isotope characteristics of groundwaters in the Pingtung Plain, southern Taiwan. *West. Pac. Earth Sci*. **3**, 1-8.

Wang, C.Y., Wang, C.H. and Manga, M. 2004a. Coseismic release of water from mountains: Evidence from the 1999 (Mw=7.5) Chi-Chi, Taiwan, earthquake: *Geology* **32**, 769–772.

Wang, C.Y., Wang, C.H. and Kuo, C.H. 2004b. Temporal change in groundwater level following the 1999 (Mw = 7.5) Chi-Chi earthquake, Taiwan. *Geofluids* **4**, 210-220.

Wang, C.H., Wang, C-Y., Kuo, C-H. and Chen, W-F. 2005 Some isotopic and hydrological changes associated with the 1999 Chi-Chi earthquake, Taiwan. *The Island Arc* **14**, 37-54.

Wang, C.Y., Manga, M., Wang, C.H. and Chen, C.H. 2012. Transient change in groundwater temperature after earthquakes. *Geology* **40**, 119-122.

Warner, N., Lgourna, Z., Bouchaou, L., Boutaleb, S., Tagma, T. Hsaissoune, M. and Vengosh, A. 2013. Integration of Geochemical and Isotopic Tracers for Elucidating Water Sources and Salinization of Shallow Aquifers in the sub-Saharan Drâa Basin, Morocco. *Applied Geochemistry*. doi:10.1016/j.apgeochem.2013.03.005.

West, J. A., Galy, A. and Bickle, M. 2005. Tectonic and climatic controls on silicate weathering. *Earth and Planetary Science Letters* **235,** 211-228.

White, A.F., Bullen, T.D., Vivit, D.V., Schulz, M.S. and Clow, D.W. 1999. The role of disseminated calcite in the chemical weathering of granitoid rocks. *Geochim. Cosmochim. Acta* **63**, 1939–1953.

Willet, S.D., Slingerland, R. and Hovius, N. 2001. Uplift, shortening, and steady-state topography in active mountain belts. *American Journal of Science* **201**, 455-485.

Willett, S.D., Fisher, D., Fuller, C., Yeh, E-C. and Lu, CY. 2003. Erosion Rates and Orogenic-wedge Kinematics in Taiwan Inferred from Fission-track Thermochronometry. *Geology* **31**, 945–948.

Williamson, M.A. and Rimstidt, J.D. 1994. The kinetics and electrochemical rate-determining step of aqueous pyrite oxidation. *Geochim. Cosmochim. Acta* **58**, 5443-5454.

Wiltschko, D.V., Hassler, L., Hung, J.H. and Liao, H.S. 2010. From accretion to collision: Motion and evolution of the Chaochou Fault, southern Taiwan. *Tectonics* **29**, doi:10.1029/2008TC002398.

WRA, (Water Resources Agency), Ministry of Economic Affairs, Section 3, Hsin-yi Road, Taipei, Taiwan.

WRA. 2001. *Groundwater Quality of the Taiwan Groundwater Monitoring Network: Choshui Alluvial Fan and Pingtung Plain (3/5).* MOEA/WRA-900009V3, Ministry of Economic Affairs, Taiwan (in Chinese).

WRPC, (Water Resources Planning Commission) and Delft Hydrualics. 1985. National master plan for water resources management. Set up of the analysis for Kaoping Subarea, Taiwan, 59pp.

Wu, C-C. and Kuo, Y.H. 1999. Typhoons affecting Taiwan: current understanding and future challenges. *Bull. Am. Meteorol. Soc*. **80**, 67-80.

Wu, M.C. 2003. *Groundwater resources maps of Taiwan*. In Proceedings of Conference on Investigation and Application of Hydrogeology, November 2003, Taipei, Taiwan, 149-165 (in Chinese with English abstract).

Yassir, N.A. 1987. Mud volcanoes: Evidence of neotectonic activity. *Mem. Geol. Soc. China* **9**, 513-524.

Yen, T. P. and Tien, P.L. 1986. Chaochou fault in Southern Taiwan. *Proc. Geol. Soc. China* **29**, 9-22.

Yoshimura, K., Nakao, S., Noto, M., Inokura, Y., Urata, K., Chen, M. and Lin, P.W. 2001. Geochemical and stable isotope studies on natural water in the Taroko Gorge Kart

area, Taiwan − chemical weathering of the carbonate rocks by deep source CO_2 and sulfuric acid. *Chemical Geology* **177**, 415-430.

You, C-F., Gieskes, J.M., Lee, T., Yui, T-F. and Chen, H-W. 2004. Geochemistry of Mud Volcano Fluids in the Taiwan Accretionary Prism. *Applied Geochemistry* **19**, 695–707.

Yu, S.B, Kuo, L.C., Hsu, Y.J., Su, H.H., Liu, C.C., Hou, C.S., Lee, J.F., Lai, T.C., Liu, C.C., Liu, C.L., Tseng, T.F., Tsai, C.S. and Shin, T.C. 2001. Preseismic and coseismic displacements associated with the 1999 Chi-Chi, Taiwan, earthquake. *Bulletin of the Seismological Society of America* **91**, 995-1012.

Zektzer, I. S., Ivanov, V.A. and Meskheteli, A.V. 1973. The problem of direct groundwater discharge to the seas. *J. Hydrol*. **20**, 1-36.

Zektzer, I.S. 2000. Groundwater and the Environment: Applications for the Global Community. Lewis Publishers, Boca Raton.

Data Table A. Pingtung and Choshui Plain general well data

Name	TMX	TMY	Screen begin (m)	Screen end (m)	Static water level (m)	Temp. (℃)	pH	Hydraulic conductivity ($\mu m.s^{-1}$)
Pingtung Plain								
QX1	194408	2506330	9	21	4.12	27.3	6.91	190
QX2	194408	2506330	66	90	4.11	26.2	7.35	594
QX3	194408	2506330	174	198	1.26	26.5	7.47	242
WD1	194540	2501970	18	36	5.37	26.6	6.80	273
WD2	194540	2501970	66	90	5.87	25.8	7.33	246
WD3	194540	2501970	132	174	3.52	26.7	7.68	393
CL1	190004	2496500	6	21	4.77	27.8	7.02	2190
CL2	190004	2496500	110	140	4.84	27.6	7.45	567
CL3	190004	2496500	182	194	4.35	28.8	7.07	556
LY1	186809	2490130	24	66	3.54	27.1	7.39	269
LY2	186809	2490130	114	138	2.68	28.6	6.94	94
LY3	186809	2490130	168	192	2.61	29.3	7.04	81
ZM1	188414	2493802	22	34	3.23	27.7	7.40	2
ZM2	188414	2493802	108	132	1.84	28.3	7.31	38
ZM3	188414	2493802	174	192	2.11	28.3	7.29	12
ZM4	188414	2493802	216	228	2.31	28.3	7.38	6
TK1	193156	2485971	9	18	2.49	27.7	6.85	676
TK2	193156	2485971	72	84	2.23	27.1	7.12	482
TK3	193156	2485971	126	138	1.39	27.5	6.95	404
TK4	193156	2485971	165	195	3.08	27.6	6.53	548
KT1	195798	2490241	30	48	3.93	26.0	7.15	221
KT2	195798	2490241	123	141	1.90	26.2	6.41	239
KT3	195798	2490241	168	186	3.55	26.5	6.52	503
KT4	195798	2490241	240	264	1.92	26.9	5.98	295
HY1	192774	2491800	6	24	4.92	27.8	6.20	735
HY2	192774	2491800	165	189	6.80	27.6	6.63	561
HN1	195738	2496246	9	67	4.63	26.7	6.72	348
HN2	195738	2496246	67	73	5.20	26.2	7.14	232
HN3	195738	2496246	96	126	5.26	26.7	7.25	1770
HF1	198476	2511130	14	26	3.68	26.1	6.80	2680

Data Table A continued

Name	TMX	TMY	Screen begin (m)	Screen end (m)	Static water level (m)	Temp. (℃)	pH	Hydraulic conductivity ($\mu m.s^{-1}$)
Pingtung Plain								
HF2	198476	2511130	108	144	Artesian	25.3	6.40	775
HF3	198476	2511130	187	202	2.67	25.8	6.92	108
YP1	205622	2517240	24	42	9.05	25.2	6.71	1990
YP2	205622	2517240	106	160	9.52	25.2	6.42	755
TS1	209266	2521392	62	92	7.84	25.7	5.49	378
TS2	209266	2521392	165	189	7.96	25.8	5.74	536
HS1	200397	2502704	15	33	3.46	25.7	6.93	83
HS2	200397	2502704	46	52	0.90	25.7	7.20	394
HS3	200397	2502704	67	73	2.19	25.8	7.29	113
HS4	200397	2502704	109	148	Artesian	25.1	6.99	302
MA1	208976	2511539	42	72	34.76	25.4	7.32	757
MA2	208976	2511539	116	134	35.05	25.2	7.48	616
MA3	208976	2511539	174	192	35.27	25.1	6.94	85
Choshui Plain								
CP1	168219	2602115	62	74	17.75	26.5	6.99	–
CP2	168219	2602115	150	168	20.07	29.4	6.85	–
PK1	177919	2608767	61	103	16.65	26.3	7.29	–
PK2	177919	2608767	162	180	17.05	28.6	7.49	–
DG1	168595	2607406	55	73	17.54	26.6	7.42	–
DG2	168595	2607406	195	213	16.90	30.8	7.66	–
GC1	188020	2614870	10	28	2.90	25.2	7.07	–
GC2	188020	2614870	55	64	14.98	25.8	6.83	–
GC3	188020	2614870	95	104	15.09	25.6	7.08	–
GC4	188020	2614870	180	198	15.48	26.7	7.05	–
GC5	188020	2614870	270	294	13.57	27.8	7.30	–
KH1	187220	2632820	52	64	7.45	25.6	7.56	–
KH2	187220	2632820	86	140	8.16	25.2	7.43	–
KH3	187220	2632820	195	210	12.24	26.8	7.57	–
KH4	187220	2632820	232	268	12.39	27.6	7.54	–
FR1	178954	2632222	12	48	3.07	26.2	6.72	–
FR2	178954	2632222	73	97	10.47	25.8	7.36	–

Data Table A continued

Name	TMX	TMY	Screen begin (m)	Screen end (m)	Static water level (m)	Temp. (℃)	pH	Hydraulic conductivity ($\mu m.s^{-1}$)
Choshui Plain								
FR3	178954	2632222	126	174	11.02	26.9	7.52	–
HA1	171197	2632096	50	104	14.30	27.1	7.33	–
HA2	171197	2632096	126	174	14.63	29.8	7.62	–
HL1	194891	2632723	20	38	6.30	25.4	7.08	–
HL2	194891	2632723	54	114	6.57	24.9	7.09	–

Data Table B. Hydraulic head values for the Pingtung Plain wells. Values are monthly averages (m)

Date	LY1	LY2	LY3	CL1	CL2	CL3	ZM1
01/11/1995	1.11	–	2.19	–	–	–	–
01/12/1995	0.91	–	1.81	–	–	–	–
01/01/1996	0.76	–	1.48	–	–	–	–
01/02/1996	0.74	–	1.40	–	–	–	–
01/03/1996	0.61	–	1.40	–	–	–	–
01/04/1996	0.53	–	1.40	–	–	–	–
01/05/1996	0.66	–	1.61	–	–	–	–
01/06/1996	0.65	–	1.60	–	–	–	–
01/07/1996	0.71	–	1.58	–	–	–	–
01/08/1996	1.55	–	2.54	–	–	–	–
01/09/1996	1.42	–	2.50	–	–	–	–
01/10/1996	1.21	–	2.31	–	–	–	–
01/11/1996	0.95	–	2.08	–	–	–	–
01/12/1996	0.68	–	1.76	–	1.71	1.70	–
01/01/1997	0.33	–	1.51	1.56	1.55	1.60	–
01/02/1997	0.19	1.30	1.41	1.48	1.56	1.78	–
01/03/1997	0.16	1.23	1.37	1.47	1.55	1.96	–
01/04/1997	0.17	1.20	1.34	1.51	1.51	1.77	–
01/05/1997	0.24	1.27	1.46	1.45	1.55	1.73	–
01/06/1997	1.28	2.11	2.60	3.13	3.08	2.57	–
01/07/1997	1.83	2.60	3.03	3.75	3.61	3.02	–
01/08/1997	2.36	2.93	3.40	4.09	3.88	3.29	–
01/09/1997	2.24	2.98	3.36	4.08	3.86	3.40	–
01/10/1997	1.73	2.56	2.78	3.29	3.08	2.91	–
01/11/1997	1.28	2.20	2.36	2.59	2.45	2.44	–
01/12/1997	0.83	1.85	1.96	2.09	2.02	2.05	–
01/01/1998	0.51	1.24	1.62	1.77	1.81	2.10	–
01/02/1998	0.65	1.44	1.58	1.72	1.76	2.19	–
01/03/1998	0.76	1.53	1.74	1.97	2.03	2.32	–
01/04/1998	0.82	1.59	1.83	1.94	1.97	2.15	–
01/05/1998	0.91	1.77	2.06	2.12	2.17	2.33	–

Data Table B continued

Date	LY1	LY2	LY3	CL1	CL2	CL3	ZM1
01/06/1998	2.10	2.75	3.41	3.84	3.79	3.26	_
01/07/1998	2.03	2.80	3.20	3.87	3.72	3.41	7.45
01/08/1998	1.81	2.70	3.06	3.57	3.51	3.40	7.38
01/09/1998	1.35	2.66	3.04	3.36	3.33	3.35	7.47
01/10/1998	1.21	2.43	2.71	3.06	3.11	3.26	7.37
01/11/1998	1.28	2.37	2.60	2.98	2.99	3.18	7.32
01/12/1998	1.06	2.03	2.17	2.62	2.63	2.88	7.02
01/01/1999	0.91	1.78	1.88	2.35	2.33	2.65	6.76
01/02/1999	0.78	1.60	1.73	2.03	2.04	2.43	6.48
01/03/1999	0.56	1.47	1.62	1.93	1.87	2.27	6.16
01/04/1999	0.35	1.35	1.52	1.89	1.71	2.11	6.00
01/05/1999	0.31	1.38	1.58	1.89	1.90	2.20	6.10
01/06/1999	0.65	1.70	2.03	2.51	2.53	2.62	6.45
01/07/1999	1.70	2.74	3.40	3.63	3.53	3.14	7.20
01/08/1999	2.51	3.29	3.78	4.86	4.69	3.96	7.50
01/09/1999	2.14	2.91	3.18	4.54	4.36	3.95	7.45
01/10/1999	2.10	2.98	3.33	4.21	4.08	3.89	7.53
01/11/1999	1.59	2.50	2.62	3.69	3.60	3.60	7.34
01/12/1999	1.24	2.13	2.19	3.17	3.14	3.26	7.11
01/01/2000	0.96	1.79	1.76	2.62	2.53	2.89	6.57
01/02/2000	0.89	1.66	1.72	2.34	2.32	2.78	6.64
01/03/2000	0.76	1.52	1.66	2.14	2.19	2.64	6.51
01/04/2000	0.63	1.51	1.68	1.98	2.02	2.50	6.28
01/05/2000	0.52	1.55	1.78	2.12	2.19	2.52	6.43
01/06/2000	0.47	1.51	1.70	2.18	2.25	2.63	6.41
01/07/2000	0.57	1.49	1.66	2.54	2.58	2.86	6.49
01/08/2000	1.51	2.45	3.07	4.05	3.96	3.58	7.21
01/09/2000	1.83	2.74	3.02	4.27	4.10	3.69	7.38
01/10/2000	1.49	2.32	2.53	3.65	3.53	3.40	7.16
01/11/2000	1.39	2.19	2.39	3.32	3.26	3.23	7.17
01/12/2000	1.05	1.84	1.93	2.87	2.82	2.96	6.86

Data Table B continued

Date	LY1	LY2	LY3	CL1	CL2	CL3	ZM1
01/01/2001	0.79	1.53	1.56	2.35	2.33	2.78	6.54
01/02/2001	0.70	1.43	1.51	2.06	2.07	2.54	6.42
01/03/2001	0.54	1.36	1.48	1.90	1.85	2.27	6.17
01/04/2001	0.40	1.35	1.51	1.83	1.77	2.14	6.13
01/05/2001	0.42	1.44	1.68	1.96	1.93	2.25	6.23
01/06/2001	1.26	2.32	2.85	3.44	3.43	3.25	7.11
01/07/2001	1.69	2.68	3.05	4.04	3.94	3.72	7.34
01/08/2001	1.58	2.41	2.60	3.99	3.90	3.88	7.24
01/09/2001	2.11	2.97	3.49	4.40	4.27	4.06	7.41
01/10/2001	2.17	3.04	3.31	4.61	4.49	4.23	7.39
01/11/2001	1.59	2.49	2.58	3.78	3.69	3.79	7.11
01/12/2001	1.21	2.10	2.12	3.13	3.09	3.40	6.84
01/01/2002	0.94	1.75	1.76	2.10	2.24	2.91	6.50
01/02/2002	0.81	1.66	1.75	1.49	1.68	2.60	6.29
01/03/2002	0.68	1.60	1.74	1.54	1.61	2.29	6.09
01/04/2002	0.54	1.51	1.64	1.54	1.46	1.90	5.87
01/05/2002	0.51	1.49	1.69	1.59	1.49	1.75	5.91
01/06/2002	0.69	1.77	2.02	2.03	2.08	2.28	6.17
01/07/2002	0.60	1.65	1.78	2.18	2.24	2.48	5.99
01/08/2002	0.77	1.65	1.94	2.62	2.64	2.77	6.09
01/09/2002	0.81	1.57	1.90	2.58	2.53	2.61	6.09
01/10/2002	0.68	1.51	1.79	2.36	2.32	2.36	6.14
01/11/2002	0.45	1.40	1.58	1.15	2.08	2.13	6.03
01/12/2002	0.22	1.16	1.31	_	1.86	1.95	5.72
01/01/2003	0.17	1.02	1.16	_	1.58	1.87	5.61
01/02/2003	0.16	0.96	1.12	0.76	1.45	1.76	5.35
01/03/2003	0.09	1.03	1.13	1.37	1.38	1.61	4.97
01/04/2003	0.04	1.01	1.15	1.32	1.35	1.52	4.80
01/05/2003	-0.03	0.95	1.12	1.28	1.31	1.35	4.96

Data Table B continued

Date	ZM2	ZM3	ZM4	QX1	QX2	QX3	HF1
01/11/1995	–	–	–	–	14.12	11.41	–
01/12/1995	–	–	–	–	13.91	10.93	–
01/01/1996	–	–	–	–	13.62	10.62	–
01/02/1996	–	–	–	–	13.33	10.36	–
01/03/1996	–	–	–	–	13.04	9.99	–
01/04/1996	–	–	–	–	12.94	9.84	–
01/05/1996	–	–	–	–	13.12	9.86	–
01/06/1996	–	–	–	–	13.16	9.89	–
01/07/1996	–	–	–	–	13.21	9.77	–
01/08/1996	–	–	–	–	15.00	10.83	–
01/09/1996	–	–	–	–	14.93	11.11	–
01/10/1996	–	–	–	–	14.74	11.02	–
01/11/1996	–	–	–	–	14.42	10.81	–
01/12/1996	–	–	–	–	13.99	10.44	–
01/01/1997	–	–	–	–	13.71	10.17	28.59
01/02/1997	–	–	–	–	13.60	10.09	28.66
01/03/1997	–	–	–	13.25	13.31	9.85	28.41
01/04/1997	–	–	–	13.07	13.08	9.90	28.23
01/05/1997	–	–	–	12.90	12.98	9.75	27.90
01/06/1997	–	–	–	–	14.48	10.64	28.89
01/07/1997	–	–	–	15.42	15.41	11.65	29.72
01/08/1997	–	–	–	16.02	16.01	12.52	30.37
01/09/1997	–	–	–	15.91	15.90	13.25	30.23
01/10/1997	–	–	–	15.42	15.43	13.25	29.53
01/11/1997	–	–	–	15.04	15.02	13.07	29.13
01/12/1997	–	–	–	14.70	14.70	12.81	28.87
01/01/1998	–	–	–	14.27	14.27	12.62	28.64
01/02/1998	–	–	–	13.92	13.92	12.49	28.51
01/03/1998	–	–	–	13.85	13.87	12.43	28.63
01/04/1998	–	–	–	13.78	13.81	12.22	28.39
01/05/1998	–	–	–	13.82	13.83	12.10	28.52

Data Table B continued

Date	ZM2	ZM3	ZM4	QX1	QX2	QX3	HF1
01/06/1998	–	7.46	7.12	15.32	15.37	13.03	30.09
01/07/1998	7.53	7.48	7.18	15.50	15.56	13.67	29.89
01/08/1998	7.47	7.90	7.17	15.24	15.33	13.80	29.88
01/09/1998	7.58	7.57	7.28	15.10	15.13	13.89	29.77
01/10/1998	7.48	7.50	7.25	14.80	14.82	13.81	29.55
01/11/1998	7.43	7.42	7.19	14.76	14.78	13.75	29.48
01/12/1998	7.14	7.15	6.98	14.48	14.50	13.47	29.14
01/01/1999	6.88	6.89	6.70	14.25	14.25	13.20	28.87
01/02/1999	6.59	6.60	6.45	14.03	14.02	12.84	28.57
01/03/1999	6.25	6.30	6.22	13.78	13.78	12.66	28.30
01/04/1999	6.10	6.12	6.01	13.58	13.56	12.45	27.99
01/05/1999	6.22	6.23	6.09	13.55	13.52	12.38	28.02
01/06/1999	6.61	6.58	6.37	13.96	13.93	12.53	28.51
01/07/1999	7.41	7.31	6.99	15.15	15.11	13.19	29.66
01/08/1999	7.70	7.67	7.49	16.36	16.30	14.55	30.83
01/09/1999	7.59	7.63	7.46	15.94	15.89	15.18	30.46
01/10/1999	7.62	7.71	7.54	15.57	15.53	15.36	30.27
01/11/1999	7.57	7.54	7.37	15.14	15.12	15.12	29.61
01/12/1999	7.35	7.33	7.18	14.90	14.88	14.90	29.32
01/01/2000	6.74	6.97	6.88	14.17	14.63	14.64	28.83
01/02/2000	6.82	6.83	6.72	14.44	14.43	14.46	28.47
01/03/2000	6.68	6.73	6.60	14.26	14.24	14.22	28.26
01/04/2000	6.45	6.58	6.41	14.07	14.05	14.02	28.10
01/05/2000	6.62	6.64	6.46	13.98	13.96	13.99	27.92
01/06/2000	6.61	6.63	6.45	14.03	14.02	13.92	27.96
01/07/2000	6.70	6.72	6.52	14.33	14.33	14.08	28.42
01/08/2000	7.47	7.42	7.14	15.90	15.89	15.28	30.31
01/09/2000	7.33	7.33	7.14	15.26	15.80	15.93	30.07
01/10/2000	7.36	7.36	7.19	15.28	15.27	15.82	29.44
01/11/2000	7.36	7.42	7.24	15.03	15.04	15.67	29.50
01/12/2000	7.05	7.04	6.94	14.80	14.82	15.41	29.25

Data Table B continued

Date	ZM2	ZM3	ZM4	QX1	QX2	QX3	HF1
01/01/2001	6.72	6.76	6.69	14.51	14.54	15.15	28.94
01/02/2001	6.62	6.64	6.57	14.24	14.26	14.94	28.82
01/03/2001	6.33	6.36	6.34	14.03	14.04	14.67	28.52
01/04/2001	6.30	6.30	6.25	13.89	13.89	14.47	28.26
01/05/2001	6.41	6.45	6.33	14.11	14.12	14.47	28.39
01/06/2001	7.35	7.31	7.05	15.76	15.76	15.53	30.32
01/07/2001	7.57	7.57	7.37	16.12	16.10	16.33	30.58
01/08/2001	7.47	7.46	7.33	15.96	15.96	16.79	30.65
01/09/2001	7.60	7.66	7.51	15.98	15.99	16.98	30.68
01/10/2001	7.64	7.65	7.54	15.83	15.83	17.32	30.24
01/11/2001	7.40	7.39	7.28	15.05	15.06	16.95	29.58
01/12/2001	7.15	7.16	7.07	14.53	14.55	16.68	29.46
01/01/2002	6.80	6.83	6.80	14.17	14.20	16.24	29.20
01/02/2002	6.58	6.63	6.60	14.02	14.06	15.99	28.96
01/03/2002	6.38	6.42	6.40	13.93	13.94	15.51	28.64
01/04/2002	6.16	6.20	6.17	13.72	13.72	15.07	28.29
01/05/2002	6.17	6.17	6.11	13.67	13.67	14.67	28.09
01/06/2002	6.48	6.46	6.41	14.01	14.01	14.60	28.45
01/07/2002	6.30	6.35	6.28	13.97	13.99	14.42	28.67
01/08/2002	6.40	6.44	6.33	14.44	14.47	14.80	29.57
01/09/2002	6.40	6.44	6.33	14.29	14.32	14.76	29.25
01/10/2002	6.44	6.47	6.36	14.03	14.06	14.53	28.98
01/11/2002	6.36	6.37	6.29	13.83	13.86	14.22	28.78
01/12/2002	6.04	6.07	6.05	13.66	13.68	13.98	28.65
01/01/2003	5.92	5.93	5.93	13.54	13.56	13.93	28.49
01/02/2003	5.62	5.59	5.64	13.48	13.49	13.69	28.24
01/03/2003	5.20	5.20	5.28	13.36	13.37	13.38	27.98
01/04/2003	5.04	5.02	5.07	13.27	13.27	13.14	27.83
01/05/2003	5.23	5.18	5.14	13.15	13.14	12.88	27.53

Data Table B continued

Date	HF2	HF3	WD1	WD2	WD3	HS1	HS2
01/11/1995	–	–	–	–	–	–	15.51
01/12/1995	–	–	–	–	–	–	15.41
01/01/1996	–	–	–	–	–	–	15.21
01/02/1996	–	–	–	–	–	–	14.93
01/03/1996	–	–	–	–	–	–	14.59
01/04/1996	–	–	–	–	–	–	14.76
01/05/1996	–	–	–	–	–	–	15.14
01/06/1996	–	–	–	–	–	–	15.05
01/07/1996	–	–	–	–	–	–	14.87
01/08/1996	–	–	–	–	–	–	16.21
01/09/1996	–	–	–	–	–	–	15.94
01/10/1996	–	–	–	–	–	–	15.94
01/11/1996	–	–	–	–	–	–	15.72
01/12/1996	–	–	–	8.32	7.06	–	15.50
01/01/1997	–	–	8.53	8.10	6.97	–	15.44
01/02/1997	–	–	8.31	7.91	6.96	14.33	15.47
01/03/1997	–	–	8.10	7.74	6.88	14.19	15.19
01/04/1997	–	–	7.95	7.57	6.73	14.03	15.07
01/05/1997	–	–	7.75	7.34	6.65	13.99	14.90
01/06/1997	–	–	8.60	8.69	7.48	14.75	15.75
01/07/1997	–	–	9.63	9.57	8.21	14.61	15.87
01/08/1997	–	–	10.48	10.42	8.82	14.40	15.94
01/09/1997	–	–	11.03	10.71	9.33	14.25	15.94
01/10/1997	–	–	10.70	10.16	9.20	13.81	15.53
01/11/1997	–	–	10.23	9.65	8.92	13.59	15.18
01/12/1997	–	–	9.71	9.17	8.68	13.65	15.11
01/01/1998	–	–	9.21	8.72	8.60	13.87	15.13
01/02/1998	–	–	8.88	8.45	8.55	13.86	15.05
01/03/1998	–	–	8.71	8.37	8.60	14.03	15.31
01/04/1998	–	–	8.56	8.22	8.37	13.96	15.08
01/05/1998	–	–	8.58	8.24	8.43	14.11	15.37

Data Table B continued

Date	HF2	HF3	WD1	WD2	WD3	HS1	HS2
01/06/1998	33.42	29.26	9.72	9.78	9.32	14.74	16.14
01/07/1998	33.56	30.89	10.43	10.12	9.72	14.38	15.82
01/08/1998	33.59	30.91	10.39	9.96	9.76	14.54	16.03
01/09/1998	33.57	30.90	10.17	9.72	9.79	14.44	16.08
01/10/1998	33.33	30.79	9.88	9.52	9.71	14.30	15.90
01/11/1998	33.14	30.68	9.86	9.49	9.70	14.15	15.75
01/12/1998	32.75	30.34	9.65	9.25	9.47	14.07	15.64
01/01/1999	32.31	29.96	9.35	8.88	9.21	13.89	15.42
01/02/1999	31.73	29.46	9.02	8.52	8.85	13.81	15.12
01/03/1999	31.07	28.99	8.72	8.26	8.64	13.66	14.88
01/04/1999	30.30	28.34	8.46	8.04	8.41	13.59	14.71
01/05/1999	30.22	28.09	8.33	8.00	8.42	14.05	15.11
01/06/1999	30.94	28.51	8.54	8.29	8.65	14.44	15.51
01/07/1999	32.63	29.62	9.35	9.24	9.22	14.66	15.94
01/08/1999	34.46	31.19	10.61	10.53	10.28	14.70	16.38
01/09/1999	34.38	31.49	10.97	10.68	10.71	14.54	16.25
01/10/1999	34.11	31.32	10.98	10.58	10.91	14.42	16.22
01/11/1999	33.46	30.86	10.70	10.17	10.68	14.09	15.73
01/12/1999	33.00	30.46	10.27	9.75	10.44	14.17	15.75
01/01/2000	32.37	30.04	9.87	9.36	10.11	14.05	15.51
01/02/2000	31.79	29.49	9.47	8.90	9.85	14.02	15.36
01/03/2000	31.19	29.03	9.12	8.58	9.70	13.72	15.05
01/04/2000	30.65	28.51	8.81	8.30	9.53	13.62	14.85
01/05/2000	30.32	28.17	8.55	8.06	9.52	13.58	14.77
01/06/2000	30.46	28.10	8.35	7.96	9.49	13.77	14.84
01/07/2000	31.63	28.70	8.47	8.24	9.61	14.38	15.43
01/08/2000	33.77	30.34	10.02	10.03	10.66	14.71	16.22
01/09/2000	34.11	31.05	10.63	10.25	11.13	14.30	16.02
01/10/2000	33.66	30.93	10.37	9.87	10.91	14.05	15.74
01/11/2000	33.47	30.70	10.12	9.66	10.90	14.15	15.78

Data Table B continued

Date	HF2	HF3	WD1	WD2	WD3	HS1	HS2
01/12/2000	33.08	30.51	9.85	9.34	10.66	13.92	15.53
01/01/2001	32.57	30.14	9.51	8.95	10.33	13.86	15.32
01/02/2001	32.05	29.65	9.16	8.59	10.11	13.92	15.31
01/03/2001	31.28	29.01	8.82	8.23	9.84	13.68	14.97
01/04/2001	30.71	28.50	8.47	7.98	9.72	13.52	14.84
01/05/2001	30.74	28.22	8.35	8.14	9.76	13.90	14.95
01/06/2001	33.35	30.01	9.75	9.75	10.83	14.73	16.07
01/07/2001	34.21	30.97	10.57	10.32	11.36	14.76	16.23
01/08/2001	34.33	31.44	10.89	10.37	11.76	14.88	16.41
01/09/2001	34.47	31.55	11.25	11.11	11.96	14.95	16.59
01/10/2001	34.56	31.76	11.65	11.25	12.36	14.61	16.32
01/11/2001	33.98	31.30	11.25	10.74	12.00	14.39	15.97
01/12/2001	33.38	30.76	10.84	10.36	11.71	14.37	15.81
01/01/2002	32.69	30.26	10.46	9.87	11.34	14.28	15.62
01/02/2002	32.09	29.81	9.99	9.38	11.01	14.15	15.48
01/03/2002	31.33	29.23	9.53	8.91	10.55	13.94	15.14
01/04/2002	30.54	28.54	9.07	8.48	10.21	13.61	14.75
01/05/2002	30.03	27.95	8.66	8.06	9.86	13.86	14.82
01/06/2002	30.50	28.26	8.75	8.36	9.99	14.09	15.20
01/07/2002	31.51	28.82	8.58	8.22	9.90	14.40	15.48
01/08/2002	33.07	30.06	8.83	8.60	10.15	14.58	15.91
01/09/2002	33.14	30.39	8.84	8.49	10.05	14.12	15.57
01/10/2002	32.87	30.25	8.59	8.22	9.81	14.02	15.42
01/11/2002	32.44	30.01	8.35	7.98	9.57	14.02	15.35
01/12/2002	31.99	29.60	8.19	7.83	9.41	14.17	15.45
01/01/2003	31.52	29.27	8.01	7.60	9.28	14.06	15.34
01/02/2003	30.95	28.78	7.84	7.45	9.06	13.83	15.02
01/03/2003	30.34	28.27	7.73	7.33	8.82	13.68	14.82
01/04/2003	29.83	27.82	7.59	7.20	8.62	13.58	14.64
01/05/2003	29.30	27.35	7.44	7.05	8.44	13.46	14.46

Data Table B continued

Date	HS3	HS4	TK1	TK2	TK3	TK4	HN1
01/11/1995	16.39	_	_	_	_	_	5.20
01/12/1995	16.17	_	_	_	_	_	4.91
01/01/1996	15.89	_	_	_	_	_	4.70
01/02/1996	15.61	_	_	_	_	_	4.67
01/03/1996	15.10	_	_	_	_	_	4.68
01/04/1996	15.35	_	_	_	_	_	4.68
01/05/1996	15.86	_	_	_	_	_	4.92
01/06/1996	15.63	_	_	_	_	_	4.92
01/07/1996	15.53	_	_	_	_	_	4.90
01/08/1996	17.41	_	_	_	_	_	5.53
01/09/1996	17.37	_	_	_	_	_	5.54
01/10/1996	17.51	_	_	_	_	_	5.45
01/11/1996	17.05	_	_	_	_	_	5.27
01/12/1996	16.59	_	_	-0.18	_	_	5.01
01/01/1997	16.48	_	-0.29	-0.20	-1.63	-2.28	4.71
01/02/1997	16.37	17.30	-0.15	-0.24	-1.90	-2.25	4.51
01/03/1997	15.91	17.44	-0.12	-0.46	-2.16	-2.41	4.58
01/04/1997	15.76	17.09	-0.10	-0.63	-2.22	-2.58	4.54
01/05/1997	15.52	16.93	0.03	-0.70	-2.39	-2.61	4.54
01/06/1997	16.52	18.11	0.27	0.03	-1.35	-1.92	5.28
01/07/1997	17.04	18.80	-0.50	0.14	-1.16	-1.81	5.51
01/08/1997	17.56	19.49	-0.75	0.39	-0.78	-1.55	5.78
01/09/1997	17.74	19.72	-0.90	0.51	-0.59	-1.48	6.04
01/10/1997	17.15	19.01	-0.42	0.27	-1.14	-1.82	5.72
01/11/1997	16.41	18.25	-0.11	-0.05	-1.25	-1.94	5.33
01/12/1997	16.26	18.10	-0.08	0.04	-1.13	-1.88	5.03
01/01/1998	15.98	17.71	-0.07	-0.07	-1.49	-1.95	4.73
01/02/1998	15.80	17.61	0.00	-0.32	-1.73	-2.08	4.71
01/03/1998	16.08	17.85	0.06	-0.35	-1.30	-2.08	4.81
01/04/1998	15.64	17.44	0.09	-0.58	-1.65	-2.26	4.81
01/05/1998	16.18	18.09	0.12	-0.44	-1.24	-2.12	4.89

Data Table B continued

Date	HS3	HS4	TK1	TK2	TK3	TK4	HN1
01/06/1998	17.09	19.12	0.46	0.42	-0.53	-1.22	5.66
01/07/1998	16.80	18.76	0.16	0.15	-0.99	-1.47	5.59
01/08/1998	17.05	19.22	0.21	-0.07	-1.26	-1.65	5.51
01/09/1998	17.29	19.50	0.21	-0.02	-0.83	-1.60	5.42
01/10/1998	17.14	19.38	0.21	-0.02	-0.84	-1.56	5.24
01/11/1998	16.90	18.85	0.18	0.12	-0.73	-1.42	5.20
01/12/1998	16.63	18.73	0.12	-0.06	-0.66	-1.79	4.99
01/01/1999	16.18	18.21	0.12	-0.29	-1.00	-2.10	4.78
01/02/1999	15.60	17.73	0.05	-0.77	-1.73	-2.48	4.75
01/03/1999	15.25	17.02	0.08	-1.02	-1.96	-2.62	4.80
01/04/1999	15.02	16.90	-0.23	-1.37	-2.32	-2.90	4.82
01/05/1999	15.52	17.48	-0.08	-0.99	-1.78	-2.54	4.93
01/06/1999	15.80	17.73	0.30	-0.65	-1.32	-2.22	5.09
01/07/1999	16.60	18.89	0.42	-0.14	-0.87	-1.68	5.57
01/08/1999	17.57	19.93	0.45	0.55	-0.20	-0.98	6.24
01/09/1999	17.52	19.97	0.35	0.60	-0.14	-0.94	6.30
01/10/1999	17.59	20.00	0.37	0.74	0.12	-0.81	6.27
01/11/1999	16.78	18.92	0.08	0.43	-0.26	-1.09	5.90
01/12/1999	16.88	19.10	-0.02	0.41	-0.24	-1.12	5.58
01/01/2000	16.35	18.18	0.05	-0.10	-0.72	-1.83	5.30
01/02/2000	16.02	17.96	0.13	-0.22	-1.18	-1.97	5.21
01/03/2000	15.64	17.48	0.10	-0.36	-1.33	-2.12	5.20
01/04/2000	15.40	17.18	0.02	-0.52	-1.42	-2.24	5.16
01/05/2000	15.31	17.11	0.09	-0.54	-1.40	-2.29	5.24
01/06/2000	15.15	16.82	0.02	-0.53	-1.25	-2.27	5.03
01/07/2000	16.01	18.08	0.29	-0.40	-1.11	-2.12	5.10
01/08/2000	17.25	19.46	0.48	0.23	-0.33	-1.47	6.00
01/09/2000	17.25	19.48	0.25	0.10	-0.35	-1.64	6.17
01/10/2000	16.94	19.15	0.16	-0.11	-0.76	-1.86	5.75
01/11/2000	17.00	19.15	0.27	0.06	-0.49	-1.73	5.53
01/12/2000	16.69	18.79	0.10	-0.02	-0.61	-1.82	5.25

Data Table B continued

Date	HS3	HS4	TK1	TK2	TK3	TK4	HN1
01/01/2001	16.16	18.16	0.19	-0.12	-1.12	-1.93	4.93
01/02/2001	16.02	18.08	0.30	-0.16	-1.28	-1.95	4.95
01/03/2001	15.52	17.34	0.20	-0.46	-1.51	-2.25	4.89
01/04/2001	15.45	17.27	0.20	-0.53	-1.56	-2.35	4.91
01/05/2001	15.40	17.42	0.34	-0.55	-1.49	-2.28	5.04
01/06/2001	16.94	18.98	0.49	0.24	-0.64	-1.56	5.62
01/07/2001	17.38	19.58	0.53	0.36	-0.48	-1.50	5.89
01/08/2001	17.58	19.85	0.39	0.25	-0.54	-1.49	5.82
01/09/2001	17.80	20.17	0.59	0.57	-0.06	-1.26	6.30
01/10/2001	17.68	19.93	0.37	0.66	-0.06	-1.22	6.56
01/11/2001	17.19	19.41	0.23	0.27	-0.44	-1.53	6.02
01/12/2001	16.81	18.94	0.01	0.27	-0.53	-1.55	5.64
01/01/2002	16.38	18.32	-0.20	0.23	-0.62	-1.61	5.36
01/02/2002	16.23	18.07	0.05	0.18	-1.02	-1.65	5.34
01/03/2002	15.70	17.48	0.12	-0.09	-1.27	-1.86	5.33
01/04/2002	15.19	16.82	0.14	-0.32	-1.55	-2.02	5.23
01/05/2002	15.19	16.94	0.30	-0.44	-1.48	-2.05	5.21
01/06/2002	15.60	17.23	0.33	-0.03	-0.77	-1.79	5.31
01/07/2002	15.99	17.95	0.15	-0.07	-0.82	-1.80	5.32
01/08/2002	16.67	18.70	-0.12	0.18	-0.52	-1.59	5.54
01/09/2002	16.52	18.66	-0.23	0.13	-0.51	-1.67	5.39
01/10/2002	16.11	18.22	-0.20	0.00	-0.68	-1.78	5.02
01/11/2002	16.02	17.98	-0.04	-0.03	-0.73	-1.75	4.72
01/12/2002	16.16	18.09	0.10	0.18	-0.52	-1.63	4.55
01/01/2003	15.92	17.77	0.13	0.12	-0.81	-1.74	4.40
01/02/2003	15.50	17.21	0.16	-0.11	-1.38	-1.91	4.51
01/03/2003	15.33	16.94	-0.47	-0.20	-1.38	-2.01	4.55
01/04/2003	15.10	16.68	-0.63	-0.30	-1.40	-2.11	4.60
01/05/2003	14.90	16.45	-0.57	-0.42	-1.61	-2.19	4.53

Data Table B continued

Date	HN2	HN3	HY1	HY2	KT1	KT2	KT3
01/11/1995	3.92	3.83	_	-2.39	_	_	_
01/12/1995	3.85	3.81	_	-2.22	_	_	_
01/01/1996	3.15	3.02	_	-2.32	_	_	_
01/02/1996	2.59	2.46	_	-2.59	_	_	_
01/03/1996	2.30	2.16	_	-3.04	_	_	_
01/04/1996	2.54	2.49	_	-3.17	_	_	_
01/05/1996	3.34	3.34	_	-2.89	_	_	_
01/06/1996	3.05	2.97	_	-3.24	_	_	_
01/07/1996	2.54	2.47	_	-3.38	_	_	_
01/08/1996	4.81	4.83	_	-1.81	_	_	_
01/09/1996	4.36	4.37	_	-1.96	_	_	_
01/10/1996	4.62	4.68	_	-1.89	_	_	_
01/11/1996	4.35	4.37	_	-2.06	_	_	_
01/12/1996	3.91	3.88	_	-2.20	_	_	_
01/01/1997	3.20	3.08	-3.09	-2.27	_	_	_
01/02/1997	3.20	3.19	-3.13	-2.30	_	_	_
01/03/1997	3.19	3.16	-3.33	-2.54	_	_	_
01/04/1997	2.91	2.79	-3.66	-2.80	_	_	_
01/05/1997	3.00	2.89	-3.91	-2.87	_	_	_
01/06/1997	4.28	4.25	-2.71	-2.01	_	_	_
01/07/1997	4.70	4.71	-1.89	-1.99	_	_	_
01/08/1997	5.27	5.19	-1.03	-1.66	_	_	_
01/09/1997	5.56	5.52	-0.68	-1.63	_	_	_
01/10/1997	4.96	4.84	-1.11	-2.08	_	_	_
01/11/1997	4.38	4.23	-1.68	-2.26	_	_	_
01/12/1997	4.38	4.38	-2.17	-2.16	_	_	_
01/01/1998	3.36	3.21	-2.62	-2.76	_	_	_
01/02/1998	3.46	3.51	-2.78	-2.62	_	_	_
01/03/1998	3.93	3.99	-2.73	-2.36	_	_	_
01/04/1998	3.51	3.46	-2.73	-2.62	_	_	_
01/05/1998	4.11	4.12	-2.58	-2.48	_	_	_

Data Table B continued

Date	HN2	HN3	HY1	HY2	KT1	KT2	KT3
01/06/1998	5.05	4.96	-0.80	-1.40	_	1.04	0.02
01/07/1998	4.84	4.75	-0.45	-1.88	0.56	0.86	-0.05
01/08/1998	4.76	4.75	-0.73	-2.07	0.62	0.58	-0.34
01/09/1998	5.15	5.16	-0.89	-2.00	0.82	0.63	-0.26
01/10/1998	5.17	5.17	-1.13	-1.92	0.98	0.66	-0.16
01/11/1998	5.31	5.34	-1.15	-1.78	0.81	0.89	-0.01
01/12/1998	5.18	5.23	-1.35	-2.24	0.68	0.88	0.02
01/01/1999	3.87	3.78	-1.60	-2.71	0.55	0.56	-0.29
01/02/1999	3.36	3.26	-1.77	-3.13	0.65	-0.13	-0.79
01/03/1999	3.11	2.99	-2.10	-3.43	0.49	-0.48	-1.13
01/04/1999	2.77	2.62	-2.70	-3.79	0.48	-0.98	-1.58
01/05/1999	3.71	3.71	-3.03	-3.31	0.56	-0.56	-1.17
01/06/1999	3.72	3.56	-3.07	-2.88	0.94	-0.18	-0.75
01/07/1999	4.88	5.55	-1.88	-2.21	1.36	0.47	-0.12
01/08/1999	5.68	5.79	-0.46	-1.46	1.38	1.24	0.60
01/09/1999	5.68	5.69	-0.10	-1.56	1.08	1.27	0.57
01/10/1999	6.01	6.06	-0.10	-1.40	1.13	1.51	0.76
01/11/1999	5.39	5.41	-0.36	-1.75	0.53	1.12	0.41
01/12/1999	5.50	5.56	-0.62	-1.80	0.54	1.06	0.37
01/01/2000	3.97	3.78	-0.98	-2.34	0.33	0.81	-0.95
01/02/2000	3.42	3.21	-1.20	-2.16	0.58	0.56	-1.15
01/03/2000	3.47	3.20	-1.50	-2.12	0.36	0.36	-1.40
01/04/2000	3.15	2.88	-1.96	-2.00	0.27	0.18	-1.47
01/05/2000	3.40	3.23	-2.29	-1.94	0.29	0.12	-1.48
01/06/2000	2.76	2.57	-2.72	-1.87	0.05	0.11	-1.45
01/07/2000	3.63	3.63	-2.94	-1.69	0.75	0.28	-1.29
01/08/2000	5.37	5.45	-1.63	-0.88	1.49	1.09	-0.49
01/09/2000	5.12	5.10	-0.73	-1.99	0.78	1.24	-0.80
01/10/2000	4.54	4.51	-1.01	-2.53	0.46	0.94	-0.96
01/11/2000	4.91	4.93	-0.92	-2.18	0.72	1.15	-0.53
01/12/2000	4.55	4.51	-1.25	-2.25	0.36	0.97	-0.53

Data Table B continued

Date	HN2	HN3	HY1	HY2	KT1	KT2	KT3
01/01/2001	3.13	2.89	-1.65	-2.33	0.35	0.71	-0.59
01/02/2001	3.22	3.05	-1.80	-2.40	0.61	0.56	-0.63
01/03/2001	2.77	2.55	-2.30	-2.66	0.44	0.23	-0.83
01/04/2001	2.74	2.45	-2.79	-2.80	0.34	0.10	-0.92
01/05/2001	3.24	3.13	-2.90	-2.64	0.71	0.10	-0.75
01/06/2001	4.42	4.25	-1.81	-1.80	1.22	0.99	0.15
01/07/2001	5.01	4.95	-0.80	-1.68	1.13	1.18	0.31
01/08/2001	5.02	4.94	-0.40	-1.89	0.83	1.29	-0.24
01/09/2001	5.82	5.81	0.20	-1.73	1.38	1.64	-0.34
01/10/2001	5.67	5.63	1.04	-1.77	0.90	1.80	-0.17
01/11/2001	5.30	5.23	0.57	-2.16	0.59	1.27	-0.49
01/12/2001	5.21	5.16	0.27	-2.13	0.41	1.22	-0.46
01/01/2002	3.90	3.64	-0.01	-2.21	0.35	1.15	-0.48
01/02/2002	3.23	2.92	-0.23	-2.35	0.56	1.01	-0.51
01/03/2002	3.00	2.66	-0.52	-2.56	0.40	0.65	-0.67
01/04/2002	2.19	1.90	-1.03	-2.80	0.23	0.41	-0.86
01/05/2002	2.66	2.44	-1.44	-2.66	0.55	0.45	-1.26
01/06/2002	2.85	2.56	-1.37	-2.48	0.55	0.92	-1.09
01/07/2002	3.40	3.30	-1.68	-2.54	0.62	0.80	-1.07
01/08/2002	3.79	3.65	-1.32	-2.33	0.81	1.10	-0.81
01/09/2002	3.47	3.31	-1.22	-2.41	0.54	0.96	-0.82
01/10/2002	3.28	3.07	-1.25	-2.54	0.28	0.79	-0.86
01/11/2002	3.16	3.00	-1.30	-2.52	0.18	0.73	-0.85
01/12/2002	3.37	3.21	-1.35	-2.34	0.16	0.95	-0.65
01/01/2003	2.05	1.76	-1.41	-2.43	0.15	0.90	-0.66
01/02/2003	1.98	1.68	-1.52	-2.66	0.33	0.54	-0.88
01/03/2003	2.00	1.69	-1.78	-2.82	0.22	0.36	-0.99
01/04/2003	1.80	1.49	-2.24	-2.91	0.17	0.27	-1.06
01/05/2003	2.05	1.87	-2.60	-2.99	0.01	0.18	-1.11

Data Table B continued

Date	KT4	YP1	YP2	TS1	TS2	MA1	MA2
01/11/1995	–	–	–	–	–	46.49	–
01/12/1995	–	–	–	–	–	43.51	–
01/01/1996	–	–	–	–	–	41.02	–
01/02/1996	–	–	–	–	–	39.02	–
01/03/1996	–	–	–	–	–	37.43	–
01/04/1996	–	–	–	–	–	36.19	–
01/05/1996	–	–	–	–	–	37.46	–
01/06/1996	–	–	–	–	–	41.93	–
01/07/1996	–	–	–	–	–	43.39	–
01/08/1996	–	–	–	–	–	49.40	49.00
01/09/1996	–	–	–	–	–	48.89	48.51
01/10/1996	–	–	–	–	–	46.03	45.84
01/11/1996	–	–	–	–	–	44.32	44.20
01/12/1996	–	–	45.53	–	49.19	43.30	43.07
01/01/1997	–	44.70	44.42	52.55	52.44	41.30	41.12
01/02/1997	–	43.91	43.69	50.80	50.69	39.87	39.75
01/03/1997	–	42.97	42.75	49.18	49.10	38.32	38.26
01/04/1997	–	42.41	42.23	48.54	48.47	37.47	37.47
01/05/1997	–	41.75	41.71	48.10	48.04	37.02	37.00
01/06/1997	–	44.52	44.74	52.13	52.08	37.60	38.89
01/07/1997	–	47.20	47.00	57.56	57.41	43.05	42.92
01/08/1997	–	48.99	48.54	61.20	60.89	46.85	46.67
01/09/1997	–	49.77	49.15	63.17	62.82	48.71	48.52
01/10/1997	–	48.56	48.05	60.74	60.46	47.23	46.98
01/11/1997	–	47.08	46.67	57.40	57.14	44.58	44.41
01/12/1997	–	45.61	45.29	54.43	54.22	42.03	41.93
01/01/1998	–	44.37	44.13	51.86	51.69	39.84	39.75
01/02/1998	–	43.45	43.23	50.05	49.94	39.41	39.30
01/03/1998	–	44.00	43.98	50.09	50.10	39.21	39.17
01/04/1998	–	44.01	43.86	50.72	50.71	40.00	39.90
01/05/1998	–	44.96	44.89	52.59	52.57	40.65	40.55

Data Table B continued

Date	KT4	YP1	YP2	TS1	TS2	MA1	MA2
01/06/1998	0.93	48.89	48.55	59.47	59.25	47.50	47.26
01/07/1998	0.79	49.17	48.60	60.57	60.33	49.01	48.68
01/08/1998	0.51	49.06	48.57	60.21	60.01	48.29	48.02
01/09/1998	0.56	49.03	48.54	60.02	59.80	47.74	47.51
01/10/1998	0.66	48.67	48.15	58.84	58.68	46.45	46.28
01/11/1998	0.81	48.60	47.97	58.32	58.17	45.93	45.84
01/12/1998	0.76	47.36	46.94	56.22	56.07	44.64	44.46
01/01/1999	0.44	45.89	45.54	53.88	53.73	42.81	42.62
01/02/1999	-0.01	44.20	43.90	51.23	51.10	41.19	40.98
01/03/1999	-0.22	42.62	42.28	48.79	48.69	39.50	39.32
01/04/1999	-0.58	41.07	40.77	46.63	46.46	38.00	37.86
01/05/1999	-0.15	40.80	40.91	46.04	45.94	37.47	37.42
01/06/1999	0.25	44.98	45.32	50.84	50.93	39.98	39.99
01/07/1999	0.87	48.24	47.93	57.54	57.43	44.61	44.49
01/08/1999	1.44	51.20	50.44	63.99	63.70	52.12	51.72
01/09/1999	1.23	50.77	50.03	63.37	63.00	52.47	52.20
01/10/1999	1.39	50.02	49.43	61.72	61.40	50.26	50.08
01/11/1999	0.98	48.69	48.17	58.61	58.38	48.27	48.00
01/12/1999	0.94	47.00	46.61	55.75	55.55	45.64	45.36
01/01/2000	-1.03	45.39	44.97	53.04	52.86	43.10	42.87
01/02/2000	-0.32	43.81	43.84	50.59	50.55	41.07	40.86
01/03/2000	-0.08	42.51	42.14	48.77	48.65	39.62	39.47
01/04/2000	-0.04	41.36	41.19	47.53	47.43	38.71	38.56
01/05/2000	0.02	41.27	41.23	47.48	47.42	38.42	38.32
01/06/2000	0.01	42.89	43.25	49.63	49.62	39.31	39.26
01/07/2000	0.26	47.01	46.89	55.56	55.55	42.80	42.84
01/08/2000	1.17	50.36	49.74	63.05	62.62	49.42	49.25
01/09/2000	-0.68	50.51	49.74	63.13	62.73	52.09	51.85
01/10/2000	-0.24	49.08	48.49	60.22	59.90	49.86	49.51
01/11/2000	0.36	48.91	48.48	58.50	58.39	48.04	47.88

Data Table B continued

Date	KT4	YP1	YP2	TS1	TS2	MA1	MA2
01/12/2000	0.26	47.73	47.20	56.43	56.25	47.14	46.86
01/01/2001	0.12	45.86	45.45	53.64	53.43	44.63	44.35
01/02/2001	0.10	44.30	43.96	51.28	51.16	42.30	42.08
01/03/2001	-0.10	42.62	42.36	48.85	48.66	40.33	40.03
01/04/2001	-0.11	41.27	41.03	47.06	46.92	38.88	38.64
01/05/2001	0.08	41.65	41.99	47.34	47.18	39.30	39.05
01/06/2001	0.98	49.61	49.19	58.91	58.86	48.57	48.35
01/07/2001	1.14	51.04	50.22	62.24	62.10	51.88	51.48
01/08/2001	-0.21	50.87	50.05	62.75	62.41	51.28	50.90
01/09/2001	-0.01	50.81	50.13	63.30	62.63	50.76	50.47
01/10/2001	0.63	51.18	50.28	63.59	63.19	53.73	53.29
01/11/2001	0.31	49.59	48.90	60.22	60.00	50.76	50.39
01/12/2001	0.31	47.69	47.19	56.91	56.68	47.23	46.92
01/01/2002	0.26	45.75	45.33	53.69	53.49	44.03	43.78
01/02/2002	0.22	44.14	43.78	51.09	51.03	41.70	41.56
01/03/2002	0.01	42.51	42.20	48.60	48.50	39.70	39.61
01/04/2002	-0.20	40.91	40.65	46.38	46.33	38.14	38.10
01/05/2002	-1.33	39.80	39.83	44.65	44.57	36.66	36.60
01/06/2002	-0.44	44.42	44.78	50.49	50.48	38.48	38.58
01/07/2002	0.03	47.22	47.08	56.32	56.17	43.04	43.01
01/08/2002	0.48	49.87	49.21	61.69	61.34	47.18	47.08
01/09/2002	0.43	49.14	48.66	60.09	59.81	47.79	47.55
01/10/2002	0.31	48.22	47.75	58.13	57.93	46.31	46.10
01/11/2002	0.29	46.49	46.09	55.49	55.27	44.40	44.22
01/12/2002	0.49	44.80	44.50	52.56	52.36	41.96	41.86
01/01/2003	0.42	43.55	43.26	50.40	50.25	40.12	40.09
01/02/2003	0.17	42.07	41.75	48.16	48.01	38.86	38.76
01/03/2003	0.02	40.61	40.33	46.04	45.89	37.48	37.47
01/04/2003	-0.06	39.35	39.12	44.35	44.24	36.48	36.52
01/05/2003	-0.11	38.32	38.12	43.11	43.00	35.69	35.76

Data Table B continued

Date	MA3
01/11/1995	–
01/12/1995	–
01/01/1996	–
01/02/1996	–
01/03/1996	–
01/04/1996	–
01/05/1996	–
01/06/1996	–
01/07/1996	–
01/08/1996	–
01/09/1996	–
01/10/1996	–
01/11/1996	–
01/12/1996	–
01/01/1997	40.88
01/02/1997	39.55
01/03/1997	38.10
01/04/1997	37.32
01/05/1997	36.83
01/06/1997	38.73
01/07/1997	42.63
01/08/1997	46.31
01/09/1997	48.17
01/10/1997	46.65
01/11/1997	44.11
01/12/1997	41.67
01/01/1998	39.62
01/02/1998	39.14
01/03/1998	39.05
01/04/1998	39.70
01/05/1998	40.34

Data Table B continued

Date	MA3
01/06/1998	46.79
01/07/1998	48.24
01/08/1998	47.64
01/09/1998	47.19
01/10/1998	46.00
01/11/1998	45.52
01/12/1998	44.16
01/01/1999	42.36
01/02/1999	40.73
01/03/1999	39.09
01/04/1999	37.63
01/05/1999	37.21
01/06/1999	39.79
01/07/1999	44.17
01/08/1999	51.23
01/09/1999	51.76
01/10/1999	49.72
01/11/1999	47.66
01/12/1999	45.04
01/01/2000	42.62
01/02/2000	40.60
01/03/2000	39.21
01/04/2000	38.28
01/05/2000	38.07
01/06/2000	39.02
01/07/2000	42.56
01/08/2000	48.77
01/09/2000	51.34
01/10/2000	49.04
01/11/2000	47.48

Data Table B continued

Date	MA3
01/12/2000	46.42
01/01/2001	43.95
01/02/2001	41.73
01/03/2001	39.76
01/04/2001	38.41
01/05/2001	38.79
01/06/2001	47.92
01/07/2001	51.04
01/08/2001	50.53
01/09/2001	50.04
01/10/2001	52.61
01/11/2001	49.95
01/12/2001	46.65
01/01/2002	43.78
01/02/2002	41.86
01/03/2002	40.28
01/04/2002	38.26
01/05/2002	36.46
01/06/2002	38.50
01/07/2002	42.70
01/08/2002	46.69
01/09/2002	47.11
01/10/2002	45.75
01/11/2002	43.90
01/12/2002	41.58
01/01/2003	39.88
01/02/2003	38.53
01/03/2003	37.21
01/04/2003	36.21
01/05/2003	35.49

Data Table C. Choshui River daily ($m^3.s^{-1}$) and average annual ($L.yr^{-1}$) discharges measured at river gauging station 1510H057

Date	$m^3.S^{-1}$	$L.yr^{-1}$	Date	$m^3.S^{-1}$	$L.yr^{-1}$
11/03/2005	82.6	5.55E+12	**08/08/2006**	143.9	4.29E+12
20/03/2005	116.9	5.32E+12	**22/08/2006**	46.5	1.33E+12
11/04/2005	117.3	2.67E+12	**01/09/2006**	74.4	1.99E+12
25/04/2005	49.7	6.23E+11	**22/09/2006**	108.2	4.70E+12
10/05/2005	501.7	1.58E+13	**28/09/2006**	45.4	1.53E+12
20/05/2005	142.0	9.78E+12	**19/10/2006**	18.9	5.49E+11
27/05/2005	104.1	3.28E+12	**09/11/2006**	36.6	8.37E+11
10/06/2005	46.5	2.47E+12	**17/11/2006**	32.1	1.01E+12
20/06/2005	193.5	9.73E+12	**23/11/2006**	54.4	2.38E+12
19/07/2005	3972.9	1.85E+14	**06/12/2006**	16.8	7.78E+11
16/09/2005	201.9	6.37E+12			
23/09/2005	377.9	1.37E+13			
20/10/2005	56.6	8.29E+11			
28/10/2005	20.2	5.90E+11			
09/11/2005	16.7	5.03E+11			
18/11/2005	17.0	5.44E+11			
29/11/2005	18.6	4.45E+11			
26/12/2005	11.4	2.80E+11			
25/01/2006	12.9	5.38E+11			
17/02/2006	5.1	2.33E+11			
14/03/2006	7.3	1.84E+11			
28/03/2006	41.0	1.80E+12			
21/04/2006	17.0	4.35E+11			
28/04/2006	196.1	1.62E+12			
09/05/2006	147.9	6.15E+12			
30/05/2006	942.9	2.81E+13			
07/06/2006	639.0	1.54E+13			
14/06/2006	1120.8	3.99E+13			
03/07/2006	306.3	4.93E+12			
17/07/2006	1686.7	4.89E+13			
31/07/2006	188.9	5.11E+12			

Data Table D. Chemical properties of Tunnel groundwaters and related surface waters. Ions and SiO_2 are in µmol.L^{-1} and isotopes are in ‰. SR = surface runoff

Sample ID	Distance from entrance (m)	Na^+	K^+	Ca^{2+}	Mg^{2+}	SO_4^{2-}
Tunnel 1						
CMTW-09-71	370	312.8	48.4	2715.2	187.9	545.2
CMTW-09-72	338	530.3	75.1	1985.6	374.2	1369.8
CMTW-09-73	248	532.3	69.1	3024.9	502.6	1579.8
CMTW-09-74	138	777.4	314.2	3839.4	3606.0	5809.3
CMTW-09-75	117	318.3	214.6	3160.9	3660.3	4547.0
CMTW-09-76	20	1107.1	188.2	2832.4	1974.8	3596.5
CMTW10-05	18	3034.8	130.9	2100.3	1049.4	2518.7
CMTW10-06	116	267.9	174.6	2572.8	3311.3	3948.9
CMTW10-07	212	552.8	150.6	3226.9	1089.5	3289.5
CMTW10-08	258	451.3	59.9	3021.2	431.5	1260.9
CMTW10-09	332	329.7	35.3	2242.4	195.3	480.5
CMTW10-10	362	259.2	73.5	2221.1	175.9	597.8
BYYANG 26-6-13	13	1754.6	134.0	3271.7	1505.4	2821.6
BYYANG-26-6-15	15	3231.4	138.2	2118.8	1008.2	2488.4
BYYANG-26-6-34	34	292.4	47.2	1535.4	185.8	730.9
BYYANG-26-6-218	218	307.4	147.1	9541.6	3060.5	12082.4
BYYANG-26-6-334	334	398.3	57.0	2670.4	415.8	1310.0
BYYANG-26-7-15	15	3338.5	137.9	2173.3	1039.4	2545.2
BYYANG-26-7-250	250	446.8	66.5	1384.0	412.6	1258.7
BYYANG-27-7-14.4	14.4	1664.1	140.8	3410.2	1592.3	2875.1
BYYANG-27-7-334	334	261.3	24.5	1548.9	185.1	743.2
BYYANG-27-7-398	398	687.1	111.1	2481.4	766.5	2626.6
BYYANG-27-7-517	517	341.2	51.5	1732.5	190.1	545.1
BYYANG-31-7-14.4	14.4	1599.2	130.9	3398.5	1587.5	2892.2
BYYANG-31-7-15.2	15.2	3386.8	142.7	2145.9	1017.7	2533.1
BYYANG-1-8-6.7	6.7	220.0	471.6	7224.5	1444.0	6819.3
BYYANG-1-8-271	271	700.7	112.5	2452.0	764.4	2608.1
BYYANG-1-8-334	334	264.6	24.3	1457.8	185.4	756.5
TW09-48	342	281.0	25.9	1712.0	188.0	766.0

Data Table D continued

Sample ID	Distance from entrance (m)	Na^+	K^+	Ca^{2+}	Mg^{2+}	SO_4^{2-}
TW09-51	328	314.0	31.9	2504.0	167.0	608.0
TW09-50	297	488.0	62.8	1849.0	350.0	1231.0
TW09-52	203	529.0	66.0	2863.0	481.0	1523.0
TW09-53	172	604.0	184.6	3541.0	1233.0	3259.0
TW09-55	139	575.0	233.8	3388.0	1659.0	3508.0
TW09-49	62	495.0	163.7	3613.0	3928.0	5603.0
TBD-18	380	139.8	9.0	1437.8	159.1	212.1
TBD-19	340	202.2	17.5	2099.5	139.8	364.1
TBD-22	125	546.0	257.1	3510.1	2719.3	4078.1
TBD-20	43	725.4	120.0	3312.7	1739.3	3636.6
TBD-21	11	1019.0	112.0	2858.6	994.3	2364.4
BYYANG-22-9-6.5	SR-10 m	168.9	243.8	1510.9	685.6	1362.4
BYYANG-22-9-8	SR-10 m	191.2	227.2	1515.7	764.9	1380.7
CMTW10-04	SR-14 km	110.3	39.3	1191.0	272.9	141.6
CMTW-09-81	SR-14 km	144.2	54.6	1382.6	325.5	162.1
Tunnel 6						
CMTW10-11	–	127.3	99.7	1648.5	499.7	823.8
CMTW10-14	–	155.0	113.7	2755.6	679.1	1318.1
CMTW-09-89	–	152.9	127.2	1858.0	566.1	977.5
Tunnel 8						
CMTW10-12	–	506.3	48.9	1380.0	303.5	508.2
CMTW10-13	–	550.8	85.0	1437.5	309.2	531.8
CMTW-09-86	–	575.6	51.5	1515.2	336.9	599.4
CMTW-09-87	–	585.5	50.2	1562.4	343.9	601.9
CMTW-09-88	–	599.1	50.3	1592.9	353.5	631.1
Tunnel 28						
CMTW-09-103	134	139.2	30.9	1244.6	543.8	442.1
CMTW-09-104	202	314.4	50.9	1667.3	940.0	951.2
CMTW-09-105	333	141.6	22.1	809.6	344.3	246.2
CMTW-09-106	340	116.9	19.5	758.2	307.7	200.9

Data Table D continued

Sample ID	Distance from entrance (m)	Na^+	K^+	Ca^{2+}	Mg^{2+}	SO_4^{2-}
CMTW-09-107	404	412.1	26.5	812.8	424.5	321.3
CMTW-10-25	183.5	196.6	29.1	1294.3	609.7	641.2
CMTW-10-26	278	482.9	48.2	1808.4	1033.0	1252.0
CMTW-10-27	469	121.4	20.0	888.1	369.7	311.3
CMTW-10-28	514	188.7	23.5	956.3	426.1	421.1
CMTW-09-108	SR-100 m	437.0	26.8	553.9	175.5	132.4
CMTW-09-98	SR-2 km	173.4	19.3	456.0	274.7	181.3
CMTW-09-99	SR-2 km	108.5	26.7	654.9	325.4	424.2

Sample ID	Distance from entrance (m)	Cl^-	Sr^{2+}	HCO_3^-	SiO_2
Tunnel 1					
CMTW-09-71	370	73.5	3.8	5003.4	245.7
CMTW-09-72	338	103.0	6.1	2482.4	431.1
CMTW-09-73	248	77.6	7.4	4419.2	435.3
CMTW-09-74	138	94.4	21.5	4269.2	213.5
CMTW-09-75	117	96.8	10.4	4984.6	230.3
CMTW-09-76	20	75.2	29.6	3641.6	237.6
CMTW10-05	18	32.6	31.3	4395.1	219.0
CMTW10-06	116	74.2	8.4	4238.8	191.5
CMTW10-07	212	71.8	14.7	2685.5	380.7
CMTW10-08	258	53.3	6.5	4841.5	409.9
CMTW10-09	332	70.6	4.0	4208.7	374.0
CMTW10-10	362	55.5	3.6	3875.6	208.1
BYYANG 26-6-13	13	35.7	32.6	5763.9	220.8
BYYANG-26-6-15	15	35.0	31.9	4611.8	224.1
BYYANG-26-6-34	34	45.2	3.9	2275.1	231.8
BYYANG-26-6-218	218	29.9	39.4	1464.1	78.6
BYYANG-26-6-334	334	47.4	6.4	3959.1	–
BYYANG-26-7-15	15	30.2	31.6	4781.3	222.3

Data Table D continued

Sample ID	Distance from entrance (m)	Cl^-	Sr^{2+}	HCO_3^-	SiO_2
BYYANG-26-7-250	250	50.9	6.3	1538.2	383.0
BYYANG-27-7-14.4	14.4	28.2	33.3	6031.4	223.6
BYYANG-27-7-334	334	43.9	4.0	2223.3	228.8
BYYANG-27-7-398	398	49.4	12.6	1991.4	388.2
BYYANG-27-7-517	517	56.5	3.8	3091.3	367.0
BYYANG-31-7-14.4	14.4	28.4	33.2	5889.1	223.5
BYYANG-31-7-15.2	15.2	25.2	31.4	4765.4	221.7
BYYANG-1-8-6.7	6.7	33.7	23.6	4356.4	117.4
BYYANG-1-8-271	271	55.0	12.5	1974.7	388.0
BYYANG-1-8-334	334	43.1	3.9	2019.3	226.6
TW09-48	342	49.1	3.7	2529.0	–
TW09-51	328	54.7	3.6	4419.0	–
TW09-50	297	96.9	5.6	2390.0	–
TW09-52	203	56.7	7.3	4189.0	–
TW09-53	172	68.5	28.7	3798.0	–
TW09-55	139	77.4	33.6	3867.0	–
TW09-49	62	81.2	22.9	4497.0	–
TBD-18	380	38.0	2.3	2866.1	173.7
TBD-19	340	45.3	2.9	3924.2	217.5
TBD-22	125	87.1	20.2	5054.8	203.5
TBD-20	43	58.3	21.7	3639.3	168.7
TBD-21	11	34.5	19.6	4103.8	170.6
BYYANG-22-9-6.5	SR-10 m	57.8	7.3	527.4	120.0
BYYANG-22-9-8	SR-10 m	58.9	8.2	660.6	135.6
CMTW10-04	SR-14 km	68.8	1.1	1536.7	116.6
CMTW-09-81	SR-14 km	93.5	1.3	1817.6	137.1
Tunnel 6					
CMTW10-11	–	23.7	6.1	–	106.6
CMTW10-14	–	26.3	7.4	–	122.4
CMTW-09-89	–	25.2	6.9	–	131.0

Data Table D continued

Sample ID	Distance from entrance (m)	Cl^-	Sr^{2+}	HCO_3^-	SiO_2
Tunnel 8					
CMTW10-12	–	33.3	5.6	–	114.0
CMTW10-13	–	31.1	5.6	–	115.8
CMTW-09-86	–	32.7	5.9	–	132.7
CMTW-09-87	–	31.5	6.1	–	136.5
CMTW-09-88	–	31.5	6.2	–	140.4
Tunnel 28					
CMTW-09-103	134	12.9	2.0	2849.7	115.7
CMTW-09-104	202	91.0	4.3	3586.7	131.2
CMTW-09-105	333	16.5	1.7	1962.6	104.9
CMTW-09-106	340	15.8	1.4	1850.7	98.8
CMTW-09-107	404	14.3	2.2	2256.5	126.0
CMTW-10-25	183.5	18.7	2.5	2732.8	126.4
CMTW-10-26	278	14.8	5.1	3694.9	130.4
CMTW-10-27	469	14.7	1.8	2019.5	98.3
CMTW-10-28	514	14.7	2.1	2120.1	103.7
CMTW-09-108	SR-100 m	15.4	2.1	1642.3	112.1
CMTW-09-98	SR-2 km	18.5	1.5	1273.1	113.4
CMTW-09-99	SR-2 km	18.3	1.1	1229.2	101.9

Sample ID	Distance from entrance (m)	$^{87}Sr/^{86}Sr$	$\delta^{18}O_{H2O}$	$\delta^{18}O_{SO4}$	$\delta^{34}S_{SO4}$	$\delta^{13}C$
Tunnel 1						
CMTW-09-71	370	0.716244	-12.8	–	0.3	-14.6
CMTW-09-72	338	–	-8.0	–	–	-7.9
CMTW-09-73	248	–	-10.3	–	–	-10.1
CMTW-09-74	138	–	-11.1	–	–	-4.4
CMTW-09-75	117	–	-11.0	-4.0	-5.0	-4.7
CMTW-09-76	20	0.708745	-10.0	3.2	-11.3	0.3
CMTW10-05	18	0.709074	-11.8	6.9	9.2	-2.6

Data Table D continued

Sample ID	Distance from entrance (m)	$^{87}Sr/^{86}Sr$	$\delta^{18}O_{H2O}$	$\delta^{18}O_{SO4}$	$\delta^{34}S_{SO4}$	$\delta^{13}C$
CMTW10-06	116	–	-11.2	–	–	-3.7
CMTW10-07	212	–	-9.5	–	–	-5.3
CMTW10-08	258	–	-10.9	–	–	-10.1
CMTW10-09	332	–	-9.7	–	–	-12.0
CMTW10-10	362	–	-11.4	–	–	-11.5
BYYANG 26-6-13	13	0.708928	-12.2	4.7	-3.9	-3.6
BYYANG-26-6-15	15	–	-12.3	7.6	12.3	-3.9
BYYANG-26-6-34	34	–	-11.8	–	–	-8.6
BYYANG-26-6-218	218	0.707994	-9.1	-5.3	-26.5	-1.1
BYYANG-26-6-334	334	–	-11.8	5.1	-0.2	-7.8
BYYANG-26-7-15	15	–	-12.5	7.0	12.9	-2.9
BYYANG-26-7-250	250	–	-11.5	–	–	-3.1
BYYANG-27-7-14.4	14.4	–	-11.9	4.9	-5.0	-2.0
BYYANG-27-7-334	334	–	-12.8	2.2	-0.3	-7.4
BYYANG-27-7-398	398	–	-11.0	–	–	-4.3
BYYANG-27-7-517	517	–	-11.9	–	–	-8.2
BYYANG-31-7-14.4	14.4	–	-12.1	4.7	-5.0	-1.6
BYYANG-31-7-15.2	15.2	–	-12.2	7.1	13.3	-2.8
BYYANG-1-8-6.7	6.7	–	-8.2	-3.3	-26.8	-2.1
BYYANG-1-8-271	271	–	-10.8	–	–	-4.6
BYYANG-1-8-334	334	–	-12.1	–	–	-7.4
TW09-48	342	0.715922	-11.2	0.2	0.5	-9.3
TW09-51	328	–	-10.5	4.1	1.8	-14.1
TW09-50	297	0.716497	-8.1	2.4	-0.1	-8.4
TW09-52	203	–	-10.3	4.9	1.0	-10.9
TW09-53	172	–	-11.1	3.6	-5.7	-7.8
TW09-55	139	0.708912	-11.4	1.0	-10.6	-7.4
TW09-49	62	0.708247	-11.2	-3.6	-13.8	-2.0
TBD-18	380	0.714230	–	–	–	–
TBD-19	340	0.716244	–	–	–	–

Data Table D continued

Sample ID	Distance from entrance (m)	$^{87}Sr/^{86}Sr$	$\delta^{18}O_{H2O}$	$\delta^{18}O_{SO4}$	$\delta^{34}S_{SO4}$	$\delta^{13}C$
TBD-22	125	0.709018	-10.9	–	–	–
TBD-20	43	0.708383	–	–	–	–
TBD-21	11	0.708769	–	–	–	–
BYYANG-22-9-6.5	SR-10 m	–	-12.6	-4.3	-10.1	-6.5
BYYANG-22-9-8	SR-10 m	–	-12.4	-4.4	-9.5	-5.7
CMTW10-04	SR-14 km	–	-10.8	–	–	-10.2
CMTW-09-81	SR-14 km	–	-10.7	–	–	-10.1
Tunnel 6						
CMTW10-11	–	–	–	–	–	-7.0
CMTW10-14	–	–	–	–	–	-6.7
CMTW-09-89	–	–	–	–	–	–
Tunnel 8						
CMTW10-12	–	–	–	–	–	-4.2
CMTW10-13	–	–	–	–	–	-3.9
CMTW-09-86	–	–	-12.6	–	–	–
CMTW-09-87	–	–	-12.6	–	–	-4.7
CMTW-09-88	–	–	-12.6	–	–	–
Tunnel 28						
CMTW-09-103	134	–	-11.3	–	–	-11.4
CMTW-09-104	202	–	-10.8	–	–	-8.9
CMTW-09-105	333	–	-10.6	–	–	-10.0
CMTW-09-106	340	–	-10.5	–	–	-10.2
CMTW-09-107	404	–	-10.5	–	–	-9.2
CMTW-10-25	183.5	–	-10.4	–	–	-10.6
CMTW-10-26	278	–	-10.8	–	–	-7.8
CMTW-10-27	469	–	-10.7	–	–	-9.9
CMTW-10-28	514	–	-10.9	–	–	-9.0
CMTW-09-108	SR-100 m	–	-10.7	–	–	-10.7
CMTW-09-98	SR-2 km	–	-10.6	–	–	-13.0
CMTW-09-99	SR-2 km	–	-11.1	–	–	-12.7

Data Table D continued

Sample ID	Distance from entrance (m)	Saturation index (calcite)	Temp. (℃)	pH
Tunnel 1				
CMTW-09-71	370	1.28	22.8	8.32
CMTW-09-72	338	0.77	22.4	8.25
CMTW-09-73	248	1.09	22.2	8.18
CMTW-09-74	138	1.22	23.5	8.36
CMTW-09-75	117	1.11	24.0	8.22
CMTW-09-76	20	1.10	24.3	8.36
CMTW10-05	18	1.06	22.2	8.35
CMTW10-06	116	0.82	21.2	8.09
CMTW10-07	212	0.92	21.8	8.26
CMTW10-08	258	1.04	21.4	8.09
CMTW10-09	332	1.04	20.6	8.24
CMTW10-10	362	1.07	21.4	8.31
BYYANG 26-6-13	13	1.24	–	–
BYYANG-26-6-15	15	0.99	–	–
BYYANG-26-6-34	34	0.67	–	–
BYYANG-26-6-218	218	0.93	–	–
BYYANG-26-6-334	334	1.08	–	–
BYYANG-26-7-15	15	1.01	–	–
BYYANG-26-7-250	250	0.43	–	–
BYYANG-27-7-14.4	14.4	1.28	–	–
BYYANG-27-7-334	334	0.66	–	–
BYYANG-27-7-398	398	0.71	–	–
BYYANG-27-7-517	517	0.85	–	–
BYYANG-31-7-14.4	14.4	1.26	–	–
BYYANG-31-7-15.2	15.2	1.01	–	–
BYYANG-1-8-6.7	6.7	1.36	–	–
BYYANG-1-8-271	271	0.70	–	–
BYYANG-1-8-334	334	0.60	–	–
TW09-48	342	0.75	–	–

Data Table D continued

Sample ID	Distance from entrance (m)	Saturation index (calcite)	Temp. (℃)	pH
TW09-51	328	1.13	–	–
TW09-50	297	0.73	–	–
TW09-52	203	1.12	–	–
TW09-53	172	1.10	–	–
TW09-55	139	1.08	–	–
TW09-49	62	1.11	–	–
TBD-18	380	0.77	–	–
TBD-19	340	1.03	–	–
TBD-22	125	1.18	–	–
TBD-20	43	1.04	–	–
TBD-21	11	1.07	–	–
BYYANG-22-9-6.5	SR-10 m	–	–	–
BYYANG-22-9-8	SR-10 m	–	–	–
CMTW10-04	SR-14 km	–	22.1	8.35
CMTW-09-81	SR-14 km	–	23.1	8.38
Tunnel 6				
CMTW10-11	–	–	22.0	8.12
CMTW10-14	–	–	22.4	8.20
CMTW-09-89	–	–	25.9	8.39
Tunnel 8				
CMTW10-12	–	–	22.0	8.01
CMTW10-13	–	–	22.1	8.19
CMTW-09-86	–	–	23.2	8.42
CMTW-09-87	–	–	22.4	8.05
CMTW-09-88	–	–	22.5	8.06
Tunnel 28				
CMTW-09-103	134	0.69	19.1	8.30
CMTW-09-104	202	0.94	19.1	8.38
CMTW-09-105	333	0.36	18.9	8.28
CMTW-09-106	340	0.33	19.0	8.30

Data Table D continued

Sample ID	Distance from entrance (m)	Saturation index (calcite)	Temp. (℃)	pH
CMTW-09-107	404	0.32	19.1	8.18
CMTW-10-25	183.5	0.80	24.0	8.37
CMTW-10-26	278	0.83	23.0	8.18
CMTW-10-27	469	0.29	23.2	8.10
CMTW-10-28	514	0.33	23.3	8.10
CMTW-09-108	SR-100 m	0.28	20.1	8.40
CMTW-09-98	SR-2 km	−	18.4	8.36
CMTW-09-99	SR-2 km	−	20.1	8.24

Data Table E. Recorded weights during solid sample preparation prior to ICP-AES analysis. All weights are in grams

Sample	Initial	Acetate solution plus vial	0.5 mL leachate plus vial	beaker minus 0.5 mL leachate	H_2O solution plus vial
92A-2-1	0.20242				
92A-2-2	0.20128				
09-92A-4	0.20583				
Savillex vial Set 1					
A22-H_2O	13.40827				19.21840
P10-H_2O	13.83373				19.62664
N34-H_2O	13.5664				18.9916
Th29-HAc	13.5612	19.4602		18.9295	
Th48-HAc	13.5308	19.3519		18.8179	
Th70-HAc	13.3500	18.7170		18.1958	
Savillex vial Set 2					
N57-HAc	13.4696		14.0005		
85-HAc	13.4261		13.9531		
N31-HAc	13.4985		14.0185		

	Initial	1.0 mL 1.0 M nitrate solution plus beaker	10 mL 0.1 M nitrate solution plus beaker (add 9 mL H_2O)	1 mL 0.1 M nitrate solution plus tube	0.1 mL 0.1 M nitrate solution plus tube	0.1 M nitrate solution plus tube (add 9 mL 0.1 M HNO_3)	0.1 M nitrate solution plus tube (add 9 mL 0.1 M HNO_3)
Dilution Beaker							
92A-2-1	11.2496	12.3081	21.0393				
92A-2-2	11.2718	12.3500	21.1536				
92A-4	11.2354	12.2984	21.1147				
Dilution Tube							
92A-2-1-10	6.8460			7.8241		16.8476	
92A-2-2-10	6.8966			7.8425		16.8851	
92A-4-10	6.8789			7.8813		18.1940	
92A-2-1-100	6.8270				6.9228		16.7360
92A-2-2-100	6.8907				7.0390		16.7249
92A-4-100	6.8768				7.0246		16.8933

Data Table F. Results of chemical analyses for groundwaters from the Pingtung and Choshui plains, and surface waters from the Kaoping and Choshui Rivers. Hot-spring water from from Song and Liu (2006).

	Ca^{2+}	Mg^{2+}	Na^{+}	K^{+}	Sr^{2+}	Li^{+}	Ba^{2+}	Cl^{-}
Pingtung Plain	$mmol.L^{-1}$	$mmol.L^{-1}$	$mmol.L^{-1}$	$\mu mol.L^{-1}$	$\mu mol.L^{-1}$	$\mu mol.L^{-1}$	$nmol.L^{-1}$	$mmol.L^{-1}$
ZM1	1.68	0.66	1.74	46.45	3.06	2.63	425.0	1.10
ZM2	1.58	0.72	1.86	54.92	3.09	3.34	589.0	1.02
ZM3	1.56	0.69	1.87	52.49	2.88	3.29	447.0	0.86
ZM4	1.51	0.77	2.67	64.00	2.92	3.45	619.0	1.62
HN1	3.37	1.01	1.32	79.64	10.33	1.29	920.0	0.78
HN2	1.53	0.48	0.89	24.46	4.59	1.01	620.0	0.02
HN3	1.13	0.34	2.46	34.78	3.91	1.13	207.0	0.51
CL1	4.37	1.27	3.05	144.00	6.76	2.97	1678.0	2.17
CL2	1.39	0.58	2.69	53.46	4.09	1.77	1381.0	0.13
CL3	0.65	0.38	4.33	32.65	1.22	0.67	212.0	2.92
LY1	2.81	1.81	5.65	190.00	9.57	1.97	245.0	4.82
LY2	14.07	14.60	199.26	1394.00	80.05	22.30	–	266.69
LY3	14.93	17.01	190.75	1856.00	89.24	23.20	12471.0	290.92
TK1	8.56	43.74	324.61	9645.00	70.90	16.23	377.0	460.09
TK2	1.86	2.27	7.74	370.00	25.92	1.81	2942.0	8.25
TK3	12.68	16.08	148.41	1351.00	62.45	18.21	1001.0	216.90
TK4	11.80	44.19	355.91	8580.00	86.92	38.77	382.0	522.45
KT1	2.62	0.74	1.11	45.52	7.08	1.28	1047.0	0.59
KT2	6.63	2.42	7.61	32.02	16.26	1.78	864.0	19.50
KT3	23.64	30.17	277.51	729.00	105.31	31.47	806.0	405.17
KT4	16.29	37.22	352.37	1758.00	105.88	54.48	476.0	486.76
HY1	3.57	1.17	2.56	956.00	8.76	4.59	1047.0	2.99
HY2	15.80	36.59	199.02	5370.00	106.49	27.20	435.0	480.22
HF1	2.79	0.88	0.45	34.26	6.80	0.96	159.0	0.29
HF2	1.15	0.39	0.46	22.06	3.03	1.15	17.3	0.06
HF3	1.63	0.54	0.74	21.63	4.25	2.03	418.0	0.04
HS1	3.19	0.83	0.60	47.35	8.00	0.83	46.0	0.64
HS2	2.18	0.60	0.47	22.81	5.54	1.08	129.0	0.11
HS3	2.13	0.60	0.41	30.30	5.32	0.79	54.3	0.13

Data Table F continued

	Ca^{2+}	Mg^{2+}	Na^{+}	K^{+}	Sr^{2+}	Li^{+}	Ba^{2+}	Cl^{-}
Pingtung Plain	$mmol.L^{-1}$	$mmol.L^{-1}$	$mmol.L^{-1}$	$\mu mol.L^{-1}$	$\mu mol.L^{-1}$	$\mu mol.L^{-1}$	$nmol.L^{-1}$	$mmol.L^{-1}$
HS4	1.94	0.58	0.36	34.13	5.24	0.35	3.0	0.11
QX1	3.75	0.74	1.04	256.00	7.54	1.77	194.0	0.70
QX2	2.47	0.70	0.67	31.30	6.25	1.40	841.0	0.21
QX3	1.50	0.45	1.63	29.21	3.35	2.75	179.0	0.17
WD1	4.60	1.03	1.60	177.00	8.28	2.27	1058.0	1.66
WD1	2.39	0.69	0.56	31.23	6.13	1.38	437.0	0.15
WD3	1.45	0.29	1.10	22.94	2.76	1.63	229.0	0.04
TS1	0.57	0.38	0.43	16.62	1.44	0.82	41.1	0.12
TS2	0.38	0.29	0.48	13.24	0.95	0.76	11.5	0.04
YP1	2.03	0.81	0.29	20.29	3.82	0.37	9.9	0.05
YP2	1.17	0.57	0.34	15.72	2.46	0.52	21.7	0.06
MA1	2.18	0.80	0.32	27.51	6.26	1.14	1.4	0.09
MA2	1.75	0.56	0.35	31.38	5.13	0.76	12.1	0.06
MA3	1.53	0.51	0.38	34.20	4.63	0.26	7.0	0.05
Kaoping River								
07/03/2005	1.58	0.63	0.78	60.08	4.88	2.52	174.0	0.17
04/04/2005	1.41	0.65	0.72	58.90	4.30	1.49	202.0	0.11
09/04/2005	1.73	0.70	0.82	62.95	5.64	3.10	234.0	0.24
20/05/2005	1.31	0.52	0.43	72.44	3.85	1.47	136.0	0.08
06/06/2005	1.39	0.63	0.47	50.57	4.10	1.58	136.0	0.09
20/06/2005	1.28	0.54	0.34	54.07	3.38	1.32	116.0	0.06
01/07/2005	1.47	0.61	0.49	50.97	4.34	1.62	119.0	0.13
11/07/2005	1.74	0.69	0.61	67.88	5.28	1.99	139.0	0.30
18/07/2005	0.72	0.23	0.16	85.60	1.58	0.56	83.9	0.04
25/07/2005	1.28	0.49	0.34	91.45	3.08	1.17	113.0	0.07
01/08/2005	1.57	0.58	0.48	97.40	4.18	1.38	113.0	0.16
Choshui Plain								
CP1	2.85	6.68	69.22	1456.49	31.84	5.29	2108.0	91.21
CP2	1.01	0.49	4.92	86.34	3.94	3.56	777.0	3.72
PK1	0.92	0.32	2.36	39.17	2.80	3.06	438.3	0.06

Data Table F continued

	Ca^{2+}	Mg^{2+}	Na^{+}	K^{+}	Sr^{2+}	Li^{+}	Ba^{2+}	Cl^{-}
Choshui Plain	$mmol.L^{-1}$	$mmol.L^{-1}$	$mmol.L^{-1}$	$\mu mol.L^{-1}$	$\mu mol.L^{-1}$	$\mu mol.L^{-1}$	$nmol.L^{-1}$	$mmol.L^{-1}$
PK2	0.76	0.18	1.81	29.93	2.33	3.55	296.1	0.08
GC1	3.81	1.89	4.50	74.74	10.64	4.26	796.1	3.88
GC2	0.76	0.47	2.23	187.01	2.47	3.31	544.0	0.28
GC3	0.68	0.32	1.91	35.90	2.09	3.42	498.9	0.08
GC4	0.72	0.19	1.19	27.96	1.87	3.29	270.4	0.12
GC5	0.96	0.20	1.57	34.13	2.09	4.11	433.2	0.21
KH1	1.07	0.74	0.71	38.56	4.58	3.16	399.9	0.06
KH2	1.88	0.67	0.60	33.15	4.48	3.05	230.3	0.03
KH3	1.65	0.44	1.30	27.79	4.31	3.00	263.6	0.03
KH4	1.40	0.35	1.48	31.69	3.76	3.72	265.7	0.04
HL1	5.70	2.18	0.92	74.66	12.54	4.58	760.4	0.75
HL2	3.99	1.67	0.76	60.07	10.44	4.32	283.5	0.03
DG1	0.75	0.45	3.74	69.30	3.08	3.16	639.7	1.72
DG2	0.76	0.16	1.61	30.62	2.08	3.50	216.8	0.05
FR1	5.25	3.01	1.91	108.13	19.27	5.43	510.6	1.06
FR2	2.04	0.70	0.85	30.36	4.86	3.11	337.1	0.06
FR3	1.50	0.40	1.55	30.96	4.11	0.48	174.3	0.03
HA1	3.48	1.26	5.27	119.30	10.03	4.15	1890.3	0.62
HA2	1.08	0.27	1.70	30.50	3.29	3.71	207.4	0.06
Choshui River								
11/03/2005	1.54	0.78	0.46	51.20	4.22	2.17	−	0.04
20/03/2005	1.45	0.69	0.42	53.30	4.07	1.73	−	0.04
11/04/2005	1.67	0.80	0.45	46.90	4.62	2.07	−	0.05
25/04/2005	1.87	0.86	0.55	54.40	5.08	1.94	−	0.10
10/05/2005	1.07	0.43	0.37	74.60	2.85	1.07	−	−
20/05/2005	1.40	0.67	0.36	55.40	3.79	1.61	−	0.06
27/05/2005	1.48	0.74	0.39	44.10	4.21	1.99	−	0.04
10/06/2005	1.58	0.70	0.49	46.90	4.28	1.43	−	0.09
20/06/2005	1.35	0.66	0.34	46.20	3.90	1.59	−	0.05
19/07/2005	0.53	0.25	0.49	117.60	1.78	−	−	0.04

Data Table F continued

	Ca^{2+}	Mg^{2+}	Na^{+}	K^{+}	Sr^{2+}	Li^{+}	Ba^{2+}	Cl^{-}
Choshui River	$mmol.L^{-1}$	$mmol.L^{-1}$	$mmol.L^{-1}$	$\mu mol.L^{-1}$	$\mu mol.L^{-1}$	$\mu mol.L^{-1}$	$nmol.L^{-1}$	$mmol.L^{-1}$
16/09/2005	1.54	0.79	0.37	64.30	4.53	2.30	–	0.04
23/09/2005	1.10	0.53	0.25	96.80	2.90	1.63	–	–
20/10/2005	1.48	0.78	0.54	69.90	4.58	1.76	–	0.10
28/10/2005	1.64	0.79	0.78	81.10	4.83	1.69	–	0.12
09/11/2005	1.34	0.70	0.76	71.90	4.27	1.41	–	0.10
18/11/2005	1.29	0.72	0.78	72.00	4.32	1.32	–	0.10
29/11/2005	1.80	0.87	0.64	70.50	5.17	1.98	–	0.12
26/12/2005	1.53	0.75	0.92	83.40	4.52	1.28	–	0.16
25/01/2006	0.90	0.79	0.87	97.10	4.29	1.54	–	0.12
17/02/2006	1.03	0.81	0.96	108.40	4.59	1.08	–	0.18
14/03/2006	1.81	0.82	1.01	128.90	5.06	1.29	–	0.22
28/03/2006	1.98	0.99	0.72	80.10	6.14	2.33	–	0.05
21/04/2006	1.45	0.73	0.72	65.30	4.49	2.10	–	0.08
28/04/2006	1.20	0.58	0.49	56.30	3.57	1.79	–	–
09/05/2006	1.25	0.61	0.46	53.90	3.72	1.49	–	–
30/05/2006	1.28	0.52	0.38	49.70	3.72	1.11	–	0.03
07/06/2006	1.43	0.69	0.32	70.80	3.82	1.59	–	0.05
14/06/2006	1.31	0.60	0.26	94.80	3.14	1.27	–	0.03
03/07/2006	1.42	0.68	0.36	62.90	4.00	1.54	–	0.05
17/07/2006	1.16	0.54	0.27	74.60	3.07	1.47	–	0.02
31/07/2006	1.40	0.64	0.28	68.40	3.48	1.57	–	0.03
08/08/2006	1.34	0.67	0.31	59.80	3.83	1.62	–	0.03
22/08/2006	1.26	0.58	0.54	59.60	3.63	0.92	–	0.07
01/09/2006	1.09	0.48	0.47	53.40	3.22	0.70	–	0.07
22/09/2006	1.21	0.56	0.37	50.00	3.47	1.26	–	0.04
28/09/2006	1.23	0.55	0.53	54.40	3.48	–	–	0.07
19/10/2006	1.38	0.66	0.68	72.60	4.07	–	–	0.09
09/11/2006	1.55	0.78	0.44	51.60	4.63	–	–	0.06
17/11/2006	1.48	0.72	0.52	55.90	4.40	1.64	–	0.07
23/11/2006	1.25	0.58	0.47	50.10	3.55	–	–	0.04
06/12/2006	1.59	0.76	0.57	57.20	4.64	1.75	–	0.08
Hot Spring water	0.39	0.70	22.22	0.27	–	0.73	–	3.49

Data Table F continued

Pingtung Plain	SO_4^{2-} mmol.L^{-1}	HCO_3^- mmol.L^{-1}	SiO_2 mmol.L^{-1}	$\delta^{18}O$ ‰	δD ‰	$\delta^{13}C$ ‰	Saturation index (calcite)
ZM1	trace	5.37	0.50	-8.2	-54.2	-16.8	0.31
ZM2	0.01	5.54	0.54	-8.3	-53.8	-17.4	0.21
ZM3	0.01	5.59	0.55	-8.3	-54.3	-17.5	0.19
ZM4	0.01	5.72	0.50	-8.2	-54.0	-16.7	0.26
HN1	1.46	6.59	0.37	-7.8	-52.3	-9.8	-0.08
HN2	0.63	3.73	0.40	-10.4	-69.7	-7.5	-0.17
HN3	0.52	3.90	0.33	-10.2	-67.1	-10.1	-0.16
CL1	2.23	7.83	0.31	-7.3	-49.9	-11.1	0.37
CL2	0.01	6.55	0.25	-8.5	-58.6	-11.7	0.35
CL3	trace	3.55	0.39	-8.2	-55.4	-18.8	-0.57
LY1	1.32	7.74	0.24	-6.7	-46.5	-12.7	0.55
LY2	trace	−	0.34	-4.1	-28.7	-20.1	−
LY3	trace	−	0.37	-4.4	-30.4	-28.1	−
TK1	22.62	−	0.19	-1.3	-7.1	-9.7	−
TK2	0.01	8.26	0.29	-9.6	-62.7	-4.6	0.15
TK3	6.40	−	0.20	-6.4	-41.4	-14.3	−
TK4	21.24	−	0.21	-1.2	-5.4	-11.5	−
KT1	0.62	6.12	0.28	-7.4	-49.4	-10.2	0.24
KT2	0.71	5.55	0.43	-9.4	-61.4	-9.4	-0.26
KT3	13.35	−	0.30	-3.9	-24.2	-8.2	−
KT4	17.35	−	0.25	-2.0	-11.8	-10.0	−
HY1	1.16	7.60	0.27	-7.7	-50.1	-11.3	-0.51
HY2	16.15	−	0.16	-2.2	-14.2	-12.0	−
HF1	0.97	5.64	0.36	-8.9	-58.7	-7.2	-0.12
HF2	0.53	2.31	0.42	-9.3	-61.1	-7.4	-1.22
HF3	0.78	3.49	0.37	-9.9	-65.4	-8.3	-0.40
HS1	1.43	5.12	0.40	-8.4	-56.6	-9.7	0.00
HS2	0.79	4.42	0.44	-9.3	-62.1	-8.2	0.09
HS3	0.81	4.19	0.38	-9.2	-60.6	-7.7	0.15
HS4	0.69	3.67	0.38	-9.7	-64.5	-7.1	-0.25
QX1	1.02	7.53	0.34	-8.2	-55.4	-9.4	0.23

Data Table F continued

	SO_4^{2-}	HCO_3^-	SiO_2	$\delta^{18}O$	δD	$\delta^{13}C$	Saturation index
Pingtung Plain	$mmol.L^{-1}$	$mmol.L^{-1}$	$mmol.L^{-1}$	‰	‰	‰	(calcite)
QX2	0.82	5.21	0.42	-9.0	-60.4	-9.9	0.35
QX3	0.02	5.37	0.44	-9.8	-65.9	-19.6	0.32
WD1	2.03	7.44	0.44	-7.2	-50.0	-8.2	0.15
WD1	0.98	4.64	0.39	-9.2	-62.8	-8.0	0.26
WD3	0.15	4.28	–	-9.8	-66.7	-11.2	0.43
TS1	0.21	1.28	0.39	-8.3	-53.6	-8.8	-2.63
TS2	0.11	1.46	0.48	-8.0	-51.9	-10.6	-2.48
YP1	1.23	3.38	0.21	-10.5	-71.0	-6.74	-0.57
YP2	0.60	2.41	0.31	-9.1	-59.5	-6.83	-1.18
MA1	0.94	4.13	0.21	-9.8	-65.6	-10.15	0.16
MA2	0.81	3.19	0.27	-9.6	-64.0	-7.86	0.14
MA3	0.74	2.87	0.33	-10.1	-67.2	-6.28	-0.49
Kaoping River							
07/03/2005	0.93	–	0.13	–	–	–	–
04/04/2005	0.86	–	0.13	–	–	–	–
09/04/2005	0.95	–	0.16	–	–	–	–
20/05/2005	0.79	–	0.13	–	–	–	–
06/06/2005	0.81	–	0.15	–	–	–	–
20/06/2005	0.67	–	0.15	–	–	–	–
01/07/2005	0.77	–	0.16	–	–	–	–
11/07/2005	0.89	–	0.17	–	–	–	–
18/07/2005	0.28	–	0.10	–	–	–	–
25/07/2005	0.59	–	0.15	–	–	–	–
01/08/2005	0.75	–	0.16	–	–	–	–
Choshui Plain							
CP1	1.96	-5.40	0.17	-6.7	-44.4	-14.3	–
CP2	0.15	3.96	0.30	-7.5	-49.5	-14.3	-0.58
PK1	0.01	4.79	0.33	-7.8	-51.9	-7.5	0.18
PK2	0.04	3.55	0.34	-7.8	-52.2	-11.8	-0.06
GC1	3.05	6.00	0.39	-4.2	-29.5	-11.4	0.19
GC2	0.01	4.56	0.50	-7.4	-48.6	-0.4	-0.67

Data Table F continued

	SO_4^{2-}	HCO_3^-	SiO_2	$\delta^{18}O$	δD	$\delta^{13}C$	Saturation index
Choshui Plain	$mmol.L^{-1}$	$mmol.L^{-1}$	$mmol.L^{-1}$	‰	‰	‰	(calcite)
GC3	0.02	3.82	0.47	-7.6	-50.1	-5.4	-0.53
GC4	0.07	2.79	0.43	-7.5	-48.9	-9.7	-0.64
GC5	0.14	3.44	0.45	-7.4	-47.8	-11.3	-0.18
KH1	0.02	4.28	0.19	-9.7	-66.0	-8.3	0.18
KH2	0.89	3.91	0.38	-9.3	-62.8	-7.2	0.19
KH3	0.68	4.13	0.35	-9.5	-64.5	-9.1	0.33
KH4	0.54	3.88	0.36	-9.0	-60.5	-9.8	0.23
HL1	4.15	7.72	0.36	-8.1	-55.3	-8.2	0.46
HL2	2.77	6.58	0.39	-8.2	-56.0	-7.4	0.29
DG1	0.02	4.45	0.25	-7.7	-51.6	-13.6	-0.1
DG2	0.03	3.36	0.37	-7.7	-52.2	-11.6	0.12
FR1	3.91	9.65	0.37	-8.0	-54.0	-7.9	0.16
FR2	1.11	4.08	0.39	-9.9	-66.9	-7.1	0.17
FR3	0.63	4.09	0.33	-9.4	-63.3	-10.1	0.24
HA1	0.45	13.97	0.31	-8.8	-58.7	-11.0	0.84
HA2	0.20	3.97	0.35	-8.1	-54.3	-11.5	0.26
Choshui River							
11/03/2005	1.32	2.46	–	–	–	–	–
20/03/2005	1.24	2.18	–	–	–	–	–
11/04/2005	1.40	2.60	–	–	–	–	–
25/04/2005	1.51	2.95	–	–	–	–	–
10/05/2005	–	–	–	–	–	–	–
20/05/2005	1.73	0.98	–	–	–	–	–
27/05/2005	1.23	2.37	–	–	–	–	–
10/06/2005	1.18	2.59	–	–	–	–	–
20/06/2005	1.70	0.88	–	–	–	–	–
19/07/2005	0.39	1.30	–	–	–	–	–
16/09/2005	1.34	2.37	–	–	–	–	–
23/09/2005	–	–	–	–	–	–	–
20/10/2005	1.26	2.44	–	–	–	–	–
28/10/2005	1.23	3.09	–	–	–	–	–

Data Table F continued

Choshui River	SO_4^{2-} mmol.L^{-1}	HCO_3^- mmol.L^{-1}	SiO_2 mmol.L^{-1}	$\delta^{18}O$ ‰	δD ‰	$\delta^{13}C$ ‰	Saturation index (calcite)
09/11/2005	1.01	2.75	–	–	–	–	–
18/11/2005	1.03	2.68	–	–	–	–	–
29/11/2005	1.43	2.98	–	–	–	–	–
26/12/2005	1.06	3.21	–	–	–	–	–
25/01/2006	1.26	1.68	–	–	–	–	–
17/02/2006	1.13	2.25	–	–	–	–	–
14/03/2006	1.14	3.77	–	–	–	–	–
28/03/2006	2.26	2.18	–	–	–	–	–
21/04/2006	1.18	2.65	–	–	–	–	–
28/04/2006	–	–	–	–	–	–	–
09/05/2006	–	–	–	–	–	–	–
30/05/2006	1.00	1.94	–	–	–	–	–
07/06/2006	1.09	2.33	–	–	–	–	–
14/06/2006	1.00	2.09	–	–	–	–	–
03/07/2006	1.13	2.26	–	–	–	–	–
17/07/2006	0.87	1.95	–	–	–	–	–
31/07/2006	1.01	2.32	–	–	–	–	–
08/08/2006	1.08	2.19	–	–	–	–	–
22/08/2006	0.85	2.42	–	–	–	–	–
01/09/2006	0.70	2.12	–	–	–	–	–
22/09/2006	0.85	2.17	–	–	–	–	–
28/09/2006	0.76	2.48	–	–	–	–	–
19/10/2006	0.92	2.81	–	–	–	–	–
09/11/2006	1.26	2.53	–	–	–	–	–
17/11/2006	1.15	2.58	–	–	–	–	–
23/11/2006	0.96	2.18	–	–	–	–	–
06/12/2006	1.26	2.68	–	–	–	–	–
Hot Spring water	0.22	–	–	–	–	–	–

Data Table G. Results of three-end-member, two-tracer mixing and residual calculations with propagated errors.

	*f*1 (rain)	*f*2 (spring)	*f*3 (SW)	Ca^{2+}	*Ca* $^{2+}$ *σ/SE*	K^{+}	*K* $^{+}$ *σ/SE*	Mg^{2+}	*Mg* $^{2+}$ *σ/SE*
Pingtung Plain	**%**	**%**	**%**	**mmol.L^{-1}**	**mmol.L^{-1}**	**μmol.L^{-1}**	**mmol.L^{-1}**	**mmol.L^{-1}**	**mmol.L^{-1}**
ZM1	99.45	0.35	0.20	1.658	0.003	25.16	0.45	0.551	0.003
ZM2	99.37	0.45	0.18	1.560	0.003	34.92	0.48	0.619	0.003
ZM3	99.40	0.44	0.15	1.546	0.003	35.48	0.45	0.606	0.003
ZM4	99.25	0.46	0.29	1.473	0.003	32.76	0.64	0.607	0.004
HN1	99.69	0.17	0.14	3.359	0.007	64.74	0.33	0.932	0.003
HN2	99.86	0.14	0.00	1.529	0.003	23.80	0.12	0.478	0.001
HN3	99.76	0.15	0.09	1.121	0.002	24.93	0.21	0.287	0.001
CL1	99.22	0.39	0.39	4.332	0.009	102.71	0.82	1.055	0.005
CL2	99.74	0.24	0.02	1.385	0.003	50.50	0.22	0.565	0.002
CL3	99.40	0.07	0.53	0.600	0.002	-22.10	0.96	0.095	0.006
LY1	98.88	0.24	0.88	2.722	0.006	99.12	1.64	1.345	0.010
TK2	98.30	0.19	1.51	1.701	0.005	216.00	2.82	1.466	0.016
KT1	99.72	0.17	0.10	2.607	0.005	34.08	0.25	0.679	0.002
KT2	96.32	0.12	3.57	6.263	0.014	-332.76	6.41	0.521	0.037
HY1	98.85	0.61	0.54	3.507	0.007	899.65	2.26	0.876	0.006
HF1	99.82	0.13	0.05	2.787	0.005	28.49	0.15	0.853	0.002
HF2	99.84	0.16	0.01	1.153	0.002	20.54	0.13	0.379	0.001
HF3	99.72	0.28	0.00	1.629	0.003	20.28	0.22	0.539	0.002
HS1	99.78	0.11	0.11	3.181	0.006	35.08	0.24	0.767	0.002
HS2	99.84	0.15	0.02	2.182	0.004	20.49	0.12	0.592	0.002
HS3	99.87	0.11	0.02	2.132	0.004	27.62	0.11	0.590	0.002
HS4	99.94	0.05	0.02	1.934	0.004	32.03	0.08	0.568	0.001
QX1	99.64	0.24	0.12	3.736	0.007	242.22	0.60	0.667	0.002
QX2	99.78	0.19	0.03	2.465	0.005	26.91	0.17	0.682	0.002
QX3	99.60	0.37	0.03	1.500	0.003	25.20	0.29	0.435	0.002
WD1	99.40	0.30	0.30	4.566	0.009	145.38	0.69	0.867	0.004
WD2	99.79	0.19	0.02	2.382	0.005	28.11	0.16	0.670	0.002
WD3	99.78	0.22	0.00	1.451	0.003	21.77	0.18	0.281	0.001
TS1	99.87	0.11	0.02	0.566	0.001	14.20	0.10	0.367	0.001
TS2	99.89	0.10	0.00	0.382	0.001	12.34	0.08	0.281	0.001
YP1	99.94	0.05	0.01	2.030	0.004	19.17	0.06	0.804	0.002

Data Table G continued

	f 1 (rain)	*f* 2 (spring)	*f* 3 (SW)	Ca^{2+}	Ca^{2+} *σ/SE*	K^{+}	K^{+} *σ/SE*	Mg^{2+}	Mg^{2+} *σ/SE*
Pingtung Plain	**%**	**%**	**%**	**mmol.L^{-1}**	**mmol.L^{-1}**	**µmol.L^{-1}**	**mmol.L^{-1}**	**mmol.L^{-1}**	**mmol.L^{-1}**
YP2	99.92	0.07	0.01	1.168	0.002	14.36	0.06	0.566	0.001
MA1	99.83	0.15	0.01	2.178	0.004	25.45	0.13	0.795	0.002
MA2	99.89	0.10	0.01	1.751	0.003	30.06	0.10	0.552	0.001
MA3	99.96	0.04	0.01	1.532	0.003	33.23	0.08	0.504	0.001
Kaoping River									
07/03/2005	99.63	0.34	0.03	1.578	0.006	56.22	0.35	0.612	0.003
04/04/2005	99.78	0.20	0.02	1.411	0.005	56.50	0.27	0.642	0.003
09/04/2005	99.54	0.42	0.04	1.726	0.006	57.61	0.40	0.679	0.003
20/05/2005	99.79	0.20	0.01	1.308	0.005	70.53	0.31	0.516	0.002
06/06/2005	99.77	0.21	0.01	1.385	0.005	48.52	0.25	0.624	0.003
20/06/2005	99.81	0.18	0.01	1.283	0.005	52.57	0.24	0.534	0.002
01/07/2005	99.76	0.22	0.02	1.467	0.005	48.01	0.25	0.591	0.003
11/07/2005	99.68	0.27	0.05	1.732	0.006	61.73	0.34	0.663	0.003
18/07/2005	99.92	0.08	0.00	0.723	0.003	84.70	0.32	0.229	0.001
25/07/2005	99.83	0.16	0.01	1.275	0.004	89.72	0.36	0.486	0.002
01/08/2005	99.79	0.19	0.03	1.564	0.005	93.95	0.39	0.566	0.003
Choshui Plain									
CP1	83.164	0.130	16.706	1.132	0.036	-248.91	0.0369	-2.191	0.217
CP2	98.863	0.461	0.676	0.935	0.003	15.77	0.0015	0.125	0.009
PK1	99.577	0.417	0.006	0.916	0.002	37.10	0.0003	0.314	0.002
PK2	99.508	0.484	0.009	0.754	0.002	27.43	0.0004	0.167	0.001
GC1	98.741	0.555	0.704	3.737	0.010	1.05	0.0016	1.509	0.011
GC2	99.504	0.449	0.046	0.749	0.002	180.76	0.0006	0.440	0.002
GC3	99.525	0.465	0.009	0.676	0.002	33.35	0.0004	0.308	0.002
GC4	99.536	0.448	0.016	0.720	0.002	24.80	0.0004	0.180	0.001
GC5	99.410	0.559	0.031	0.959	0.003	29.12	0.0004	0.173	0.002
KH1	99.566	0.430	0.004	1.070	0.003	36.62	0.0003	0.736	0.003
KH2	99.585	0.415	0.000	1.880	0.005	31.70	0.0003	0.661	0.002
KH3	99.591	0.409	0.000	1.648	0.004	26.35	0.0003	0.438	0.002
KH4	99.492	0.507	0.001	1.394	0.004	29.85	0.0004	0.349	0.002
HL1	99.251	0.620	0.130	5.684	0.014	59.43	0.0006	2.109	0.007

Data Table G continued

	f 1 (rain)	*f* 2 (spring)	*f* 3 (SW)	Ca^{2+}	*Ca* $^{2+}$ *σ/SE*	K^{+}	*K* $^{+}$ *σ/SE*	Mg^{2+}	*Mg* $^{2+}$ *σ/SE*
Choshui Plain	**%**	**%**	**%**	**mmol.L^{-1}**	**mmol.L^{-1}**	**µmol.L^{-1}**	**mmol.L^{-1}**	**mmol.L^{-1}**	**mmol.L^{-1}**
HL2	99.413	0.588	-0.002	3.991	0.010	58.30	0.0005	1.666	0.005
DG1	99.271	0.420	0.309	0.719	0.002	36.26	0.0008	0.285	0.004
DG2	99.519	0.477	0.004	0.755	0.002	28.61	0.0004	0.150	0.001
FR1	99.080	0.733	0.187	5.225	0.013	86.75	0.0008	2.906	0.010
FR2	99.571	0.423	0.006	2.037	0.005	28.31	0.0003	0.695	0.003
FR3	99.932	0.065	0.003	1.503	0.004	30.18	0.0001	0.396	0.001
HA1	99.332	0.561	0.107	3.470	0.009	106.57	0.0006	1.197	0.004
HA2	99.490	0.505	0.005	1.080	0.003	28.29	0.0004	0.263	0.002
Choshui River									
11/03/2005	99.703	0.296	0.002	1.535	0.003	49.91	0.000	0.778	0.002
20/03/2005	99.761	0.236	0.003	1.443	0.003	51.99	0.000	0.685	0.002
11/04/2005	99.715	0.282	0.003	1.669	0.003	45.47	0.000	0.799	0.002
25/04/2005	99.723	0.264	0.013	1.865	0.003	52.01	0.000	0.846	0.002
10/05/2005	99.858	0.146	-0.004	1.071	0.002	74.30	0.000	0.433	0.001
20/05/2005	99.774	0.219	0.007	1.393	0.003	53.80	0.000	0.667	0.002
27/05/2005	99.726	0.271	0.003	1.481	0.003	42.78	0.000	0.735	0.002
10/06/2005	99.794	0.194	0.011	1.580	0.003	44.89	0.000	0.687	0.002
20/06/2005	99.779	0.216	0.005	1.347	0.002	44.80	0.000	0.657	0.002
19/07/2005	99.997	0.000	0.003	0.533	0.001	116.93	0.000	0.250	0.001
16/09/2005	99.685	0.313	0.002	1.537	0.003	62.92	0.000	0.789	0.002
23/09/2005	99.782	0.222	-0.005	1.103	0.002	96.34	0.000	0.532	0.001
20/10/2005	99.747	0.239	0.014	1.472	0.003	67.50	0.000	0.770	0.002
28/10/2005	99.753	0.230	0.017	1.634	0.003	78.41	0.000	0.779	0.002
09/11/2005	99.795	0.192	0.014	1.338	0.002	69.65	0.000	0.691	0.002
18/11/2005	99.806	0.179	0.015	1.291	0.002	69.67	0.000	0.709	0.002
29/11/2005	99.713	0.269	0.018	1.792	0.003	67.66	0.000	0.858	0.002
26/12/2005	99.802	0.173	0.025	1.525	0.003	80.09	0.000	0.730	0.002
25/01/2006	99.773	0.209	0.018	0.893	0.002	94.36	0.000	0.777	0.002
17/02/2006	99.825	0.146	0.029	1.021	0.002	104.69	0.000	0.794	0.002
14/03/2006	99.789	0.174	0.036	1.805	0.003	124.40	0.000	0.799	0.002
28/03/2006	99.679	0.317	0.004	1.975	0.004	78.51	0.000	0.983	0.002

Data Table G continued

	f 1 (rain)	*f* 2 (spring)	*f* 3 (SW)	Ca^{2+}	*Ca^{2+} σ/SE*	K^{+}	*K^{+} σ/SE*	Mg^{2+}	*Mg^{2+} σ/SE*
Choshui River	**%**	**%**	**%**	**mmol.L^{-1}**	**mmol.L^{-1}**	**µmol.L^{-1}**	**mmol.L^{-1}**	**mmol.L^{-1}**	**mmol.L^{-1}**
21/04/2006	99.705	0.286	0.010	1.443	0.003	63.21	0.000	0.721	0.002
28/04/2006	99.761	0.244	-0.005	1.197	0.002	55.79	0.000	0.576	0.001
09/05/2006	99.801	0.203	-0.004	1.252	0.002	53.48	0.000	0.613	0.002
30/05/2006	99.848	0.151	0.001	1.284	0.002	48.91	0.000	0.513	0.001
07/06/2006	99.780	0.216	0.004	1.425	0.003	69.48	0.000	0.681	0.002
14/06/2006	99.826	0.173	0.001	1.312	0.002	93.94	0.000	0.598	0.001
03/07/2006	99.786	0.210	0.004	1.416	0.003	61.58	0.000	0.678	0.002
17/07/2006	99.800	0.200	0.000	1.159	0.002	73.77	0.000	0.542	0.001
31/07/2006	99.785	0.214	0.001	1.395	0.003	67.42	0.000	0.639	0.002
08/08/2006	99.778	0.221	0.001	1.342	0.002	58.78	0.000	0.671	0.002
22/08/2006	99.866	0.125	0.010	1.262	0.002	57.96	0.000	0.568	0.001
01/09/2006	99.897	0.095	0.008	1.092	0.002	51.97	0.000	0.478	0.001
22/09/2006	99.826	0.171	0.003	1.207	0.002	48.91	0.000	0.557	0.001
28/09/2006	99.992	0.000	0.009	1.226	0.002	53.18	0.000	0.548	0.001
19/10/2006	99.987	-0.001	0.014	1.379	0.003	70.89	0.000	0.646	0.002
09/11/2006	99.993	0.000	0.007	1.553	0.003	50.52	0.000	0.776	0.002
17/11/2006	99.770	0.223	0.007	1.478	0.003	54.22	0.000	0.716	0.002
23/11/2006	99.996	0.000	0.004	1.250	0.002	49.33	0.000	0.580	0.001
06/12/2006	99.753	0.238	0.009	1.587	0.003	55.29	0.000	0.750	0.002

Data Table G continued

Pingtung Plain	Na^+ mmol.L^{-1}	Na^+ σ/SE mmol.L^{-1}	SO_4^{2-} μmol.L^{-1}	SO_4^{2-} σ/SE μmol.L^{-1}	Li^+ nmol.L^{-1}	L^+ σ/SE mmol.L^{-1}	HCO_3^- mmol.L^{-1}	HCO_3^- σ/SE mmol.L^{-1}
ZM1	0.727	0.020	-53.5	1.2	-0.12	∞	5.318	0.046
ZM2	0.896	0.020	-47.4	1.2	-0.12	∞	5.470	0.048
ZM3	1.050	0.019	-39.3	1.0	-0.12	∞	5.522	0.048
ZM4	1.196	0.028	-78.8	1.8	-0.12	∞	5.648	0.049
HN1	0.616	0.013	1420.7	4.5	-0.12	∞	6.564	0.056
HN2	0.848	0.004	624.0	1.9	-0.12	∞	3.705	0.032
HN3	1.998	0.010	489.9	1.7	-0.12	∞	3.878	0.033
CL1	1.113	0.035	2120.1	7.2	-0.12	∞	7.761	0.067
CL2	2.530	0.009	6.8	0.2	-0.12	∞	6.511	0.056
CL3	1.815	0.046	-148.1	3.3	-0.12	∞	3.525	0.030
LY1	1.475	0.075	1071.4	6.8	-0.12	∞	7.686	0.066
TK2	0.622	0.128	-415.6	9.4	-0.13	∞	8.194	0.070
KT1	0.570	0.010	594.0	2.0	-0.12	∞	6.090	0.052
KT2	-9.132	0.300	-299.7	22.3	-0.14	∞	5.445	0.047
HY1	-0.122	0.049	1003.4	4.9	-0.12	∞	7.493	0.065
HF1	0.177	0.006	959.5	3.0	-0.12	∞	5.616	0.048
HF2	0.380	0.005	528.2	1.6	-0.12	∞	2.288	0.020
HF3	0.650	0.008	782.1	2.4	-0.12	∞	3.452	0.030
HS1	0.025	0.010	1394.0	4.4	-0.12	∞	5.099	0.043
HS2	0.347	0.005	784.0	2.4	-0.12	∞	4.394	0.037
HS3	0.279	0.004	801.3	2.5	-0.12	∞	4.174	0.035
HS4	0.262	0.002	683.5	2.1	-0.12	∞	3.659	0.031
QX1	0.392	0.013	987.2	3.2	-0.12	∞	7.496	0.064
QX2	0.450	0.006	805.2	2.5	-0.12	∞	5.184	0.044
QX3	1.414	0.012	15.2	0.3	-0.12	∞	5.313	0.046
WD1	0.122	0.027	1947.8	6.5	-0.12	∞	7.384	0.063
WD2	0.400	0.006	974.6	3.0	-0.12	∞	4.608	0.039
WD3	1.024	0.007	143.7	0.5	-0.12	∞	4.244	0.036
TS1	0.303	0.004	200.9	0.64	-0.12	∞	1.265	0.011
TS2	0.433	0.003	113.0	0.36	-0.12	∞	1.442	0.012
YP1	0.236	0.002	1223.2	3.73	-0.12	∞	3.371	0.029

Data Table G continued

	Na^+	Na^+ σ/SE	SO_4^{2-}	SO_4^{2-} σ/SE	Li^+	L^+ σ/SE	HCO_3^-	HCO_3^- σ/SE
Pingtung Plain	mmol.L^{-1}	mmol.L^{-1}	µmol.L^{-1}	µmol.L^{-1}	nmol.L^{-1}	mmol.L^{-1}	mmol.L^{-1}	mmol.L^{-1}
YP2	0.268	0.002	592.9	1.82	-0.12	∞	2.397	0.020
MA1	0.213	0.005	936.3	2.87	-0.12	∞	4.107	0.035
MA2	0.277	0.003	802.0	2.45	-0.12	∞	3.174	0.027
MA3	0.334	0.001	739.2	2.26	-0.12	∞	2.867	0.024
Kaoping River								
07/03/2005	0.566	0.011	916.5	5.0	-0.12	∞	1.262	0.021
04/04/2005	0.588	0.007	854.4	4.7	-0.12	∞	1.245	0.020
09/04/2005	0.535	0.013	937.6	5.2	-0.12	∞	1.326	0.022
20/05/2005	0.324	0.006	780.9	4.3	-0.12	∞	0.920	0.015
06/06/2005	0.359	0.007	800.7	4.4	-0.12	∞	1.016	0.016
20/06/2005	0.259	0.005	669.6	3.7	-0.12	∞	0.889	0.014
01/07/2005	0.331	0.007	760.7	4.2	-0.12	∞	1.027	0.016
11/07/2005	0.304	0.009	872.9	4.8	-0.12	∞	1.113	0.018
18/07/2005	0.116	0.002	281.9	1.5	-0.12	∞	0.538	0.008
25/07/2005	0.247	0.005	586.4	3.2	-0.12	∞	0.926	0.015
01/08/2005	0.302	0.006	737.4	4.1	-0.12	∞	1.088	0.017
Choshui Plain								
CP1	-9.014	1.987	-2758.0	134.5	-0.12	∞	-5.809	0.064
CP2	1.637	0.083	-39.6	5.5	-0.15	∞	3.880	0.043
PK1	2.227	0.014	10.3	0.3	-0.15	∞	4.729	0.052
PK2	1.652	0.015	35.4	0.4	-0.15	∞	3.481	0.039
GC1	1.070	0.086	2847.7	13.0	-0.15	∞	5.901	0.065
GC2	1.903	0.016	-1.5	0.5	-0.15	∞	4.491	0.049
GC3	1.745	0.015	12.2	0.3	-0.15	∞	3.748	0.042
GC4	1.001	0.014	65.7	0.4	-0.15	∞	2.722	0.031
GC5	1.289	0.017	131.4	0.7	-0.15	∞	3.352	0.038
KH1	0.575	0.013	15.9	0.3	-0.15	∞	4.219	0.046
KH2	0.489	0.012	889.2	3.4	-0.15	∞	3.850	0.042
KH3	1.194	0.012	673.6	2.6	-0.15	∞	4.069	0.045
KH4	1.342	0.015	541.8	2.1	-0.15	∞	3.804	0.042
HL1	0.165	0.024	4112.4	16.0	-0.15	∞	7.623	0.083

Data Table G continued

	Na^+	Na^+ σ/SE	SO_4^{2-}	SO_4^{2-} σ/SE	Li^+	L^+ σ/SE	HCO_3^-	HCO_3^- σ/SE
Choshui Plain	mmol.L^{-1}	mmol.L^{-1}	µmol.L^{-1}	µmol.L^{-1}	nmol.L^{-1}	mmol.L^{-1}	mmol.L^{-1}	mmol.L^{-1}
HL2	0.622	0.017	2766.5	10.6	-0.15	∞	6.496	0.071
DG1	2.181	0.040	-67.1	2.5	-0.15	∞	4.384	0.048
DG2	1.469	0.015	23.9	0.4	-0.15	∞	3.288	0.037
FR1	0.861	0.031	3856.9	15.1	-0.15	∞	9.541	0.104
FR2	0.714	0.013	1106.9	4.3	-0.15	∞	4.018	0.044
FR3	1.507	0.005	628.7	2.4	-0.15	∞	4.083	0.044
HA1	4.628	0.025	420.1	2.0	-0.15	∞	13.880	0.149
HA2	1.548	0.016	197.9	0.9	-0.15	∞	3.896	0.043
Choshui River								
11/03/2005	0.376	0.009	1314.0	3.7	-0.15	∞	2.413	0.020
20/03/2005	0.339	0.007	1240.6	3.5	-0.15	∞	2.149	0.018
11/04/2005	0.353	0.008	1392.6	3.9	-0.15	∞	2.553	0.021
25/04/2005	0.419	0.008	1503.8	4.3	-0.15	∞	2.907	0.024
10/05/2005	0.339	0.004	-0.1	0.1	-0.15	∞	-0.022	0.003
20/05/2005	0.264	0.007	1722.8	4.9	-0.15	∞	0.950	0.009
27/05/2005	0.305	0.008	1228.8	3.5	-0.15	∞	2.330	0.019
10/06/2005	0.379	0.006	1173.5	3.3	-0.15	∞	2.557	0.021
20/06/2005	0.253	0.006	1696.3	4.8	-0.15	∞	0.852	0.008
19/07/2005	0.458	0.001	390.1	1.1	-0.15	∞	1.302	0.010
16/09/2005	0.278	0.009	1338.9	3.8	-0.15	∞	2.322	0.019
23/09/2005	0.205	0.007	-0.1	0.2	-0.15	∞	-0.033	0.004
20/10/2005	0.403	0.007	1253.6	3.5	-0.15	∞	2.400	0.020
28/10/2005	0.633	0.007	1224.8	3.5	-0.15	∞	3.055	0.025
09/11/2005	0.642	0.006	1006.8	2.9	-0.15	∞	2.725	0.022
18/11/2005	0.659	0.006	1026.5	2.9	-0.15	∞	2.653	0.021
29/11/2005	0.488	0.008	1425.6	4.0	-0.15	∞	2.937	0.024
26/12/2005	0.754	0.006	1050.8	3.0	-0.15	∞	3.184	0.025
25/01/2006	0.729	0.007	1253.6	3.6	-0.15	∞	1.647	0.014
17/02/2006	0.779	0.006	1119.5	3.2	-0.15	∞	2.230	0.018
14/03/2006	0.784	0.007	1129.5	3.2	-0.15	∞	3.744	0.030
28/03/2006	0.614	0.009	2252.3	6.3	-0.15	∞	2.129	0.018

Data Table G continued

Choshui River	Na^+ mmol.L^{-1}	Na^+ σ/SE mmol.L^{-1}	SO_4^{2-} µmol.L^{-1}	SO_4^{2-} σ/SE µmol.L^{-1}	Li^+ nmol.L^{-1}	L^+ σ/SE mmol.L^{-1}	HCO_3^- mmol.L^{-1}	HCO_3^- σ/SE mmol.L^{-1}
21/04/2006	0.594	0.009	1174.8	3.3	-0.15	∞	2.611	0.021
28/04/2006	0.442	0.007	-0.1	0.2	-0.15	∞	-0.036	0.005
09/05/2006	0.419	0.006	-0.1	0.1	-0.15	∞	-0.030	0.004
30/05/2006	0.334	0.005	1002.6	2.8	-0.15	∞	1.914	0.015
07/06/2006	0.235	0.006	1088.5	3.1	-0.15	∞	2.295	0.019
14/06/2006	0.202	0.005	997.5	2.8	-0.15	∞	2.064	0.017
03/07/2006	0.275	0.006	1122.5	3.2	-0.15	∞	2.224	0.018
17/07/2006	0.212	0.006	868.8	2.5	-0.15	∞	1.921	0.016
31/07/2006	0.216	0.006	1009.4	2.8	-0.15	∞	2.292	0.019
08/08/2006	0.243	0.006	1078.4	3.0	-0.15	∞	2.160	0.018
22/08/2006	0.455	0.004	845.1	2.4	-0.15	∞	2.397	0.019
01/09/2006	0.399	0.003	695.5	2.0	-0.15	∞	2.104	0.017
22/09/2006	0.303	0.005	845.9	2.4	-0.15	∞	2.147	0.017
28/09/2006	0.477	0.002	752.6	2.1	-0.15	∞	2.482	0.019
19/10/2006	0.605	0.002	917.3	2.6	-0.15	∞	2.805	0.022
09/11/2006	0.389	0.002	1254.0	3.5	-0.15	∞	2.530	0.020
17/11/2006	0.418	0.007	1143.6	3.2	-0.15	∞	2.546	0.021
23/11/2006	0.430	0.001	957.9	2.7	-0.15	∞	2.177	0.017
06/12/2006	0.459	0.007	1251.0	3.5	-0.15	∞	2.640	0.021